Physical Characterization of

Tin Composite Oxides and Related Anode Materials

For Lithium Ion Batteries

by

Gillian Ruth Goward

A thesis
presented to the University of Waterloo
in fulfillment of the
thesis requirement for the degree of

Doctor of Philosophy
In
Chemistry

Waterloo, Ontario, Canada, 1999

The University of Waterloo requires the signatures of all persons using or photocopying this thesis Please sign below, and give address and date.

Abstract

This thesis addresses the issues concerning the excellent electrochemical performance exhibited by the tin-composite-oxide glass, $Sn_{1.0}Al_{0.42}B_{0.56}P_{0.40}O_{3.6}$ as an anode material for rechargeable lithium ion batteries. The debate surrounding this material focuses on the nature of the lithium-tin interaction: whether it is ionic or intermetallic. The TCO anode material has been studied electrochemically, as well as by multinuclear Solid-State-NMR, X-ray Absorption Spectroscopy, and X-ray Scattering including Pair Distribution Function analysis. By examining electrode materials at various stages of discharge, corresponding to various levels of lithium insertion, the interactions between lithium, tin, oxygen, and the other components of the glass have been ascertained. The inserted lithium remains highly ionic throughout the first cycle of the cell, with no evidence for the formation of alloy phases. Extended cycling of the cell results in the formation of alloy-like domains in the parent material, SnO, but not in the case of TCO. This demonstrates that the required structural rearrangements for the formation of Li-Sn phases are kinetically prohibited; and this to a greater extend in TCO than in SnO. Two key factors account for the electrochemical properties of TCO: 1) the participation of the glass framework in sequestering the electrochemically active tin centers and providing a flexible framework for the reversible insertion of lithium 2) the proximity of oxygen to tin is maintained throughout lithium insertion process, thus oxygen may act as a charge carrier. These factors are developed in the context of several models for the interactions in the electrode, drawing on the data obtained from the physical characterizations implemented here. A comparative study of the anode material $NaMoO_3$ is also described.

Acknowledgments

When one arrives at the conclusion of such an endeavour, there are inevitably numerous people whose wisdom, leadership, support and friendship have been invaluable during the process.

I would like to begin by thanking by co-supervisors, Professors Linda Nazar and Bill Power. Thank you for your scientific creativity, your patience, and your guidance. Thanks as well to my lab mates, Tracy, Morven, Denise, Patricia, Chris, Mike, Joel, Jiangshan, Huan, Jianquan, and Fabrice, for providing an environment for lively debate and interaction, whether concerning our scientific projects, or the latest world news! A special thanks goes to Denise and Tracy for your faithfulness and friendship, particularly in the last few months.

In the various projects we have undertaken, several people have lent scientific support and insight. Thanks very much to Jim Garrett at McMaster University for his help in the synthesis of the TCO glasses. Thanks to Dr. Wojtek Dmowski and Professor Takeshi Egami for their help in acquiring and processing the PDF data. The time at the beamline was an experience to remember! Thanks to Dr. Fabrice Leroux and Professor Guy Ouvrard for acquiring and processing the XAS data.

Throughout my thesis project the members of my advisory committee have offered insights, direction and advice on several topics. Thanks goes to each of them, Profs. Richard Oakley, Ken Jeffery, Jean Duhamel and Clare Grey.

I also want to thank the friends and family who have prayed for, supported, and loved me throughout the years. Especially, I am grateful to a group of teens at Community Fellowship Church, whose passion for life and for God have challenged and encouraged me continually in the last three years. Thank you for helping me keep life in perspective. Finally, I thank God every day for my husband, James, and my parents and sisters. You are such a blessing to me.

And now unto him how is able to keep you from falling, and to present you before his glorious presence without fault and with great joy – to the only God our Saviour, be glory, majesty, power, and authority for ever and ever. Amen.

Jude 24,25.

Table of Contents

List of Tables

List of Figures

Chapter 1

Chapter 2

Chapter 3

Chapter 4

Chapter 5

Chapter 6

Chapter 7

Abbreviations

TCO	- Tin Composite Oxide
NMR	- Nuclear Magnetic Resonance
MAS	- Magic Angle Spinning
FID	- Free Induction Decay
le LURE	- le Laboratoire d'Utilisation du Rayonnement Electromagnetique
BNL	- Brookhaven National Labs
NSLS	- National Synchrotron Light Source
PXRD	- Powder X-ray Diffraction
PDF	- Pair Distribution Function
XAS	- X-ray absorption Spectroscopy
EXAFS	- Extended X-ray Absorption Fine Structure
XANES	- X-ray Absorption Near Edge Structure
DOS	- Density of States
YaEHMOP	- Yet another Extended Huckel Molecular Orbital Package

Preface

"The fugue is a contrapuntal composition in which a theme or subject of strongly marked character pervades the entire fabric, entering now in one voice and now in another. The subject constitutes the unifying idea, the focal point of interest in the contrapuntal web." *J.Machlis* *The Enjoyment of Music*

The crafting of a thesis is similar to a common musical form, the *prelude and fugue*, which achieved unsurpassable heights at the hands of J.S. Bach. This analogy will be drawn upon throughout the thesis, to bring out the subject as it is addressed in various voices, supported by the contrapuntal texture of the contributing data. The concept of counterpoint was a familiar technique to composers, as the concept of multi-disciplined study is a strength of scientific endeavours. Thus in the fugue one subject or theme, when articulated in many voices becomes musically beautiful. By analogy, the crux of a thesis, when approached with many instruments becomes elegant in its simplicity, while complex in the counterpoints (data) which support the idea.

It is the intent of this author to use the metaphor of the fugue to guide the reader's train of thought during the development of this thesis. The myriad of results may seem as complicated as the voices of a fugue. Yet the way in which these results are presented is designed to give the reader a clear picture of the unifying ideas and their support, found in the contrapuntal voices of the data.

Many sections of the thesis are written in the style of a prelude, presenting previously published data in order to provide context. The development of the theoretical aspects of specific techniques is analogous to the episodes which introduce the main theme of the fugue. The data themselves are presented in the context of each technique and its use in related work. Each technique used to address the issues presented can be considered a different instrument, each of which are given a turn to echo the theme, using its own voice. Thus the counterpoint is created by the complementary data obtained from the diverse selection of techniques, each focusing on the unifying idea from a different perspective.

Chapter 1 Introduction and Motivation

Lithium ion batteries have revolutionized the rechargeable battery industry over the last 10 years. Prior to the conception of lithium ion batteries, the development of reusable energy storage was hampered by a dependency on high cost, high toxicity materials such as the commercialized nickel-cadmium system. Although there are many challenges yet to overcome, the lithium ion battery offers a cost effective, non-toxic, reusable source of energy. As our society depends more and more on portable electronics, today's consumers increasingly demand reliable light weight energy sources.

The chemistry of these systems is incredibly intricate and complex. Interplay between the various components of the battery system place stringent demands on the materials involved. The desire to improve the basic components: the cathode (positive electrode), anode (negative electrode) and electrolyte, drives multi-million dollar research programs world-wide. The materials science behind the cathode and anode materials has been the focus of research groups working in areas as diverse as transition metal oxide solid state synthesis to the chemistry of conductive polymers. A wide variety of criteria must be met for a material to be considered a candidate as a cathode or anode. These criteria, as well as the methods of evaluating battery performance, and the commercially viable candidates for both cathodes and anodes will be presented in the introduction. The focus of this thesis has been on the new class of tin-composite-oxide (TCO) glasses presented by Fuji as candidates for anode materials in lithium ion batteries. Thus a detailed history of the electrochemistry of tin metal and other tin-based electrodes is presented in Chapter 3.

1.1 Motivation for the Project

This thesis focuses on the tin-composite oxide (TCO) glass of composition $Sn_{1.0}Al_{0.42}B_{0.56}P_{0.40}O_{3.6}$. The interest in this system as an anode material began with the reports, including patents as well as a publication in *Science*, that documented the superior electrochemical performance of this composite compared to graphitic carbon as an anode material.[1] Immediately following the introduction of this material, controversy arose as to the mechanism of lithium insertion into these types of materials. While Idota and co-workers

stated in their original report that the process was one of 'lithium insertion' and thus the lithium remained in an ionic environment, reports by Dahn and co-workers presented an alternate mechanism, in which the lithium reacts with the anode *via* the reduction of tin to tin metal, and subsequently to the various Li-Sn alloy phases. In the latter case the lithium is anticipated to take on metallic, or inter-metallic character.

Our motivation in this project was to improve the understanding of these materials and resolve this controversy. Following a thorough investigation of the electrochemical data as well as systematic studies of the electrode materials using solid-state-NMR, X-ray absorption spectroscopy and X-ray scattering we have established a clearer picture as to the mechanisms and characteristics to explain the enhanced performance of these anodes. This thesis attempts to bring reconciliation to these seemingly opposing mechanisms.

1.2 Layout of this Thesis

The thesis comprises a series of chapters each of which address one technique used to study the TCO system. These chapters include a discussion of relevant theory and a review of the background of other investigations on electrode systems using the given technique. Subsequently the experimental method, the results obtained, and a discussion of the results in the context of the broader picture of the thesis are presented. Chapter 2 presents the synthesis of the tin composite glasses and the lithium-tin line phases, as well as their characterization using X-ray diffraction. Chapter 3 gives a detailed background of the properties of tin-based electrode materials and presents the electrochemical results obtained for TCO glasses and their parent tin oxides. Chapter 4 introduces solid-state-NMR including a synopsis of the various studies that have used NMR to investigate electrochemical systems, followed by the multi-nuclear NMR results obtained for the tin-based electrodes. Chapter 5 presents a series of density of states extended Hückel calculations showing the electron density on lithium in the various Li-Sn alloys. Chapter 6 presents two complementary X-ray studies; the X-ray absorption spectroscopy (XAS) results obtained at le LURE in France, and the X-ray diffraction data, obtained at the National Synchrotron Light Source (NSLS) at Brookhaven National Laboratory, which was analyzed using the pair-distribution-function (PDF) method.

Chapter 7 presents a parallel study of a contrasting anode material, $NaMoO_3$, and draws comparisons to the tin oxide systems. The thesis is completed with a summary of the results, offering several insights and conclusions, as well as a proposal for future studies.

1.3 Electrochemistry Basics

The defining feature of an electrochemical cell is the generation of electronic current which passes through an external circuit, caused by the chemical reaction between the two electrodes. In the case of a Li-ion cell, lithium ions pass from one electrode to the other *via* the electrolyte concurrent with the movement of the electrons through the external circuit. A cell that has not reached chemical equilibrium can do electrical work as the reaction between the electrodes drives electrons through an external circuit. The amount of work that a given transfer of electrons can accomplish depends on the difference in chemical potential between the positive and negative electrodes. For this reason a low work function at the negative electrode, coupled with a high work function at the positive electrode will give a cell with a maximized voltage difference. The two redox processes, or half reactions, are physically separated from one another by the ionically conductive but electronically insulating separator. The amount of work that the cell is able to do is determined by the potential difference between the electrodes. The potential difference $\Delta\varepsilon_{00}$ between the standard electrode potential of the two half reactions, $\Delta\varepsilon_0$, gives the voltage of the cell. Thus, the greater the difference in the work functions of the two electrodes, the greater the voltage of the cell. Lithium metal has a strongly negative standard potential, $\Delta\varepsilon_0$ = -3.02 vs H_2 /$2H^+$ and is therefore an ideal candidate for a negative electrode. **Figure 1.1** shows a schematic of the standard potentials of a variety of materials, of interest in secondary batteries.

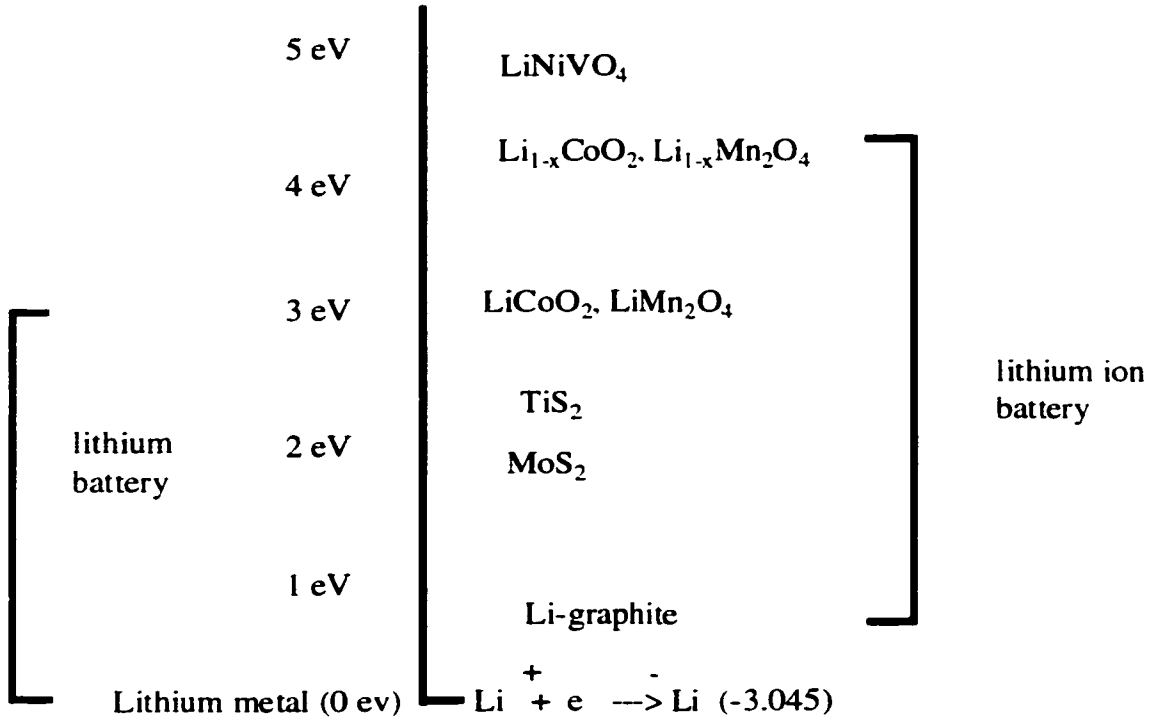

Figure 1.1 Chemical Potential/Redox scale with respect to Lithium

Thermodynamically, the electrochemical reaction is described by the changing concentration of the guest lithium atoms. The change in the Gibbs free energy, G, at constant temperature and pressure is related to the number of inserted lithium atoms by the chemical potential, μ.[2]

$$\mu = \left(\delta G / \delta n\right)_{T,P} \tag{1.1}$$

The chemical potential is measured directly from the voltage difference between the electrodes. For example, consider an intercalation electrode with chemical potential μ, in a cell with lithium metal as the counter electrode, having chemical potential μ_o. For every electron which is passed through the external circuit, moving through a potential difference of $\Delta\varepsilon_{00}$, the amount of work done to insert the corresponding lithium ion into the intercalation host is given by

$$\mu - \mu_o = -e\Delta\varepsilon_{00} \tag{1.2}$$

where e is the charge on an electron. For ions with charge greater than 1, a factor z is added to the equation. Since the focus of this thesis is on lithium ion batteries, where lithium has a charge of +1, z has been omitted from the equation.

During discharge of a cell, the measure of the chemical potential which varies with the insertion of lithium into a host is given by measuring the cell voltage at equilibrium as a function of the charge passed between the electrodes. The cell is completely discharged when the value of $\Delta\varepsilon_{00}$ reaches zero, and the chemical potentials of the two electrodes are equal.

In the general case, for liquids, the chemical potential of a cell half reaction, μ_i is related to the concentration, c_i of the species which reacts at that electrode, according to[3]

$$\mu_i = \mu_{i,0} + RT \ln c_i \tag{1.3}$$

The Nernst equation is the most important electrochemical descriptor: relating the concentration dependence c_i of the equilibrium voltage, $\Delta\varepsilon_0$, for a half cell to the standard potential, $\Delta\varepsilon_{00}$, and Faraday's constant, F.

$$\Delta\varepsilon_0 = \Delta\varepsilon_{00} + \frac{RT}{zF} * \sum \nu_i * \ln c_i \tag{1.4}$$

Faraday's law will be described in reference to particular sites for lithium insertion and the various types of electrode materials which can be considered in the section on cathode materials (1.6.2).

Discharging a cell requires the movement of Li^+ ions from one electrode to the other. This reaction can be described mathematically as[3]

$$m = \frac{M}{zF} * It \tag{1.5}$$

where m is the active mass or amount of lithium exchanged, M is the molar mass of lithium, z is the number of electrons exchanged (one in this case), and F is Faraday's constant. The details of the particular electrochemical experiments used in this thesis are described in Chapter 3.

1.4 Thermodynamics of Solid State Electrochemistry

The insertion reaction of lithium ions into a host can be generalized as follows

$$\Delta x Li^+ + \Delta x e^- + Li_x MX \underset{Charge}{\overset{Discharge}{\rightleftharpoons}} Li_{x+\Delta x}\, MX$$

where x is greater than or equal to zero, X is either an oxide or sulfide, and M is the transition metal ion. Two important factors determine the voltage (V) of the cell. The open circuit voltage of the cell, which is the difference between the chemical potential of lithium in the two electrodes, $\mu_{Li}^{cathode}$ and μ_{Li}^{anode}, is expressed as[4]

$$V = -\frac{(\mu_{Li}^{cathode} - \mu_{Li}^{anode})}{nF} \qquad (1.6)$$

where n is the number of electrons transferred, and F is Faraday's constant. To ensure a large cell voltage, the cathode material of choice must have a low μ_{Li}, which can be broken down into a contribution from the lithium ion and the corresponding electron.

$$\mu_{Li}^{cathode} = \mu_{Li^+}^{cathode} + \mu_{e^-}^{cathode} \qquad (1.7)$$

where μ_{Li^+} and μ_{e^-} are the chemical potentials of the lithium ion and electron respectively. From this description it is apparent that the potential of the cathode, and thus the voltage of the cell is dependent on the energy of the lithium ions and electrons in the host. Moreover, electrons which are inserted into the host will be inserted into the Fermi level, E_F of the cathode,

$$E_f = \mu_{e^-} \qquad (1.8)$$

Hence the desirable cathode material will have a low Fermi level, giving rise to a high overall cell potential. The position of the Fermi level is determined by the energies of the valence bands. Thus oxides, whose valence band is primarily 2p in character, will have a lower Fermi level than corresponding sulfides, which have a predominantly 3p valence band. For this reason, oxides are favoured as cathode materials. Within the various transition metal oxides, the d level orbitals of the cations determine the Fermi level of the material. These are described individually for the industrially attractive transition metal oxides.

Electrochemical intercalation is the most common form of lithium insertion into cathode materials. This process is a solid state reaction in which one chemical species (Li^+) is

inserted into the host structure. Two simultaneous processes occur: the intercalation of a cation into a crystallographically accessible site in the host matrix; and the addition of a corresponding electron to the host acceptor. Thus the cathode material must include a reducible or oxidizable element, as well as crystallographic sites which are able to accept the inserted cation. These materials may be classified into three groups, based on the thermodynamics of their redox reactions.[5] **Type I** materials are characterized by solid solution behaviour. This means that the integrity of the host material is maintained throughout the lithium insertion process, with the sole variation being the changing oxidation state of the host and the concurrent variation of the concentration of the guest (Li^+). In **Type II** materials the insertion of lithium causes phase transitions (either structural or electronic or both) in the host material. The origin of such changes can be electrostatic interactions (such as staging in graphite), elastic constraint, caused by the reduction or oxidation of the metal, or Jahn-Teller distortions. **Type III** materials are those which are unstable with respect to lithium insertion and undergo drastic irreversible phase changes. The tin-oxide-based anode materials discussed in this thesis are classed as Type III materials.

The intercalation process in a solid solution (Type I) material, is characterized by the Nernst equation, where x_i represents insertion of an ion (Li^+) into a site x, and $x_{i(max)}$ represents the maximum concentration of ions in site x. In this case it is assumed that there is no interaction between the inserted ions.

$$\mu_{Li+} = \mu^o_{Li+} + RT \ln \frac{x_i}{x_{i(\max)} - x_i} \tag{1.9}$$

Similarly, the insertion of the corresponding electrons into the host lattice is described by the Nernst equation, where x_e represents the sites that can be occupied by electrons.

$$\mu_e = \mu^o_e + RT \ln \frac{x_e}{x_{e(\max)} - x_e} \tag{1.10}$$

Putting the ionic and electronic contributions together yields

$$\mu_{Li} = \mu^o_{Li} + \nu RT \ln \frac{x}{1-x} \tag{1.11}$$

where ν equals 1 or 2. For ν = 1, the system is limited by the number of ionic sites or electronic sites in the host, such that there are either more oxidizable metal ions than sites for lithium ion insertion, or *vice versa*. In the case where ν = 2, both electronic and ionic sites are

limiting, and the amount of energy to intercalate an equivalent amount of lithium is greater than in the case of $v = 1$.

By setting the potential of lithium (μ_{Li}°) as a reference, equal to zero, we obtain

$$E = E^{o} + \frac{vkT}{e} \ln \frac{x}{1-x} \tag{1.12}$$

To this equation we can add contributions for the attraction or repulsion between lithium, which will change as a function of the amount of lithium inserted. This yields

$$E = E^{o} - \gamma U(x)x + \frac{vkT}{e} \ln \frac{x}{1-x} \tag{1.13}$$

where γ is the number of nearest neighbors in the first shell of lithium, and U is either positive or negative, resulting in attraction or repulsion between lithium ions respectively. These descriptions apply to solid solution insertion.

Typical voltage profiles for systems under thermodynamic equilibrium in which a phase transformation occurs during electrochemical insertion of lithium consist of steps and plateaux. The steps, illustrated in **Figure 1.2a**, are two-phase regions, in which the voltage is constant during the transformation of one phase into another. The single-phase regions correspond to the sharp steps in voltage, where no corresponding change in composition is

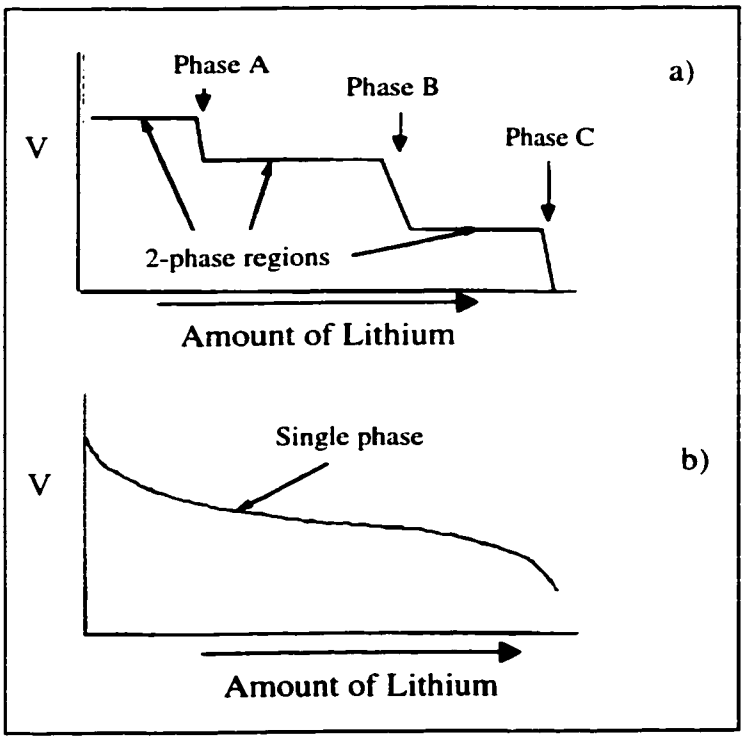

Figure 1.2 Schematic voltage profiles of a) 2-phase processes, and b) a single phase process.[6]

observed. In contrast to this, the voltage profiles of amorphous or glassy materials are very smooth, sloped curves, in which no clear steps are distinguished (illustrated in **Figure 1.2b**). This is representative of the electrochemical processes taking place, in which the lithium insertion occurs over a range of voltages, with no clearly defined two phase, or single phase regions. Such a voltage profile is also observed in systems which are far from equilibrium during electrochemical lithium insertion.[6]

1.5 Evaluating Battery Performance

Due to the range of applications that utilize portable energy sources, and their diverse demands, no single battery is able to meet all of the criteria required by every system. For example, the same battery that meets the low constant current consumption required by watches or heart pace makers will not be effective as a starter battery for a vehicle, or for the continuous higher energy density required in a laptop, camcorder, or cellular phone. The diverse demands for energy sources have led to the innumerable variety of batteries available on the market today. Yet improvements are still being made, as materials are developed which last longer and provide more power. Six criteria are important for evaluating a rechargeable battery: potential, discharge/charge profile, capacity, energy density, coulombic efficiency, and cycle life.

The first criteria used to evaluate battery performance is the potential difference between the two electrodes, which should be maximized within the limits of the electrolyte. For example, the commercialized $LiCoO_2$ cathode material when coupled with a metallic lithium anode gives a voltage of greater than 4V. Secondly, the electrical power produced by the cell, which is the product of current and voltage, P = I*V, should be maximized. The power density of the cell is given in W/kg.[3]

Another tool for measuring the performance of a battery is the characteristic discharge/charge curve for the material. A sample electrochemical curve is shown in **Figure 1.3**. A plot of voltage versus capacity should ideally have a constant voltage for the entirety of the cell capacity, such that the voltage of the cell drops to zero only when the stored energy is completely consumed. The rate at which the cell can be discharged is also critical. The discharge rate, C is the reciprocal of the time required to discharge the cell. For example,

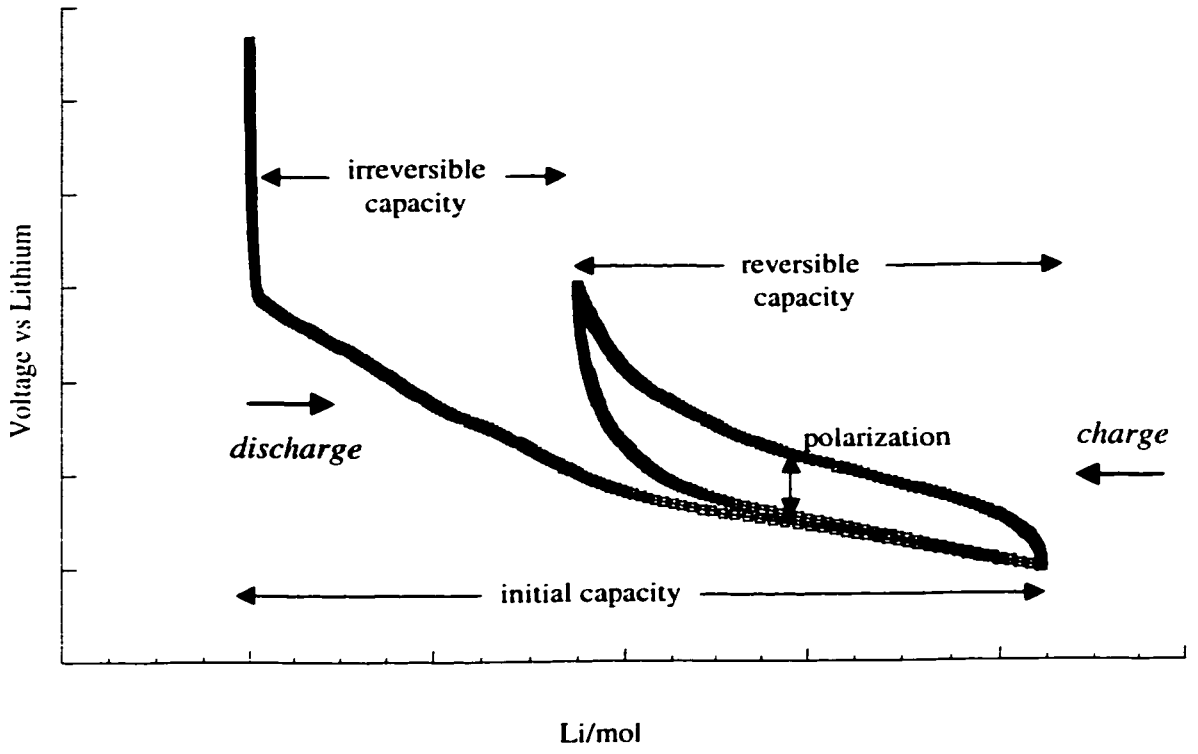

Figure 1.3 Voltage profile showing the initial, irreversible and reversible capacities of a typical electrochemical cell.

C/10 corresponds to discharging the cell over a period of 10 hours. For a given material, increasing the discharge rate decreases the obtainable capacity of the cell, since the kinetics of the reaction may not be fast enough to respond to extremely high currents.

Specific energy and energy density of a cell indicate the amount of energy in watt hours which can be obtained per unit mass and volume respectively. Both of these criteria should be maximized in a marketable material. When evaluating individual electrode candidates, specific capacity (Ah/kg) or volumetric capacity (Ah/L) are generally stated, as opposed to specific energy and energy density. The former values are unique to either the cathode or anode, whereas the latter are derived by multiplying the specific capacity or volumetric capacity by the average voltage of the cell. Lithium ion batteries lead the market in both of these criteria.

Measuring the Coulombic efficiency (q_{Ah}) of a cell indicates the efficiency of electrochemical energy conversion. Q represents a quantity of electricity, measured in coulombs, or current times time.

$$q_{Ah} = \frac{Q_{discharge}}{Q_{charge}} \tag{1.14}$$

The value of Q_{charge} necessary to recharge a cell is always higher than the charge $Q_{discharge}$ released during discharge. As well, the voltage on charge is higher than that on discharge, due to the internal resistance in the cell, and the over potential required to reverse the electrochemical reaction. This is readily observed in the discharge/charge curve and is termed polarization or hysteresis. The Coulombic efficiency of Ni-Cd batteries is between 70-90%, whereas lithium ion cells achieve nearly 100% efficiency.[3]

Cycle life is also critical to the marketability of a battery. Due to both economic and ecological reasons a long cycle life is necessary. The number of cycles indicates how often a secondary cell can be charged before the reversible capacity drops below a lower limit, typically 80% of the original capacity, which is defined as failure of the cell. When comparing the cycle life for various cells, it is important to note that the current density and depth of discharge must be the same in all systems for a fair comparison to be made.

1.6 Portable Power Sources

There are three main types of electrochemical power sources; primary cells, secondary or rechargeable cells, and fuel cells. Primary cells provide electrical energy during discharge, but cannot be reused; these include the familiar batteries used in flashlights and "walkmen". Secondary cells also provide electrical energy during discharge, but can be recharged and cycled many times. Lithium ion batteries are one subset of the current secondary battery technology. Fuel cells, which have attracted much attention in recent years, rely on a constant supply of hydrogen (or methanol) and oxygen external to the cell. This makes this technology nearly impossible to implement in portable electronics, but current research focuses on the use of such cells in electric vehicles. Efforts in our lab have focussed on the development of materials for positive and/or negative electrodes for secondary batteries. Typical non-aqueous

primary cells have specific energies of 400Wh/kg, while secondary cells give only 120Wh/kg. For aqueous systems, a primary cell provides 100Wh/kg and a secondary cell, 60Wh/kg.[7]

Two very old battery technologies are the Pb-acid and Ni-Cd cells. Both these cells incorporate a solid elemental metal anode and an aqueous electrolyte which is acidic and alkaline respectively. The former is still used commercially in starter batteries for cars, since is can supply a large amount of power, over a short period of time. The obvious disadvantage of the lead-acid system is the weight of lead. The Ni-Cd system was marketed in 1961 by Sanyo in a sealed cell arrangement.[7] This cell is still in use although concerns about the toxicity of cadmium are driving it from the market. The cathode material is nickel hydroxide, and the anode is a cadmium containing compound. Potassium hydroxide acts as the electrolyte. The overall cell reaction is

$$2NiOOH + Cd + 2H_2O \underset{Charge}{\overset{Discharge}{\rightleftharpoons}} 2Ni(OH)_2 + Cd(OH)_2$$

The standard potential for this cell is 1.32V. This system is known to have a "memory effect" which prevents the cell from being fully recharged after repeated cycling, thus decreasing the available energy from the cell. Subsequent to the commercialization of the Ni-Cd system, an alternative technology was marketed. The Ni-metal hydride cell also uses a nickel hydroxide cathode, but the anode was replaced with a hydrogen absorbing alloy. This alloy reversibly adsorbs and desorbs hydrogen in alkaline solution. The electrochemical reaction depends on the electrolytic reaction of water.

$$NiOOH + H_2O + e^- \underset{Charge}{\overset{Discharge}{\rightleftharpoons}} Ni(OH)_2 + OH^- \qquad \text{(cathode)}$$

$$MH + OH^- \underset{Charge}{\overset{Discharge}{\rightleftharpoons}} M + H_2O + e^- \qquad \text{(anode)}$$

$$NiOOH + MH \underset{Charge}{\overset{Discharge}{\rightleftharpoons}} Ni(OH)_2 + M \qquad \text{(overall reaction)}$$

In these equations M represents the metal alloy, and MH is the metal hydride. The standard potential of this reaction is also 1.32V. Alloys that can be used in this type of cell are typically rare earth based compounds such as $LaNi_5$. The discharge capacity of a Ni-metal hydride cell is about 80% greater than that of a standard Ni-Cd cell.[8] As well, the alloys adsorb and desorb hydrogen with excellent reversibility. The disadvantages of this system are the cost and environmental toxicity of the cells.

Innovations in lithium batteries have dominated research in the area of rechargeable batteries in the last 15 years. A bias towards lithium based cells arose for numerous reasons. In particular, the low density of the metal ($0.54 g/cm^3$) and its low electrochemical potential make it an excellent candidate as an anode material, resulting in both good specific capacity and a good cell voltage when paired with an appropriate high potential cathode material. There are numerous primary lithium cells on the market. More interesting in the context of this thesis are the rechargeable lithium and lithium ion cells. Secondary lithium metal cells have included Li-MnO_2, Li-MoS_2 Li-V_2O_5, Li-polyaniline, and Li-carbon cells. Secondary lithium ion cells, or rocking chair batteries, were developed to address the safety issues surrounding the use of lithium metal as an anode material. These cells incorporate lithium ions as the electrochemically active, mobile ion, but the lithium is introduced in ionic form within the cathode or less frequently, the anode material.

Figure 1.4 shows the enhancement in both specific (gravimetric) and volumetric capacities which have been achieved by the lithium-ion battery technologies.[3] From this figure the motivation for research in the area of lithium ion cells is clear, as the two most rigorous demands for commercial cells, low weight and small size, are optimized in the lithium ion systems.

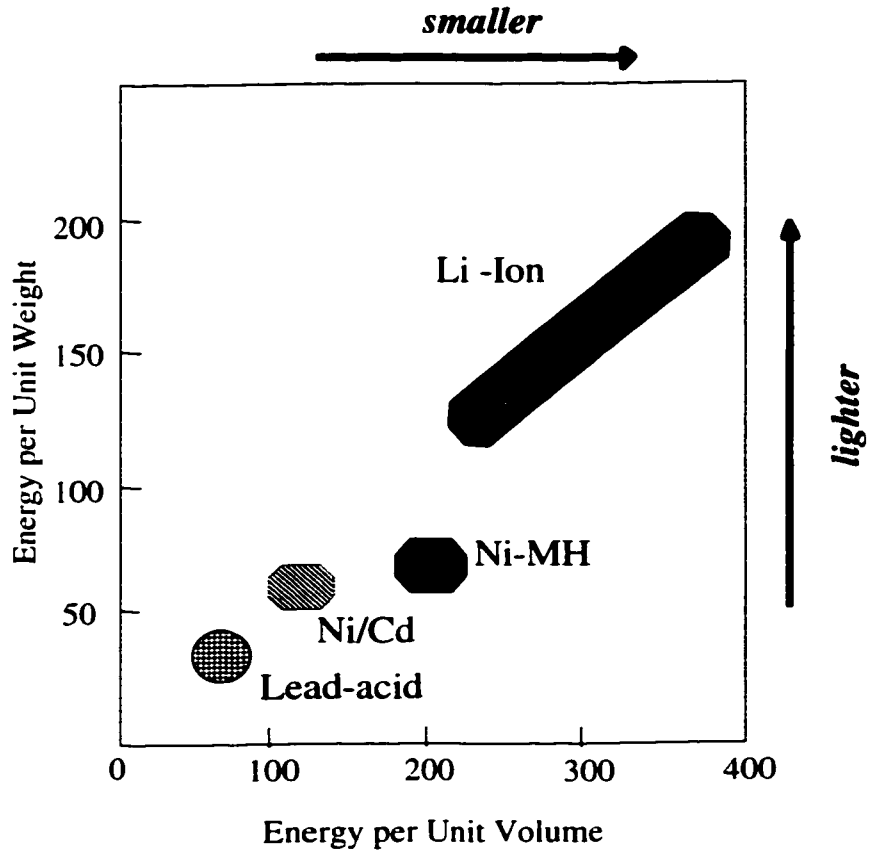

Figure 1.4 Progress in rechargeable battery technology as a function of volume and mass.[8]

1.7 Components of Lithium Ion Cells

1.7.1 Electrolytes

One challenge in electrochemistry is the search for appropriate electrolytes that can withstand very large voltage potentials within the cell. The electrolyte must not be oxidized by the positive electrode, or reduced by the negative electrode; i.e. its band gap must span those of the electrodes. [9] This is shown schematically in **Figure 1.5**. The highest electron donor state of the anode (HOMO) must be lower than the lowest unoccupied molecular orbital (LUMO) or lowest electron acceptor state of the electrolyte in order to prevent reduction of the electrolyte at the anode. Similarly, the LUMO of the cathode must lie above the HOMO of the electrolyte to prevent the oxidation of the electrolyte at this electrode. Polymer

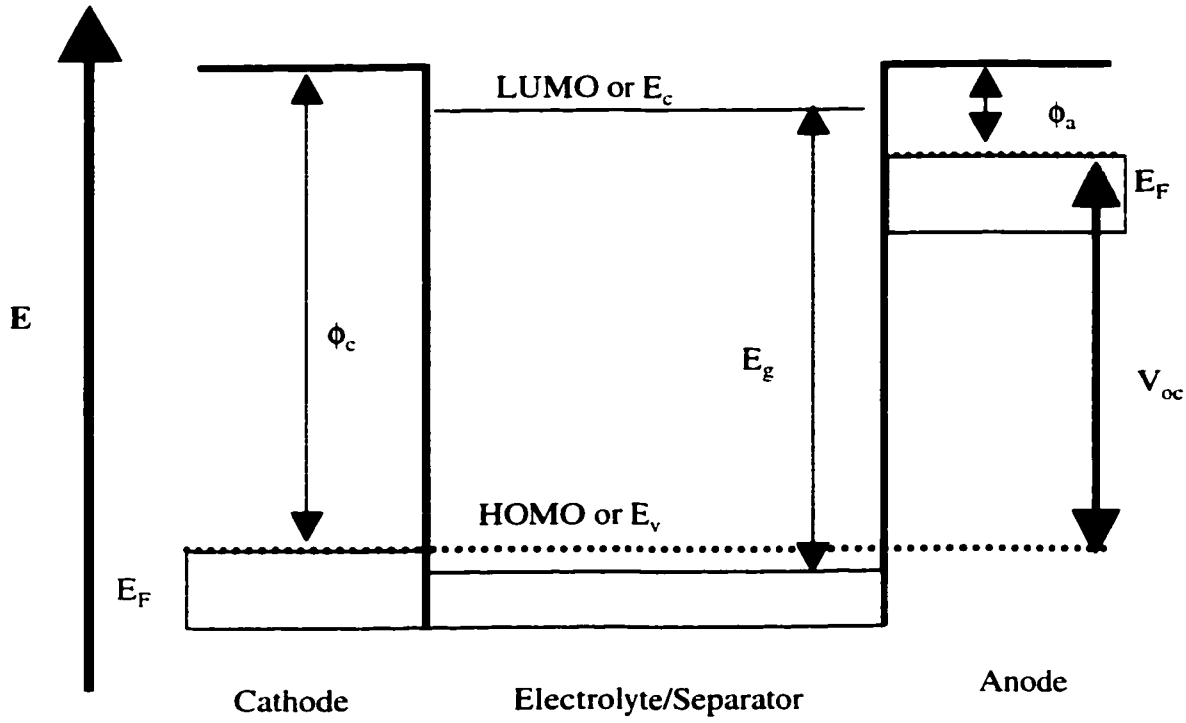

Figure 1.5 Matching reaction window of solid or metallic electrodes with a liquid electrolyte. E_v = valence band energy level, E_c = conduction band energy level, E_F = Fermi level, E_g = energy of band gap, V_{OC} = open circuit voltage, ϕ_C = cathode work function, and ϕ_A = anode work function [9]

electrolytes are stable to chemical degradation, but in this case the rates of ionic diffusion within the electrolyte are inevitably reduced. Finding an effective balance among these criteria is one of the materials issues within electrochemistry.

For fundamental electrochemical studies liquid electrolytes are preferred due to their superior ionic conductivity. In commercialized cells, a solid or polymer electrolyte is highly desirable due to the reduced safety hazards of a solid compared to a liquid. Examples of currently used electrolytes include propylene carbonate, which is stable at high voltage (4.2V), but degrades at low voltage (<0.6-0.7V) A mixture of ethylene carbonate and dimethyl carbonate is chosen for low voltage systems.

1.7.2 Cathodes

Three intercalation systems are of primary interest in the commercialization of lithium ion cells. These include lithium cobalt oxide, lithium nickel oxide, and lithium manganese oxide. The former two are structurally similar, being layered compounds, whereas the lithium manganese oxide that has been investigated relentlessly is a three dimensional material, the $LiMn_2O_4$ spinel. **Table 1.1** lists a variety of materials which have been considered as candidates for cathode materials.

Cathode Material	Molecular Weight	Density (kg/L)	Reversible Range Δx	Specific capacity (Ah/kg)	Volumetric capacity (Ah/L)
Charged					
TiS_2	112.01	3.27	1.0	239	782
MoS_2	160.06	5.06	0.8	134	378
V_2O_5	181.88	3.36	1.0	147	495
V_6O_{13}	513.64	3.91	3.6	188	734
MnO_2	86.94	5.03	0.5	154	775
$NbSe_3$	329.81	8.7	3.0	244	2121
Discharged					
$LiCoO_2$	97.87	5.16	0.5	137	706
$LiNiO_2$	97.63	4.78	0.7	192	919
$LiMn_2O_4$	180.82	4.28	1.0	148	634

Table 1.1 Characteristics of representative cathode (positive electrode) materials for lithium ion batteries.[25]

$LiCoO_2$ and $LiNiO_2$ both have an α-$NaFeO_2$ structure that occurs in space group $R\bar{3}m$, in which the oxygen ions are cubic close packed on the 6 (c) sites, and the transition metal and lithium ions fill the octahedral 3(a) and 3(b) sites respectively.[10] This gives rise to a layered structure that allows for facile mobility of the lithium ions within the layers. This structure is shown in **Figure 1.6a**. In lithium cobalt oxide Co^{3+} is $3d^6$, in the low spin state with $t_{2g}^6 e_g^0$. Extraction of lithium ions from between the oxide layers results in the oxidation of Co^{3+} to Co^{4+} which is low spin d^5. This redox couple occurs at a 4V voltage plateau. Lithium nickel oxide is in a Ni^{3+} d^7 low spin state, with $t_{2g}^6 e_g^1$ before any lithium has been extracted. The one electron in the e_g level causes the localized Jahn-Teller distortion to be active. The Ni^{3+}/Ni^{4+} couple has a higher Fermi level than the corresponding cobalt couple, due to the occupation of the e_g level, thus the redox potential is reduced by several hundred millivolts with respect to the Co^{3+}/Co^{4+} couple.[4] This is in fact a beneficial feature of the nickel oxide system, since the problems of electrolyte degradation which occur in the cobalt system are avoided at the lower cell potential. As well, lithium nickel oxide is cheaper than lithium cobalt oxide. Unfortunately there are synthetic difficulties in obtaining the stoichiometric $LiNiO_2$ phase. This results in phases that are deficient in lithium and contaminated with Ni^{2+} that resides in the lithium layers, having stoichiometries of the general type $Li_{1-\delta}Ni_{1+\delta}O_2$. The best electrochemical performance is achieved for phases closest to $\delta = 0$. Thus, inspite of its advantages in terms of cell potential and cost, the problems with synthesis led to its disqualification as a commercial electrode material. Effort has been expended to improve on the properties of the nickel based oxide by doping with other ions. For examples, the complete range of $Li(Ni_{1+y}Co_y)O_2$ compounds have been studied.[11,12] As well doping with aluminum ions has produced some intriguing materials.[13] Sony introduced the first generation of lithium ion rechargeable batteries using lithium cobalt oxide as the cathode material.

Both lithium cobalt oxide and lithium nickel oxide were originally thought to experience a range of solid solutions upon deintercalation of lithium. Evidence now shows that in fact, a series of phase changes occur in both materials, thus these are classified as Type II materials.

$LiMn_2O_4$ crystallizes in space group $Fd\bar{3}m$, with the transition metal ions on the octahedral 8(a) sites, lithium ions on the tetrahedral 16(d) sites, and oxygen in the 32(e) sites.

a)

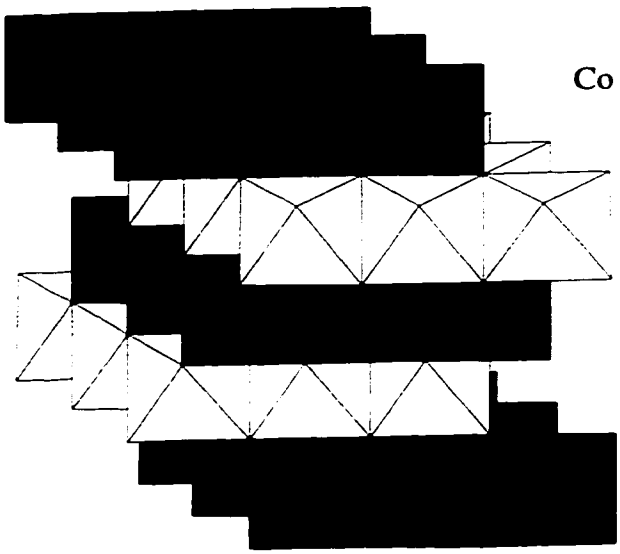

b)

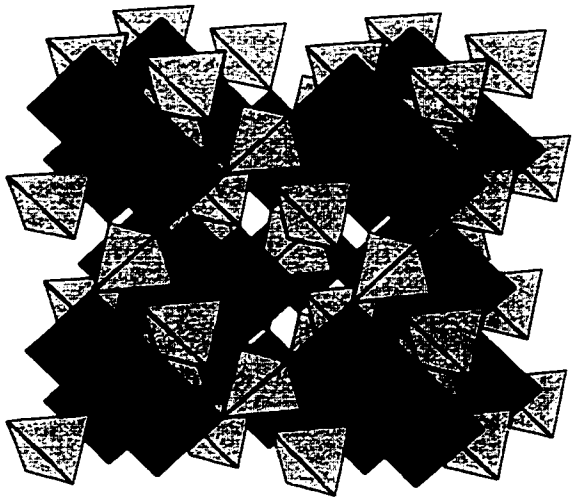

Figure 1.6 a) $LiCoO_2$ or $LiNiO_2$ layered structure
b) $LiMn_2O_4$ spinel structure

While this is a three dimensional structure as opposed to the lamellar $LiCoO_2$ and $LiNiO_2$ structures, lithium ion mobility is facilitated *via* migration of the lithium ions through the unoccupied octahedral 16(c) sites.[4] This structure is shown in **Figure 1.6b**. The boundless interest in the manganese oxides systems is based on 1) manganese oxide is 1% of the cost of cobalt oxide, and 2) manganese oxide is environmentally benign, occurring naturally in high abundance in the earth.

The three dimensional host is comprised of half Mn^{3+} and half Mn^{4+}. Mn^{4+} is a $3d^3$ $t_{2g}^3e_g^0$ ion and Mn^{3+} is a high spin $3d^4$ $t_{2g}^3e_g^1$ ion. The latter is Jahn-Teller active, but since the d electrons are localized and only one half of the manganese atoms are Mn^{3+}, no distortion is observed at ambient temperature. This spinel can react electrochemically at either 3V or 4V. The first involves the extraction of one lithium from the 8(a) site, resulting in λ-MnO_2. This reaction occurs at a 4V plateau. During the extraction of the first 0.5Li the material passes through a continuous range of solid solutions. After this point, the remaining lithium is ordered on half of the tetrahedral 8(a) sites, creating a second spinel phase. Throughout the remainder of the lithium extraction these two cubic spinels co-exist.[14,15] The cycling performance in this regime is superior to the 3V regime, but disappointing in terms of commercialization possibilities. The cause of this poor cyclability is proposed to be the dissolution of Mn^{2+} from the spinel, or the degradation of the electrolyte at high voltage.[16,17]

The second possible reaction, at 3V, involves the insertion of a second lithium into the structure, filling the octahedral 16(c) sites. The insertion of lithium occurs *via* formation of a solid solution up to $Li_{1+x}Mn_2O_4$ where x=0.1. Beyond this the concentration of Mn^{3+} is great enough to cause a cooperative Jahn-Teller distortion, lowering the symmetry from octahedral to tetragonal symmetry at these sites. Between lithium concentrations of x = 0.1-2 the two spinel structures co-exist, with the continuous conversion of the higher symmetry to the lower symmetry phase.[18,19] This phase change is purported to be detrimental to the cycling of the cell. To improve the cyclability of the material various groups have doped the spinel, replacing a portion of the Mn^{3+} to Mg^{2+}, Li^+ or Zn^{2+}. These dopants increase the average oxidation state of the material to above 3.5, with the aim of suppressing the Jahn-Teller distortion.[4] Alternatively, Al^{3+}, Fe^{3+}, Ni^{3+}, Co^{3+}, or Cr^{3+}, have been substituted into the Mn^{3+} sites, decreasing the concentration of Jahn-Teller active ions, without lowering the oxidation

state. Although some of these mixed-ion spinels exhibit improved cyclability compared to the parent system, in all cases the specific capacity is lowered compared to $LiMn_2O_4$ itself.[25]

Besides these three cathode candidates, a great number of other systems have been investigated as lithium intercalation compounds. These include lamellar $LiMnO_2$ among numerous manganese oxide based candidates, iron oxides, vanadium oxides, and molybdenum oxides, to name a few. Research efforts in our own laboratory have focused on more complex cathode alternatives, such as tunnel structured manganese oxides (todorokite)[20], transition metal oxide/conductive polymer nanocomposites (PANI-V_2O_5, PPY-V_2O_5, PTH- V_2O_5, PANI-MoO_3),[21] templated oxides,[22] and open-framework phosphates (NASICON structures – $Li_xFe_2(PO_4)_3$, – $Li_xV_2((PO_4)_3)$.[23] In general these materials have lower specific capacities than the industrially successful lithium cobalt, nickel, or manganese oxides, but improvements are sought in the area of lithium ion mobility and cyclability.

1.7.3 Anodes

Today's commercial Li-ion cells use $LiCoO_2$ as the positive electrode and graphitic carbon as the negative electrode. Although new developments are needed for both materials, arguably the negative electrode (or anode) is a major limitation at present. Initial efforts in manufacturing lithium batteries relied on metallic lithium as the negative electrode. While this provided excellent cell voltage and specific energy, the future of these types of cells was jeopardized by the combustion of the battery on over-heating. This resulted in the demise of Moli Energy in 1989.[24] Their cell was based on the reaction of lithium metal with molybdenum sulfide, described as follows.

$$xLi + MoS_2 \underset{Charge}{\overset{Discharge}{\rightleftharpoons}} Li_xMoS_2$$

The effect that caused the combustion of the Moli cell is now understood. The reaction of elemental lithium with the electrolyte causes the formation of a passivating surface film. Although lithium ions can move through this surface-electrolyte-interface (SEI), the alternative, which is the plating of a fresh surface of lithium upon charge is favoured. This leads to the formation of dendrites which grow across the space separating the electrodes. Upon subsequent cycling the battery is short circuited. Alternatively, in the case of a battery exposed to heat, this reaction may occur spontaneously resulting in combustion. Due to the

apparent safety issues with lithium metal based cells, the industry has turned to lithium ion cells, utilizing alternative anode materials. **Table 1.2** lists several possible anode materials, and their theoretical specific capacity and theoretical volumetric capacity.[25]

Negative Electrode Material	Molecular Weight	Density (kg/L)	Theoretical specific charge (Ah/kg)	Theoretical charge density (Ah/L)
Li (primary)	6.94	0.53	3862	2047
Li_4(secondary)	27.76	0.53	965	511
LiC_6 (graphite)	79.00	2.24	339	759
LiAl	33.92	1.75	790	1383
$Li_{21}Sn_5$	739.31	2.55	761	1941
$LiWO_2$	222.79	11.30	120	1356
$LiMoO_2$	134.88	6.06	199	1206
$LiTiS_2$	118.94	3.06	225	689

Table 1.2 Characteristics of various anode (negative electrode) materials for lithium ion batteries.

Carbons have been pursued as alternatives to lithium metal, as these materials were shown to have higher specific capacities and more negative redox potentials than most competing materials. There are several types of carbons of varying crystallinity that have varying electrochemical performance. The general reaction is as follows

$$Li_xC_n \underset{Charge}{\overset{Discharge}{\rightleftharpoons}} xLi^+ + xe^- + C_n$$

where C_n can represent any of the variety of available carbons. The types of carbon can be classified as graphitic and non-graphitic or disordered. The graphitic forms vary in terms of crystallite size, but collectively these carbons become more ordered with heat treatment between 1500-3000°C. This is permitted since there is no cross-linking between layers. In contrast, non-graphitic carbons also constitute planar hexagonal networks, but in the absence of long range order. These carbons are formed during the pyrolysis of polymers or other organic pre-cursors, at temperatures below 1500°C. The resulting structure comprises amorphous regions crosslinked with graphitic regions, thus crystallization at high temperature is inhibited.

Lithium intercalation into graphitic carbon is characterized by staging. Staging is a

description of the periodic array of occupied and unoccupied layers, as shown in **Figure 1.7a.**[25] The driving force for this is the energy required to increase the van der Waals gap: by filling one "stage" at a time, this energy is minimized overall. This is balanced by the repulsion between like charges as the lithium ions begin to interact spatially within the layers. This is an example of a Type II material, in which ion-ion interactions govern the intercalation process. **Figure 1.7b** shows the theoretical electrochemical curve for graphitic carbon, in which the various levels of staging are observed as voltage plateaux corresponding to the co-existence of two phases (known as a two-phase process), and steps in single phase regimes. The lithium capacity of graphitic carbon is limited to one Li per six carbons.

Non-graphitic carbons can be further subdivided into soft carbons, such as turbostratic carbon, coke, or carbon black, and hard carbons. Soft carbons are highly cross linked and thus intercalate less lithium than the crystalline graphitic carbon, but also prevent the co-intercalation of solvent molecules. The maximum intercalation in soft non-graphitic carbon is Li_xC_6 is x = 0.5-0.8. This limited capacity is caused by the wrinkling and buckling of the layers, which makes a portion of the lithium sites inaccessible. Hard carbons have caused much excitement in the electrochemical literature, since the intercalation capacity is higher than that of graphitic carbon, with x = 1.2-5. This corresponds to a specific capacity of 400-2000mAh/g. The reason for the enhanced lithium capacity is still under debate. One proposal is that storage occurs at the edges and surface of the small particles. The disadvantage of these hard carbons is the large amount of hysterisis common in the charge/discharge profiles.

Lithium metal alloys have also been investigated as candidates for negative electrodes. These materials react with lithium according to the following description

$$Li_xM \underset{Charge}{\overset{Discharge}{\rightleftharpoons}} xLi^+ + xe^- + M$$

where M is a metal. Alloys are formed between lithium and most metals in the periodic table, for example, Al, Si, Sn, Sb. Commonly these alloys have a considerable range of phase composition. Unfortunately this large range of lithium composition is accompanied by drastic changes in the molar volume. The change in volume causes pulverization of the electrode material, and thus the bulk metals are not considered viable candidates for commercial anode materials. The issues surrounding the formation of Li-M alloys during electrochemical processes is addressed in Chapter 3.

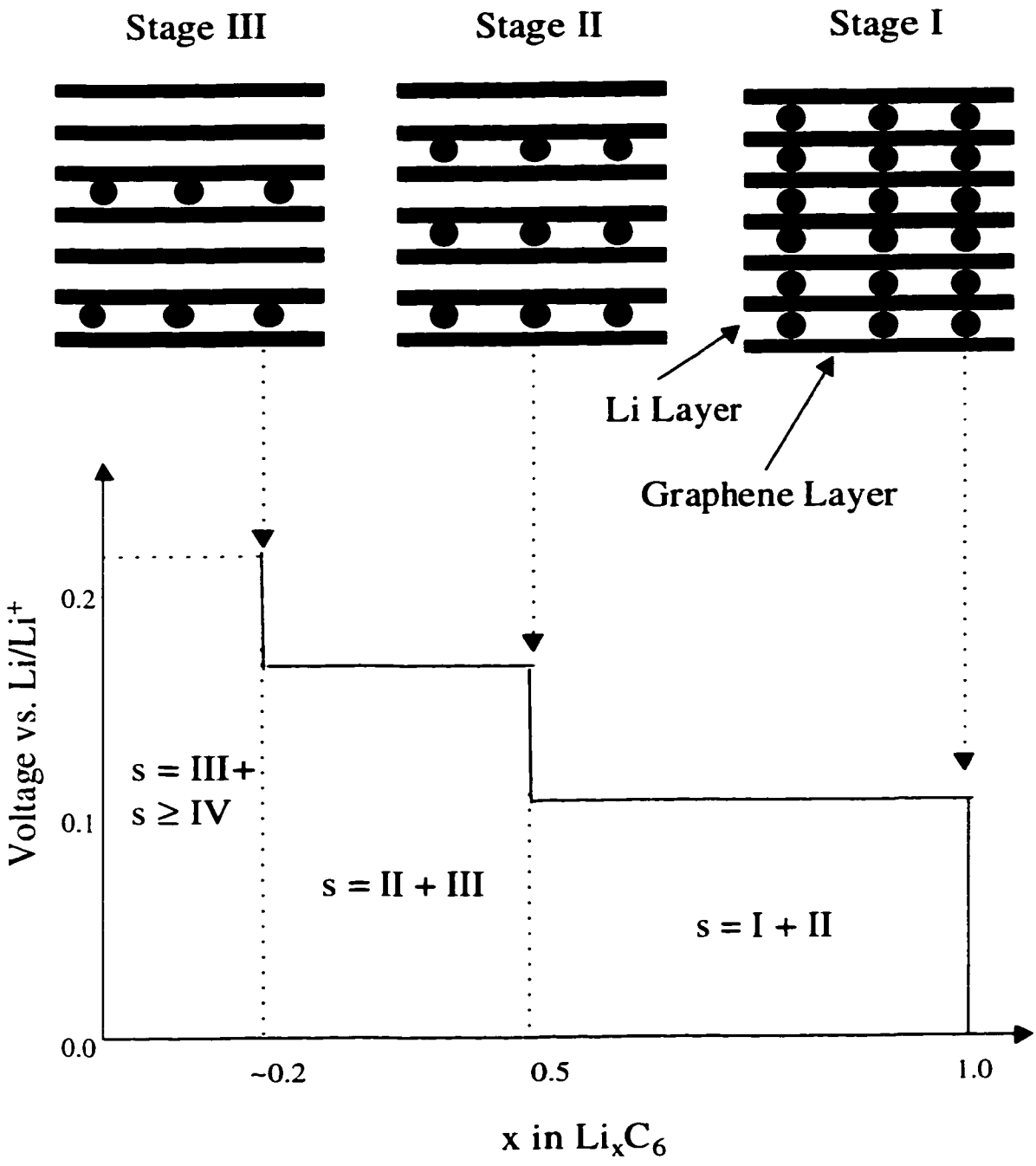

Figure 1.7 Staging of lithium ions inserted into graphitic carbon, with corresponding schematic voltage profile of electrochemical process.[25]

An important need remains: to find materials with a slightly greater intercalation voltage (to completely eliminate the risks of Li plating and be less reactive towards electrolyte reduction), and a larger electroactive capacity than that of today's carbons. Graphitic materials are limited to an insertion of approximately $Li_{1+x}C_6$ and display poor volumetric energy density. The discovery of promising Li insertion properties of various new materials in recent years has led to exploration of systems such as amorphous nanocomposites, and crystalline materials such as metal oxides. Oxides have experienced renewed interest. Studies within the last three years have detailed low-potential Li insertion in $LiMVO_4$ (M=Zn, Cd, Ni),[26] Li_xMO_z and $Li_xM_yV_{1-y}Oz$ (M=Ti, V, Mn, Co, Fe, Ni, Cr, Nb and Mo)[27] and in amorphous compounds such as RVO_4 (R=In, Fe)[28] and $NaMoO_3$.[29,30] These materials all display a large specific and volumetric capacity, which is also unfortunately associated with a substantial irreversible capacity, and high cell polarization on charge.

Overwhelming interest was sparked by the report of an amorphous *tin-composite-oxide* (TCO) glass to be used as a negative electrode in the manufacture of a Li ion battery.[1,31] This material was shown to be particularly stable to cycling, and exhibit minimal polarization. The mechanism of the reaction of Li with the host material is not well understood, although clearly it is not as simple as lithium insertion into classic intercalation compounds. Unfortunately, understanding this mechanism is critical to improving these new materials, and creating new ones. These materials are inherently difficult to study, as they are either amorphous materials to start (Sn-glasses), or become that way following full discharge. The methods available for the study of amorphous or partially ordered materials are severely limited compared to those used in studying crystalline compounds. This thesis was designed to address this issue by using a combination of physical techniques to examine the mechanism of Li insertion in these new oxide materials.

1.8 *Tools of the Trade : Electrochemistry, Solid-State NMR, PDF, XAS, and TEM*

Material scientists typically draw upon a wide variety of analytical techniques to answer the questions of characteristics and mechanisms within the materials of interest. Through the course of this project we have used an arsenal of techniques including primarily electrochemistry, solid-state-NMR, X-ray diffraction, and X-ray absorption in order to obtain the elusive information about our system of interest. Many features of the tin-composite-oxide glasses make them especially challenging materials to study. In particular, amorphous systems are notoriously more difficult to accurately depict than their crystalline counterparts. Similarly, the complex chemical composition adds to the intricacy of the system. Fortunately the parent systems of tin metal and tin oxide can be used effectively for comparison or analogy.

Chapter 1 has voiced the *prelude* to the thesis, including the development of electrochemistry and lithium ion batteries, as well as introducing the thrust of the current endeavours; the understanding of the newly developed TCO glasses as anode materials. Thus the theme of the *fugue* is analogous to the understanding of electrochemical performance of the tin composite oxide. The key signature of the fugue is TCO glass itself, which sets the framework for the series of studies developed here. Each of the techniques drawn upon to address this theme are considered as separate voices, contributing to the subjects and counter subjects as they arise.

1.9 References

[1] Y. Idota, T. Kubota, A. Matsufuji, Y. Maekawa and T. Miyasaka, *Science*, **276**, 1395 (1997).

[2] W.R. McKinnon Chapter 7, Solid State Electrochemistry ed. P. Bruce. Cambridge University Press, (1995).

[3] G. Hambitzer, K. Pinkwart, C. Ripp, and C. Schiller in Chapter 1, Handbook of Battery Materials, ed. J.O.Besenhard, John Wiley and Sons, (1999).

[4] P.G. Bruce, *Chemical Communications*, 1817 (1997).

[5] M. B. Armand in Materials for Advanced Batteries, ed. D.W. Murphy and B.C.H. Steele. NATO Conference Series VI: Material Science (1979). pg 145.

[6] R.A. Huggins *Journal of Power Sources*, **81-82**, 13 (1999).

[7] K. Nishio and N. Furukawa, in Chapter 1, Handbook of Battery Materials, ed. J.O.Besenhard, John Wiley and Sons, (1999). pg 21.

[8] K. Nishio and N. Furukawa, in Chapter 1, Handbook of Battery Materials, ed. J.O.Besenhard, John Wiley and Sons, (1999). pg 30.

[9] J.B. Goodenough *Solid State Ionics*, **69**, 184 (1994).

[10] K. Nishio and N. Furukawa, Practical Batteries (Chapter 2 of Besenhard book) pg 47-50.

[11] C. Delmas, I. Saadoune and A. Rougier, *Journal of Power Sources*, **43/44**, 595 (1993).

[12] C. Delmas in Lithium Batteries. New Materials, Developments and Perspectives. ed. G. Pistoia, Elsevier Science B.V., Amsterdam, 1994.

[13] T. Ohzuku, A. Ueda, and M. Wouguchi, *Journal of the Electrochemical Society*, **142**, 4033 (1995).

[14] M.M. Thackeray, P.J.Johnson, L.A. de Picciotto, W.I.F. David, P.G. Bruce, and J.B. Goodenough, *Materials Research Bulletin*, **19** 179 (1984).

[15] T. Ohzuku, M. Kitagawa, and R. Hirai, *Journal of the Electrochemical Society*, **137**, 769 (1990).

[16] G. Pistoia, A. Antonni, R.Rosati and D. Zane, *Electrochimica Acta*, **41** 2683 (1996).

[17] J.M.Tarascon, F. Coowar, G. Amatuci, F.K. Shokoohi and D.G. Guyomard. *Journal of Power Sources* **54** 103 (1995).

[18] M.M. Thackeray, W.I.F. David, P.G.Bruce, and J.B.Goodenough, *Materials Research Bulletin*, **18** 461 (1983).

[19] J. B. Goodenough, M.M. Thackeray, W.I.F. David and P.G. Bruce, *Rev. Chim. Minér.* **21** 435 (1984).

[20] M.J. Duncan, F. Leroux, J.M. Corbett, and L.F. Nazar, *Journal of the Electrochemical Society*, **145**, 3746 (1998).

[21] G.R. Goward, F. Leroux, and L.F. Nazar, *Electrochimica Acta*, **43**, 1307 (1998).

[22] F. Leroux, B.E. Koene, and L.F.Nazar, *Journal of the Electrochemical Society*, **143**, L181 (1996).

[23]C. Masqualier, J. Gaubichier, and L.F. Nazar, *Chemistry of Materials*, in press, (1999).

[24] K. Nishio and N. Furukawa, Practical Batteries (Chapter 2 of Besenhard book) pg 56.

[25] M. Winter, J.O. Besenhard, M.E. Spahr, P. Novak *Advanced Materials*, **10**, 725 (1998).

[26] C. Sigala, D. Guyomard, Y. Piffard, and M. Tournoux, *C. R. Acad. Sci. Paris*, **320**, 523 (1995).

[27] N. Kumagai, Japanese Patent, 08-241707 (1996).

[28] S. Denis, E. Baudrin, M. Touboul, and J-M. Tarascon, *Journal of the Electrochemical Society*, **144**, 4099 (1997).

[29] F. Leroux, G. R. Goward, W. P. Power and L.F. Nazar, *Electrochemical and Solid State Letters*, **1**, 255 (1998)

[30] F. Leroux and L.F. Nazar, U. S. Patent # 9-199,635.

[31] Y. Idota, U.S. Patent, 5478671 (1995), H. Tomayama, Jap. Patent, 07-029608 (1995).

Chapter 2 Materials Synthesis and Characterization

This chapter describes the challenges encountered and the successes achieved in the synthesis of the tin composite oxide glasses, as well as three lithium-tin phases. These materials were characterized using standard powder X-ray diffraction and single crystal X-ray diffraction. A brief discussion of diffraction theory precedes the description of the synthetic methods. This order was chosen to allow for the simultaneous discussion of the synthesized materials and their characterization. The synthetic efforts of this thesis project were somewhat limited in their scope, due to the greater efforts devoted to physical characterization of the materials of interest. Nevertheless the synthesis of the tin composite oxide glasses presented a significant challenge. The glasses procured were analyzed using powder X-ray diffraction methods. Supplementary to the study of the TCO materials was the characterization of the bulk lithium-tin phases. This was undertaken in order to create a frame of reference for the NMR studies of the electrode materials. A point of interest, which arose when pursuing the synthesis and characterization of the Li-Sn phases, concerned the exact nature of these phases. Thus, a discussion of the Zintl versus metallic character of these phases is discussed. Also at issue has been the precise composition of the phase known as $Li_{22}Sn_5$. The full single crystal X-ray diffraction study of this material, presented in this work, adds another piece to this puzzle.

In the analogy to the *fugue*, the material, TCO, represents the key signature of the thesis. All studies are based in on the properties of TCO as an anode material, as in the fugue, all themes and subjects are developed within the musical framework of the chosen key. Hence, the successful synthesis of the TCO glass, described in this chapter, forms the framework for the subjects and themes developed in the subsequent chapters.

2.1 Review of Diffraction Theory and Methodology

Various forms of X-ray studies have been used through the course of this thesis. These included powder X-ray diffraction (PXRD), single crystal X-ray diffraction, as well as X-ray scattering combined with Fourier analysis, known as the pair distribution function method, and X-ray Absorption Spectroscopy. The theory behind PDF and XAS is left to Chapter 6. A brief

review of the theory involved in the more common X-ray diffraction methods starts with Bragg's law.

$$n\lambda = 2d\sin\theta \tag{2.1}$$

where n is an integer, λ is the wavelength of the X-ray radiation, d is the spacing between the lattice planes in a crystal, and θ is the angle of the incident beam. This law was derived based on the recognition that there is a reciprocal relationship between the angular spread of the scattering or diffraction pattern in a particular direction and the corresponding dimensions of the lattice causing the scattering.[1] Diffraction gives rise to a pattern which is characterized by Bragg peaks or reflections, where the intensity of each reflection is correlated to a structure factor dependent on the atomic composition of the scattering material. X-rays are scattered by electrons. The coherent or elastic scattering gives rise to diffracted photons of the same wavelength as the incident radiation. For coherent scattering, represented by an atomic scattering factor, f, the extent of the scattering depends on the atomic number of the atom and the angle of the scattering. The values of f are listed for each element in the International Tables of Crystallography.[2] For a group of atoms, the amplitude and phase of the X-rays scattered by one unit cell are represented by the structure factor F, which includes the scattering factors of all atoms within that unit cell.

$$F(hkl) = A(hkl) + iB(hkl) \tag{2.2}$$

for each reflection, where

$$A(hkl) = \sum_j f_j \cos 2\pi\left(hx_j + ky_j + lz_j\right) \tag{2.3}$$

and

$$B(hkl) = \sum_j f_j \sin 2\pi\left(hx_j + ky_j + lz_j\right) \tag{2.4}$$

The absolute value of the structure factor, |F|, is dependent on the relative positions of the atoms. The phase angle, α is equal to $\tan^{-1}(B/A)$, and the amplitude of |F| is equal to $(A^2+B^2)^{1/2}$. From a trial structure the amplitudes and phases of the structure factors can be readily calculated, giving $|F_c|$. This is compared with the observed amplitudes for $|F_o|$. The discrepancy index, R, gives a confidence level for the structure refinement. The lower the R value, the greater the confidence level that can be placed in the refinement.

$$R = \frac{\sum(|F_o| - |F_c|)}{\sum(|F_o|)} \tag{2.5}$$

For the analysis of a single crystal structure three general steps are required. The first is the determination of the unit cell and space group, followed by the formulation of a trial structure and subsequently the refinement of that structure to obtain the best fit between the experimental and calculated structures. A Siemens P4 diffractometer with a Mo source (λ = 0.7107Å) was used for single crystal data collection. The direct-methods refinement was performed using SHELX 97 software.

In one-dimensional powder diffraction, the positions of the reflections can be used for indexing and determination of structure using Rietveld methods (not discussed here). As well, the width of the reflections is related to the crystallite size, according to the Debye-Scherrer equation[3]

$$B(2\theta) = \frac{\alpha\lambda}{L\cos\theta} \qquad (2.6)$$

where B(2θ) is the full width in radians of a given *hkl* reflection measured at half its maximum intensity, λ is the wavelength of the X-rays, α is a constant usually equal to 0.9, and L is the crystallite size in the direction perpendicular to the reflecting planes.

Powder diffraction data was collected on a Siemens D500 X-ray diffractometer, with a Cu radiation source (λ = 1.542Å). The samples were mounted in a flat plate geometry with a Be window or Kynar film used to protect air-sensitive samples.

2.2 *Synthesis of Tin-Composite Oxide Glasses*

TCO glasses were prepared by grinding stoichiometric amounts of SnO, $Sn_2P_2O_7$, Al_2O_3, and B_2O_3 (Aldrich) and pressing pellets of the mixture into discs. Three stoichiometries of glasses were prepared and tested electrochemically. These included the TCO itself, which was prepared from a ratio of the elements Sn:B:P:Al of 1.0:0.6:0.4:0.4, according to the original report by Fuji ($Sn_{1.0}Al_{0.42}B_{0.56}P_{0.40}O_{3.6}$). An example of the starting material used would include SnO, $Sn_2P_2O_7$, Al_2O_3, and B_2O_3 in the mass ratio 3.23g : 3.30g : 0.82g : 0.84g. This mixture was divided among several pellets for arc melting. The second glass, Sn-rich-TCO ($Sn_{1.5}Al_{0.42}B_{0.56}P_{0.40}O_{4.2}$), was prepared in a similar fashion, with the only adjustment

being an increase in the amount of SnO, corresponding to a 50% increase in the tin concentration. The third material was also based on the TCO glass, with a portion of the boron oxide being replaced with bismuth oxide. Three ratios of Bi:B were attempted, but only the least amount of Bi produced a true glassy material. The Bi-doped-TCO contained $1/12^{th}$ Bi that replaced $1/12^{th}$ of the B ($Sn_{1.0}Al_{0.42}B_{0.51}Bi_{0.05}P_{0.40}O_{3.6}$).

Several attempts were made to synthesize the TCO glass reported by Idota *et al.*[4] before any success was achieved. These included numerous experiments following the described procedure in the *Science* publication; grinding stoichiometric amounts of the reactant materials, and heating overnight in an argon atmosphere to 1100°C in an alumina crucible. The material was cooled using a gentle 10-20°C per minute cooling rate. This method was completely unsuccessful in terms of creating the desired clear yellow glass. Products ranged from white to pale yellow, but were in all cases opaque and gave diffraction patterns indicative of the crystallization of phosphates, rather than the formation of a true glass.

Some degree of success was achieved by carrying out the reaction within a quartz tube furnace and quenching the reaction by lifting the tube out of the furnace at 1100°C. This formed an opaque compound filled with tiny yellow bubbles with glassy-looking surfaces. This material had to be chiseled out of the crucible. **Figure 2.1** presents the diffraction patterns for the mixture of starting materials before any heat treatment, as well as two representative diffraction patterns for products obtained by the above method of synthesis. The diffraction pattern of the starting materials is dominated by reflections corresponding to SnO (*).[5] Other weaker reflections match the aluminum oxide, boron oxide, and tin pyrophosphate. Although the synthesis was carried out under argon, the diffraction patterns of the product materials both contain strong reflections corresponding to crystallization of SnO_2(**).[6] Aluminum phosphates, known to crystallize readily, are also visible in both products, indicated by the triangles and square markers.[7] The amount of SnO_2 is greater in the first sample than the second, as is the signal to noise ratio, which indicates an improvement in the synthesis methods. Electrochemical experiments performed on this material (presented in Chapter 3) did not meet with the reported capacity reported by Fuji. Hence we continued our efforts to obtain a true glass.

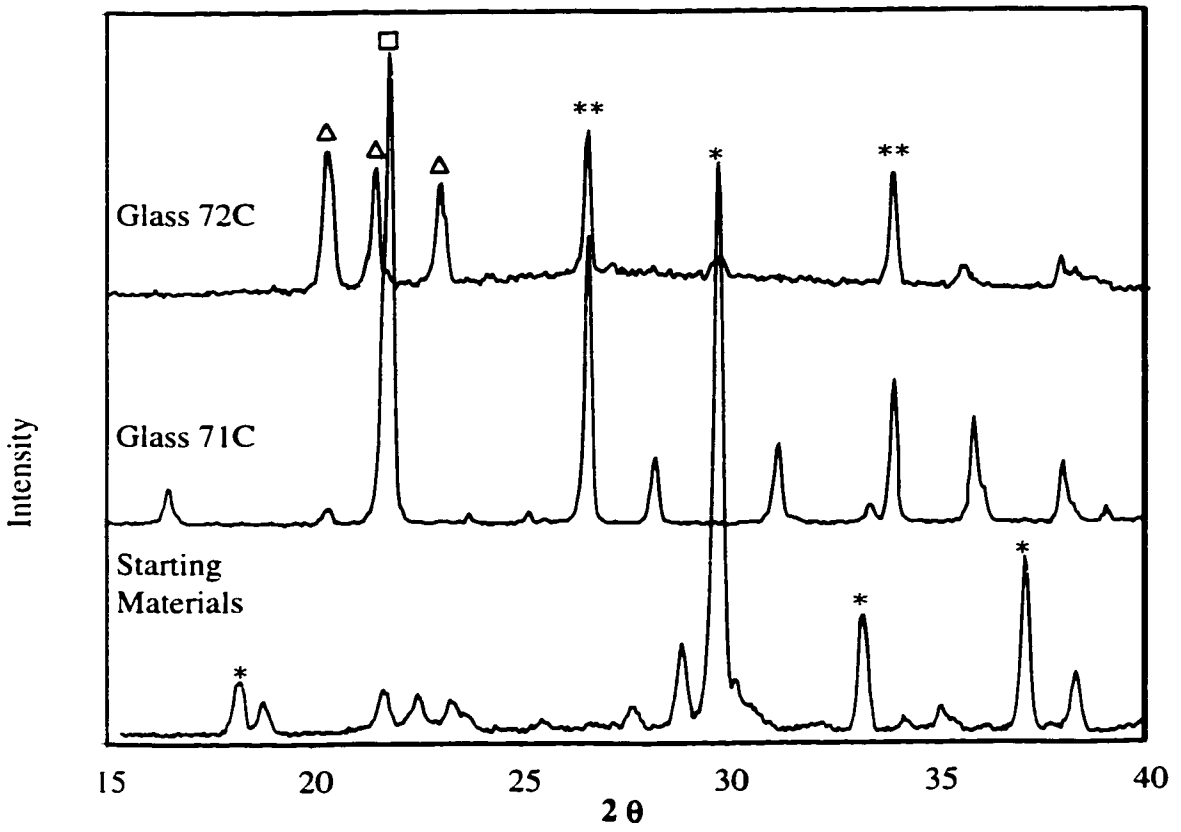

*Figure 2.1 Powder X-ray diffraction patterns for TCO starting materials and crystallized TCO glasses 71C and 72C. SnO reflections are indicated by *, and SnO_2 by **. Aluminum phosphate reflections are indicated by Δ and □.*

The successful method was an arc melting procedure, performed at McMaster University, with the assistance of Jim Garrett. The samples were prepared by pressing approximately 1 g of the ground precursor material in a 1 cm-diameter die. This produced relatively fragile pellets about 4 mm in thickness. The pellets were placed on a copper hearth, and subject to evacuation under a glass bell. The bell was then back-filled with half an atmosphere of argon. The arc was formed by drawing the stinger away from the hearth and the power was adjusted using a foot pedal control. The melt was started at high power, and then the arc power was backed down to ~50% to avoid vaporization of the glass components. Best results were obtained when the pellet melted into a single bead, which had a shimmery-yellow surface. The arc was quenched as soon as the bead 'sat-down', fully wetting the copper hearth. The hearth was water cooled, therefore the glass cooled to RT within seconds of the arc being quenched. Unsuccessful attempts produced dark grey or black products, which were opaque. Only products with excellent clarity were used in the electrochemical experiments. **Figure 2.2** shows two diffraction patterns obtained for products of the arc melting procedure. The top diffraction pattern was obtained from a sample that was yellowish, but opaque, whereas the bottom diffraction pattern was obtained from a clear yellow bead. This diffraction pattern matches that reported by Fuji. Thus "good" glasses could be distinguished from products which contained crystallization impurities on the basis of their optical transparency.

2.3 Synthesis of Li-Sn Phases

The syntheses of single crystals of stoichiometric lithium tin phases have been reported in a series of papers, dating from 1964. Common synthesis methods were used in each case, although containment was clearly an issue, as a variety of crucibles were used, including stainless steel, tantalum, and molybdenum. More recent methods include the enclosure of the metal crucible within a quartz tube, to further reduce the risk of exposure to oxygen. The reaction temperatures were dependent on the ratio of Li:Sn, and the melting point of the desired product, described in the phase diagram (**Figure 2.3**). In all cases, the single crystals were extracted from a heterogeneous product.

Our original strategy for obtaining bulk Li-Sn phases involved combining the elements in the appropriate ratio in a molybdenum crucible in an argon glove box. The sealed crucibles were then contained under vacuum

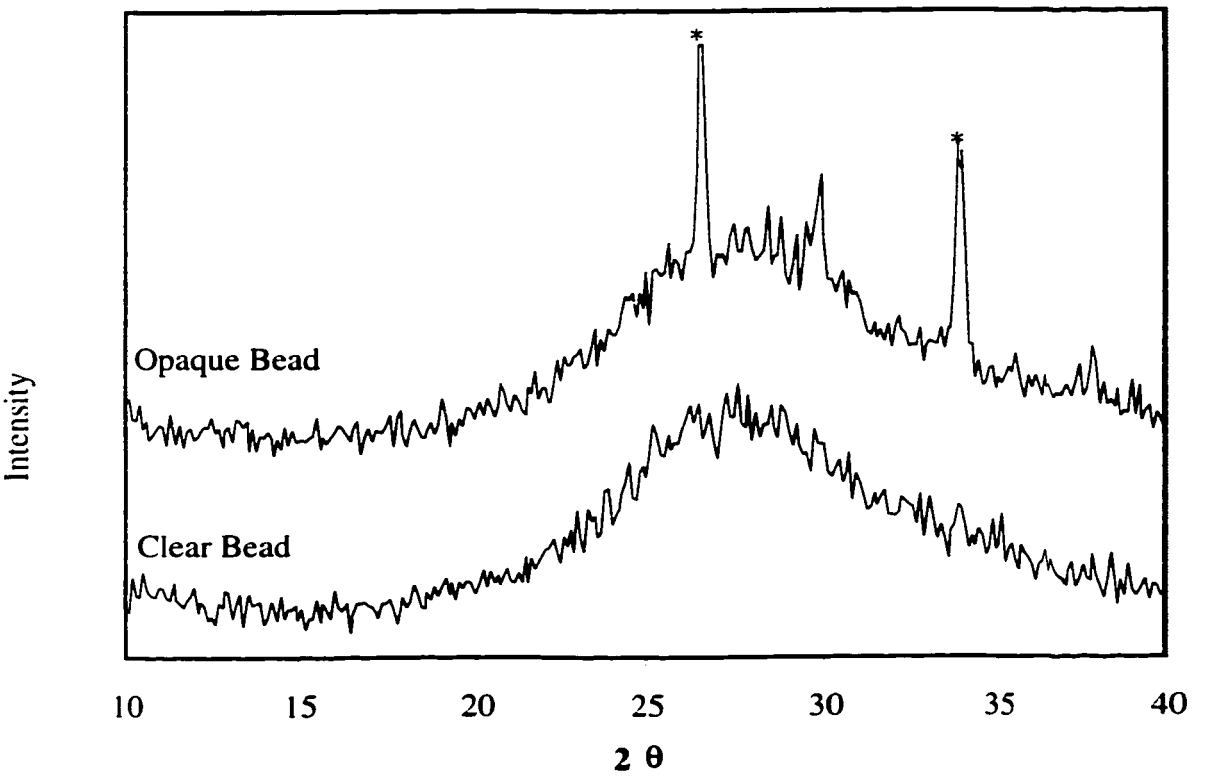

Figure 2.2 Powder diffraction patterns for arc-melted TCO samples: opaque bead and clear bead. Crystalline SnO impurity marked with (*).

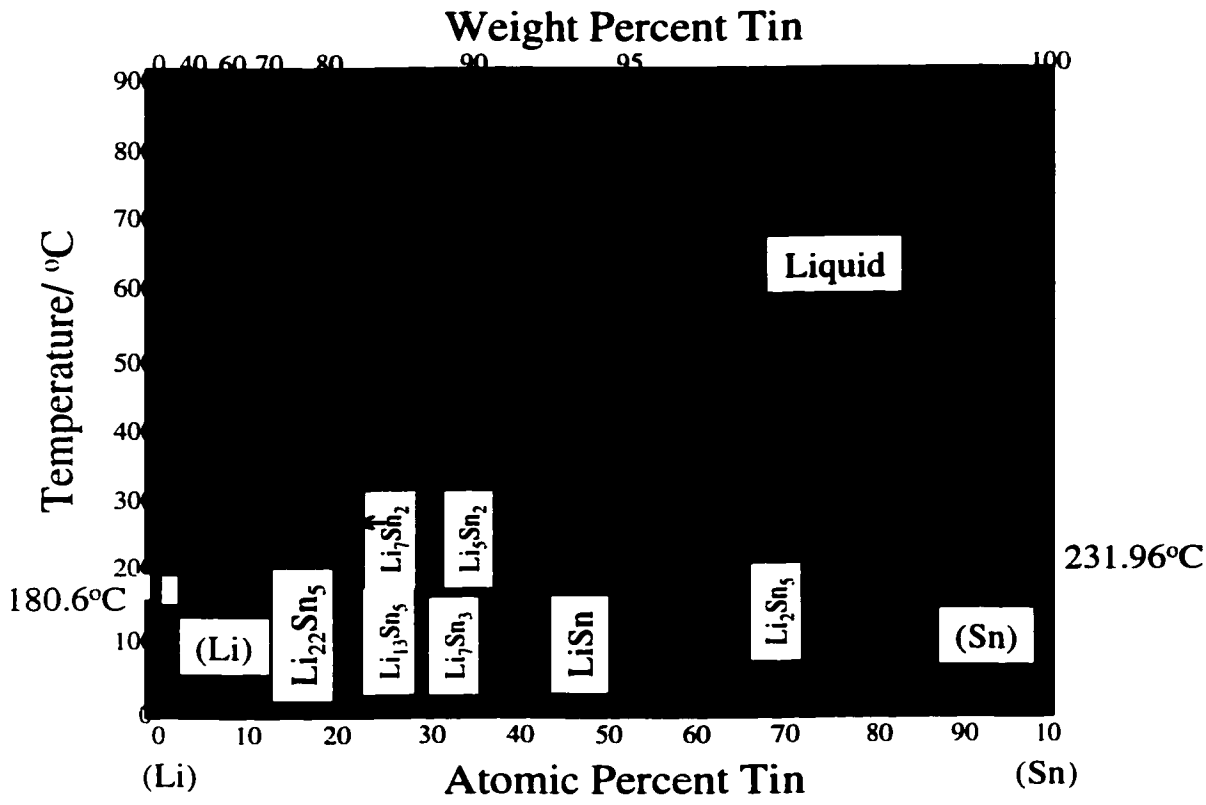

Figure 2.3 Binary lithium-tin phase diagram[8]

within quartz tubes. The samples were heated to 800°C for 2 hours and cooled at 10° C/min in a tube furnace. The reaction product was extracted from the crucible in the glove box, and transferred to an airtight X-ray diffraction sample tray for structural characterization. The products obtained by this method were not single phase. A variety of reasons can be considered which would result in this undesirable result. First, the reactants may not have been thoroughly mixed once the components were molten, resulting in a composition gradient within the crucible. Secondly, the annealing temperature and/or time may not have been sufficient for the formation of the desired phase. Two products obtained by this method were analyzed by X-ray diffraction. The diffraction patterns are shown in **Figure 2.4a**. The reflections corresponding to the Li_2Sn_5, LiSn, Li_7Sn_3, Li_5Sn_2, $Li_{13}Sn_5$, Li_7Sn_2, and $Li_{22}Sn_5$ diffraction patterns, found in the JC-PDS data base,[9] or generated in Cerius[2] when other diffraction data was unavailable are shown in **Figure 2.4b**.[10] The first product was obtained from a stoichiometric mixture of Li and Sn corresponding to $Li_{22}Sn_5$. The second product was obtained from a one to one molar ratio of lithium and tin. The diffraction pattern corresponds to a mixture of Li_5Sn_2 and LiSn, indicating that, in this case in particular, the reaction took place without thorough mixing of the components. The most striking thing about the diffraction patterns is the strong overlap of the diffraction lines for the various Li-Sn phases. While neither of the phases formed were pure, there was still a visible difference in their diffraction patterns. The diffraction patterns of both products include reflections which match with the starting material, β-tin (*). This is clear evidence that the two elements were not sufficiently mixed in the molten state, which resulted in mixed-phase products. From now on they will be referred to as the lithium-rich and lithium-poor phases. Solid-state NMR spectra obtained for these two products are presented in Chapter 4.

Based on the phase diagram, the most accessible phases are the highest content of lithium; $Li_{22}Sn_5$, and the intermediate phase, LiSn. The latter is easily obtained by using an excess of lithium. By exceeding the melt temperature of the chosen ratio of Li:Sn, achieving homogenized melt by maintaining this temperature for a few hours, and then cooling slowly, the desired phase will crystallize out at the temperature where the solidus/liquidus boundary is crossed, and excess lithium will be rejected into the melt. This temperature, considered the annealing temperature, is maintained for a minimum of several hours, or preferably several days, allowing for crystallization to occur. From this point the mixture can be cooled relatively

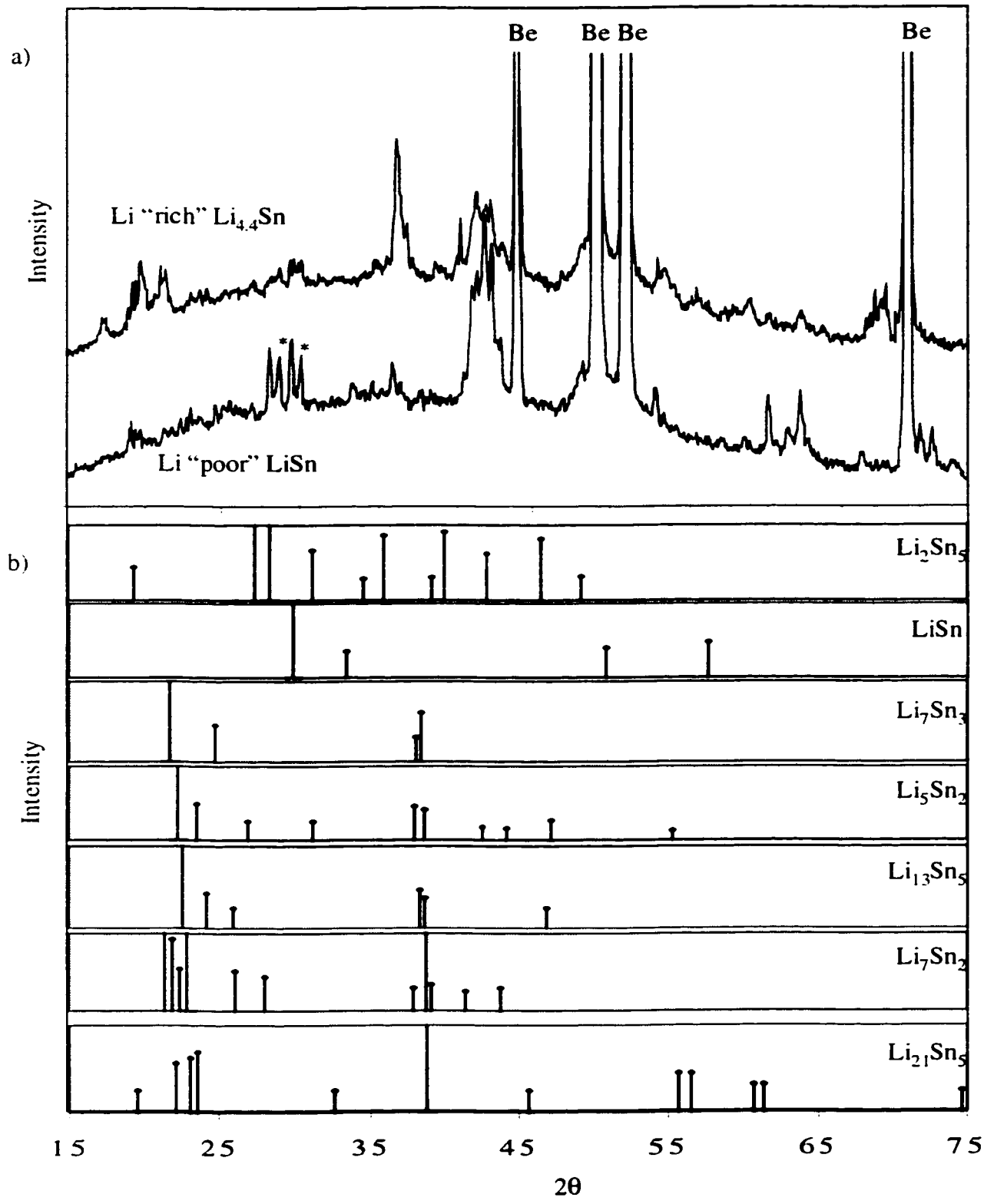

Figure 2.4 Powder diffraction patterns of Li-rich and Li-poor lithium tin phases, with corresponding diffraction reflections for Li-Sn phases.
** mark reflections corresponding to Sn metal impurities*

quickly, as the only remaining liquid is the excess lithium metal. While this sounds plausible in theory, it is in fact quite difficult to achieve. An added level of ingenuity was acquired, with the advice of Prof. Allan Ardell (UCLA). A system was designed whereby the annealing process took place across a very gradual temperature gradient, enhancing the propensity for crystallization. The basic reaction components were the same as previously, except that a Pyrex™ tube was chosen, which was suspended within the vertically mounted tube furnace. Beginning at the center (hottest point), the reaction tube was lowered through the furnace by a distance of 20cm over a period of 3 days. To achieve this very slow rate of motion, a stepper motor controlled by a LabView program was implemented. The furnace was heated to 460°C and the sample was annealed for several hours to achieve a homogenous melt before the stepper motor program was initiated. At the end of the reaction, the Pyrex™ tube was then transferred to the glove box and the sample was extracted. The top layer of the product comprised light silver colored, malleable lithium metal, beneath this were the much darker, brittle, highly reflective crystals. The majority of the crystals were embedded in the soft lithium, and could not be easily retrieved, particularly within the confines of a glove box!

One single crystal of $Li_{22}Sn_5$ was successfully extracted and analyzed using single crystal X-ray diffraction. This crystal had the appearance of smoked glass with a metallic luster. The goal was to grow a single crystal of volume $1mm^3$ that could be used for single crystal NMR studies, but unfortunately this was not achieved.

2.4 *Single Crystal Analysis*

The crystal, which is known to be highly reactive, was mounted in silicon grease directly onto the diffractometer at –76°C, to avoid any oxidation or exposure to moisture. Preliminary evaluation of the crystal quality was established by taking a rotation photograph. The crystal reflected extremely well and the unit cell was determined based on 28 reflections. Data was collected in the positive octant, to $2\theta=70^{\circ}$, giving 3900 data points. The refinement, including absorption correction, gave an R value of 1.89, which is exceptionally good. The cubic space group is $F\bar{4}3m$, with a = 19.6898Å. The fractional coordinates, including the isotropic thermal parameters are listed in **Table 2.1**.

	Atom	X	Y	Z	Average Thermal Parameter
e	Sn (1)	0.66666	0.66666	0.66666	0.00783
e	Sn (2)	0.90970	0.90970	0.90970	0.00755
f	Sn (3)	0.68020	0.00000	0.00000	0.00784
g	Sn (4)	0.42924	0.25000	0.25000	0.00690
d	Li (1)	0.75000	0.75000	0.75000	0.01422
e	Li (2)	0.58086	0.58086	0.58086	0.02356
e	Li (3)	0.82452	0.82452	0.82452	0.01919
e	Li (4)	0.16785	0.16785	0.16785	0.01341
e	Li (5)	0.05209	0.05209	0.05209	0.01871
e	Li (6)	0.30603	0.30603	0.30603	0.01471
e	Li (7)	0.43786	0.43786	0.43786	0.01860
f	Li (8)	0.82588	0.00000	0.00000	0.02557
g	Li (9)	0.57750	0.25000	0.25000	0.01780
h	Li (10)	0.08717	0.08717	0.75544	0.02487
h	Li (11)	0.34104	0.34104	0.51158	0.02261
h	Li (12)	0.09826	0.09826	0.27114	0.03211
h	Li (13)	0.34353	0.34353	0.01603	0.01630

Table 2.1 Atomic positions for $Li_{21.25}Sn_5$ including thermal parameters and Wycoff site labels (a-h).

The space group differs from that originally published by Gladyeshevskii[11] *et al.*, of the accentric cubic F23. Their assignment was made on the basis of Debye photographs, with a very limited number of data points. The structural analysis of the related phase, $Li_{22}Pb_5$ was performed using data taken from a Wiesenberg camera in 1958.[12] The structure was refined in the accentric space group, F23, with an R value of 19%. The data set was plagued with absorption due to the high concentration of lead atoms. Interestingly, the positions of the lead atoms are equivalent in both the F23 and $F\bar{4}3m$ space groups, with the positions of the lithium atoms differentiating between the two. Since then, Nesper *et al.* published a correction to the original isostructural $Li_{22}Si_5$, re-assigning it to the $F\bar{4}3m$ space group, and removing one lithium from the composition, such that the true formula was now $Li_{21}Si_5$.[13] In terms of distinguishing between the two possible space groups, it is important to note that the relative scattering from lead and lithium versus tin and lithium or silicon and lithium drastically favours the latter pair. This means that it would be much easier to locate the lithium atoms in the latter structure since they would contribute much more to the overall scattering. Technological

advances in the last 4 decades also allow for the accurate determination of absorption effects, allowing for the improved R values in the more recent work.

Published in the dissertation of Nesper is the corrected $Li_{21}Sn_5$ structure.[14] Their work on the lithium silicon analogue, $Li_{21}Si_5$ concluded that the special positions 4a, 4b, 4c, and 4d could not be occupied by lithium, since this gave rise to unreasonably short interatomic distances. Our space group agrees with his assignment, but on the basis of our absorption correction and refinement, we found that one of the four special positions is in fact occupied by lithium. Since our data set was refined on more than twice the number of unique data points obtained by Nesper *et al.*, and since our R (1.89%) is substantially better than theirs (5.2%), we are convinced that the correct formula for this compound should be $Li_{21.25}Sn_5$, or $Li_{17}Sn_4$. This phase will nevertheless be referred to for the remainder of the thesis as $Li_{21}Sn_5$, for clarity and simplicity. The explanation for this surprising result was found in a thorough comparison of the Li-Sn and Li-Si structural data, in particular, examination of the lithium interactions. The silicon and tin atoms occupy the same crystallographic positions in both structures, with no significant changes in interatomic distances. On the other hand, the lithium-lithium interactions, especially around the four tetrahedral sites, show significant dissimilarities. The site that is occupied in the tin structure has expanded compared to that in the silicon structure, such that there is space available to be filled by a lithium atom in the former, while in the latter the volume of this site is prohibitive. These four sites are illustrated in **Figure 2.5** (only lithium atoms shown), where **2.5(a-c)** represent the unoccupied tetrahedral sites in both the $Li_{21}Si_5$ and $Li_{21.25}Sn_5$ structures, and **2.5(d)** illustrates the occupied tetrahedral site for the latter phase. This site is not occupied in the silicon analogue. **Figure 2.6a)** shows the unit cell for $Li_{21.25}Sn_5$, including all lithium and tin atoms occuring on three-fold axes. **Figure 2.6b)** shows the coordination environment around Sn(1), and **2.6c)** shows the coordination environment around Li(1). **Figure 2.7** shows the tetrahedral coordination environments of the tin atoms (lithium atoms excluded for clarity). The interatomic distances in the Li-Si structure are compared with those for the Li-Sn structure in **Table 2.2**. The significant distances related to the tetrahedral sites, which are lengthened in the tin structure compared to the silicon structure, are highlighted.

An intriguing interpretation of this data is that both structures are correct. This hypothesis is based on the possible trend within the series of group four lithium compounds,

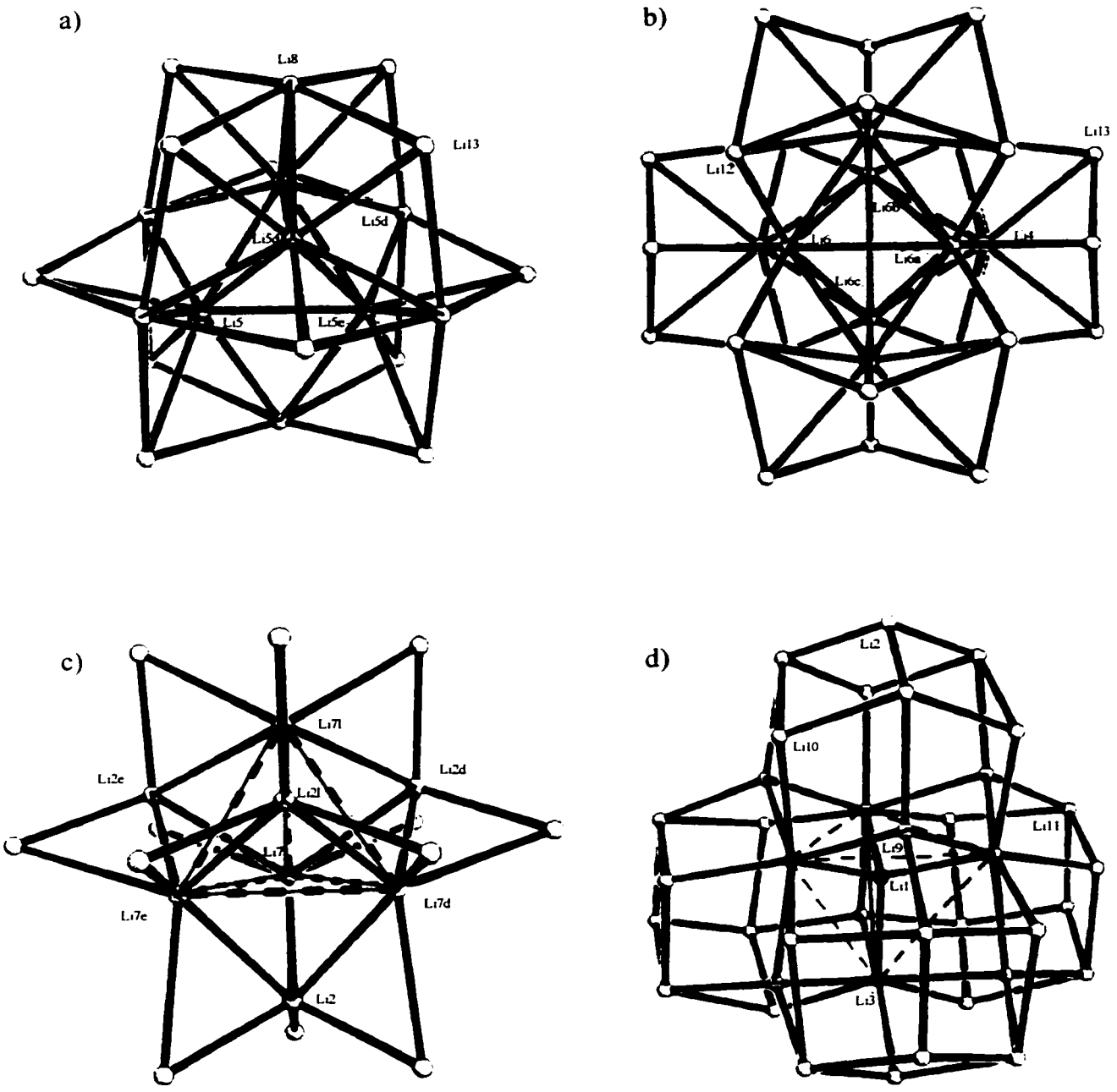

Figure 2.5 Illustrations of coordination environments at lithium on tetrahedral sites (red lines) in $Li_{21.25}Sn_5$ crystal structure a) unoccupied, b) unoccupied, c) unoccupied, and d) occupied.

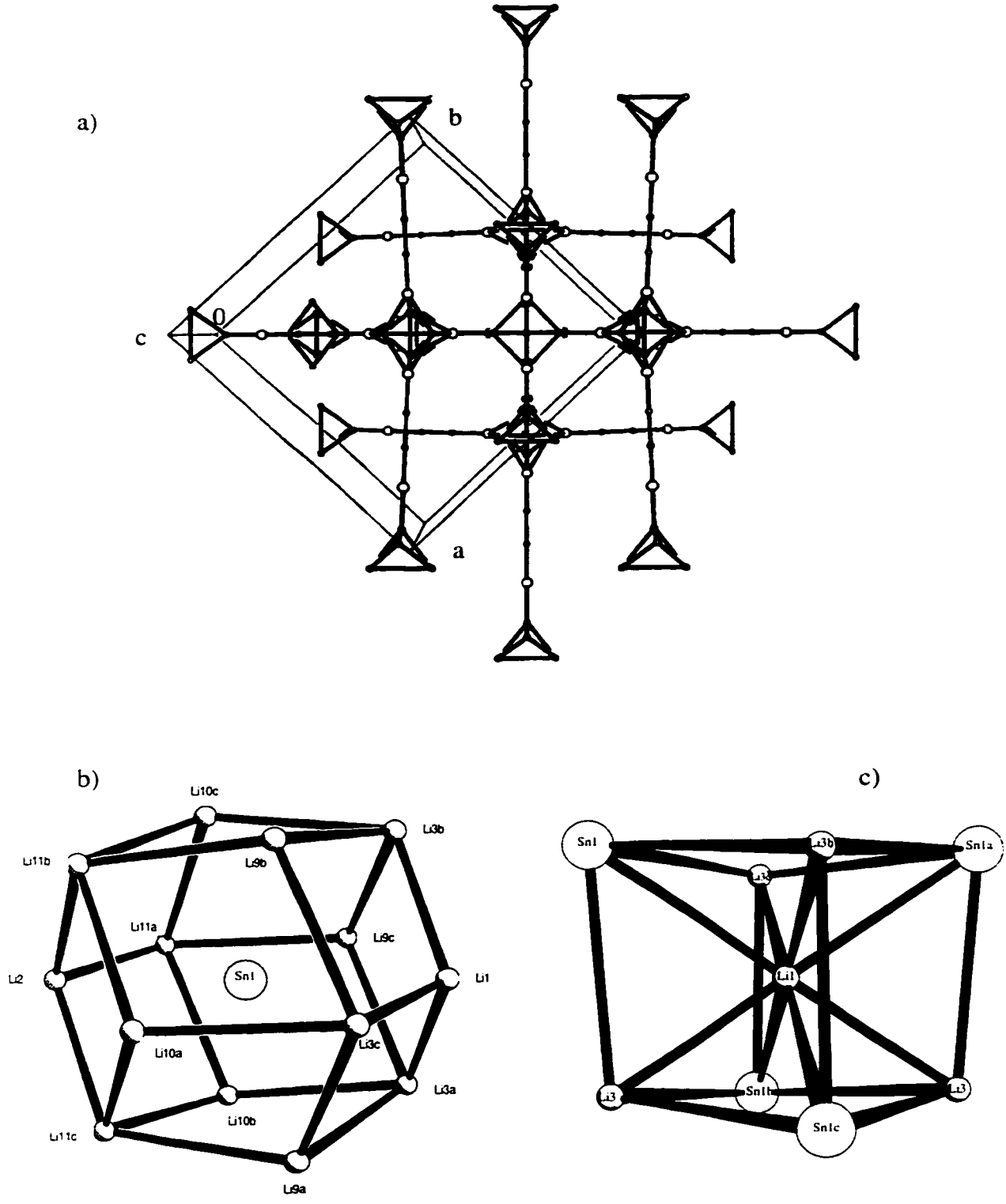

Figure 2.6 Illustrations of $Li_{21.25}Sn_5$ crystal structure a) all atoms on three-fold symmetry sites b) coordination environment around Sn1 c) coordination environment around Li1

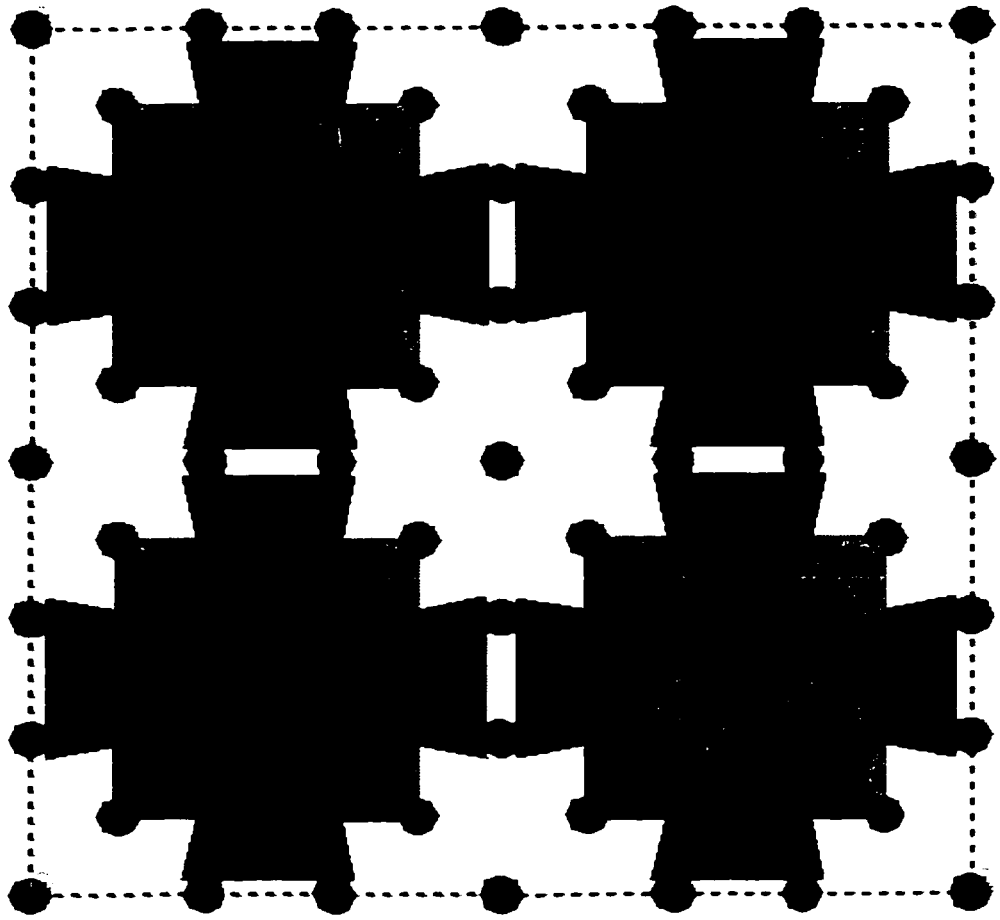

Figure 2.7 Illustration of $Li_{21.25}Sn_5$ crystal structure, showing only tin atoms and tin tetrahedra.

Sn(1)	282	265	Li(10)	3x
	291	277	Li(9)	3x
	291	287	Li(2)	
	291	289	Li(3)	3x
	306	293	Li(11)	3x
Sn(2)	279	262	Li(13)	3x
	291	287	Li(3)	
	300	287	Li(5)	3x
	301	289	Li(8)	3x
	304	299	Li(10)	3x
Sn(3)	284	262	Li(10)	2x
	287	266	Li(8)	
	290	272	Li(12)	2x
	290	276	Li(7)	2x
	298	283	Li(2)	2x
	317	306	Li(11)	2x
Sn(4)	282	268	Li(13)	2x
	289	272	Li(6)	2x
	292	277	Li(9)	
	301	279	Li(11)	2x
	298	283	Li(4)	2x
	306	293	Li(12)	4x
Li(1)	254		Li(3)	4x
Li(2)	258	255	Li(11)	3x
	286	268	Li(7)	3x
	298	283	Sn(3)	3x
	291	287	Sn(1)	
	344	321	Li(10)	3x
Li(3)	254	-	Li(1)	4x
	283	269	Li(9)	3x
	281	280	Li(10)	3x
	291	287	Sn(2)	
	312	289	Sn(1)	3x
Li(4)	281	269	Li(12)	3x
	282	273	Li(6)	3x
	298	283	Sn(4)	3x
	301	291	Li(13)	3x
Li(5)	281	271	Li(8)	3x
	290	286	Li(5)	3x
	281	286	Li(13)	3x
	300	287	Sn(2)	3x
Li(6)	275	259	Li(12)	3x
	289	272	Sn(4)	3x
	282	272	Sn(4)	3x
	312	312	Li(6)	3x
Li(7)	286	268	Li(7)	3x
	290	276	Sn(3)	3x
	306	299	Li(11)	3x
	343	326	Li(12)	3x
	346	328	Li(6)	3x

Li(8)	279	265	Li(10)	2x
	287	266	Sn(3)	
	281	271	Li(5)	2x
	301	289	Sn(2)	2x
	312	299	Li(13)	4x
	334	311	Li(12)	2x
Li(9)	285	262	Li(11)	2x
	283	269	Li(3)	2x
	292	277	Sn(4)	
	291	277	Sn(1)	2x
	319	294	Li(13)	2x
	321	308	Li(10)	4x
Li(10)	280	259	Li(11)	
	284	262	Sn(3)	
	275	265	Li(8)	
	282	265	Sn(1)	
	282	280	Li(3)	
	300	285	Li(13)	
	304	299	Sn(2)	
	322	308	Li(9)	2x
	344	321	Li(2)	
	>354	345	Li(12)	2x
Li(11)	258	255	Li(2)	
	280	259	Li(10)	
	284	262	Li(9)	
	283	267	Li(12)	
	301	279	Sn(4)	
	306	293	Sn(1)	
	306	299	Li(7)	
	317	303	Sn(3)	2x
	>354	339	Li(13)	2x
Li(12)	275	259	Li(6)	
	283	267	Li(11)	
	281	269	Li(4)	
	290	272	Sn(3)	
	301	288	Li(13)	2x
	306	293	Sn(4)	2x
	334	312	Li(8)	
	343	326	Li(7)	
	>354	345	Li(10)	2x
	>354	349	Li(12)	2x
Li(13)	279	262	Sn(2)	
	282	268	Sn(4)	
	299	285	Li(10)	2x
	299	286	Li(5)	
	301	288	Li(12)	2x
	302	291	Li(4)	
	320	294	Li(9)	
	312	299	Li(8)	2x
	>354	339	Li(11)	2x

Table 2.2 Interatomic distance comparison: $Li_{21.25}Sn_5$ (left) and $Li_{21}Si_5$(right)

$Li_{21+x}M_5$, where M = Si, Ge, Sn, or Pb. It is conceivable that there is a progression within this series involving an increasing occupancy of the tetrahedral site. The tetrahedral sites in the $Li_{21}Si_5$ structure are too small to allow for occupation by lithium. Full analysis of this series would involve the synthesis of single crystals of each member, ideally including analysis by single crystal NMR. However this work falls outside of the scope of this thesis. This result arose as an aside to the real focus of this thesis project, which was to study these phases, and their relation to the electrochemically created lithium-tin interactions using solid-state NMR. Other interesting discussions of this system are described in the next section, on Zintl anions.

2.5 *Thoughts Concerning Zintl Phases*

Zintl phases are of interest in the context of this thesis, since the Li-Sn phases are classified as Zintl phases. These phases were first identified by Zintl, as a series of intermetallics in which the distribution of charge was not the same as that found in metals, but rather involved an electropositive element which would give up its electron to its electronegative counterpart.[15] The original phase studied by Zintl was NaTl. The description of the electron distribution is Na^+Tl^-, such that both elements fulfill the octet rule. This is the classical rule which applies to insulating compounds. The accomplishment of Zintl was to show that this description of chemical bonding applies to metal-*meta*-metal compounds as well.

Lithium compounds of group 14 elements indicate the extent of the overlap between Zintl phases and intermetallics. For low lithium content, the compounds are normal Zintl phases, but with the increasing ratio of lithium to tin (or other group 14 element), the standard electron counting rules fail and the electron distribution becomes quite complex. For example, the phase $Li_{21}Si_5$ can be described as two large Zintl ions, $[Li_{22}Si_4]^{4+}$ and $[Li_{20}Si_6]^{4-}$. These large ions arrange themselves on a lattice which matches the simple NaTl structure.[15]

Table 2.3 lists the Li-Sn phases, their crystal structure data and the Zintl anions predicted for each phase.[15] The premise of the electrochemical reaction between lithium and tin is that this series of Li-Sn alloys are formed in situ within the electrode. As the electronic structure of these Zintl phases themselves is distinct from a simple intermetallic phase, it is significant to consider the distribution of electronic charge within the electrode materials as well. This will be developed in later chapters.

Phase	Zintl (poly)anion	Space Group	Lattice Constants (Å)	Density	Reference
Li_2Sn_5	$[Sn_5^{2-}]_\infty$ framework	P4/mbm	10.274, 3.125	6.11	[16]
LiSn	$[Sn^-]_\infty$ puckered net	P2/m	5.17, 3.18, 7.74, γ=104.5	4.97	[17]
Li_7Sn_3	Linear $[Sn_3^{7-}]$ group	$P2_1/m$	9.45, 8.56, 4.72 γ=109.95	3.72	[18]
Li_5Sn_2	$[Sn_2^{4-}]$	$R\bar{3}m$	4.74, 19.83	3.56	[19]
$Li_{13}Sn_5$	$[Sn^{4-}]$, $[Sn_2^{4-}]$	$P\bar{3}m1$	4.70, 17.12	3.46	[20]
Li_7Sn_2	$[Sn^{4-}]$, $[Sn_2^{6-}]$	Cmmm	9.80, 13.80, 4.75	2.99	[21]
$Li_{21}Sn_5$	$[Sn^{4-}]$	$Fm\bar{3}m$	19.760	2.55	[22]

Table 2.3 Zintl Ions in Li-Sn Phases[15]

2.6 References

[1] J. Pickworth Glusker and K.T. Trueblood Crystal Structure Analysis: a Primer Oxford University Press, London 1972.

[2] International Tables of Crystallography Volume C: Mathematical, Physical and Chemical Tables, ed. A.J.C. Willson, Kluwer Academic Publishers, (1992).

[3] B.E.Warren, X-ray Diffraction Dover Publications, New York (1990).

[4] Y. Idota, T. Kubota, A. Matsufuji, Y. Maekawa and T. Miyasaka, *Science*, **276**, 1395 (1997).

[5] JC-PDS # 6-0395I International Center for Diffraction Data, 1996, U.S.A.

[6] JC-PDS # 41-1445 International Center for Diffraction Data, 1996, U.S.A.

[7] JC-PDS # 20-0044 and 11-0500 International Center for Diffraction Data, 1996, U.S.A.

[8] Binary Alloy Phase Diagrams 2nd Ed. Vol. 3 ed. T.B. Massalski, ASM International, (1990).

[9] JC-PDS International Center for Diffraction Data, 1996, U.S.A.

[10] Cerius^2 Molecular Simulations Incorporated, San Diego USA, 1997.

[11] E.I. Gladyeshevskii, G.I.Oleksiv, and P.I.Kripyakevich, *Soviet Physics – Crystallography*, **9**, 269 (1964).

[12] A. Zalkin and W.J. Ramsey, *Journal of Physical Chemistry*, **62**, 689 (1958).

[13] R. Nesper and H.G. vonSchneering *Journal of Solid State Chemistry* **7048** (1987).

[14] R. Nesper Dissertation University Stuttgart, 1997.

[15] R. Nesper, *Progress in Solid State Chemistry*. **20** 1 (1990).

[16] D.A. Hansen, L.J. Chang *Acta Crystallographica* **B25** 2392 (1969).

[17] W. Mueller, H. Schaefer, *Z.Naturforschung*, **28b** 246 1973).

[18] W. Mueller, *Z.Naturforschung* **29b** 304 (1974).

[19] U.Frank, W.Mueller, H.Schaefer *Z.Naturforschung* **30b** 1 (1975).

[20] U. Frank, W. Mueller, *Z.Naturforschung* **30b** 316 (1975).

[21] U. Frank, W. Mueller, H. Schaefer *Z.Naturforschung* **30b** 6 (1975).

[22] R. Nesper, H.G. vonSchneering, J.Curda, unpublished

Chapter 3 Electrochemical Studies of Anode Materials

3.1 Introduction: Tin metal and other Tin-based anodes

The electrochemical investigations in this thesis have focussed primarily on systems in which tin is the electroactive nucleus. Tin metal has been recognized as being electrochemically reactive toward lithium metal since the early report of the reaction of various metals with lithium when connected through an external circuit in an organic electrolyte.[1] Since that time a variety of groups have investigated the electrochemical properties of tin metal, tin oxides, tin-lithium alloys and other tin based composite anode materials. A short review of the electrochemistry of tin is appropriate at this time, to set the stage for the electrochemical studies presented in this thesis

3.1.1 Tin Metal Anodes

Tin metal reacts with lithium to a maximum lithium to tin ratio of 4.4:1, giving tin a very high theoretical capacity. While tin intercalates a large amount of lithium on a per mole basis, its molar mass gives it a comparatively low specific capacity, in mAh/g. The thermodynamics of lithium insertion into tin metal at high temperature were first investigated by Wen *et al.*[2] **Figure 3.1** shows the electrochemical profile obtained at 415°C, in which the various two-phase and single phase regions can be clearly identified by the plateaux and vertical steps respectively. By *ab initio* calculation, Courtney *et al* have presented a voltage profile of the reaction between Li and Sn which agrees well with their ambient temperature electrochemical results.[3] These results both indicate that the electrochemical lithium insertion into tin occurs *via* discrete processes, in which the horizontal voltage plateaux represent the co-existence of two phases, and the vertical lines represent single phases, which match stoichiometrically with the phases in the Li-Sn phase diagram (**Figure 2.3**). The agreement between the phase diagram and the electrochemical curve is much better for the high-temperature process, indicating that the kinetics of diffusion may inhibit the complete formation of the appropriate phases at ambient temperature.

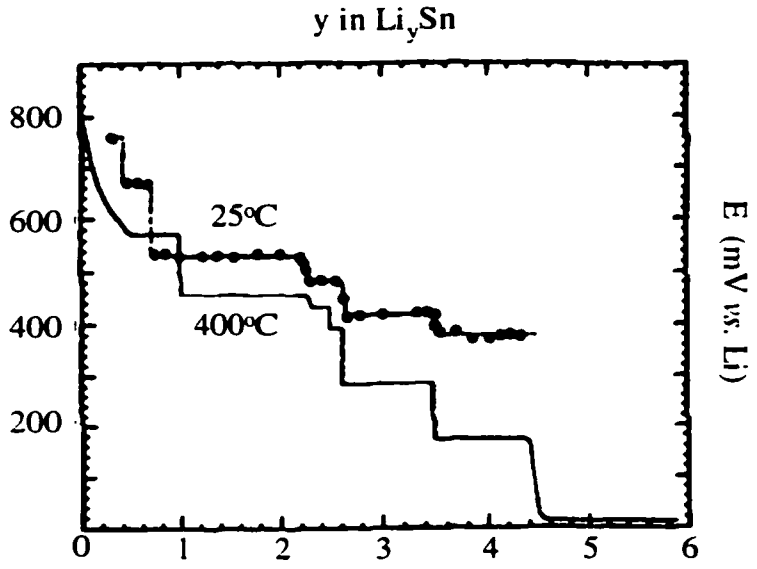

Figure 3.1 Potential versus composition of the Li-Sn system at 25°C compared with data at 400°C [4]

Pristine tin metal is not a viable anode material because of the volume expansion experienced by the metal during the insertion of lithium. Listed in **Table 3.1** are the percentage volume expansions for each of the anodes between the starting material and the maximum lithium concentration. The value for Sn is extremely large, 676%. This causes problems of crumbling and cracking within the anode material during cycling, resulting in a loss of contact and battery failure. Besenhard *et al.* studied the lithium insertion process in a series of tin anodes of varying particle size. SEM images of the electrode materials before and after lithium insertion showed that the particles were severely cracked.[5] The volume change, which caused the particles to crack, was most detrimental in coarse grained, or macrostructured metal particles. By controlling morphology using smaller particles, intermetallics, and composites, the crumbling effect can be limited. This concept is illustrated in **Figure 3.2**, which shows the propensity for small particles to withstand changes in the volume of the particle, without degradation of the particle, since the absolute dimensions of the particle remain small, even after the uptake of large amounts of lithium. While this concept is excellent in principle, if the small particles are not physically separated from one another, the tendency to aggregate and

Unlithiated Compound	Lithiated Compound	Volume change / %
Al	LiAl	97
Bi	Li_3Bi	177
Cd	Li_3Cd	268
Pb	$Li_{4.4}Pb$	234
Sn	$Li_{4.4}Sn$	676
Si	Li_4Si	323
Zn	LiZn	71
C	LiC_6	6

Table 3.1 Volume changes which occur upon lithiation of various metal.[6]

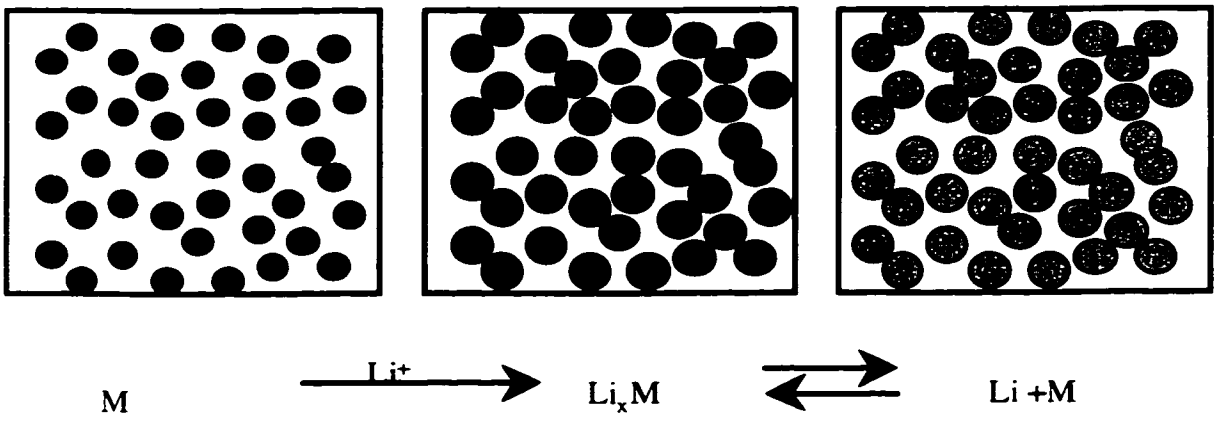

Figure 3.2 Model of lithium insertion into well-separated small-particle metal matrix. Even 100% volume expansion does not necessarily crack the particle, and overall dimensions remain relatively stable on cycling.[5]

thereby lower the surface energy of the system, will eventually result in failure of the anode material. Therefore many groups have investigated ways to isolate the electroactive particles from each other. These efforts fall into two distinct classes; the 'mixed conductor matrix' concept, and the 'convertible oxides' concept.

3.1.2 *The Mixed Conductor Matrix*

The 'mixed conductor matrix' concept was patented by Huggins *et al.* in 1984 and involves an anode in which an electroactive component is embedded in an inactive conducting metallic matrix.[7] The basic idea is that the electroactive particles are dispersed within a matrix that is both electronically and ionically conductive. If the particle size of the active component is sufficiently small, this will provide a high surface area and facilitate access of the lithium ions through the ionically conducting matrix to the active particles. As well, when the lithium is removed, the active particles are confined by the matrix material, thus reducing problems of particle aggregation. The voltage range must be chosen such that the inactive matrix does not react with lithium, but such that the active material has the largest possible lithium capacity. Since the matrix is also electronically conductive, it can act as the current collector for the electrode as well. The critical factor in such systems is the chemical diffusion coefficient of lithium within the matrix material. **Table 3.2** lists the chemical diffusion coefficients for a series of Li-Sn alloys as well as some other possible matrix materials.

One classic example of the mixed matrix concept was the combination of $Li_{13}Sn_5$ as a matrix material with finely divided silicon, the electroactive component.[8] This composite took advantage of the extremely high conductivity of lithium within $Li_{13}Sn_5$ at 400°C, which allowed the lithium to easily access the active silicon. The voltage of this system must be maintained within the narrow regime of 0.28-0.39V, to prevent the $Li_{13}Sn_5$ from reacting further with lithium, as is shown in **Figure 3.3**.[4] The available voltage range is determined by the length of the vertical, single phase region in the Li-Sn voltage profile. This range overlaps with the first Li_ySi plateau, giving the active silicon particles a possible Li uptake of $Li_{1.7}Si$. While the electrochemical performance of this material is good, the limited lithium insertion capacity, as well as the temperature at which the cell was run prevent it from being a viable candidate for commercialized lithium ion cells.

Composition		Max D_{chem}	Temp. °C
Nominal	Range (%Li)	(cm^2s^{-1})	
LiAl	16.4	$1.2*10^{-4}$	415
Li_3Sb	0.05	$7.0*10^{-5}$	360
Li_3Bi	1.37	$2.0*10^{-4}$	380
$Li_{12}Si_7$	0.54	$8.1*10^{-5}$	415
Li_7Si_3	3.0	$4.4*10^{-5}$	415
$Li_{13}Si_4$	1.0	$9.3*10^{-5}$	415
$Li_{22}Si_5$	0.4	$7.2*10^{-5}$	415
LiSn	1.9	$4.1*10^{-6}$	415
Li_7Sn_3	0.5	$4.1*10^{-5}$	415
Li_5Sn_2	1.0	$5.9*10^{-5}$	415
$Li_{13}Sn_5$	0.5	$7.6*10^{-4}$	415
Li_7Sn_2	1.4	$7.8*10^{-5}$	415
$Li_{22}Sn_5$	1.2	$1.9*10^{-4}$	415
LiGa	22.0	$6.8*10^{-5}$	415
LiIn	33.0	$4.0*10^{-5}$	415
LiCd	63.0	$3.0*10^{-6}$	415

Table 3.2 Data on chemical diffusion in lithium alloy phases[9]

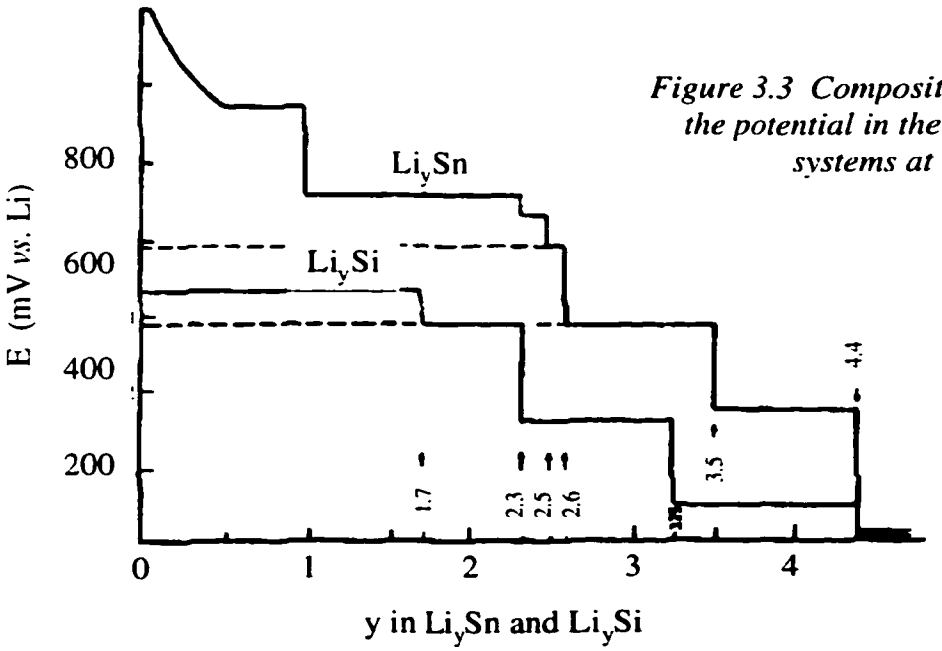

Figure 3.3 Composition dependence of the potential in the Li-Sn and Li-Si systems at 415°C.[4]

Other groups reported on similar systems, including the work of Yang *et al.* on the SnSb embedded in a Sn matrix.[10] In this case, the ductility of the Sn matrix was used to advantage, allowing the composite to easily accommodate volume changes as the SnSb phase reacted with lithium, to a maximum concentration of Li_3SnSb. This system offer advantages of porous microstructure and high reactant surface area. This results in a high achievable current density on the macroscopic scale, while allowing the active particles to maintain low local charge, and limiting aggregation of these active particles on the microscopic scale.

A recent example of this type of electrode material is the intermetallic compound, Cu_6Sn_5, which undergoes a two-phase reaction, yielding $Li_xCu_6Sn_5$ where $x = 3$.[10] This phase was chosen in order to take advantage of the excellent electrical properties of copper. It was shown by powder X-ray diffraction that the crystallographic changes which occur during lithium insertion are highly ordered and reversible. The Cu-subarray remains unchanged, while the tin atoms shift to allow for the insertion of lithium into these lattice sites. The fact that the original structure is reformed on charge distinguishes this phase from other mixed conductive matrix materials, in which the structural changes are neither so well defined, nor reversible.

Also in the category of mixed conductive matrix electrodes are the tin-iron composites published by Mao *et al.*[11,12] This work, published under the description of an active/inactive nanocomposite, demonstrates how the ideas in the field of tin metal anodes are coming full circle. While this work followed the recent resurgence of interest in tin-oxide based anodes, the ideas described are very similar to those developed fifteen years ago by Huggins *et al.* The advantages and disadvantages of oxide based electrodes are described in the subsequent section. The studies of the Fe-Sn materials, which are prepared by high energy ball-milling, include extensive Mossbauer effect spectroscopy, probing the tin and iron centers.[13] Comparative studies with the tin-oxide electrodes conclude that in both cases the iron, or oxide, is inactive, and the tin centers interact with lithium *via* the formation of lithium tin alloys.[14,15] The disadvantage of the oxide systems, which is overcome by the Fe-Sn, and other mixed conductive matrix electrode materials, is the irreversible capacity that arises from the initial reaction between lithium and oxygen to form lithia. Thus, following the excitement created in the area of tin oxide electrode materials, at least one group has returned to mixed conductive

matrix, or active/inactive nanocomposite materials in search of an anode material which will meet the criteria of high capacity, low irreversibility, and excellent cycling behaviour.

These composite materials were developed to improve the cyclability of tin metal by allowing the volume changes within the active material to occur without causing crumbling of the electrode. A related approach, which offers similar benefits, is the use of a tin-oxide based starting material.

3.1.3 Convertible Oxides

The preeminent work in this area is that of Idota *et al.*, who developed the tin-composite-oxide (TCO) glasses that are currently being commercialized as alternative anode materials. The original report, published in *Science*, supported by over 200 patents, and currently being prepared for market by the newly created Fujifilm Celltec Co. under the trade name STALION,[16,17] has generated overwhelming interests from the electrochemical community. The new glass is reported to have a volumetric capacity of 2200mAh/cm^3, and a gravimetric capacity of greater than 600mAh/g. This compares extremely favorably to carbon based anodes, which typically achieve four times lower volumetric capacity, and half the specific capacity of the TCO glass. These results, which significantly improve upon the current commercial technologies, have sparked a great number of reports on the electrochemical behaviour of various tin-composite oxides, as well as the parent oxides, SnO and SnO_2 themselves. Moreover, the great puzzle in this field arises from the disputed mechanism of the reaction between the active material and lithium. The original *Science* paper claimed that the mechanism of reaction was simple lithium insertion, and that no evidence for the formation of metallic tin, or lithium-tin alloys was found. In their proposed insertion mechanism the lithium ion interacts with the bonding orbital of Sn-O, with accompanying partial electronic reduction of both the Sn(II) and lithium ion. The proposal is based on their ^{7}Li NMR spectra, in which even at deepest discharge, the chemical shift of the lithium is only 10ppm. They comment that this shift is 'small enough' to be assigned to lithium in a highly ionic state. They maintain that this material participates in a lithium insertion mechanism which is unique to that observed in crystalline SnO.

Subsequent reports claimed that the only possible mechanism is one of *in situ* metallic tin particle formation, followed immediately by alloying of the tin aggregates with lithium,

forming the thermodynamically predicted Li-Sn phases. The contrasting mechanism was proposed by Courtney *et al.* The supporting evidence is primarily a series of *in situ* diffraction studies studies performed by the group of Jeff Dahn that are described in detail below. These data are all collected on systems other than the TCO glass reported by Idota *et al.*, including SnO, SnO_2, Li_2SnO_3, $SnSiO_3$, and SnO_2BPO_6. While these studies are valid in their own right, and have offered substantial information regarding the class of tin-oxide based materials, we maintain that there is something unique about the formulation of the TCO glass. The surprising feature of all the studies of the tin-composite oxide system, subsequent to the original report, is the omission of aluminum from the composite.

When lithium is inserted into tin oxide, the initial reaction is the reduction of $Sn^{2+/4+}$ to Sn^0 with the concomitant formation of Li_2O. This reaction is presumed to be irreversible. Thereafter the reaction between lithium and tin is surmised to proceed in a similar fashion to that which exists in the metal-based composites. In this case, the reduced tin metal is formed *in situ*, and occurs therefore as domains of nano-structured or even amorphous tin. Thus the sequestering of the active particles is an *in situ* process, as opposed to being mechanically formed during the preparation of the composite. Hence the term "convertible oxides" was coined. The drawback of such a system is the requisite irreversible capacity within the cell. Lithium oxide is the inactive matrix, in this case being ionically conducting, but not electronically conducting. The lithium oxide acts as the "solid electrolyte". Using SnO_2 as an example, the proposed reaction mechanism is:

$$SnO_2 + 4Li^+ + 4e^- \rightarrow Sn + 2Li_2O \quad \text{(Decomposition)}$$

$$yLi^+ + Sn + ye^- \rightarrow Li_ySn \quad \text{(Alloying)}$$

This proposed mechanism is shown schematically in **Figure 3.4**, first presented by Courtney *et al* in 1997.[18] The Li_2O matrix stabilizes the electrochemically active species during charge and discharge; limiting the aggregation of these particles. This is similar to the role played by the inactive mixed conducting matrix described in the previous section. In the case of Fuji's TCO glass, the matrix is not simply lithium oxide, but a glassy matrix including aluminium, phosphorus, and boron oxides as well. In 1997, at the time of the report by Idota *et al.* and Courntey *et al.*, the role of these 'spectator ions' in stabilizing the electrochemical process had not yet been explored.

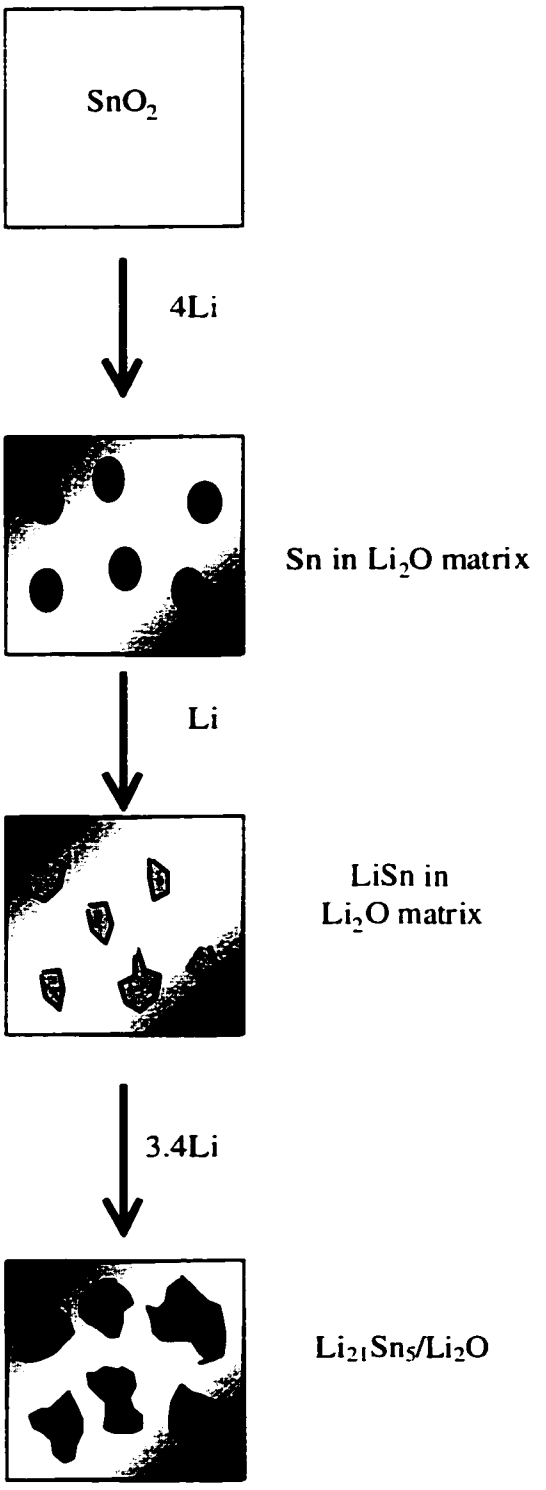

Figure 3.4 Reaction mechanism schematic for the reaction of lithium with tin(IV) oxide, as proposed by Courtney et al.[18]

Initial insertion of lithium causes formation of matrix and Sn metal particles. Further reduction causes formation of Li-Sn alloy domains, of increasing size and increasing ratio of Li/Sn. These domains are not well defined structurally.

Examining the work of Dahn *et al.* in greater detail gives insight concerning the source of the controversy in this field. In a series of papers, the first of which appeared in 1997, this group have probed the electrochemical reaction between tin and lithium in a variety of systems. Their mechanism, described above, was based upon an extensive study using *in situ* X-ray diffraction. The data presented clearly show that in SnO, the initial reaction results in the formation of metallic Sn, followed by Li_2Sn_5, and LiSn. Each of these phases are readily identified by the reflections in the diffraction pattern. Subsequent discharge is assumed to result in the formation of the other Li:Sn line phases, but the diffraction data become ambiguous at this point. The reflections are no longer well defined, but severely broadened features are attributed to the anticipated phases. The data for SnO is the most definitive. All other data, particularly those for $SiSnO_3$ and Li_2SnO_3, do not exhibit well defined reflections at any point in the discharge process. Nevertheless, based on similarities in the voltage profiles, the mechanism of reaction is purported to be identical in all cases. This result is extrapolated by inference to include the TCO glass developed by Fuji, although this glass itself had not been studied.

Following the *in situ* diffraction study a paper was published in which the diffraction pattern of a disordered $Li_{4.4}Sn$ phase was calculated.[19] The motivation for calculating such a pattern was to understand the observed diffraction for the electrochemically prepared $Li_{2.5}Sn$ - $Li_{4.4}Sn$ phases. Such samples consistently produced diffraction patterns dominated by broad oscillations. Calculations demonstrated that a similar diffraction pattern could be obtained from Sn tetrahedra, randomly oriented on a body centered cubic lattice. This work is described in greater detail in reference to our PDF studies, presented in Chapter 6.

The electrochemical response of two systems, SnO_2 and a glassy Sn_2BPO_6, was subsequently tested under a variety of voltage limits. The conclusion drawn from this work was that the grains of tin must be kept as small as possible to ensure excellent discharge/charge capacity retention. If the regions in which Sn is formed are kept sufficiently small, the coexistence of two-phase domains between bulk Li-Sn alloys is prohibited. By avoiding two phase regions the volume-change conditions, which cause crumbling of the electrode, can be avoided. Sharp features in the voltage profile were correlated with the formation of larger Sn

aggregates, and should therefore be avoided. Limiting the cycling range of the cell to 0.0-0.8V resulted in the smoothest voltage profile.

The electrochemical insertion of lithium into two types of glass of composition $SnO:(B_2O_3)_x:(P_2O_5)_y$ and $SnO:(B_2O_3)_{0.5}:(P_2O_5)_{0.5}(K_2CO_3)$, and pristine SnO were compared in order to prove the inconsequential role played by the glass matrix.[20] The same reaction mechanism as that reported in their original paper is claimed. The tin metal aggregates are thought to be as small as a few Sn atoms, although no evidence for this is given. The other components of the glasses, boron and phosphorus oxides are inert with respect to lithium, and are termed "spectator ions". The size of the tin aggregates is inversely proportional to the ratio of tin to spectator ions, but all materials showed aggregation upon extensive cycling. Aggregation continued until a saturation point was reached, which was dependent on the Sn:spectator ion ratio. As evidence of the lack of spectator ion participation in the electrochemistry of the material, a plot is shown in which the weight percent of tin is plotted versus the reversible capacity of the system. The data falls on a straight line going through the origin, indicating that the spectator ions do not contribute to the reversible capacity of the glass.

This body of work is quite conclusive, still it is notable that the materials studied here all omit aluminum for the composition, and thus are not necessarily comparable to the TCO glass reported by Idota *et al.*[16] More importantly, the mechanism reported by Courntey *et al.*[18] conflicts directly with the mechanism intimated by Idota *et al.* in their original work. With successive publication, Dahn *et al.* have softened their original proposal, indicating that the formation of *bulk* alloys is not expected, but rather small amorphous regions which resemble the lithium tin alloys stoichiometrically, but are not large enough to have well ordered structure.[21] The role of oxygen, first indicated to be significant by Idota *et al.*, has not been further investigated.

While tin based systems are fairly well understood systems from electrochemical point of view, in the case of the TCO glass developed by Idota *et al.*, there was ambiguity as to the origin of the enhanced capacity compared to stoichiometric tin oxides. Thus the motivation for the electrochemical investigations is two-fold. First, to thoroughly probe the electrochemical behaviour of three TCO glasses; TCO, Sn-rich-TCO, and Bi-doped-TCO and compare their electrochemical properties to those of the parent materials, Sn, SnO, and SnO_2, and thus obtain

a complete understanding of the reasons for the enhanced behaviour of the TCO materials. Second, in order to augment our understanding of the electrochemical properties of these systems, electrode samples were extracted at various levels of charge/discharge for *ex situ* study using multi-nuclear solid-state NMR, X-ray diffraction, and X-ray absorption spectroscopy.

3.2 Electrochemical Studies

The mathematical descriptions of the various types of electrochemical experiments are given in this section. These include voltage profiles, cycling experiments, potentiostatic experiments, and current pulse experiments.

3.2.1 Galvanostatic Voltage Profiles

When a constant current is passed through a galvanic cell lithium ions are transported from the negative electrode to the positive electrode, thus changing the composition of the positive electrode according to Faraday's Law:

$$\Delta\delta = \frac{M}{zmF}\int_0^t I dt \qquad (3.1)$$

where $\Delta\delta$ is the change in concentration of lithium within the positive electrode (also called x), M is the molecular weight of the sample, m is the initial mass of active material, z is the number of electrons transferred per ion (z = 1 for Li^+) and F is Faraday's constant (96485C/mol).[22] Typical voltage profiles are plotted as voltage (V) vs x, where x represents the number of moles of lithium inserted into the active material. In a galvanostatic experiment, the rate at which lithium is forced into the positive electrode is controlled by the current (mA). Increasing the current results in non-equilibrium conditions in the cell and is used to measure the ability of the test material to respond to high current densities, such as those required by the majority of device applications. The capacity of an electrode material can also be reported in Q, where Q is measured in mAh/g, and is calculated according to

$$Q = I * \frac{t}{m} \qquad (3.2)$$

I is the applied current, t is the time, and m is the mass of the active material. In this case the capacity is independent of the exact molecular weight of the material, and thus by plotting voltage versus Q, possible errors in the analysis of more complex, possibly non-stoichiometric materials can be avoided.

3.2.2 *Cycling Experiments*

In industry, a critical test for any battery system is its cyclability, or its ability to retain its reversible capacity over a large number of cycles. This is typically tested over hundreds or thousands of cycles, and in order to meet industrial standards, a material must retain better than 99% of its cycling capacity over hundreds of cycles. By plotting the reversible capacity versus cycle number, a capacity fade curve is obtained. The ideal material would show no capacity fade. This is impossible, according to thermodynamics, since energy will be lost in the system, but excellent battery candidates are those which exhibit minimal capacity fade.

Since the goal of this thesis was to understand the mechanism of lithium insertion into these materials, as opposed to testing their marketability, extensive cycling tests were not performed. To explore the changes in the cells upon cycling, several electrodes were cycled for 10 cycles, after which solid-state NMR experiments were performed. The reversible capacity as a percentage of the reversible capacity achieved on the first cycle is plotted versus cycle number.

3.2.3 *Potentiostatic Cyclic Voltammograms -*

The majority of the electrochemical data in this thesis were acquired under potentiostatic conditions. Because in this type of experiment the voltage is stepped at a specified rate, and the current is allowed to flow in response to the redox process at a given voltage point, the electrodes are presumed to be close to equilibrium. This is in contrast to the galvanostatic experiment, in which the current is applied at a constant rate, and the electrode is forced to accept the flux of lithium accordingly. In the potentiostatic experiment the extent of the reaction between lithium and tin is measured by the current at a given potential. The same type of information may be obtained in the galvanostatic experiment by taking the derivative (dV/dx) of the voltage profile, plotted against voltage. This is evident considering the following

$$I = \frac{dx}{dt} = \frac{dx}{dV} * \frac{dV}{dt} \tag{3.3}$$

The potentiostatic experiment also yields the voltage profile of the material. Thus the data obtained from the two experiments is interchangeable, with the advantage of the potentiostatic experiment arising from its closer approximation of equilibrium conditions.

A plot of current versus voltage will exhibit strong peaks in the current at voltages that correspond to a specific redox process or occupation of a specific potential site for lithium insertion. In a crystalline material, these peaks will be very well defined, since the binding energy for lithium at any one site is well defined with respect to its potential energy. In such a case, the peak represents a two-phase process, in which one phase, (corresponding to the binding of lithium in potential site A) is being consumed to form the second phase (corresponding to binding of lithium in potential site B). The peak corresponds to a plateau in the voltage profile; the voltage remains constant during the first order transition. In contrast, in glassy systems, where higher-order, or continuous phase transitions occur, there is no co-existence of two phases; but rather a smooth slope in the voltage profile, or broad feature in the cyclic voltammogram. This contrast between the lithium insertion process in a crystalline *vs.* disordered material is clearly illustrated in **Figure 3.4**.[22]

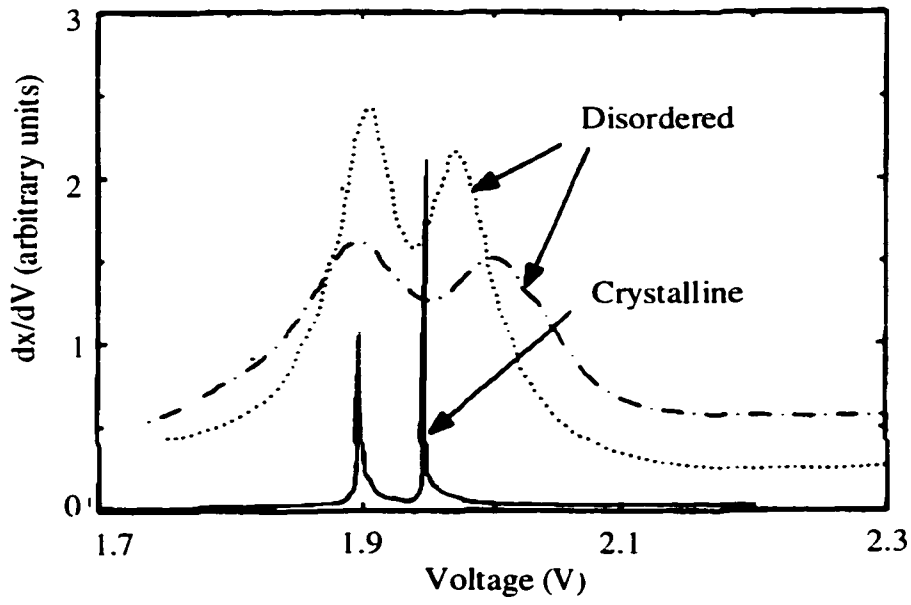

Figure 3.5 Comparing dx/dV for strongly disordered and crystalline materials.[22]

Even though the potentiostatic experiment is intended to closely approximate equilibrium conditions, the issue of electronic versus ionic equilibrium has been an issue in our studies. The issue is simply that an equilibrium electronic process, one which is slow enough to allow the system to incorporate the inserted electrons, may not be at ionic equilibrium, meaning the distribution of lithium ions within the electrode material may not be equilibrated. This is a particular problem in the case of Type III materials, such as SnO and TCO, where significant phase changes may be occurring on the atomic scale during the lithium insertion process. In order to alleviate this issue, all cells were equilibrated for 48hours at the desired voltage before being examined using other techniques.

3.2.4 Current Pulse Relaxation Experiments

Current pulse relaxation experiments (CPR) were used to study the kinetics of the reaction of the electrode materials with lithium ions. This technique is also known as Galvanostatic Intermittent Titration Technique (GITT), where the data is used for the calculation of diffusion coefficients. Such diffusion coefficients can only be considered meaningful for systems in which the electrochemical reaction is known to be single-phase. In the TCO glasses, the electrochemical reaction involves the segregation of discrete particulate phases and therefore the movement of grain boundaries, a condition which cannot be accounted for in the calculation of diffusion coefficients. Because such calculations would not have any real meaning in our systems, we have simply used current pulse relaxation experiments to qualitatively investigate the kinetic behaviour of lithium in TCO and tin oxide.

During a CPR experiment, current pulses are applied to the system. These pulses are separated by a relaxation period, during which the cell is put in open circuit voltage (OCV) to allow equilibrium to be established. The pulse time has been chosen to allow 0.25Li to react with the active material and the OCV is monitored until the potential varies by less than 4mV per hour. At this point the system is close to equilibrium and the next titration step is initiated. During the pulse the potential of the system departs from the equilibrium potential, owing to structural and/or kinetic hysterisis, and following this the potential relaxes toward that of the equilibrium. As a consequence, the larger the potential variation upon OCV, the further the system is perturbed from equilibrium during the pulse, and thus the slower the kinetics. By

plotting voltage versus capacity (in mAh/g or Li/mol) the kinetic response can be judged by the depth of the potential variation between the end of the pulse and the point at which the equilibrium condition is achieved. Alternately, by plotting voltage versus time (in hours), we can directly observe the changes in the rate at which the system achieves that equilibrium condition.

3.2.5 *Make up of Cell*

Figure 3.6 shows a schematic of the swagelock cells used in all our electrochemical studies. The casing is made of stainless steel. For examination of anode materials both posts are made of nickel, fitted with polymer rings which allow the casing to be tightened around the electrode and spring assembly. The active material is electronically separated from the counter and reference electrode, lithium metal, by the glass fiber separator. The separator allows the liquid electrolyte and lithium ions to pass from one electrode to the other, but prevents physical contact between the electrodes. The partially assembled cell is heated at 80°C for one hour, before being assembled in the argon glove box. The electrolyte is composed of a 1M solution $LiPF_6$ in 1:1 mixture (by volume) of ethylene carbonate to dimethly carbonate.

Electrodes were prepared from a mixture of 80% active material, 15% acetylene 50 carbon, and 5% poly-vinylidenefluoride (PVDF). The active material was first ground through a 625 mesh. A slurry of the electrode composite was prepared by adding 1-2ml of cyclopentanone. The mixture was either mixed in a vial containing glass beads or ground together in a mortar and pestle, for the thicker slurries. The latter method was preferred when electrodes of greater than 20mg active material were required. The use of a thicker slurry prevented the separation of the composite during drying, but each slurry had to be made and used immediately. For smaller electrodes, used in the NMR experiments, as well as the electrochemical testing, 5mg of active material settled well onto the nickel disk from a more dilute slurry. These slurries were made in 100mg batches, and could be stored in vials for future use.

SnO, SnO_2, and Sn metal were obtained from Aldrich (particle size~325mesh). Lithium metal foil, of 1mm thickness was obtained from Aldrich, and was cleaned by scraping the surfaces. For ^6Li NMR data acquisition it was found that natural abundance spectra were

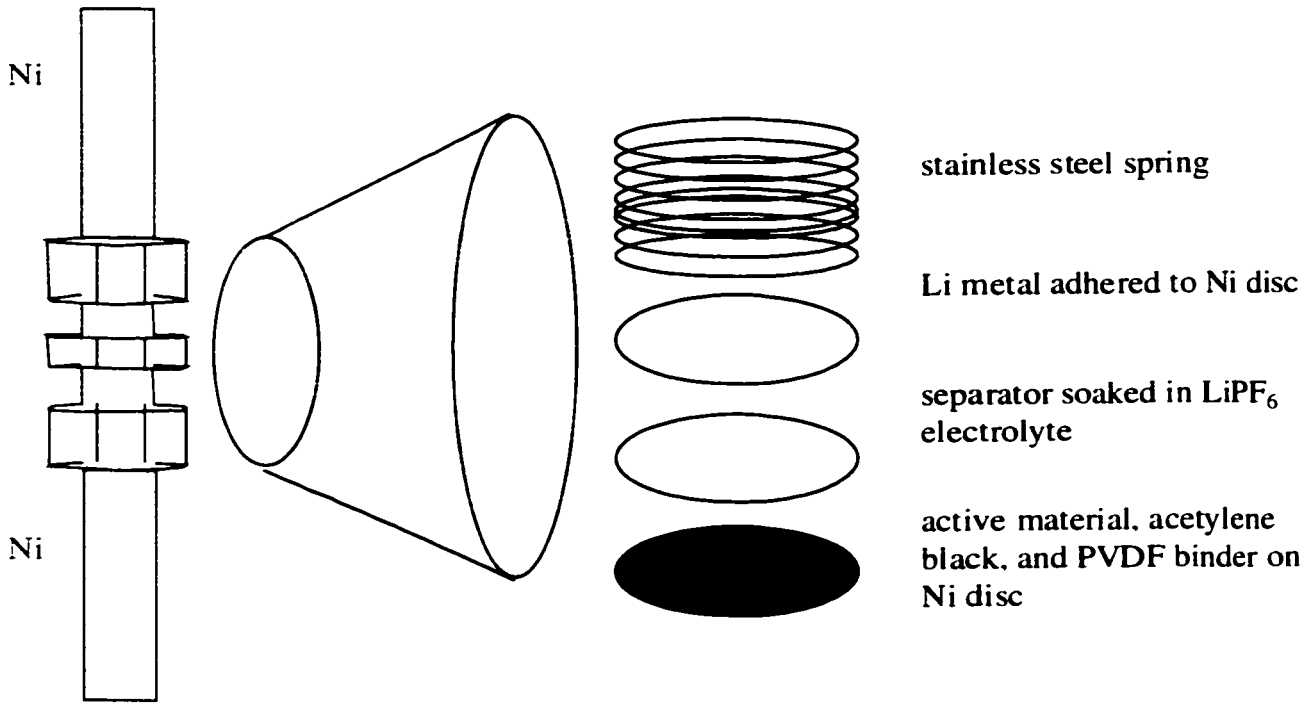

Figure 3.6 Swagelock cell used in electrochemical studies

unsatisfactory. Therefore several sets of electrodes were prepared from 99% enriched ^{6}Li metal "chunk", obtained from Aldrich.

The experiments were performed on a MacPile™ system.[23] Potentiostatic experiments were carried out using voltage steps of 10mV/hr for electrodes of 20-30mg, and at 50mV/hr for electrodes of 5-10mg. The voltage window used for cycling was 0.0-1.5V, which was chosen to limit the aggregation of tin particles reported for voltage cutoffs above 1.5V. Current pulse relaxation studies were carried out using relaxation criteria of 4mV/hr. Lithium was inserted at a rate of C/10, with insertion of 0.25Li between each equilibration period.

3.3 Results

3.3.1 The first cycle: Potentiostatic experiments

Figure 3.7 shows the voltage profiles for Sn metal, SnO, and SnO_2, following discharge to 0.0V and charge to 1.5V. In each case the materials reach approximately theoretical capacity, with Sn metal inserting 4.4Li per mole, SnO inserting 5.9Li/mol, and SnO_2 inserting 7.4 Li/mol. On charge both SnO and SnO_2 exhibit the expected irreversible capacity, corresponding to the stoichiometric reaction of oxygen with lithium in each case. **Figure 3.8** shows the electrochemical curves for TCO, Sn-rich TCO and Bi-doped TCO on the first cycle. TCO achieves an initial lithium uptake of 8.0Li, with a reversible capacity of 4.9 Li, while Sn-rich-TCO reaches an initial lithium uptake of 10.7Li, with a reversible capacity of 6Li per mole of glass or 4 Li per Sn atom. Bi-doped-TCO reaches a lithium capacity of 8.6Li on first discharge, with a reversible capacity of 5Li. Comparing these values on first discharge the three materials are very similar, reaching 1100, 1050, and 1070mAh/g respectively.

The sharpness of the features in the discharge/charge curve of SnO as compared to the glassy TCO materials is as expected for crystalline versus amorphous materials. The shapes of the voltage profiles give important information about the mechanism of the reaction of lithium with the electrode material. By comparing the voltage profiles of the parent materials (Sn, SnO and SnO_2) to those of the TCO glasses, it is evident that the processes occurring in the parent materials are well defined, having voltage plateaux corresponding to lithium insertion into specific sites. In contrast, the glasses exhibit smooth voltage profiles.

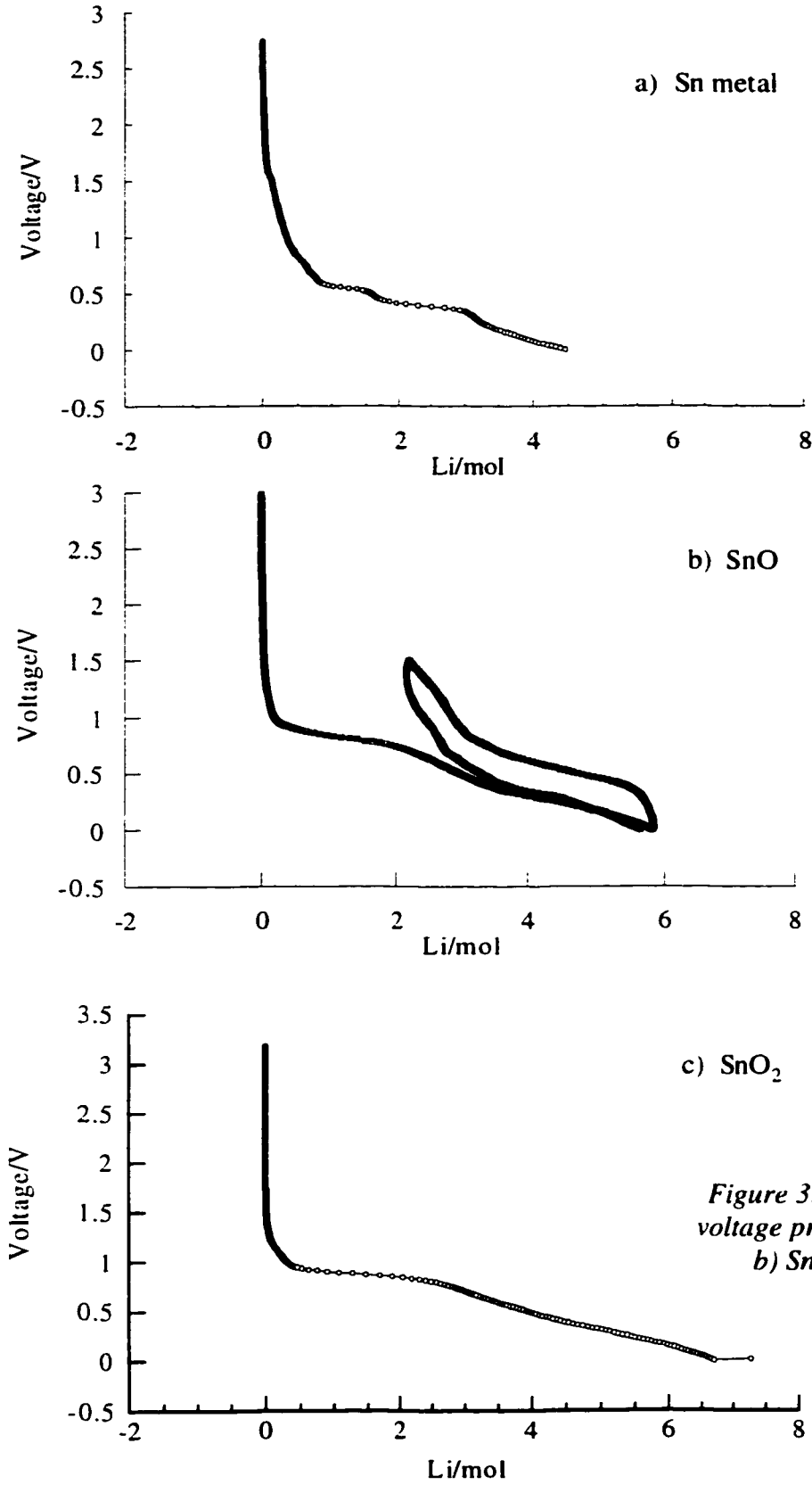

Figure 3.7 Electrochemical voltage profiles of a)Sn metal, b) SnO, and c) SnO_2

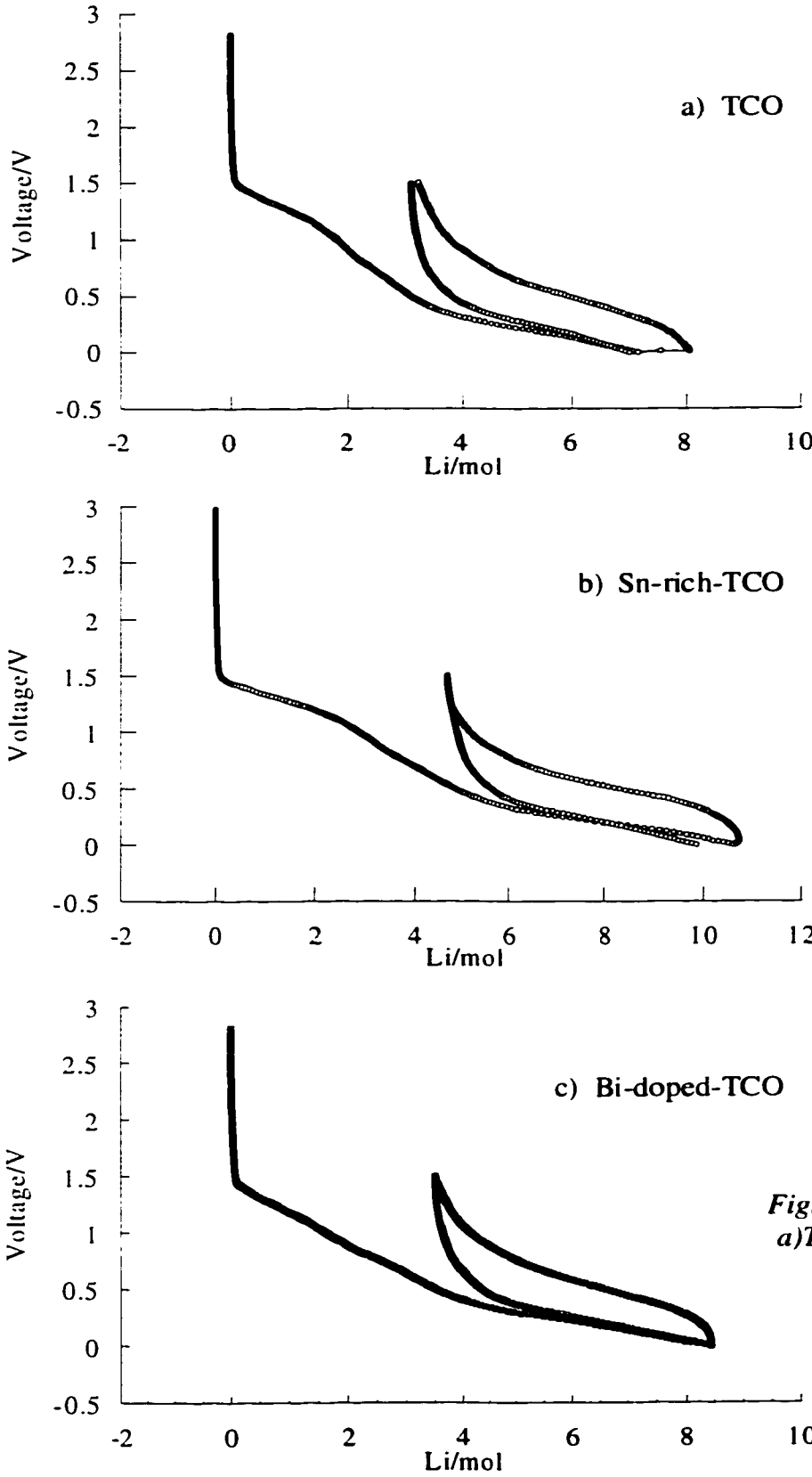

Figure 3.8 Voltage profiles of a)TCO, b) Sn-rich-TCO, and c) Bi-doped TCO

In the cyclic-voltammograms (CV) for each of the electrochemical curves, the small changes in slope in the voltage profile become clearly visible as peaks. This illustrates the different types of sites being accessed in the crystalline parent compounds, as opposed to the glassy counterparts. The cyclic voltammograms for Sn, SnO, and SnO_2 are shown in **Figure 3.9**, and the CVs for TCO, Sn-rich TCO, and Bi-doped-TCO are shown in **Figure 3.10**. Peaks in the current versus voltage curves correspond to specific lithium potential sites within the electrode: following the initial cycle, which includes the irreversible formation of the lithium oxide matrix, the TCO glasses exhibit only broad insertion sites, while the CVs of the parent oxides shows many sharp features.

The CV of Sn metal, shown only for the cathodic sweep, has two very sharp intense features, which occur at 0.52 and 0.39V respectively. There are also several other broad, relatively minor peaks occurring at 1.6, 0.7, and 0.2V. These features correspond to the formation of lithium-tin phases, as described by Courtney *et al.* Two well-defined peaks on discharge, at 0.8V and 0.3V characterize the SnO CV.[24] These peaks are not as sharp as those observed for Sn metal. There are also several secondary processes at 0.65, 0.45 and 0.2V on the cathodic sweep. On the anodic sweep, the processes are still well defined, now occurring at 0.45 and 0.65V, with some smaller features evident between 0.6 and 0.8V. Two dominant processes also characterize the CV for SnO_2. The processes occurring at low voltage, centered at 0.35V, are broadened substantially compared to the feature corresponding to the formation of lithium oxide. The relative intensity of the two peaks is shifted in favour of the initial process compared to that observed in SnO. This is as anticipated, since the inserted lithium must first consume two oxygen atoms per mole in SnO_2 as compared with only one in SnO. The formation of Li_2O in both materials occurs at approximately 0.8V, and is not reversible in the anodic sweep. As well, this peak is not observed in the CV of Sn metal itself, since in this case, only residual surface oxide is present.

The CVs of the glasses are generally much broader and smoother than those of the parent oxides. For TCO on discharge peaks are observed at 1.3V and 0.2V, with a small feature evident around 0.5V. On charge a broad feature at 0.5V along with a smaller feature at 0.85V is observed. Sn-rich TCO shows somewhat sharper features than TCO itself, due to the enhanced Sn concentration in the former glass. The sharpness of the CV features thus result from the increased ratio of Sn:spectator ions in Sn-rich-TCO compared to TCO, as opposed to

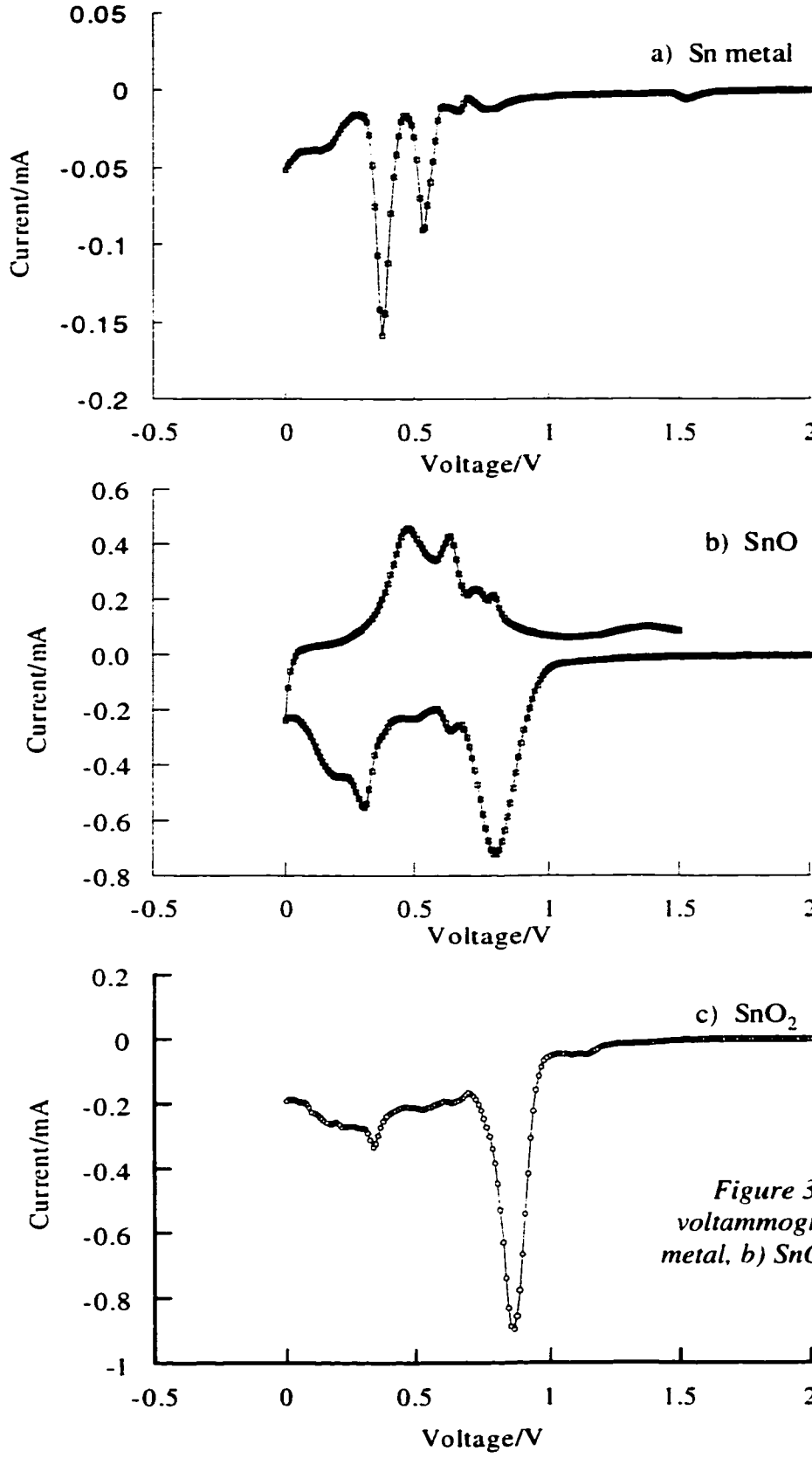

Figure 3.9 Cyclic voltammograms of a) Sn metal, b) SnO, and c) SnO_2

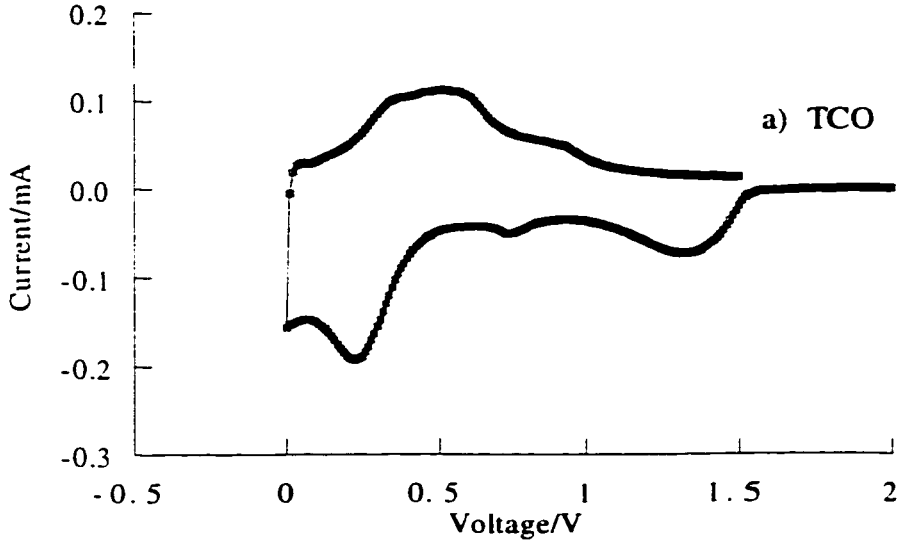

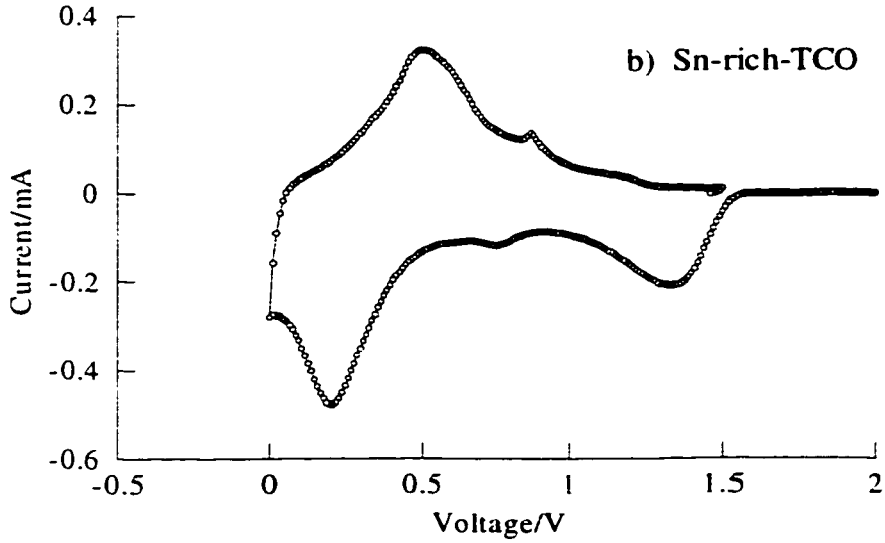

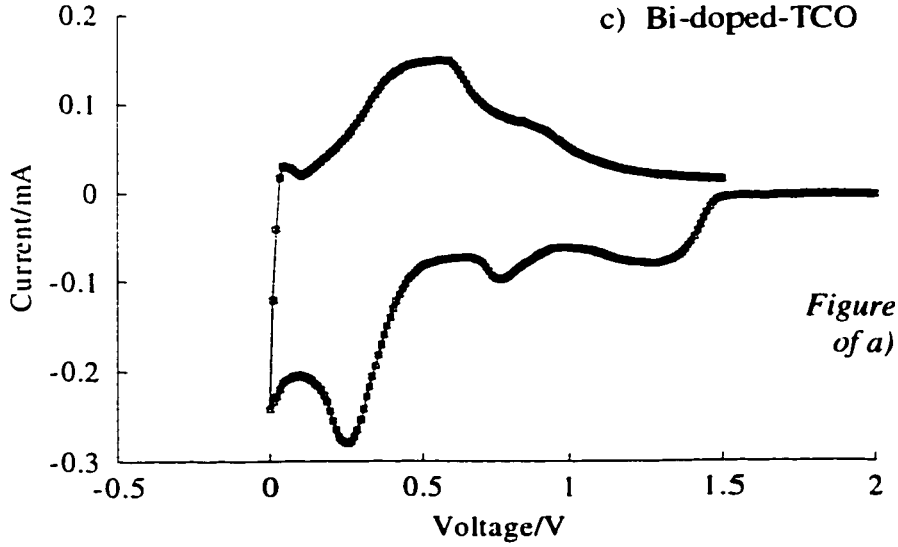

Figure 3.10 Cyclic voltammograms of a) TCO, b) Sn-rich-TCO, and c) Bi-rich-TCO

resulting solely from the crystallinity or disorder of the electrode material. The Sn-rich TCO material contains a 50% higher molar concentration of Sn atoms than in TCO itself. On a statistical basis, this would result in a more ordered lithium insertion process compared to TCO. The CV of Bi-doped TCO is very similar to that of TCO itself, with insertion processes at 1.3, 0.7, and 0.25V.

3.3.2 CPR Results

The results of the CPR tests for Sn, SnO and SnO_2 are shown in **Figure 3.11.** The CPR results for TCO, Sn-rich-TCO and Bi-doped-TCO are shown in **Figure 3.12**. The curves in all cases except that of Sn metal show two distinct regions, characterized by the amplitude of the potential variation during the relaxation period. The region from 0 to approximately 400mAh/g shows the slowest kinetic response. This process ends at the completion of Li_2O matrix formation which is correlated with the insertion of the first 2 lithium into SnO, or the first ~3 lithium into TCO and Sn-rich-TCO. The second process continues to the end of discharge. The latter process is facile, as indicated by the small amplitude of the potential variation observed here for all materials.

Sn metal displays relatively rapid kinetics throughout the CPR experiment. The initial steps are somewhat more kinetically inhibited than those beyond 0.6Li, corresponding to the break down of the oxide film on the Sn particles.

The differences between the TCO glasses and SnO itself are most significant during the early stages of discharge. In the TCO materials, this portion of the GITT curve is characterized by a large potential variation during OCV corresponding to long relaxation periods. This is indicative of a kinetically inhibited electrochemical process; one which is far from equilibrium. In the tin-composite oxide glasses, the two general processes are evident, but the first process appears to be separable as two secondary processes, distinguished by a slight change in slope as well as deeper relaxation periods at lithium insertion levels of greater than 1Li. In TCO the first process exhibits potential variation of 0.5V up to 1Li, and subsequently ~0.9V up to 2.5Li. In Sn-rich-TCO, the first portion of the curve is characterized by potential variations of 0.4V, which deepen slightly beyond 1Li to ~0.5V. In SnO, the GITT curve is flat during the first process and the amplitude of the potential variance is typically 0.3V. From these results we

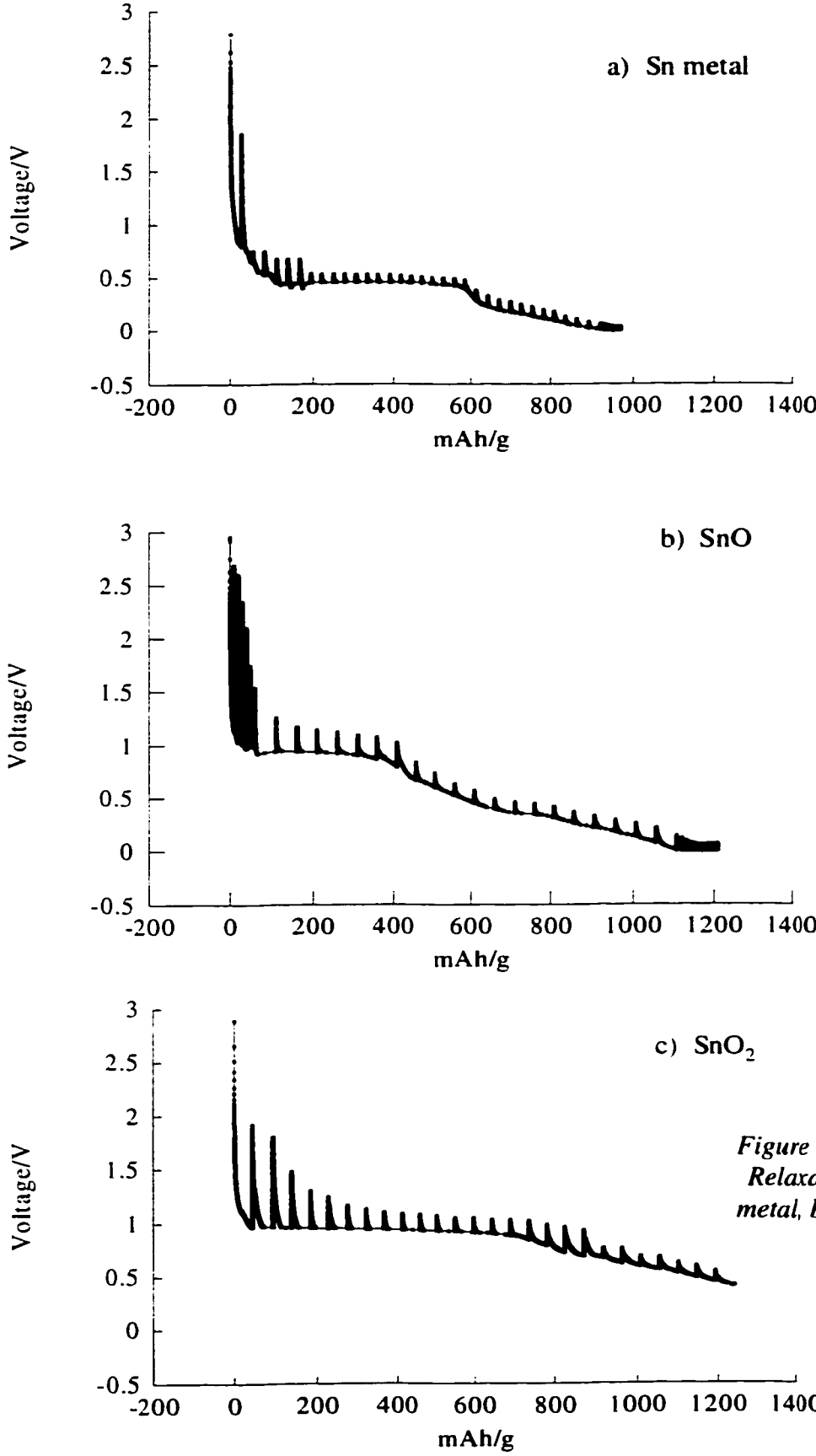

Figure 3.11 Current Pulse Relaxation data for a) Sn metal, b) SnO, and c) SnO_2

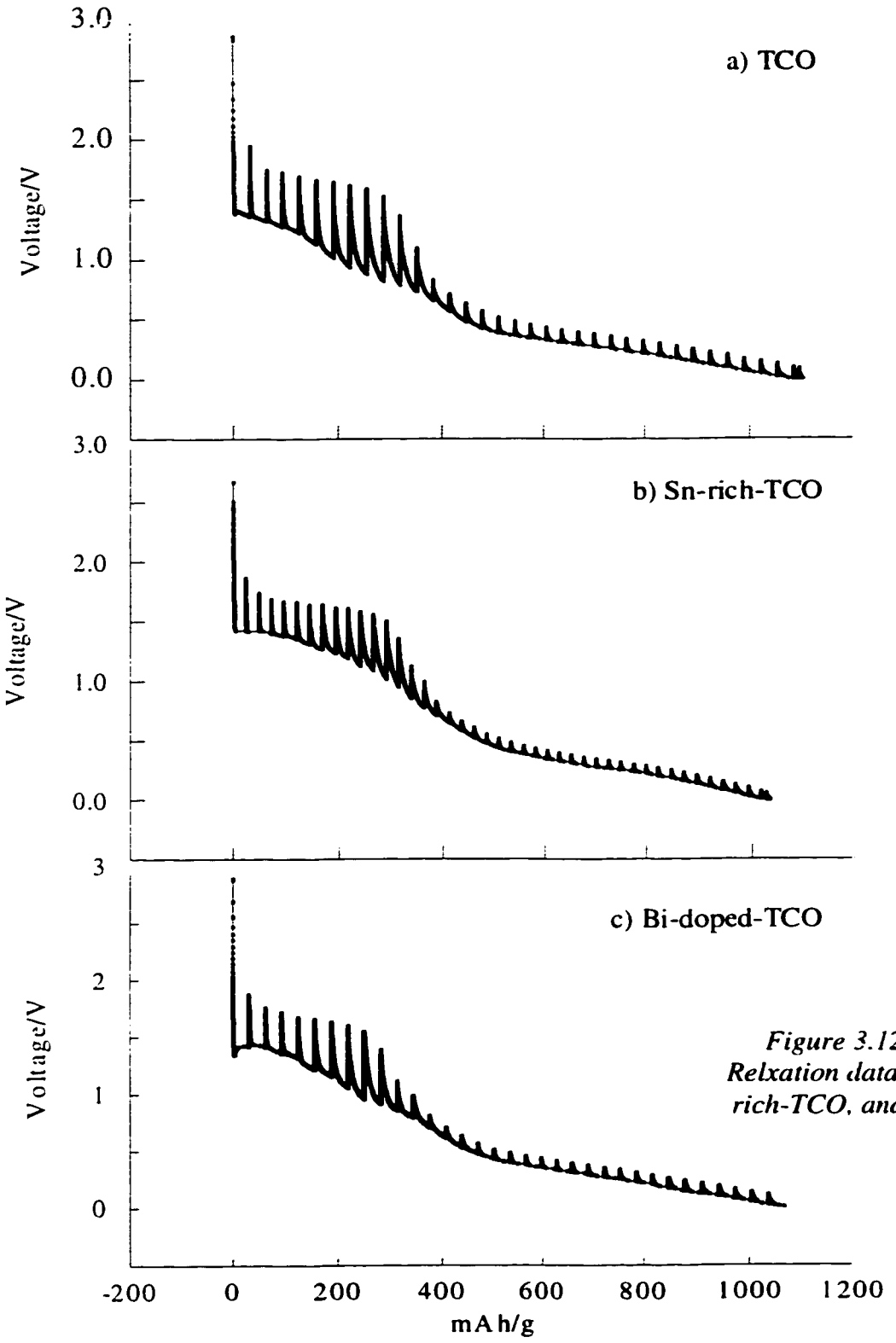

Figure 3.12 Current Pulse Relxation data for a) TCO, b) Sn-rich-TCO, and c) Bi-doped-TCO

observe that the rearrangement of the glass is concurrent with the reduction of $Sn^{2+/4+}$ to Sn^0, and demands more energy than the simple reaction of SnO with Li to form Sn metal and Li_2O. The CPR data for Bi-doped TCO shows similar behaviour to that of TCO. Two processes are distinguished during the insertion of the first 2.5Li, the first ending after the insertion of 1Li. Again, the magnitude of the potential variation is greater during this initial insertion process compared to the latter portion of the curve.

There is a change in slope at about 2-3 Li, beyond which the lithium insertion process becomes much easier. This is demonstrated by the much faster kinetic response in this latter portion of the electrochemical process. In this region, both the glasses and the parent oxides respond similarly. In the TCO glasses beyond 3Li, the amplitude of the potential variations become smaller, reaching an average value of 0.1V. As the second process begins in SnO the potential variations are reduced (~0.15V), and are maintained at this value throughout the remainder of the discharge process. In all cases the kinetics become much faster during deep discharge relative to the initial processes. This is attributed to an increase in the conductivity of the materials as the Sn centers are reduced to metallic tin. Support for this hypothesis is found in the CPR curve of Sn metal, which being metallic has a high conductivity and exhibits efficient kinetic response for electron transport throughout the electrochemical process.

3.3.3 Cycling experiments

Figure 3.13 shows the voltage profiles for Sn metal following 2 cycles and SnO following 5 cycles while **Figure 3.14** shows the corresponding voltage profiles for TCO, Sn-rich-TCO following ten cycles and Bi-doped TCO following eight cycles. Because we were examining cells with large masses of active material, in order to perform *ex-situ* experiments, the maximum number of cycles for the cycling experiments was limited to 10. Nevertheless, none of these materials would have much chance of reaching commercialization, considering the capacity fade after only 10 cycles. The capacity of the TCO glass was reported to decrease by 37% following the first cycle, and subsequently maintains nearly 100% of its reversible capacity.[16] The difference between those results and ours is likely due to the reliability of the cell design itself. Swagelock cells are subject to a high degree of variability, particularly on cycling, compared to the coin cell design preferred in industrial testing.

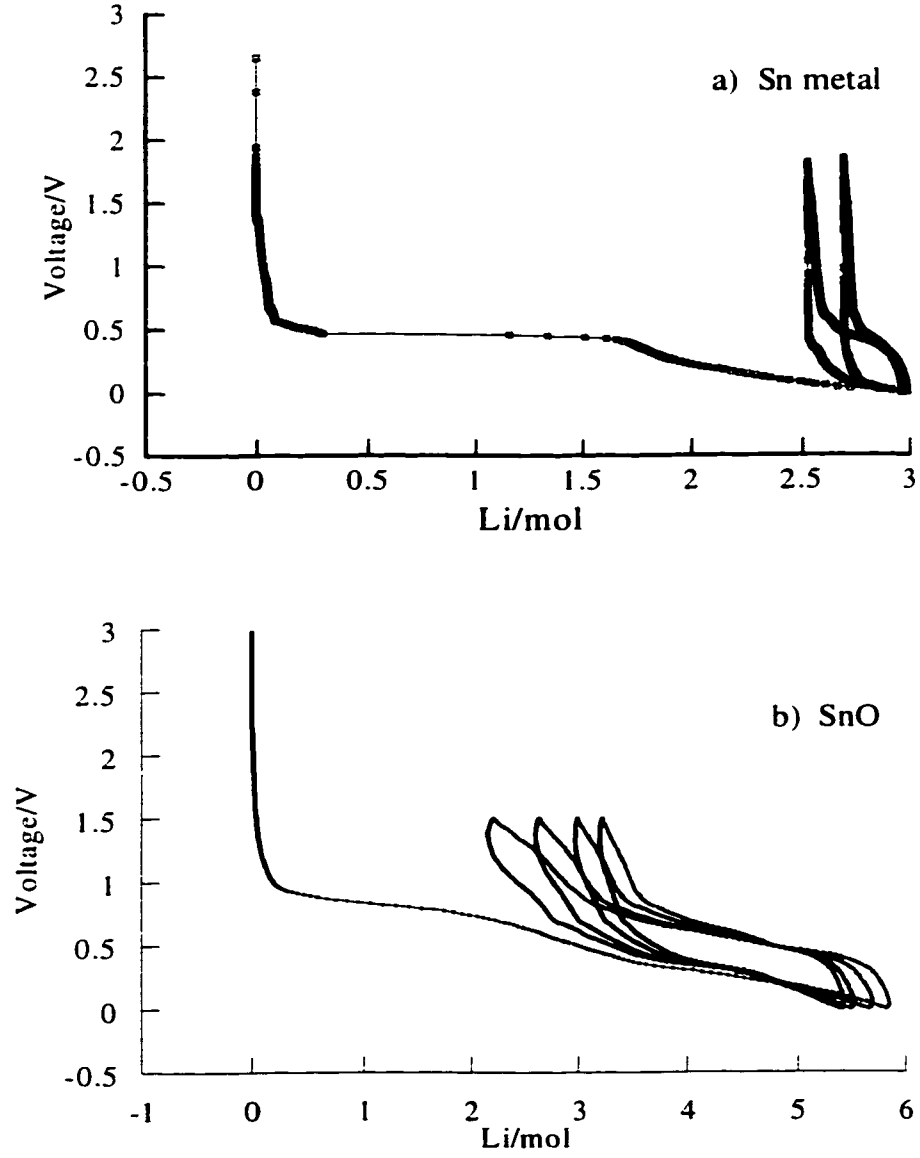

Figure 3.13 Cycling data for a) Sn metal and b) SnO

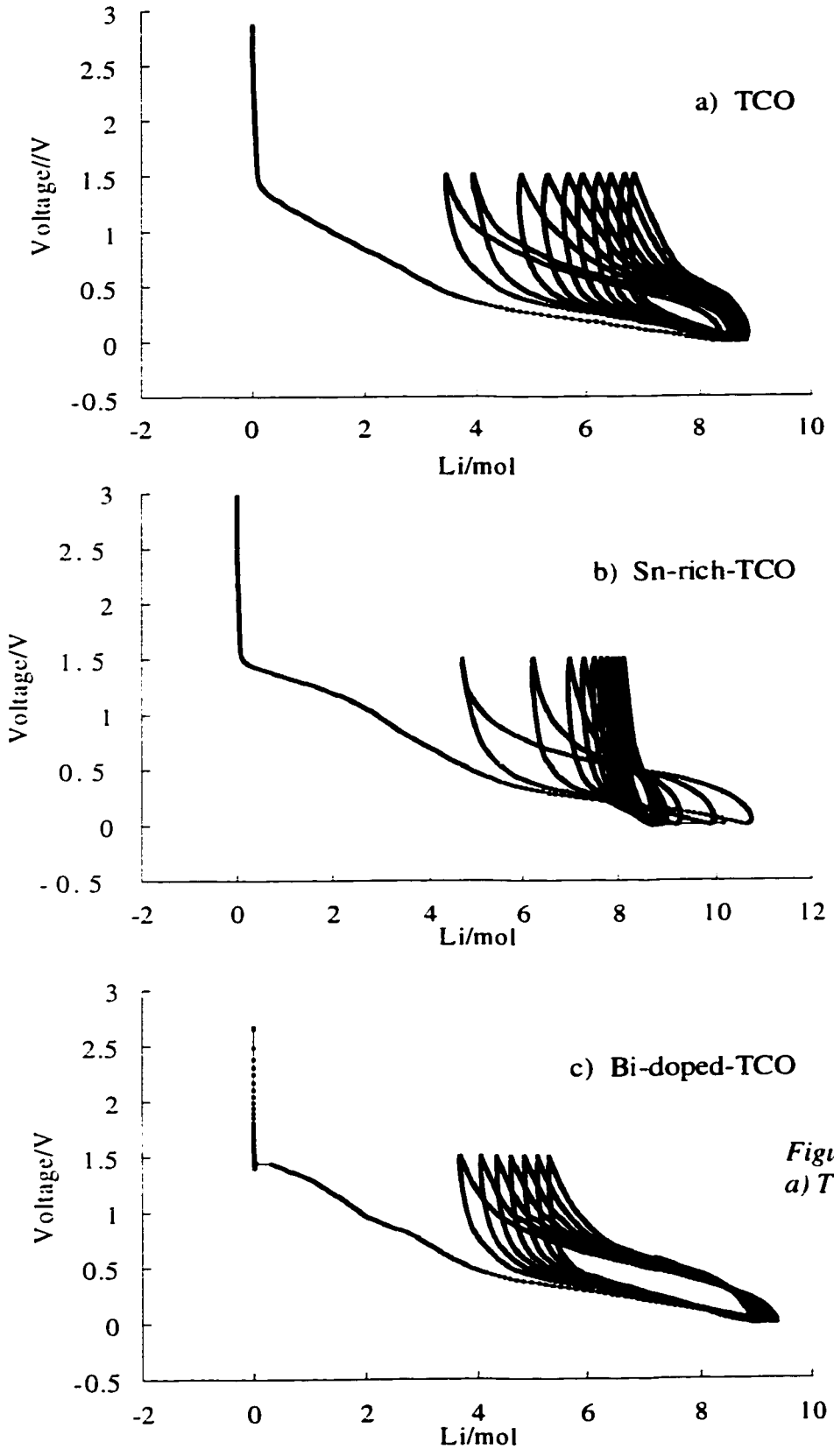

Figure 3.14 Cycling data for a) TCO, b) Sn-rich-TCO, and c) Bi-doped-TCO

By calculating the capacity obtained on initial discharge, and assuming this to represent 100%, the capacity fade upon cycling can then be determined from the relative percentage of lithium uptake upon subsequent cycles. Sn metal demonstrates extreme irreversibility, and upon the second cycle retains only 15% of the original capacity. SnO is somewhat better, maintaining 28% of its original capacity following 5 cycles.

By comparing the three TCO-glass materials, it is clear that the enrichment of the glass with 50% higher tin content has a drastic negative effect on the cyclability of the glass; after 10 cycles the capacity has dropped to just 6% of its original capacity. In contrast, TCO retains 23% of its original capacity. Bi-doped-TCO performs better than TCO itself not only in initial discharge capacity, but also upon extended cycling; retaining 40% of its original capacity after 8 cycles. This data is plotted in **Figure 3.15**.

3.3.4 Electrochemical Performance of Crystallized TCO "Glasses"

To illustrate the significance of the formation of a completely homogeneous, amorphous glass on the electrochemical performance of the material, two examples are provided. Two samples (labeled 71C and 72C) were examined that had the correct stoichiometry of reactants, but where the products contained crystalline aluminum phosphates, as described in Chapter 2. **Figure 3.16** shows the electrochemical profiles obtained from these materials. The first sample, Glass 71C, had a first discharge capacity of only 3 lithium, with a reversible capacity of just greater than 1.5Li. Glass 72C had a slightly improved initial capacity of 4.8Li, but this is still well below the expected capacity for the TCO glass. Moreover, sharp steps, indicative of the crystalline nature of the materials characterize both of these voltage profiles. It is clear from these results that the presence of tin oxide, in a macroscopic mixture of crystalline aluminum phosphates and borates does not give the same electrochemical performance as the same tin oxide, confined within a glassy matrix.

3.4 Discussion of Electrochemical Data

Considering the voltage profiles of the crystalline electrode materials, compared to those of the various glasses studied, several trends are significant. First of all, as has been noted, the voltage profiles of the crystalline materials are marked by discrete steps, most obviously in the case of tin metal itself. In contrast, the voltage profiles of the glasses are

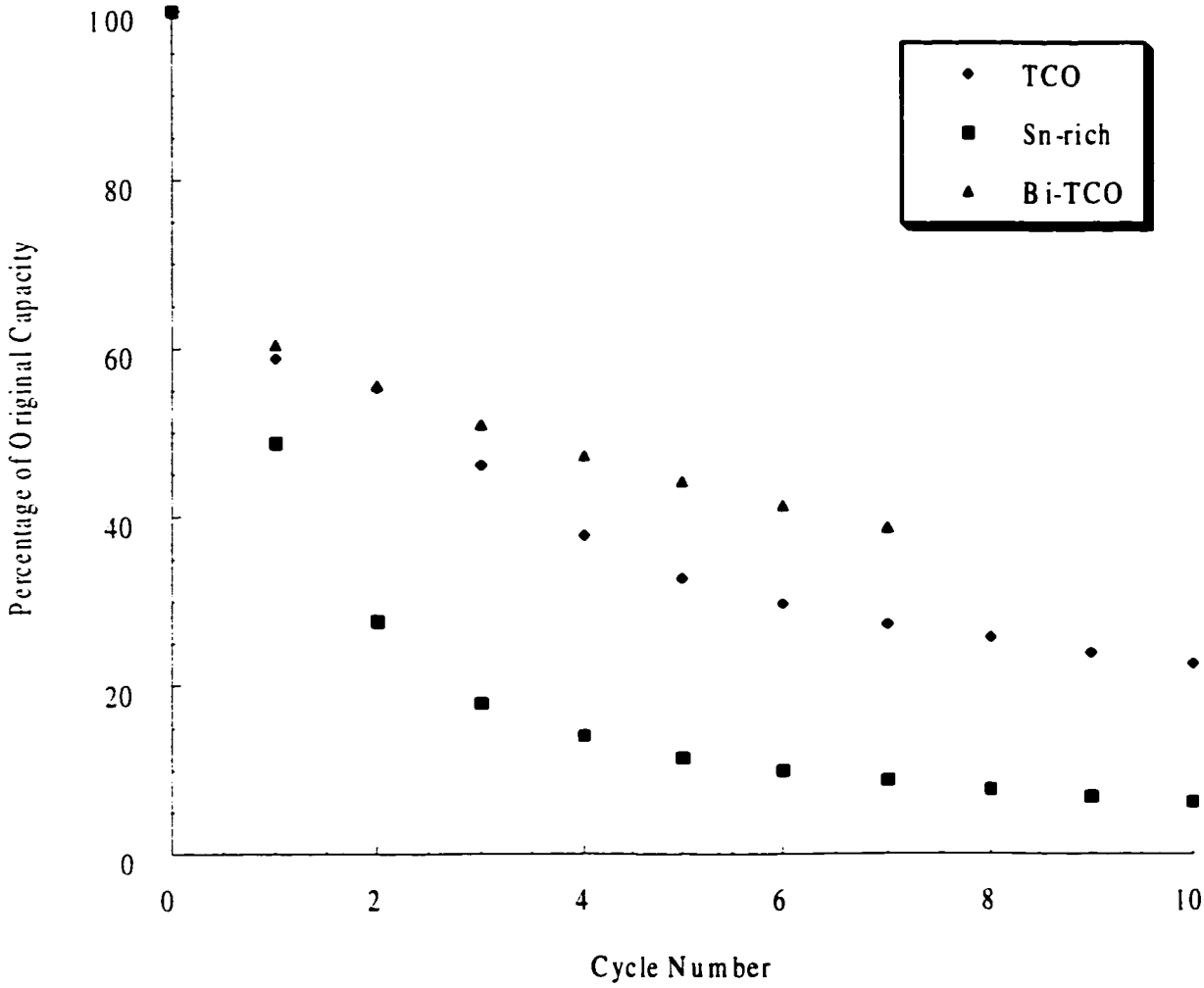

Figure 3.15 Capacity fade for TCO glasses plotted as a percentage of the initial capacity versus cycle number. for TCO, Sn-rich-TCO, and Bi-doped-TCO.

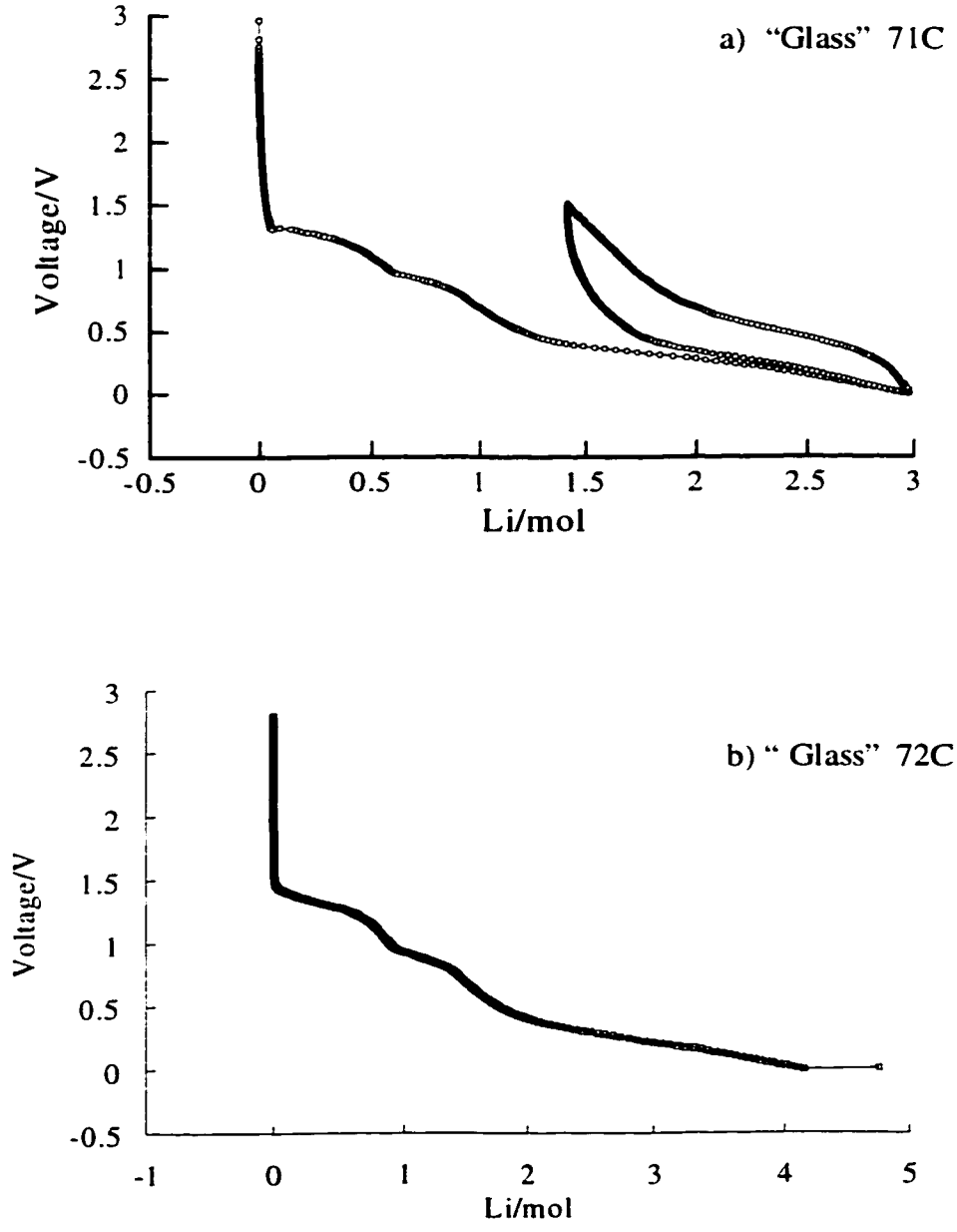

Figure 3.16 Voltage profiles for crystallized TCO glasses, a) Glass 71C and b) Glass 72C

much smoother, indicating a more gradual, less clearly defined transformation of the electrode host. The glasses also experience a greater degree of hysterisis in the cycling profile than does SnO. This is due to the greater concentration of non-electroactive species in the glasses, which respond more slowly to the reversal of current than does SnO. Most significantly, the TCO glass has a greater fraction of cyclable lithium than does the corresponding SnO. While the premise of the reaction mechanism is that the tin particles created in the glass matrix react with lithium in the same manner as those in SnO, and should thus insert and de-insert a 4.4Li mol ratio, in accordance with the formation of the most lithium rich Li-Sn phase, in fact, it is observed that 4.9Li are reversibly cycled in TCO. This surprising finding leads to the intriguing hypothesis that the non-electroactive species in TCO may in fact contribute to the electrochemical process. This hypothesis will be further developed within the thesis, particularly in regards to the possible participation of oxygen. As yet the evidence is minimal, but it will be shown that a case can be presented which supports this hypothesis.

Also fascinating is the enhanced electrochemical performance which results from doping TCO with a small fraction of bismuth. The synthesis was attempted due to the known oxygen transport properties of bismuth oxide. The reduction potential of Bi_2O_3 is quite high, thus it is likely that the bismuth oxide was in fact reduced to bismuth particles during the arc melting of the glass. Nevertheless, the addition of bismuth resulted in a small enhancement of the cyclable portion of lithium, but more significantly, improved cycling performance compared to TCO. This is tentatively attributed to enhanced electronic conduction mechanisms within the glass, due to the presence of metallic Bi particles, but time prevented further investigations of this potentially fruitful system.

Also striking are the differences between the CPR responses of the crystalline electrode materials, compared to the glasses. In the case of SnO, as for SnO_2, a single process occurs during the insertion of the first 2-3 equivalents of Li, however the TCO glasses can be considered to undergo two distinct processes. In the latter cases, the two processes are distinguished by a change in slope and shape of the CPR features following insertion of approximately the first lithium. To explain this observation we can consider the types of bonds that are broken and reformed in each case. For SnO and SnO_2, Li can only insert into the Sn-O-Sn bond, whereas the TCO network comprises both Sn-O-X as well as X-O-X interactions, where X = Al, B or P. It is questionable as to whether the lithium should be expected to insert

into an X-O type bond, but both our CPR data and several of the NMR spectra of the 'spectator ions' (presented in Chapter 4) point to this conclusion. The CPR results for TCO indicate that the insertion process up to the first 2-3 Li is much more kinetically inhibited than the equivalent process in SnO. If the lithium were selectively inserted into Sn-O bonds only in both cases, the kinetics of the reaction would be expected to be equivalent. On this basis, it seems likely that the lithium is not selective, but reacts as well with the other bonds present. The fact that these oxides themselves are electrochemically inert suggests that the reason for the slow kinetics is the initial step as the glass is rearranged.

The insights offered by the electrochemical performance of the TCO glasses are considered the first theme of the *fugue*, being addressed by the voice of the electrochemical methods. As voices are added to the work, the key questions of the theme will be resolved. Namely, what is the nature of the interaction of lithium with tin, what is the effect of particle size on the electrochemical performance and what is the role that oxygen and the other 'spectator ions' play in the electrochemical process.

3.5 References

[1] A.N. Dey, *Journal of the Electrochemical Society*, **118**, 1547 (1971).

[2] C.J. Wen, R.A. Huggins, *Journal of the Electrochemical Society*, **128**, 1181 (1981).

[3] I.A. Courtney, J.S. Tse, O. Mao, J. Hafner, and J.R. Dahn *Physical Review B*, **58**, 15583 (1998).

[4] J.Wang, I.D. Raistrick and R.A. Huggins *Journal of the Electrochemical Society* **133** 457 (1986).

[5] J. Yang, M. Winter, J.O. Besenhard *Solid State Ionics* **90**, 281 (1996).

[6] D. Fauteux, R. Koksbang *Journal of Applied Electrochemistry*, **23,** 1 (1993).

[7] R.A. Huggins, B.A. Boukamp, US Patent 4436796, (1984).

[8] B.A. Boukamp, G.C. Lesh, R.A. Huggins *Journal of the Electrochemical Society*, **128**, 725 (1981).

[9] R.A. Huggins in Handbook for Battery Materials, ed. J.O. Besenhard, John Wiley and Sons. (1999). pg. 367.

[10] J.Yang, M.Wachtler, M.Winter, J.O. Besenhard *Electrochemical and Solid-State Letters*, **2,** 161 (1999).

[11] O. Mao, R.L. Turner, I.A. Courtney, B.D. Fredericksen, M.I. Buckett, L.J. Krause, J.R. Dahn, *Electrochemical and Solid-State Letters*, **2**, 3 (1999).

[12] O. Mao, R.A. Dunlap, I.A. Courtney, J.R. Dahn, *Journal of the Electrochemical Society*, **145**, 4195 (1998).

[13] O. Mao, R.A. Dunlap, J.R. Dahn, *Journal of the Electrochemical Society*, **146**, 405, 414, 423 (1999).

[14] R.A. Dunlap, O. Mao, J.R. Dahn, *Physical Review B*, **59**, 3494 (1999).

[15] I.A. Courtney, R.A. Dunlap, and J.R. Dahn, *Electrochimica Acta* (submitted – pre-print provided by authors).

[16] Y. Idota, T. Kubota, A. Matsufuji, Y.Maekawa, T.Miyasaka, *Science* **276** 1395 (1997).

[17] http://www.fujifilm.co.jp/eng/news_e/nr079.html

[18] I.A. Courtney and J.R. Dahn, *Journal of the Electrochemical Society*, **144** 2045 (1997).

[19] J.R. Dahn, I.A. Courtney, O. Mao, *Solid State Ionics*, **111**, 289 (1998).

[20] I.A. Courtney, W.R. McKinnon, J.R. Dahn, *Journal of the Electrochemical Society*, **146**, 59 (1999).

[21] O. Mao, R.L. Turner, I.A. Courtney, B.D. Fredericksen, M.I. Buckett, L.J Krausse, and J.R. Dahn, *Electrochemical and Solid State Letters*, **2**, 3 (1999).

[22] P.G. Bruce Solid State Electrochemistry University Press, Cambridge (1995). p. 219.

[23] MacPile A-3.22 Biologic, Claix, France (1994).

[24] I.A. Courtney and J.R. Dahn *Journal of the Electrochemical Society*, **144**, 2943 (1997).

Chapter 4 NMR Studies

4.1 Introduction

Solid-state NMR is an excellent probe of the environment around a nucleus, whether in a crystalline or amorphous material. In this thesis multinuclear NMR was the primary tool used to study the various NMR-active nuclei present in the TCO glasses. Li NMR is particularly amenable to addressing the issue of the nature and role of the Li_2O matrix formed during the discharge of the tin oxide cell. By examining the materials using $^{6,7}Li$ solid-state NMR, we can probe directly the interactions of lithium with the various components of the electrode. An inherent assumption in the discussions of the TCO glass to date has been the inconsequential role of the Al, B, and P ions in the glass structure. The premise has been that these 'spectator' ions simply prevented aggregation of the Sn atoms following discharge, and other than that were inert. Solid-state NMR permits the investigation of the role that the spectator ions play (if any) in the structural rearrangements occurring during the electrochemical reaction with lithium. ^{27}Al, ^{31}P, and ^{11}B NMR are used here to demonstrate the participation of these ions throughout the electrochemical processes to which the TCO glass is subjected.

Since a large portion of this thesis relies on the collection and interpretation NMR data, it is appropriate to give a detailed review relevant of NMR theory; this review is limited to those topics pertinent to the experimental results described below.

4.2 Fundamentals of Solid State NMR theory

4.2.1 The Microscopic Picture

Nuclear magnetic resonance (NMR) is similar to other forms of spectroscopy, except that NMR manipulates the nuclear transitions, as oppose to electronic, vibrational, or rotational transitions. This allows NMR unique selectivity for the isotope of interest. NMR spectroscopy takes advantages of the magnetic moment (μ) and angular momentum ("spin" I) of the nucleus,

$$\boldsymbol{\mu} = \gamma \hbar \mathbf{I} \tag{4.1}$$

where γ is the gyromagnetic ratio, a constant which is unique for each nucleus. All nuclei with an odd number of either protons or neutrons possess nuclear spin angular momentum, I, and hence a magnetic moment. According to laws of quantization, there are 2I +1 states for a nucleus of given spin, I. These levels are degenerate in the absence of a magnetic field. Immersing the sample of interest in an external magnetic field, $\mathbf{B_o}$, removes the degeneracy of the energy levels, according to the Zeeman interaction.[1]

$$\mathcal{H}_z = \boldsymbol{\mu} \cdot \mathbf{B_o} \tag{4.2}$$

This results in discrete energy levels, with energy E_m

$$E_m = -m\gamma\hbar B_{loc} \tag{4.3}$$

for a non-degenerate level, m. B_{loc} is the magnetic field experience by the nuclei, which includes the external magnetic field, and the interactions between the nuclei and its environment. Transitions between the energy levels gives rise to the observed NMR signal. For a magnetic field in the **Z** direction in the laboratory frame, the Zeeman interaction can be expressed as

$$\mathcal{H}_z = \gamma \mathbf{B_o} \mathbf{I_z} \tag{4.4}$$

and the frequency $\omega_o = \gamma \mathbf{B_o}$ is known as the Larmor frequency. This describes the precession of the nuclear magnetic moment in the uniform magnetic field. Within the magnetic field, a torque is exerted on the magnetic moments, aligning them with the external field. Since the torque affects only the components of angular momentum perpendicular to **B** and μ, the result is to cause precession of the magnetic moment (μ) about a cone with its axis $\mathbf{B_o}$. The rate of precession corresponds to the Larmor frequency for a given nucleus. The z axis of the precession may be either parallel or anti parallel to $\mathbf{B_o}$.

4.2.2 *The Macroscopic Picture*

In a macroscopic sample, containing a large number of spins, the net magnetization is determined by the population difference between the non-degenerate energy states according to the Boltzmann distribution.

$$\frac{N_m}{N_n} = \exp\left(-\frac{E_m - E_n}{kT}\right) \tag{4.5}$$

where N_m and N_n represent the number of spins in states n and m respectively. The relative populations will depend on the energy difference between the states, and on temperature. In

the external magnetic field, the assembly of spins will produce a macroscopic magnetization, $\mathbf{M_o}$, which is the resultant of magnetic moments, μ, for all the nuclei in the sample.

$$\sum \bar{\mu}_i = \boldsymbol{M_o} \tag{4.6}$$

Besides the external, static magnetic field, $\mathbf{B_o}$, a second magnetic field is important in the NMR experiment. This is the applied, radio frequency time-dependent field, $\mathbf{B_1}$. While the Zeeman effect, caused by the external field, $\mathbf{B_o}$, is the strongest interaction in NMR, this interaction does not itself contain information regarding structure or dynamics. Since magnetization cannot be observed in the direction parallel to the external magnetic field, a radio-frequency magnetic field, $\mathbf{B_1}$ is applied to rotate the magnetization away from $\mathbf{B_o}$. By perturbing the sample, using a radio frequency pulse matched to the resonant Larmor frequency of the nuclei of interest, the nuclear magnets are rotated away from their alignment with the external field. To rotate the nuclear magnetic moments, we apply rf at the resonance frequency, according to

$$|\omega_1| = \gamma|\mathbf{B_1}| \tag{4.7}$$

The time for which the rf pulse is applied determines the degree of the flip angle. The commonly used 90° pulse is determined by appropriate selection of τ_{90} as follows

$$\pi/2 = |\omega_1|\tau_{90} = \gamma\mathbf{B_1}\tau_{90} \tag{4.8}$$

Typical 90 degrees pulse lengths in solid-state NMR are between τ = 2-5μs.

The local field at a nucleus of interest arises from the combination of the external magnetic field and the unique interaction of a nucleus with its electronic environment, indicated here by B_{int}.

$$B_{loc} = B_o + B_{int} \tag{4.9}$$

In solid materials, three physical effects can give rise to B_{int}. These include dipole-dipole coupling between like or unlike nuclear magnets, chemical shielding or deshielding of the nuclear magnet by proximal electrons, and quadrupole coupling, in cases of I >1/2. Indirect (J) coupling is usually small and safely ignored for solid state experiments. Thus the NMR Hamiltonian must include all of these contributions.

$$\mathcal{H} = \mathcal{H}_Z + \mathcal{H}_{rf} + \mathcal{H}_D + \mathcal{H}_{CS} + \mathcal{H}_Q \tag{4.10}$$

Because it is these physical influences on the nuclear environment which are of interest to the material scientist, each will be examined in greater detail.

4.2.3 Comments Particular to NMR of Solids

Several challenges are encountered when acquiring NMR spectra of solids as opposed to solutions. These include lower sensitivity, as compared to 100% natural abundance ^{1}H, the most common form of solution NMR spectroscopy. In the solid state, protons are rarely the nucleus of choice, due to the extremely large dipolar coupling, which causes very broad lineshapes and yield minimal information. Therefore solid state NMR experiments are typically performed on other nuclei, which frequently have lower natural abundance and lower gyromagnetic ratios compared to ^{1}H resulting in decreased sensitivity. As well, in solution the relaxation times are usually short on account of the free tumbling of molecules in solution. For spin ½ nuclei relaxation times can be extremely long in the solid state since the atoms are locked in position whether in the crystal or amorphous solid. On the other hand, the presence of paramagnetic impurities in either a solid or solution can induce relaxation times which are so fast that the acquisition of useful data becomes impossible. Dipolar broadening is another interaction that can dominate the solid-state NMR spectrum. Finally, the influence of orientation dependence on the NMR lineshape is both an asset and a disadvantage. In the case of solution NMR spectroscopy the free rotation of the molecules averages the orientation dependence such that only the isotropic resonance is observed. In contrast, the solid-state NMR spectrum includes orientation dependent information which results in more complicated anisotropic lineshapes. These lineshapes can be used to advantage, however, in systems such as single crystals, or other preferentially oriented materials.

4.2.4 *Important Interactions*

Two observables are critical to the spectroscopist: 1) the resonance frequency, including the lineshape and 2) the relaxation time. Both of these observables have been used to advantage in this work. First we will consider the interactions that affect the NMR lineshape.

Direct dipolar coupling is a through space interaction, which therefore does not require that atoms be connected via bonding electrons. This interaction describes the effect of the local magnetic fields in the environment of the nuclear magnet. The strength of a specific dipolar coupling is influenced by the strength of and the distance between the two nuclear magnets. The relationship follows

$$\mathcal{H}_D = \gamma_1\gamma_2\hbar^2 r^{-3} (A+B+C+D+E+F) \quad (4.11)$$

It is thus inversely proportional to the cube of the distance between the nuclei of interest, and related to the product of the gyromagnetic ratios. The factors A-F, are referred to as the NMR alphabet, and are listed below. The geometric factors describe the symmetry of the Legendre polynomial, in the same way as atomic orbitals are differentiated based on the symmetry in space.

$$A = -I_{1z}I_{2z}(3\cos^2\theta-1) \quad (4.12)$$

$$B = (1/4)\{I_{1+}I_{2-} + I_{1-}I_{2+}\}(3\cos^2\theta-1) \quad \text{(known as the "flip-flop" term)} \quad (4.13)$$

$$C = (-3/2)\{ I_{1z}I_{2+} + I_{1+}I_{2z}\}\sin\theta\cos\theta\exp(-i\phi) \quad (4.14)$$

$$D = (-3/2)\{ I_{1z}I_{2-} + I_{1-}I_{2z}\}\sin\theta\cos\theta\exp(i\phi) \quad (4.15)$$

$$E = (-3/4)I_{1+}I_{2+}\sin^2\theta\exp(-2i\phi) \quad (4.16)$$

$$F = (-3/4)I_{1-}I_{2-}\sin^2\theta\exp(2i\phi) \quad (4.17)$$

The angles θ and ϕ are the spherical polar coordinates, which orient the vector between the nuclei, I_1 and I_2 within the magnetic field, B_o.

Chemical shielding gives rise to the observed chemical shift and is the result of the electronic environment of the nucleus in question. It can be broken down into three contributing interactions: the chemical shift, caused by surrounding closed electronic shells; the paramagnetic contact shift caused by interaction of the nuclear moment with nearby unpaired electron spins; and the Knight shift, caused by the effects of proximal conduction electrons. These three interactions, while physically distinct, are not separable in the NMR

resonance. Rather, the combined effect of these contributions will give rise to the observed signal.

The chemical shielding Hamiltonian is as follows.

$$\mathcal{H}_{CS} = \mathbf{I}(1-\sigma)\mathbf{B}_o \tag{4.18}$$

In which σ is a 3x3 second rank tensor with diagonal elements σ_{11}, σ_{22} and σ_{33} in the principal axis system. The isotropic chemical shift is equal to

$$\sigma_{iso} = (1/3)(\sigma_{11}+\sigma_{22}+\sigma_{33}) \tag{4.19}$$

Chemical shift is orientation dependent, and this orientation dependence has direct consequences for the NMR lineshape. The symmetry of the molecule gives rise to the observed resonance. Three examples are shown in **Figure 4.1.** The first represents a spherically symmetric chemical shift tensor, the second an axially symmetric tensor, and the third an asymmetric tensor.

Quadrupolar coupling interactions are only applicable to spins greater than ½. In such systems, the electric field gradient at the nucleus will have a strong influence on the NMR lineshape. The quadrupole interaction perturbs the energy of the spin states from the Zeeman energy levels; this can be either a first order perturbation, or second order perturbation, depending on the strength of the quadrupole moment. The first order perturbations from the Zeeman levels for a given orientation of a single, spin 3/2 nucleus are shown schematically in **Figure 4.2**.

For nuclei with spin > ½, the asymmetric distribution of charge around the nucleus gives rise to an electric field gradient (efg). The interaction between the quadrupolar nucleus and the efg is described by the Hamiltonian

$$\mathcal{H}_Q = \frac{e^2qQ}{4I(2I-1)}\left[\left(3I_z^2 - I^2\right) + \eta\left(I_x^2 - I_y^2\right)\right] \tag{4.20}$$

where Q is the quadrupole moment, e is the charge on an electron, eq is the field gradient, and η is the asymmetry parameter. The latter two parameters are taken from the electrostatic potential (V) where eq is equal to the second derivative (Laplacian) of the potential,

$$eq = \nabla^2 V \tag{4.21}$$

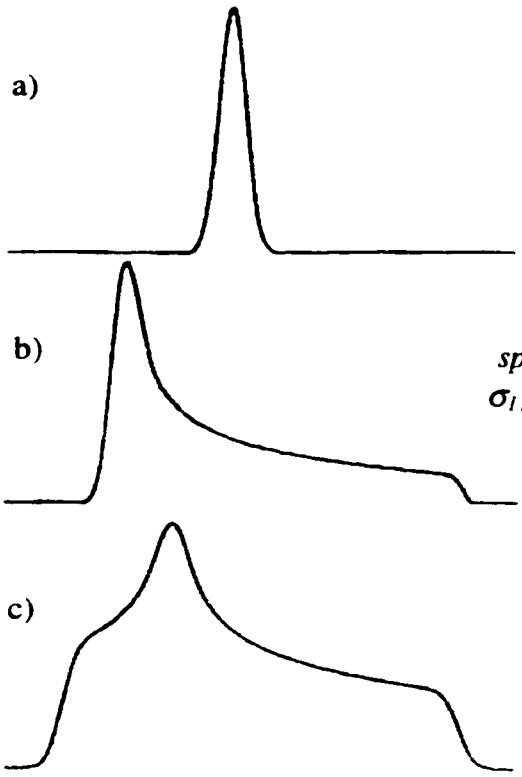

Figure 4.1 NMR spectra for a) spherical, $\sigma_{11} = \sigma_{22} = \sigma_{33}$, b) axial, $\sigma_{11} = \sigma_{22} \neq \sigma_{33}$ and c) less than axial symmetry $\sigma_{11} \neq \sigma_{22} \neq \sigma_{33}$

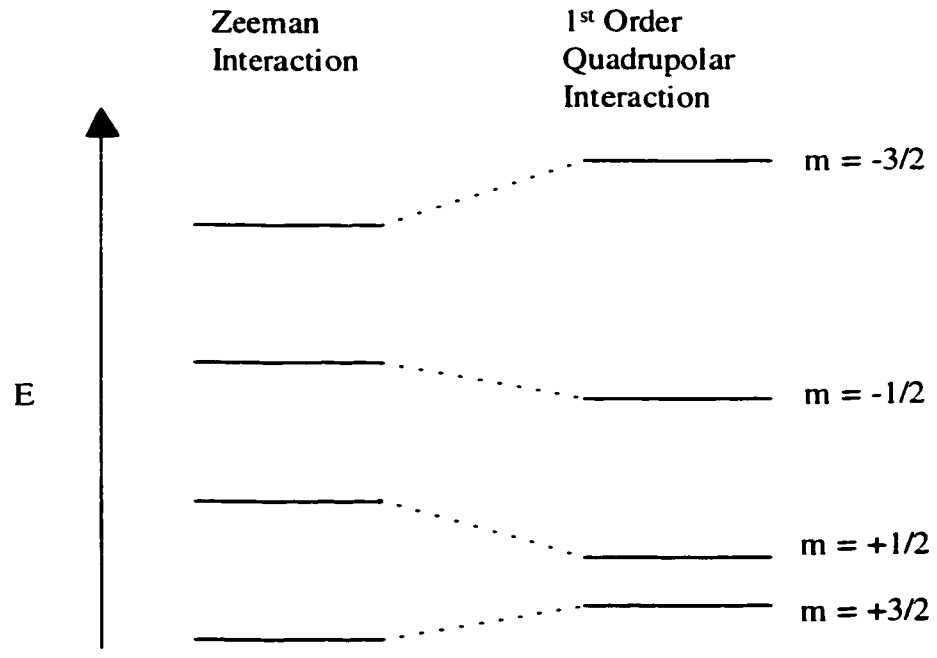

Figure 4.2 First order quadrupolar perturbation of the Zeeman interaction for a particular orientation of a spin 3/2 nucleus

and η is equal to $$\eta = \frac{eq_{xx} - eq_{yy}}{eq_{zz}} \quad (4.22)$$

The factor e^2qQ/h, is termed the quadrupolar coupling constant and given the symbol χ. The magnitude of this influence is determined by the quadrupole moment of the nucleus in question. **Table 4.1** includes a compilation of the various NMR parameters of the nuclei investigated in this study. Of particular consequence to this study are the relatively small quadrupole moments for ^{6}Li and ^{7}Li.

Nuclear Isotope	Spin	Natural Abundance	Magnetogyric Ratio $\gamma/10^7 radT^{-1}s^{-1}$	Quadrupole moment $10^{28}Q/m^2$	Larmor Frequency at 11.7T ω_o/MHz
^{6}Li	1	7.42	3.9371	$-8x10^{-4}$	73.578
^{7}Li	3/2	92.58	10.3975	$-4x10^{-2}$	194.318
^{11}B	3/2	80.42	8.5843	$4.1x10^{-2}$	160.42
^{17}O	5/2	0.037	-3.6279	$-2.6x10^{-2}$	67.785
^{27}Al	5/2	100	-1.639	0.15	130.288
^{31}P	½	100	10.841	N/A	202.405
^{119}Sn	½	8.58	-10.21	N/A	186.632

Table 4.1 Characteristics of relevant nuclear isotopes

4.2.5 *Magic Angle Spinning*

In solid state NMR the broad lineshapes caused by dipolar and quadrupolar coupling often obscure valuable information. Recognizing the dependence of the dipolar coupling on the second order Legendre polynomial, $P_2(\cos\theta) = 3\cos^2\theta - 1$, and that this term will go to zero for the appropriately chosen value of θ, the technique of magic angle spinning (MAS) was developed. Theta is the angle between a particular vector, for example the vector between two nuclei which are dipolar coupled to one another, and the external magnetic field, B_o. Macroscopic rotation of the sample at an angle χ as shown in **Figure 4.3a**, imposes a second term upon the interaction, and the overall interaction will be time averaged according to the following relationship,[1]

$$\langle 3\cos^2\theta - 1 \rangle = (1/2)(3\cos^2\chi - 1)*(3\cos^2\beta - 1) \quad (4.23)$$

where the angular brackets indicated the time average over a complete rotor period. The product of the molecular interaction, at an angle β with respect to the rotor axis, and the interaction of the imposed macroscopic rotation at the angle of χ, goes to zero when the angle χ is set to 54.74°. The frequency of the observed signal, ω, is related to the isotropic frequency, ω_o, the angle of the interactions with respect to the rotor axis, and the macroscopic rotation of the sample with respect to B_o according to:

$$\omega = \omega_{iso} + (3\cos^2\beta - 1 - \eta\sin^2\beta\cos 2\alpha)\delta\,[3\cos^2\chi - 1] \qquad (4.24)$$

where η is the asymmetry parameter, α is the azimuthal angle, and δ is the anisotropy. The effects of various rates of sample rotation are shown in **Figure 4.3b**. A spinning side band manifold is observed if the rate of rotation, in kHz, is less than the span of the lineshape in kHz.

4.2.6 Relaxation

Relaxation is the second important NMR observable, used to describe the processes by which the perturbed nuclei return to their equilibrium positions. Two classes of relaxation are distinguished. Spin-spin relaxation, characterized by a time constant, T_2, describes the entropic processes which allow a spin to achieve equilibrium *via* interaction with the other nuclear spins, whereas spin-lattice relaxation, characterized by T_1, includes all enthalpic means by which a spin can return to its thermal equilibrium state. As shown in 4.2.1, the total magnetization, M, is the summed projection of all nuclear moments, μ_i, along the magnetic field. When excited with a pulse the net magnetization is flipped from its equilibrium position. The components of magnetization parallel and perpendicular to the static magnetic field decay independently, and are described by the time constants, T_1 and T_2. Following a pulse, thermodynamic equilibrium is restored according to[1]

$$M_z(t) - M_o = [M_z(0) - M_o]\exp\left(-t/T_1\right) \qquad (4.25)$$

along the magnetic field, and

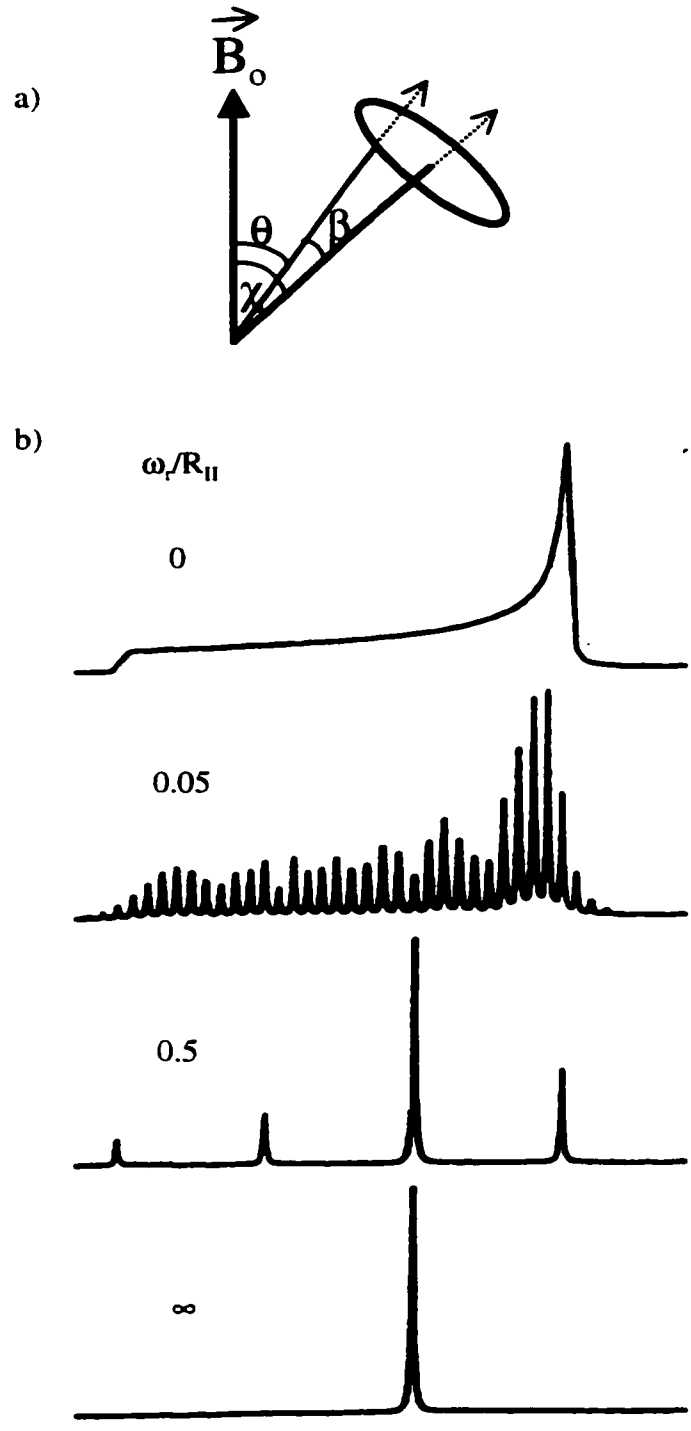

Figure 4.3 a) *Angular interactions in an MAS experiment and b) effect of spinning on NMR lineshape where* ω/R_{II} *is the ratio of the rate of MAS spinning to the span of the spectrum.*[2]

$$M_y(t) = M_y(0)\exp\left(-t/T_2\right) \tag{4.26}$$

perpendicular to the magnetic field, where t is time, and M_j represents the bulk magnetization. Relaxation is described as a first order kinetic process and therefore T_1^{-1} and T_2^{-1} are relaxation rate constants.

T_1 is measured experimentally using the inversion-recovery pulse sequence. In this experiment the variable delay, τ, is incremented through a series of values for which a signal is acquired. The pulse sequence is described by

$$[180^\circ - \tau - 90^\circ(\text{FID}) - T_d]_n$$

where (FID) represents the acquisition of the signal for a given delay, τ, and T_d represents the fixed delay between pulse sequences. The intensity of the signal S(t) compared to the signal at infinite delay, S(∞) are related according to[3]

$$\ln[S(\infty) - S(t)] = \ln 2 + \ln S(\infty) - \tau/T_1 \tag{4.27}$$

where S(∞) is the signal intensity for long values of τ, and the value of T_1 is equivalent to $\tau_{null}/\ln 2$. For very short values of τ the signal is negative, at intermediate τ the signal is zero, and at long values of τ the signal is positive and at a maximum intensity. By measuring the T_1 value for a sample over a given temperature range a T_1 curve is obtained. Typically such a curve is a plot of $\ln T_1$ versus 1000/T, and is characterized by three regions: the extreme narrowing, slow tumbling and T_1 minimum. These regions correspond to increasing T_1 with increasing temperature, decreasing T_1 with increasing temperature, and the minimum value of T_1 over the entire temperature range. The value of $T_{1(min)}$ can be used to characterize the correlation time, τ_c, for the given sample.

Relaxation theory is quite complex, but will be developed here for a simple case, in which all spins are of the same type and the field that induces relaxation is isolated and acting in a time dependent fashion. The x component of the local field, $B_{xL}(t)$ is thus time dependent, expressed as

$$B_{xL}(t) = B^\circ_{xL} f(t) \tag{4.28}$$

This field contributes a perturbation by interacting with the x component of the nuclear magnetic moment, inducing transitions at the rate[4]

$$W^{-1} = \hbar^{-2}\langle\alpha|-\gamma\hbar I_x B^{\circ}_{xL}|\beta\rangle^2 J(\omega_0) \qquad (4.29)$$

$$= 1/2\gamma^2[B^{\circ}_{xL}]^2\, J(\omega_0)$$

where B°_{xL} is the local time dependent field and $J(\omega_0)$ is the power available from the fluctuations at the frequency of the relaxation transition, ω_0. $J(\omega_0)$ is also known as the spectral density function. The spectral density function is related to the auto-correlation function, $G(\tau)$, through a Fourier transformation between the frequency domain and the time domain, expressed as

$$J(\omega) = \int_{-\infty}^{\infty} G(\tau)\exp(i\omega\tau)d\tau \qquad (4.30)$$

where

$$G(\tau) = \exp\left(-|\tau|/\tau_c\right) \qquad (4.31)$$

and τ_c is the correlation time, which in solution is defined as the time required for a molecule to rotate through a distance of one radian. Substituting 4.29 into 4.28 gives the following expression

$$J(\omega) = \frac{2\tau_c}{1+\omega_0^2\tau_c^2} \qquad (4.32)$$

Examining a plot of $J(\omega)$ versus log ω (**Figure 4.4**) two characteristic regions are evident, the first a flat region extending from the y axis corresponds to $\omega^2\tau_c^2 \ll 1$, and the second a steep drop, occurring when $\omega\tau_c \sim 1$, and corresponding to the T_1 minimum.

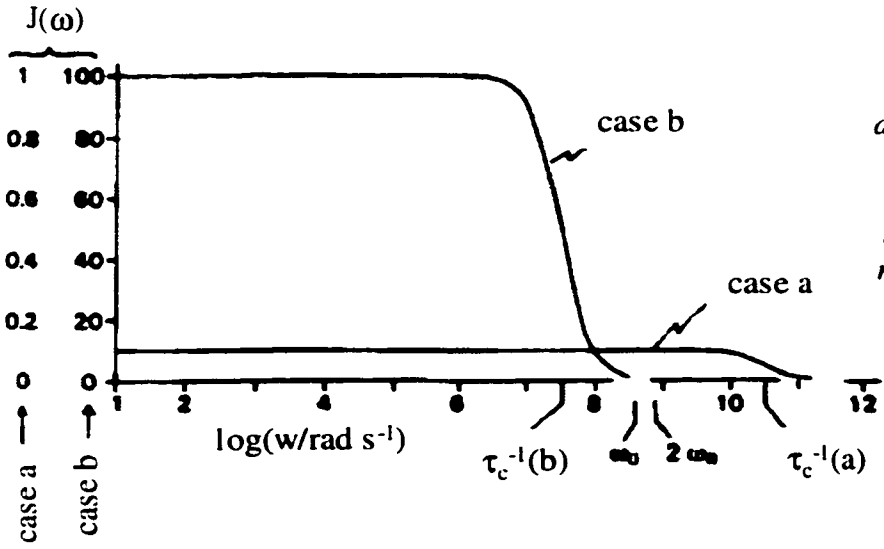

Figure 4.4 Spectral density functions for case a) small molecules in solution (extreme narrowing) and case b) macromolecules with the correlation times, τ_c^{-1} indicated.[1]

4.2.7 Interactions and Relaxation in Metals

The observable NMR phenomena in the electrode materials studied in this thesis are somewhat unique among NMR interactions. For this reason, two topics will be discussed here in greater detail: nuclear interactions with conduction electrons and with unpaired electrons. These interactions affect both the frequency of the resonance in the 1D spectrum, and the relaxation rates of the systems.

The observed shift includes all possible nuclear-electron interactions at work in the system of interest. One interaction in particular, the Knight shift, arises from the interaction between the nucleus and the motion of conduction electrons. This effect was first observed in copper metal, in which the frequency of the resonance increased by 0.63%.[5] Since then the effect has been well documented for metals, intermetallics, and alloys. The Knight shift obeys the following relationship:

$$K = \frac{\Delta H}{H_o} = \frac{8\pi}{3}\left\langle |\Psi_k(0)|^2 \right\rangle_{FS} \chi_s^e \qquad (4.33)$$

where χ_s^e is the Pauli paramagnetic spin susceptibility of the electron, and $\langle|\psi_k(0)|^2\rangle_{FS}$ is the square of the *s*-wave function at the nucleus, averaged over the electrons at the Fermi surface. Thus the Knight shift is proportional to the *s*-electron density at the nucleus.

Expressed in terms of resonance frequency, the Knight shift is described as

$$\omega_m = \omega_d + \Delta\omega \qquad (4.34)$$

where ω_m is the resonance frequency of the metal, ω_d is the resonance frequency of the same nuclei in a diamagnetic solid, and $\Delta\omega$ is the fractional shift of the resonance for the metal. The observed fractional shift is generally positive and temperature independent. As well, the ratio of $\Delta\omega$ to the diamagnetic resonance frequency is constant, regardless of the strength of the magnetic field B_o. The fractional shift increases with increasing nuclear charge, Z. **Table 4.2** lists a series of metals and their observed Knight shift, expressed as a percentage of the Larmor frequency of the nucleus. ^{6,7}Li have a comparatively small Knight shift, as a result of the small nuclear charge. The shift is nevertheless easily observable in the

Nucleus	Knight Shift in %	Nucleus	Knight Shift in %
^{7}Li	0.0261	^{63}Cu	0.237
^{23}Na	0.112	^{87}Rb	0.653
^{27}Al	0.132	^{105}Pd	-3.0
^{39}K	0.265	^{195}Pt	-3.533
^{51}V	0.580	^{197}Au	1.4
^{53}Cr	0.69	^{207}Pb	1.47

Table 4.2 Knight shifts of several metals, given as a percentage of the diamagnetic shift of the corresponding nuclei.

NMR spectrum: in the ppm scale, ionic lithium occurs at 0 ppm, while metallic lithium is substantially shifted to positive frequency, with a resonance at 256 ppm.

Metals also exhibit relaxation behaviour which is predominantly influenced by the presence of conduction electrons. The Korringa relationship, which describes this type of relaxation, predicts that the product of T_1*T should be constant. This relationship is as follows,

$$T_1\left(\frac{\Delta H}{H}\right)^2 = \frac{\hbar}{4\pi kT}\frac{\gamma_e^2}{\gamma_n^2} \tag{4.35}$$

The resonance frequency is also affected by the presence of localized unpaired electrons, through what is termed the Fermi-contact shift. The majority of the systems studied in this thesis do not have paramagnetic centres, but since many of the cathode materials used for comparison are based on transition metal oxides, in which paramagnetism is common, this interaction is included for completeness.

The Fermi contact shift is a through-bond interaction, in which the NMR-active nucleus is in contact with the paramagnetic center, either through direct orbital overlap or through indirect overlap via an intervening oxygen orbital for example. The observed shift is a measure of the unpaired electron spin density that is transferred from the paramagnetic center to the nucleus being probed by NMR. The Hamiltonian for this interaction is as follows,[11]

$$\mathcal{H}_{FC} = I_z A_s \langle S_z \rangle \tag{4.36}$$

where $\langle S_z \rangle$ is the thermally averaged value of the paramagnetic spins, and A_s is the electron-nuclear hyperfine coupling constant. The latter term controls the size of the shift. $\langle S_z \rangle$ is proportional to χB_o where χ is the paramagnetic susceptibility. Thus the interaction

scales directly with field strength. For this reason, when working with paramagnetic systems it is advantageous to work at low field strengths, for example, B_o = 4.7 T. Examples of NMR studies of paramagnetic cathode materials will be described in the next section. The Fermi-contact is not a shift mechanism which has been observed through the course of this thesis.

4.3 NMR Studies of Various Electrode Materials

Until recently the use of solid state NMR in the investigation of electrode materials was relatively rare. Within the last five years, a number of studies have been published that illustrate the types of useful, and unique data which may be obtained through NMR methods. The materials studied include cathode materials such as manganese oxides, cobalt oxides and mixed cobalt-nickel oxides, all of which contain paramagnetic species either in the starting material, or in the reduced electrode material. Paramagnetism presents several challenges to the successful acquisition of the NMR spectrum, since the unpaired electron may couple with the nuclear magnetic moment and cause extremely fast relaxation times such that the signal is not observed, or is broadened to a great extent. In spite of this several groups have successfully acquired data on these systems.

Lithiated cobalt oxide, the first commercialized cathode material used in a lithium ion battery, was studied using both 6-Li and 7-Li NMR in order to examine the relationship between the electrical conductivity properties and the corresponding cathodic behaviour.[6] The question to be answered was whether the addition of excess lithium to the starting material would result in improved electrical properties and/or enhanced reversible capacity of the electrode material. The material of interest, $Li_{1+y}CoO_2$, where y = 0, 0.08, and 0.35, was studied by NMR to identify the sites in which the excess Li^+ ions reside. The results from the 1D NMR study showed that neither the position nor the linewidth of the single $^{6,7}Li$ NMR resonance was affected significantly by the addition of excess lithium to the structure. On the other hand, the T_1 value decreased with increasing y, corresponding to the presence of paramagnetic Co^{2+}. Additionally, a small shoulder was observed, shifted to slightly higher frequency. This signal was responsible for less than 4% of the overall integrated intensity, but was significant, since its T_1 values was more than an order of magnitude faster

than the main resonance. The position of this shoulder was found to be temperature dependent, shifting to higher frequency with decreasing temperature. Thus the signal is the result of a localized paramagnetic interaction. As well, a peak at 1380 ppm with a signal intensity of <1% was observed. This is attributed to Li^+ ions which are in even closer proximity to the paramagnetic Co^{2+} sites. From these results it was concluded that the majority of the excess lithium formed ionic impurity compounds, which are not significantly different in their NMR resonance than the pristine $LiCoO_2$. Only a small amount of the excess lithium interacts with the paramagnetic centers. The electrical conductivity studies demonstrated that this material did indeed exhibit enhanced the electrical conductivity compared to the stoichiometric phase. Unfortunately no electrochemical studies were presented, so the question concerning the origin of the enhanced cathodic performance of these materials is still unanswered. Nevertheless this study clearly illustrates that the $^{6,7}Li$ NMR spectrum is extremely sensitive to changes in the local electronic environment of the lithium ions, even in materials which are not well understood from a crystallographic perspective.

A related study by Saadoune *et al.* presented the electrochemical properties of the cobalt rich phases of $Li_xNi_{1-y}Co_yO_2$.[7] In these phases a portion of the cobalt is substituted by paramagnetic Ni^{3+}. The static 1D ^7Li NMR spectra of the materials can be separated into two components. The first site, I, is shifted to high frequency with respect to the second site, II, centered at 0 ppm. Component I increases in relative intensity with increasing concentration of Ni^{3+}, and is therefore attributed to lithium ions interacting with at least one Ni^{3+} as a first 3d neighbor. This gives rise to a Fermi contact shift; the interaction with one localized electron through the intervening oxygen orbitals. Although the spectra are not deconvoluted in the paper, the maximum Fermi contact shift appears to be ~500 ppm. Component II has a narrower lineshape, and is centered at 0 ppm, similar to the observed signal for $LiCoO_2$. This resonance results from the Li^+ ions surrounded exclusively by diamagnetic cobalt as nearest neighbors.

The study of the parent compounds is balanced by an investigation of the changes in the ^7Li NMR spectra upon galvanostatic extraction of lithium from the materials. The clear trend observed among the spectra is that the first process involves the oxidation of the Ni^{3+} centers, as indicated by the decreasing intensity of resonance I. A sample of this data is shown in **Figure 4.5**. Variable temperature experiments indicated that the removal of 0.1Li

(x = 0.9) allowed for ionic mobility within the phase, which is observed *via* the broadening of the lineshape upon cooling. At deeper discharge to x = 0.7 another phenomenon is observed; the global shift of component II toward higher frequency upon cooling. This is a consequence of the changing oxidation state of the cobalt ions, which are being oxidized from 3+ → 4+. This is attributed to delocalized electrons, which give rise to a small, but observable Knight shift. The main conclusion from this work was the confirmation of the preferential oxidation of Ni^{3+} versus Co^{3+} upon deintercalation of lithium. This is an excellent example of how the electrochemical processes can be distinguished efficiently using simple NMR methods.

Studies of $LiCoO_2$ have been extended recently to include the investigation of the

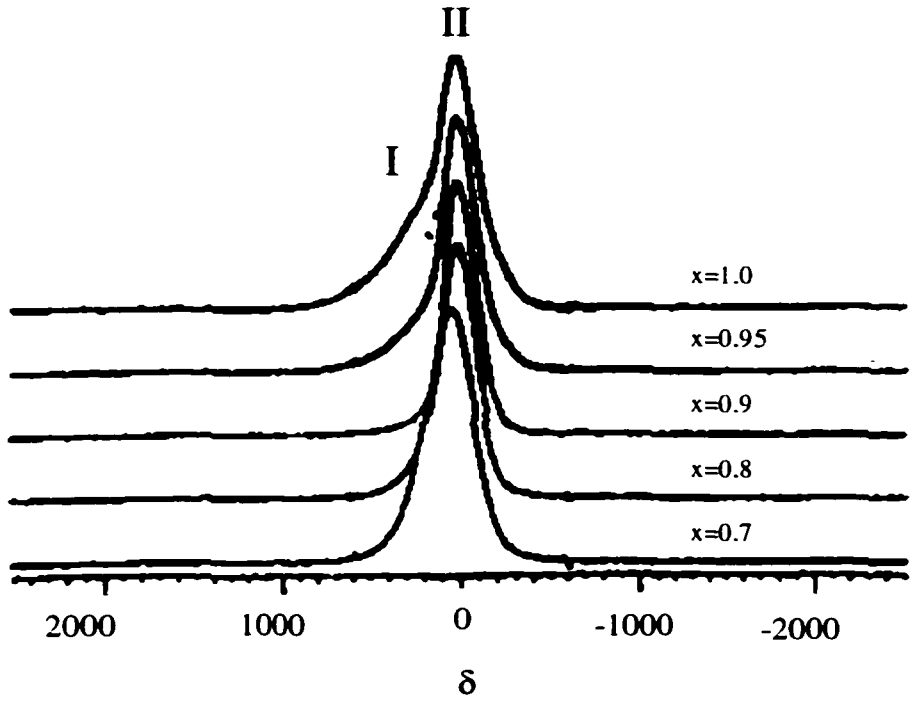

Figure 4.5 Static low temperature (153K) ^{7}Li NMR spectra of the $Li_xNi_{0.1}Co_{0.9}O_2$ phases ($1.0 \geq x \geq 0.7$).[8]

insulator-metal transition observed upon deintercalation of lithium from the structure.[8] Electrodes from which lithium had been electrochemically extracted were studied by ^{7}Li NMR in the composition range Li_xCoO_2 where $0.5<x<1$. Two phase domains were found in the region x = 0.75-0.94, identified by the two unique NMR resonances observed. The

second resonance appears at higher frequency, and grows at the expense of the original 0 ppm resonance upon increasing oxidation. From their NMR data Menetrier *et al.* suggest that the non-metal to metal transition is the driving force for the existence of biphasic domains in the electrode at these levels of deintercalation.

Another class of cathode materials which have recently received attention from the NMR community are the lithium manganese oxides.[9,10] These oxides, being notoriously strong paramagnets, seem an unlikely choice for NMR investigation. Nevertheless it has been demonstrated that useful data can be obtained and while the results may not be readily interpretable, there is an abundance of information. As yet, the studies have focussed on the parent materials, since there is such wide area of interest in the electrochemical community among the Li-Mn-O phases. Both ^{6,7}Li NMR have been used to study these systems. In this case ^{6}Li is particularly advantageous due to its smaller quadrupole moment, and hence its less complicated spinning side band manifold. Depending on the field strength of the magnet, the manifold may be on the order of +/- 2000ppm. Since the paramagnetic interaction is directly dependent on field strength, it is advanageous to work with a low field (B_o=4.7T) and high spinning speed (20-30kHz).

A seminal work in this field is the publication by Lee *et al.* which documented variable temperature studies for a series of $LiMn_2O_4$ and related phases, prepared under different reaction conditions.[11] The Fermi contact shifts observed were correlated with the various crystallographic positions of the known phases and assigned on the basis of the closest contact being correlated with the greatest shift. The $LiMn_2O_4$ phases were synthesized between reaction temperatures of 550 and 850°C, giving four materials that were structurally identical according to PXRD studies, but which gave rise to drastically different ^{6}Li NMR spectra. A single site was observed at 520 ppm for the material synthesized at the highest reaction temperature, but at lower temperatures additional sites were found. The relative intensities of theses sites increased with decreasing reaction temperature. Based on the absence of impurity phases according to the PXRD data, the secondary peaks were assigned to vacancies within the $LiMn_2O_4$ framework. Variable temperature analysis indicated that these defect signals collapse to the main resonance at 250°C, indicative of mobility within the structure. As well, it was noted that the $LiMn_2O_4$ structure has an average manganese oxidation state of +3.5. Thus the observation of only one site in the 850°C material indicates that the hopping of lithium between the sites

proximal to Mn^{3+} and Mn^{4+} occurs on a time scale faster than that of the NMR experiment such that only one site is observed. Other phases studied included $Li_2Mn_4O_9$ (Mn^{4+}), which has a single resonance corresponding to the tetrahedral lithium site, at 687 ppm, and $Li_4Mn_5O_{12}$ (Mn^{4+}), which has two resonances corresponding to tetrahedral (847 ppm) and octahedral (1980 ppm) sites. The phase $Li_2Mn_2O_4$ has an oxidation state of only 3+, and gave two signals at lower frequency, 101 and 118 ppm. Thus the magnitude of the shift was found to increase with increasing oxidation state. While this appeared counterintuitive, since the Mn^{4+} ions do not have any electrons in the e_g level, it was explained on the basis of a Fermi contact mechanism. This super exchange mechanism is dependent on the geometry of the Li-O-Mn interaction, with the greatest overlap resulting in the largest Fermi contact shift.

The significance of this paper lies more in the general correlations between physical properties and NMR observables than in the particular details of the analysis. The properties of the lithium manganates discussed, including cationic disorder, the presence of defects, the ratio of lithium to manganese, and the oxidation state of manganese, have all been implicated in assessing the viability of various phases as industrially relevant electrode materials. Thus the ability to access these features of the structure using relatively routine NMR techniques makes available to the electrochemical community a vast amount of data previously thought inaccessible due to the paramagnetic nature of the manganate phases.

In the area of anode materials there have been several NMR investigations of various forms of lithiated carbon, but relatively few studies of other potential anode materials. This is not surprising, since carbon is currently the anode of industrial choice. Lithium storage in carbon, whether graphitic or disordered, has been a topic of much investigation in the last decade. In particular, the numerous disordered carbons, which have superior electrochemical properties to the traditional graphitic carbon, are the focus of considerable attention. This is because the mechanism of lithium storage in these materials is unclear. Three studies on different carbons, each pointing to different mechanisms, serve to illustrate this point. ^7Li NMR allows for the differentiation between electrochemically relevant intercalated species, in contrast with other lithium species which are irreversibly formed and which may interact parasitically with the anode material. The extent of charge transfer, and the guest-host interactions in lithium intercalation compounds can be estimated directly from

measurements of the ^{7}Li chemical shifts. This is true both for graphite, as well as the other types of disordered carbon discussed here.

K. Sato *et al.* reported in *Science* on the lithium storage mechanism in disordered carbon derived from combustion of an organic polymer.[12] Their study included TEM imaging of the pristine and lithiated-carbon, as well as ^{7}Li NMR studies of the lithium intercalation process. The TEM results indicated a 10% expansion of the interlayer spacing upon lithium insertion, as well as an increase in the defect concentration. From this they concluded that the lithium is located among the defective carbon layers. Their ^{7}Li NMR spectrum shows three overlapping contributions; a broad signal at 9.85 ppm (A), a narrow line at –0.62 ppm (B), and a small peak at –0.90 ppm (C). Lineshape (C) is attributed to lithium carbonate or other SEI components and is ignored in the interpretation. They conclude that the lithium doped carbon includes two sites. Resonance (B) is observed throughout discharges (30-1000Ah/kg) whereas resonance (A) is only observed beyond 300Ah/kg. They suggest that resonance A results from the interaction of the lithium ion with the radical created when the accompanying electron is inserted into the LUMO of the carbon. This radical formation causes the chemical shift to occur at higher frequency, since the shift is proportional to the electron spin density at the position of the observed nucleus. Because of the minimal shift it is assumed that the electron spin density is small at the lithium nucleus. This interpretation is analogous to results obtained for graphitic carbon, in which an ionic mechanism is dominant.

Resonance (B), due to its negligible chemical shift, must result from lithium in which all spins are paired. The hypothesis reported in this paper is that the observed small chemical shift is evidence for the existence of Li_2 dimers. These dimers are purported to be mobile, such that when lithium is removed from the structure, the dimers can move to fill the vacancy, acting as a capacity reservoir. Their hypothesis is illustrated in **Figure 4.6**

Another, somewhat less speculative study of lithium insertion into carbon was reported by Dai *et al.*[13] The carbon in this study was obtained by the pyrolysis of cotton cloth. It contains small ordered regions, dispersed throughout a highly disordered matrix, and includes a residual amount of hydrogen. The voltage profile of this material includes two voltage plateaux. Three electrode samples were studied by ^{7}Li NMR; one at deepest discharge, fully lithiated, one at the end of the first, low voltage plateau, partially delithiated and the third at the top of the charging process (fully delithiated). The ^{7}Li NMR spectrum of

the first sample included three distinguishable resonances; one at 50 ppm, one at 17 ppm, and one at 0 ppm. The signal at 50 ppm is correlated with similar signals observed in graphitic carbon, is thus attributed to lithium ions residing between graphene rings in the small crystalline domains. This signal is considered the "signature" of single stage LiC_6 graphite. Conduction electrons associated with the graphene planes, supplied by the ionized lithium 2s electrons, are responsible for the observed Knight shift. The broadening of this lineshape is caused by the heterogeneous distribution of lithium sites within the disordered matrix. The spectrum obtained from the second sample includes only the 17 ppm and 0 ppm sites, indicating that upon charge the lithium is removed first from the graphene planes. Finally, the spectrum obtained from the fully delithiated sample includes only the 0 ppm resonance; at this point all reversible lithium has been removed, and the remaining resonance arises from lithium associated with the SEI. The second part of the study involved a series of comparative NMR spectra: one set collected under standard, single pulse Bloch decay conditions, and the second collected using high power proton decoupling. This was done to estimate the proximity of the protons to the lithium ions. A modest amount of line narrowing was observed under decoupling. This indicated that the Li-H distance is not greater than 3Å, and thus the 17 ppm site arises from lithium which is spatially proximal to protons. Two intercalation mechanisms are therefore invoked; lithium intercalation between turbostratically disordered graphene planes, and covalent Li-C bond formation. These two environments are illustrated in **Figure 4.7.**

A third investigation of carbon based anode materials that demonstrates yet another model for lithium insertion was published by Hayes *et al.*[14] This work involved disordered carbon derived from the pyrolysis of various polymers. In contrast to the study by Dai *et al.*, this group observed that the change in chemical shift upon charge and discharge was continuous. Whereas Dai *et al.* observed a discontinuous change in chemical shift, corresponding to the insertion of lithium into unique electronic environments, **Figure 4.8** shows a graph taken from the study by Hayes *et al.*, indicating the smooth increase in

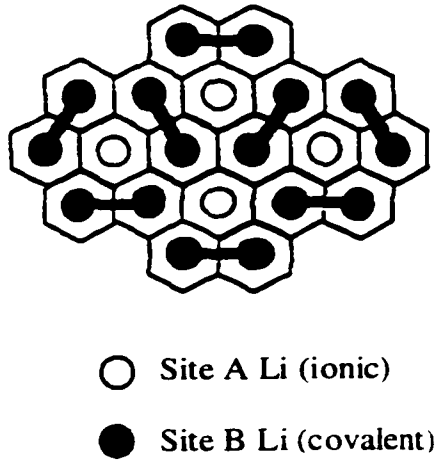

Figure 4.6 Schematic of one proposed interaction between lithium and carbon, including ionic lithium as well as lithium dimers.[12]

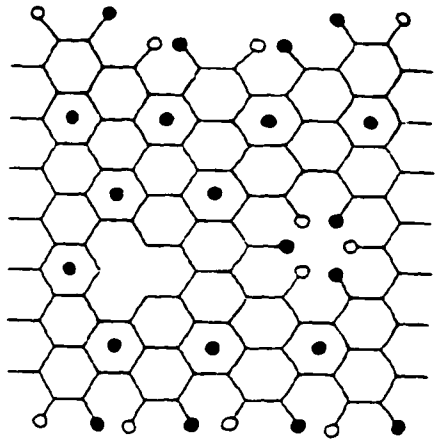

Figure 4.7 Structural model for hard carbon, depicting sites for lithium insertion (dark circles) and residual hydrogen (open circles)[13]

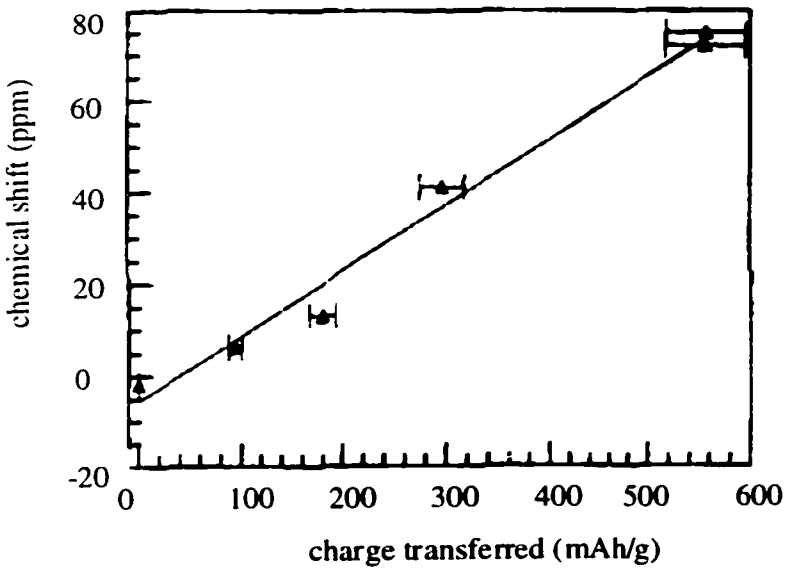

Figure 4.8 Correlation of ^{7}Li chemical shifts of lithium-intercalated carbon with degree of charge transferred.[14]

chemical shift frequency with increasing lithium content, (or mAh/g). The spectra show a peak around 0 ppm, similar to that observed by Sato *et al.* Their results do not agree with the Li_2 model though, since this peak is present throughout the charge/discharge process. They instead attribute this to a lithium carbonate, or some other parasitic reaction product. Similar to the results of Dai *et al.*, the dominant peak at high frequency after full discharge disappears upon deintercalation. This is conclusive evidence that this resonance arises from the electrochemically relevant species. The high frequency position of this peak represents the sizeable unpaired spin density or conduction electron density, typically observed in metals and metal-like compounds. These three studies of carbon anodes using lithium NMR each present differing views concerning the nature of lithium intercalation into carbon. This is the result of the varying forms of carbon used, as well as the various ways of collecting and interpreting the data. These studies are cited to illustrate the plethora of information available, and moreover, the types of controversies that arise when examining the processes occurring within electrode materials.

Collectively these studies give a sampling of the background for studying electrode materials by NMR. Among electrochemists in the last 5 years there has been a resurgence in interest for improving upon existing anode technologies. In particular the publication by Idota *et al.* announcement of the TCO glasses sparked renewed interest in this class of materials.

Two groups besides ourselves have reported ^{7}Li NMR data for the tin oxide systems. The first was Fuji themselves, in their original report to *Science*. [15] The second, by Wang *et al.*, reported on only the parent compound SnO. [16]

Idota *et al.* reported 1D static ^{7}Li NMR data for their new materials, and contrasted that with data obtained for SnO.[15] A graph of chemical shift versus Li:Sn ratio including data for Sn, SnO, and TCO, shows that the magnitude of the chemical shifts for TCO is less than that for SnO or Sn. This is given as evidence that metallic lithium is present in the SnO and Sn electrode, as in Li-Sn alloys, but that lithium in TCO remains ionic. This conclusion is quite unsubstantiated though, since the lithium shift range of Sn and SnO is between 10-15 ppm, and that of TCO between 2-9 ppm. These shifts are all significantly smaller than the shifts observed in metallic lithium itself (256ppm). As well, the spectra are collected on a 7.4 T instrument, using broad line NMR on static samples. This results in a single lithium

resonance, which in fact obscures much valuable information about the processes occurring in these electrodes.

The interpretation given in this paper is that the lithium coordination in TCO during charge and discharge reactions takes place at the Sn-O bonding orbital. It is concluded that partial reduction of both Sn^{II} and Li^{+} occurs, but without the formation of metallic species. This interpretation is in direct contradiction with the proposals of Dahn *et al.*, (Chapter 3) who presume that the reaction in tin composite glasses, as in the parent tin oxides, must follow the Li-Sn phase diagram, progressing through the series of line phases as the level of reduction in the electrode is increased. The focus of the efforts in this thesis was to resolve this issue.

The publication by Wang *et al.* concerning ^{7}Li NMR studies of the reaction between lithium and tin oxide offered more detail on the SnO system, but still left several questions unresolved.[16] Data were taken from a series of samples during discharge and charge. The ^{7}Li NMR spectra of the samples on initial discharge (0.5Li, and 2.0Li) as well as those near full charge (2.0Li and 1.8Li) all showed only one resonance, matching that of Li_2O. The spectra obtained for samples at an Li:SnO ratio of 4.3 both on lithiation and delithiation are compared to the reference alloy Li_7Sn_3. The spectra of the electrodes contain 3 resonances: a strong feature at 17 ppm, a shoulder at 0 ppm, and a small feature at 43 ppm. The 0ppm peak corresponds to Li_2O, while the other peaks match well with the observed resonances in the reference alloy. The alloy phases becomes more well defined on cycling, as indicated by the narrowing of the lineshapes. The final sample is taken at deepest discharge, with a Li:SnO ratio of 6.4. This sample is compared to the reference alloy $Li_{21}Sn_5$. The ^{7}Li NMR spectrum of the alloy has a broad dominant feature at 69 ppm, and minor peaks around 8 ppm. This contrasts sharply with the spectrum obtained from the electrode, in which only a peak at ~8ppm is observed. In this paper the significant difference is attributed to a difference in the local structure. There are other probable reasons for this discrepancy, which will be elaborated upon in the results section. Nevertheless the implied conclusion that the insertion of lithium does not follow the formation of the bulk alloys is consistent with the results we have obtained.

4.4 NMR Sample Preparation and Experimental Methods

Samples for NMR measurements were obtained following electrochemical Li insertion, performed under potentiostatic conditions at a discharge rate of 50mV/hr, on electrodes that typically contained about 5mg of active material. To ensure equilibration of the samples, the electrodes were held at the desired cutoff voltage for 48 hours before being dried and transferred to NMR rotors in the argon glove box. The rotors were sealed with Kel-F caps that were proven to be airtight by tests with known air-sensitive materials. Solid-state NMR was performed on a Bruker AMX-500 NMR spectrometer with an 11.7 T narrow bore magnet, using the resonant frequencies, and reference compounds for the nuclei of interest as follows: ^{6}Li: 73.6 MHz; ^{7}Li: 194.3 MHz ($LiNO_3$ at 0.0 ppm); ^{31}P: 202.4 MHz ($NH_4H_2PO_4$ at 0.83 ppm); ^{11}B: 160.4 MHz ($NaBH_4$ at 0.0 ppm); ^{27}Al: 130.3 MHz ($Al(NO_3)_3$(aq) at 0.0 ppm) and ^{119}Sn: 186 MHz ($Sn(C_4H_9)_4$ at –6.4 ppm). In all cases, a Bloch decay pulse sequence was used. This pulse sequence is shown schematically in **Figure 4.9**. The free induction decay (FID) is collected in the time domain, and converted *via* Fourier transform (FT) to the frequency domain. Pulse lengths were typically 2μs, corresponding to a 30-45° pulse. Delay times of 200ms were sufficient for the quadrupolar nuclei (^{27}Al and ^{11}B), while 10s was required for ^{31}P and ^{119}Sn. Lithium-6 and -7 spectra were acquired with delays of 1s. All spectra were acquired under magic angle spinning (MAS) conditions, using spinning speeds of 5-7.5 kHz. For the boron spectra, background subtraction was carried out to remove the boro-silicate glass signal arising from the variable temperature dewar in the MAS probe.

Deconvolutions of the complex lithium NMR lineshapes were executed using the software package, WINNMR.[17] The best fit was obtained with the minimum possible number of Gaussian lineshapes.

To obtain relaxation data for the systems of interest inversion-recovery experiments were performed. The temperature range of the relaxation experiments was between 300 and 360 K. Spin lattice relaxation times can be measured using an inversion-recovery pulse sequence, such as that illustrated in **Figure 4.10**. The ^{7}Li MAS spectra were obtained on a Bruker DSX-400 spectrometer, at a spinning rate of 4kHz. Spectra were referenced to solid

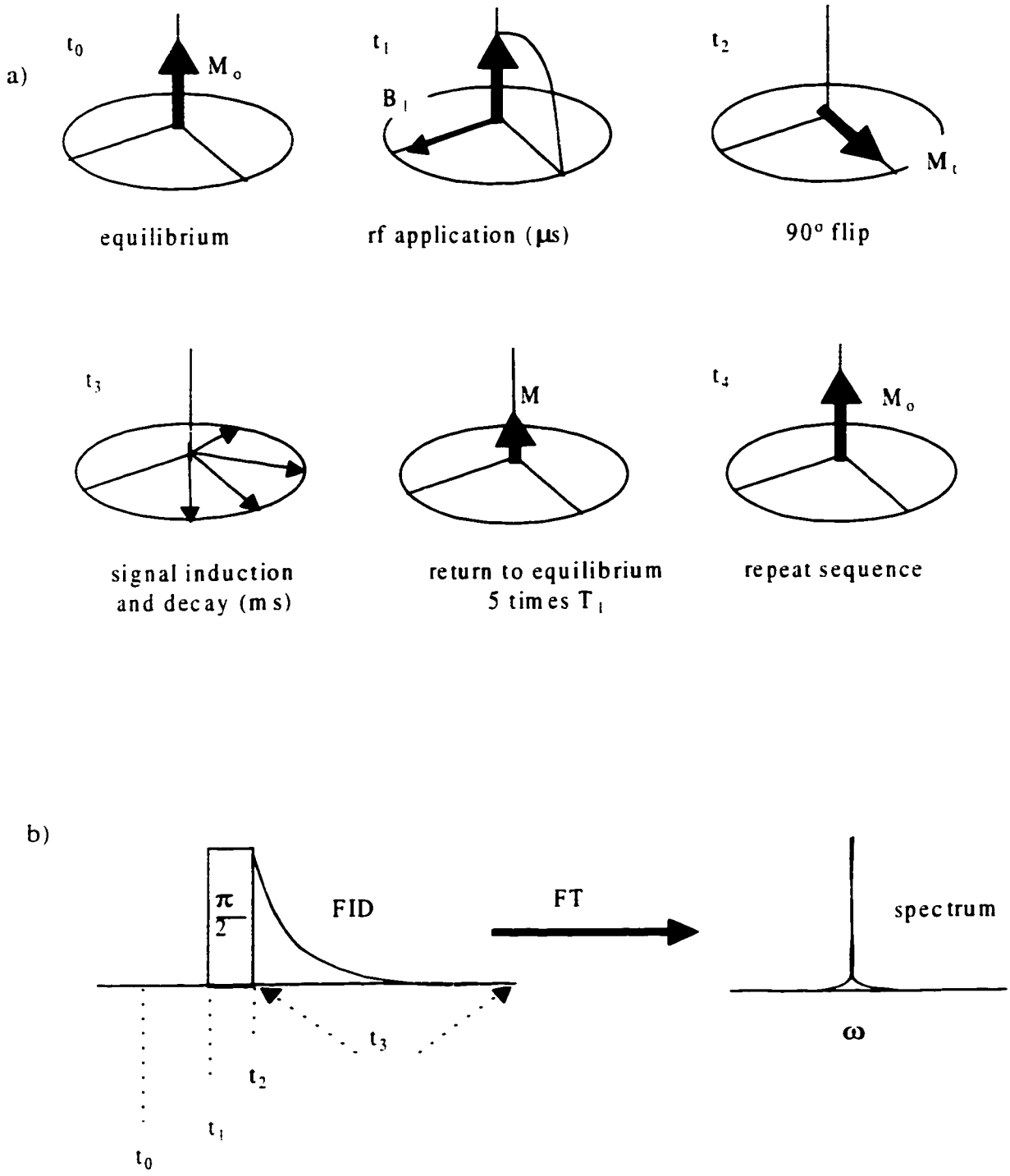

Figure 4.9 a) *Detection of NMR signals shown with respect to the magnetization, **M** (fat arrow), at various stages t_0-t_4: t_0 – spin system at equilibrium, t_1 – irradiation of the B_1 field orthogonal to the magnetization direction tips the magnetization, t_2 - the system after a 90° pulse resulting in transverse magnetization, M_1, t_3 - off resonance precession and free induction decay in the signal acquisition period. t_4 - return to equilibrium due to spin-lattice relaxation. b) Timing diagram of the experiment, followed by Fourier transform.*[18]

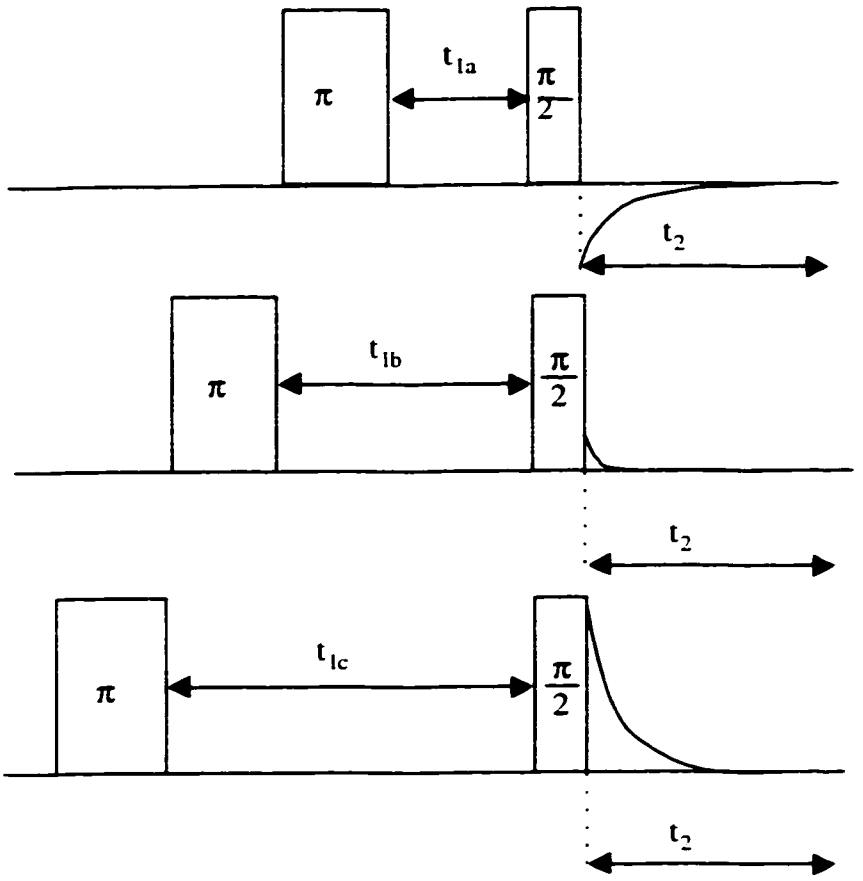

Figure 4.10 Measurement of spin-lattice relaxation time by the inversion-recovery method (180°-t_1-90°). The build up of the signal is shown for three evolution times, $t_{1a\text{-}c}$, which elapse between the 180° pulse and the final 90° detection pulse.[18]

LiCl. Li metal exhibited the expected Knight shift, of 256ppm, in agreement with literature values.

4.5 Results

This section includes NMR studies of tin oxide, tin composite oxide, tin metal, and molybdenum oxide electrode materials. It starts with the ^{7}Li NMR data for two lithium-tin alloys, which are considered model compounds in the electrochemical reaction between lithium and the various tin-based electrodes. The NMR data for each electrochemical system are presented individually, with comparisons drawn where appropriate. The following section, 4.6, will bring together the electrochemical characteristics and the NMR observations, thereby giving a more complete picture of the materials.

4.5.1 ^{7}Li NMR studies of Bulk Li-Sn phases

Two Li-Sn alloys were synthesized by high-temperature reaction. The synthesis conditions, and characterization by powder X-ray diffraction were described in Chapter 2. **Figure 4.11** shows the ^{7}Li NMR spectra for the two materials. The first material is a mixed phase of low Li:Sn ratio and the second material is nearly single phase $Li_{21}Sn_5$, the highest lithium concentration possible in the lithium tin phase diagram. The ^{7}Li lineshape of the lithium poor phase included three main contributions, likely due to the multiphase nature of the sample. The positions of these contributions are 17 ppm, 30 ppm, and 43 ppm. This lineshape is reminiscent of that found by Wang *et al.* for the Li_7Sn_3 alloy, with differences between their spectra and ours being attributed to differing ratios of contaminants in each sample. The ^{7}Li lineshape of the $Li_{21}Sn_5$ sample is dominated by a strong resonance at 114 ppm. There are several signals at lower frequency, attributed to small amounts of contamination from phases of lower lithium concentration. There is also a small signal at 256 ppm, attributed to excess metallic lithium in the reaction. In this case, the observed resonance is shifted to higher frequency than that observed by Wang *et al.* Since we have confirmed that the structure of our material is consistent with the powder diffraction pattern of $Li_{21}Sn_5$, it seems likely that the sample studied by Wang *et al.* was in fact predominantly a lower Li:Sn phase than intended. While the purity of these samples is less than ideal, the expected trend is well illustrated. An increased ratio of Li:Sn in the samples results in

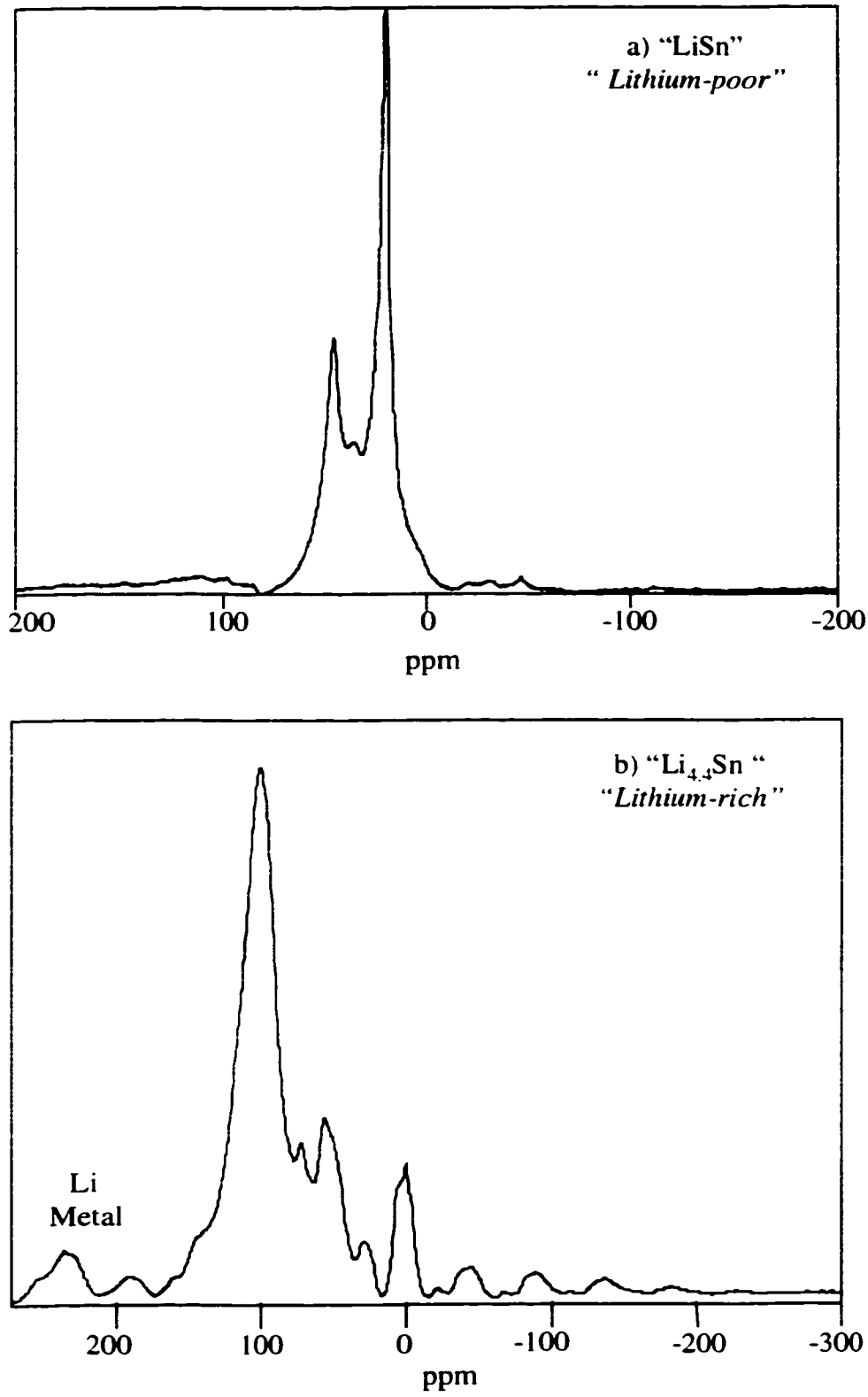

Figure 4.11 ^{7}Li NMR spectra of bulk Li-Sn phases

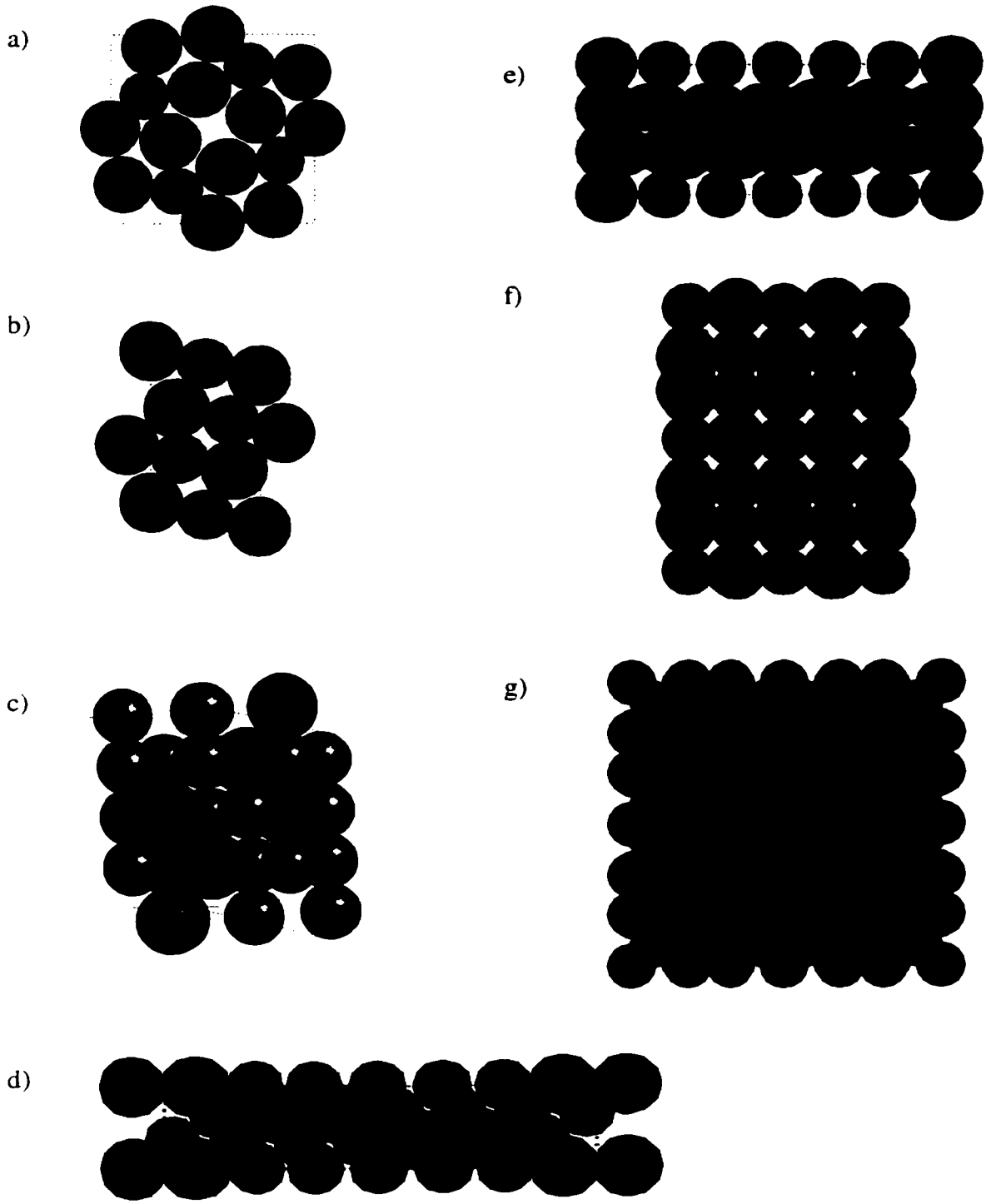

Figure 4.12 Li –Sn crystal structures, where gray circles represent tin atoms, and blue circles represent lithium atoms. a) Li_2Sn_5, b)LiSn, c) Li_7Sn_3, d) Li_5Sn_2, e) $Li_{13}Sn_5$, f)Li_7Sn_2, and g) $Li_{21}Sn_5$

increased magnitude of the observed Knight shift. This is expected from a qualitative examination of the crystal structures of the various Li:Sn phases, depicted in **Figure 4.12**. Based on the increasing number of Li-Li nearest neighbors in the series of linephases from Li_2Sn_5 through to $Li_{21}Sn_5$, it was hypothesized that the magnitude of the Knight shift would become increasingly similar to that of lithium metal itself. This hypothesis is born out in these experimental data and is also supported by the density of states calculation presented in Chapter 5. Based on this data for the bulk lithium-tin phases, we assumed that the ^7Li NMR resonance for the electrochemically formed Li-Sn species would show a similar trend.

4.5.2 $^{6,7}Li$ NMR Studies of Tin Oxides and Tin Composite Oxide Glasses

In addressing the nature of the reaction between lithium and tin-oxide based electrodes, the logical starting point is the investigation of the Li environments at various points in the electrochemical process. Using $^{6,7}Li$ NMR, unique information is obtained concerning the various types of lithium interactions occurring in these systems. Drawing on the difference observed between the behaviour of SnO compared to TCO, we begin to construct a picture of the mechanisms that give TCO its enhanced electrochemical properties compared to crystalline SnO.

Figure 4.13 shows the electrochemical profiles of SnO, TCO, and Sn-rich-TCO, including the points at which samples were extracted *ex situ* for analysis by NMR. ^7Li spectra for SnO at several points in the charge/discharge curve are presented in **Figure 4.14**. Comparing these spectra to those obtained for TCO at similar points in the electrochemical process, shown in **Figure 4.15,** several similarities and differences are observed. On discharge to 750 mV (**Figure 4.14a, 4.15a**) the broad feature at 3 ±1 ppm indicates the formation of amorphous Li_2O in both materials. Deeper discharge to 250-300 mV gives rise to a second Li environment which is readily resolved at 10 mV as a broad peak at ~10 ppm (**Figure 4.14b & 4.15b**). We ascribe this feature to Li in an environment rich in both reduced Sn and oxygen. Significantly, a high-frequency or Knight shift, typically on the order of hundreds of ppm (*e.g.*, 256 ppm for Li metal), which represents the presence of lithium in a metallic environment such as an alloy, is *not* observed. The maximum high-frequency shift observed for any of the electrodes on the first cycle was ~10 ppm; far less than the 114 ppm shift observed for a bulk $Li_{21}Sn_5$ phase (**Figure 4.11**). We surmise that the small shifts observed for *both* SnO and TCO may

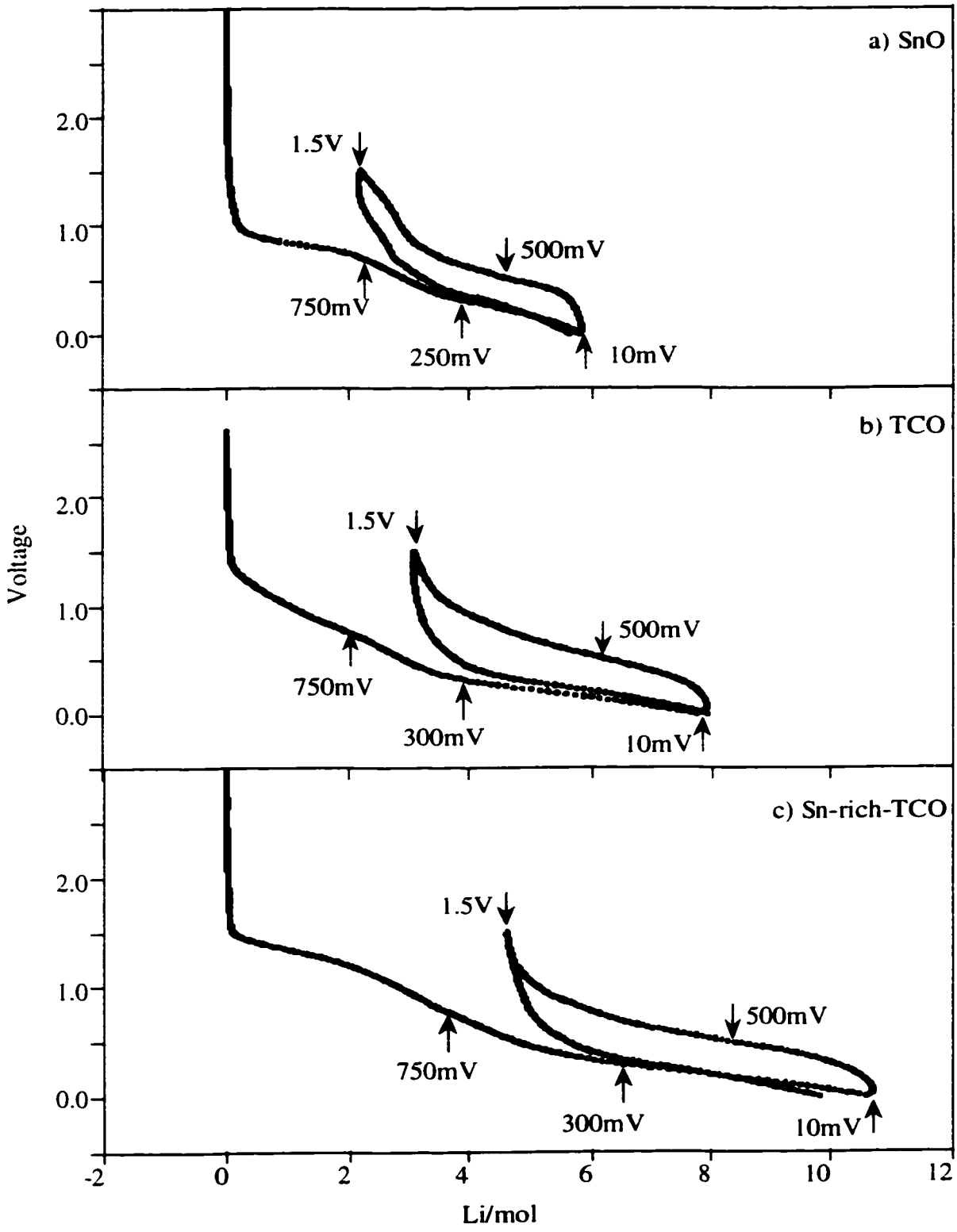

Figure 4.13 Electrochemical Profiles of SnO, TCO, and Sn-rich-TCO, with arrows indicating voltage limits for various NMR samples.

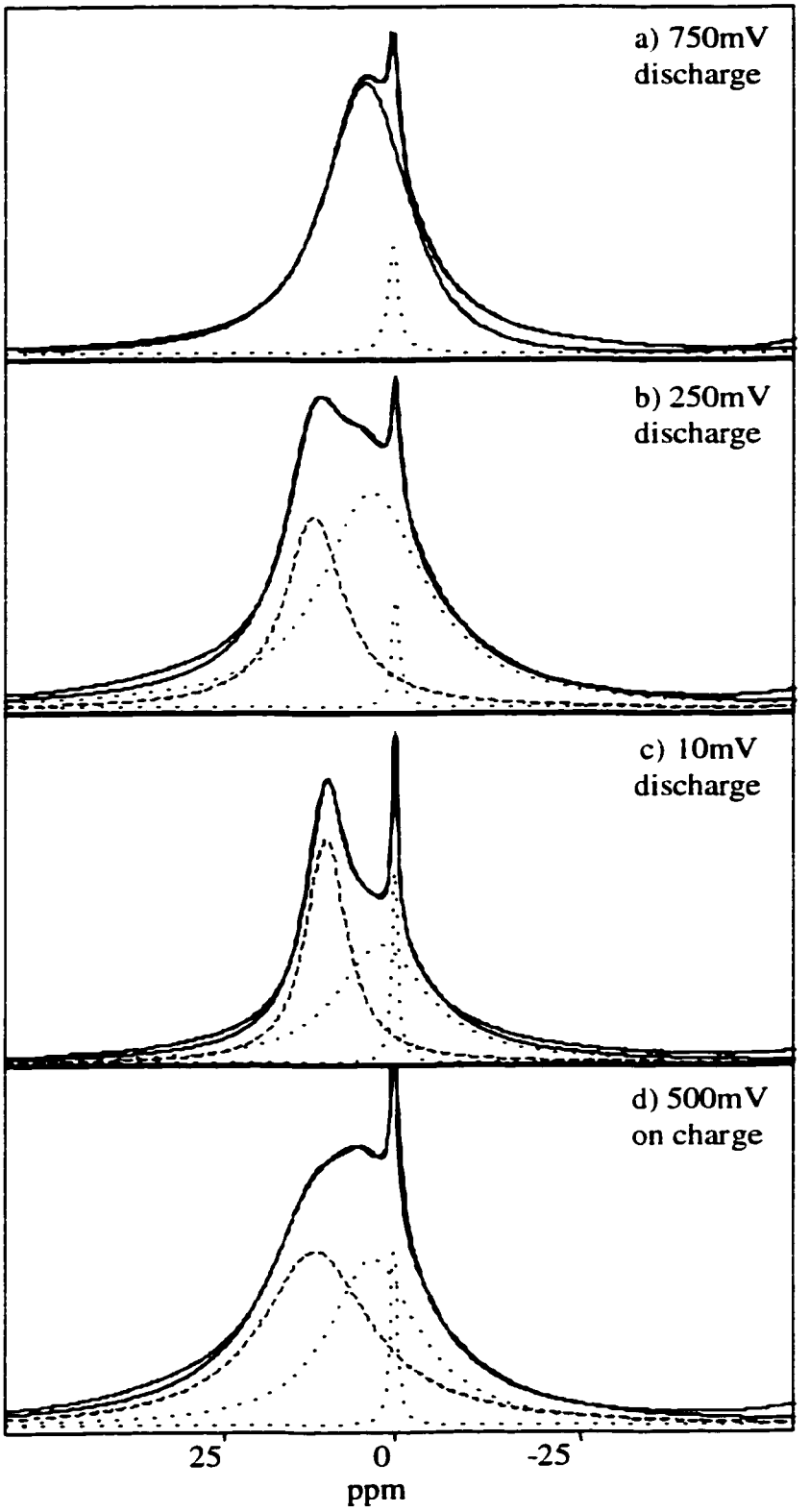

Figure 4.14 ^{7}Li NMR spectra of SnO electrodes at a) 750mV, b) 250mV, and c) 10mV on discharge, and at d) 500mV on charge. Deconvolutions of lineshapes, including total are included.

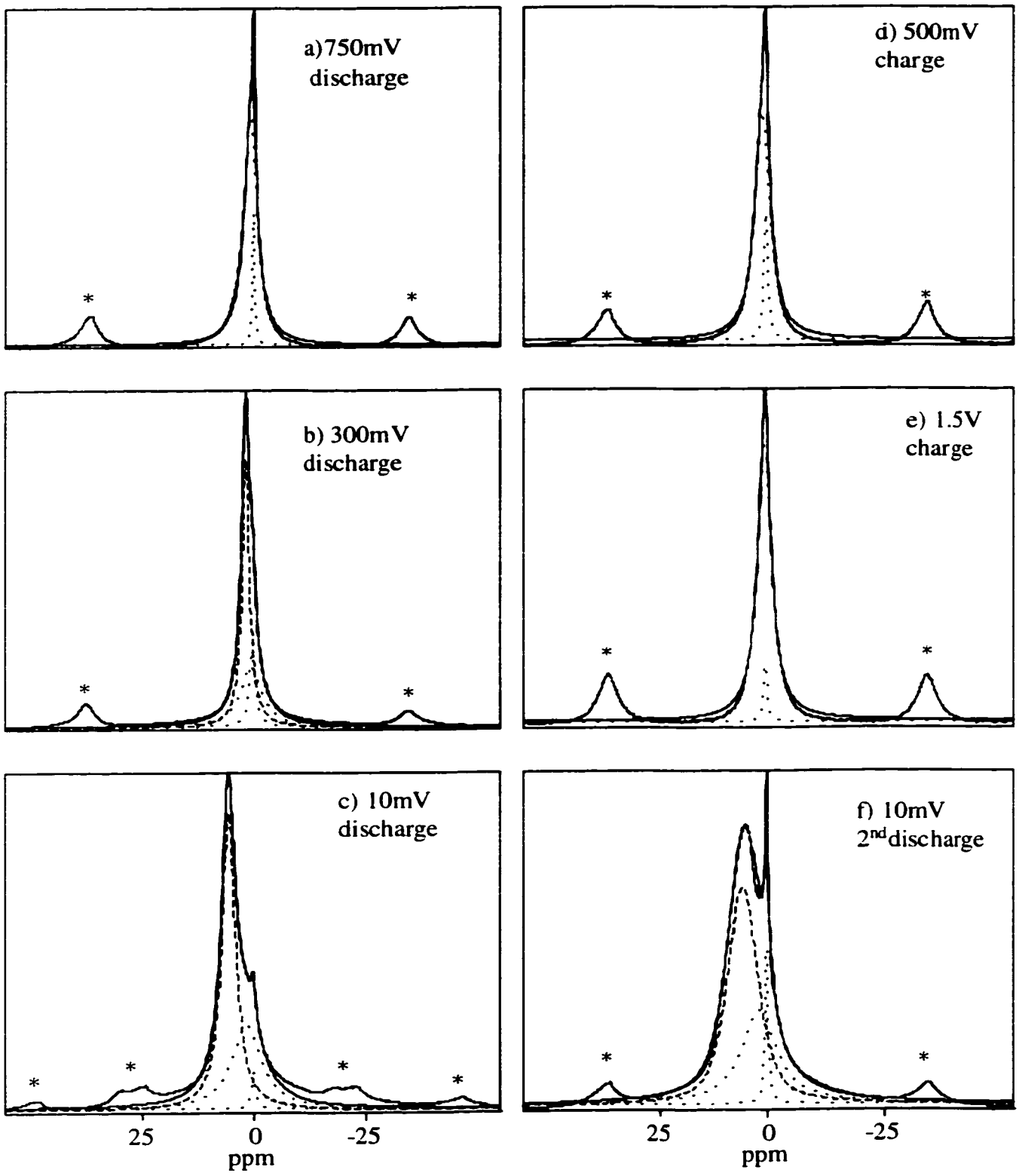

Figure 4.15 ^{7}Li NMR spectra of TCO electrodes at a) 750mV, b) 300mV, c) 10mV on discharge, and d) 500mV, e)1.5V on charge, and f) 10mV on second discharge. Spinning side bands indicated by (*). Deconvolutions indicated.

correspond to the formation of Li-Sn "nano-phases" which are intimately surrounded by the lithium-oxide environment, and hence their electronic environment is mediated by the proximity of oxygen. As suggested by Idota *et al.* the lithium in the materials is in a relatively "ionic" state even at 10 mV.

Differences between the two materials are more evident in charge. In TCO, the ^{7}Li NMR spectrum obtained at 500 mV shows that the Li-Sn contact (10ppm) is lost very early in the process. Only a broad contribution at about 3 ppm corresponding to a lithium-oxide like environment is evident midway along the charge curve, after the deinsertion of only ~ 2Li. In TCO glass the lithium is still extractable, *although it is no longer in intimate contact with metallic Sn.* In comparison, in SnO on charge at 500 mV the feature observed at 10 ppm is still present, but reduced in magnitude. A portion of the Li appears to retain its low-potential environment at this stage, but nevertheless, the ratio of the peaks on charge is consistent with an increasing lithium-oxide like contribution. The Sn particles must be relatively small in SnO but extremely small in TCO; in the latter in particular, oxygen is proximal at all times, mediating any possible Knight shift, as well as being readily re-distributed to interact with Sn as lithium is removed on charge. We believe these factors are responsible for the electrochemical performance of TCO. The contrast in behaviour is also evident upon cycling in the 1.5 - 0.010 V window.

Figures 4.15e show the ^{7}Li spectra for TCO at 1.5V on charge. The lineshape has narrowed substantially compared to the 500mV spectra, indicative of the continued breakdown of Li-Sn interactions, created at deep discharge. The spectra are quite similar to those collected at 750mV on initial discharge, again showing the cyclic nature of the interactions formed upon discharge. Further evidence of this cyclability is illustrated in **Figures 4.15f**, at 10mV following the second discharge. This spectrum is very similar to that obtained on initial discharge to 10mV, with a resonance at 10ppm reappearing, consistent with the reversible formation of the Li-Sn contact.

Figure 4.16 shows the ^{7}Li NMR spectra collected for the Sn-rich TCO glass. These data are very similar to those obtained for TCO. **Table 4.3** includes all deconvolution data for the ^{7}Li NMR data on the TCO , Sn-rich-TCO, and SnO electrodes described.

Due to the somewhat ambiguous nature of the deconvolutions of the ^{7}Li NMR lineshapes, resulting from the high degree of overlap between the spectral components, a

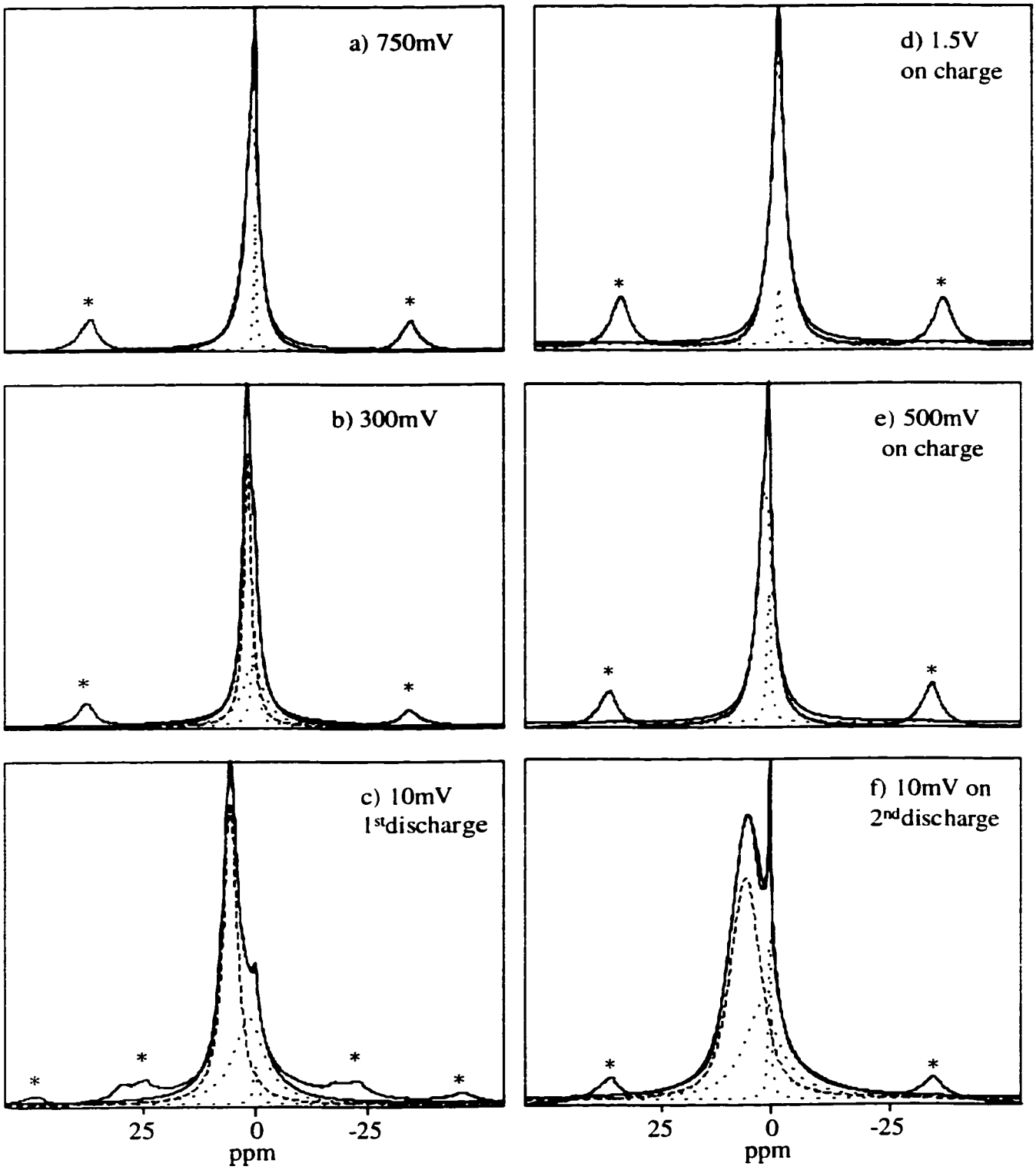

Figure 4.16 ^{7}Li NMR spectra of Sn-rich-TCO electrodes at a) 750mV, b) 300mV, c) 10mV on discharge, and d) 500mV, e) 1.5V on charge, and f) 10mV on second discharge. Deconvolutions of lineshapes, including total deconvolution are indicated.

SnO Electrode	Peak Position/ppm	Peak Width/kHz	Integrated Intensity
750mV	0.5	0.24	
	4.2	2.02	100%
250mV	0.27	0.17	
	3.29	2.47	66%
	10.9	1.46	34%
10mV	0.4	0.1	
	2.2	2.2	81%
	9.2	1	19%
500mV on charge	0.44	0.16	
	3.1	2.1	43%
	10.7	2.7	57%
TCO Electrodes			
750mV	0.3	0.15	
	1.5	1	100%
300mV	0.8	0.5	
	3.6	0.6	57%
	1.4	1.6	43%
10mV	0.3	0.3	
	3	1.1	24%
	10.4	1	76%
500mV on charge	0.8	0.3	
	2.3	1.1	100%
1.5V on charge	0.8	0.2	
	1.2	1.1	100%
10mV 2nd discharge	0.4	0.2	
	3.6	2.6	72%
	10.4	2.3	28%
Sn-rich-TCO electrodes			
750mV	0.2	0.08	
	1.9	1.3	100%
300mV	0.14	0.2	
	2.2	1.6	39%
	7.9	1.2	61%
10mV	0.1	0.3	
	2.5	1.1	16%
	8.1	2.2	28%
	10.9	5.2	56%
500mV on charge	0.9	0.3	
	2.2	1.2	100%
1.5V on charge	0.4	0.1	
	1.3	0.9	100%

Table 4.3 Parameters for deconvolutions of ^{7}Li NMR spectra, including peak positions in ppm, linewidths in kHz, and integrated intensities (the SEI peak is omitted from the calculation of relative intensity).

complementary series of ^{6}Li NMR studies were undertaken. The main objective of these studies was to confirm the ^{7}Li data, using a nucleus with a smaller quadrupole moment, and smaller magnetogyric ratio and therefore improved resolution of the contributing resonances. Both quadrupole coupling and dipolar coupling contribute to the linewidths of the lithium resonances. Therefore, by comparing spectra obtained for each isotope, the nature of the dominant coupling mechanism within the system can be deduced.

Figure 4.17 shows a ^{7}Li NMR spectrum of TCO at 10 mV, compared to a ^{6}Li NMR spectrum from a sample at the same level of reduction. The difference in the linewidths is immediately apparent. This difference is on the order of 2, which is comparable to the ratio of the magnetogyric ratios of ^{6}Li versus ^{7}Li, and is much smaller than the ratio of their respective quadrupole moments (a factor of 50). Thus it is clear that the major mechanism of coupling in the electrode materials arises from homonuclear dipolar coupling between the lithium nuclei.

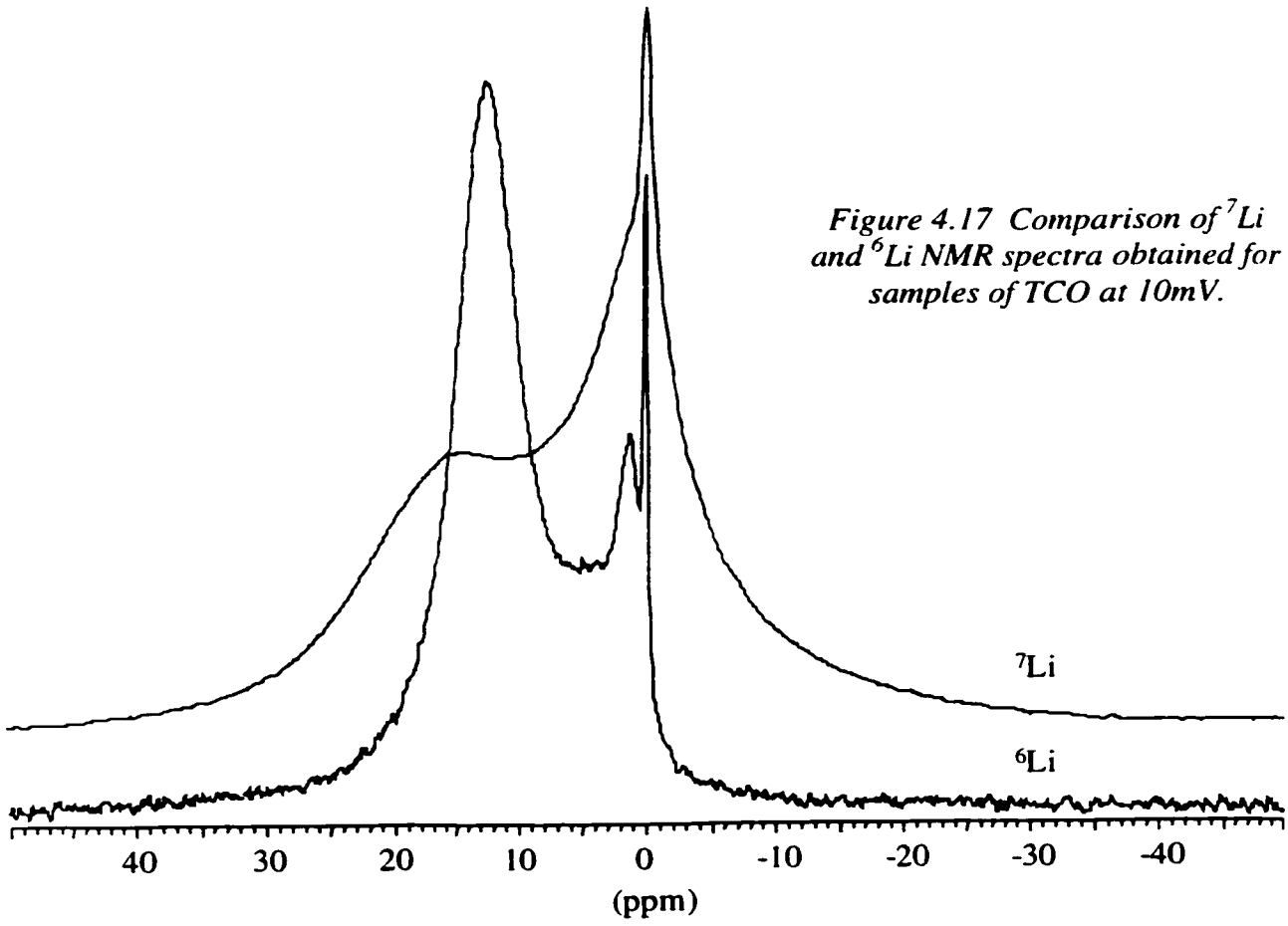

Figure 4.17 Comparison of ^{7}Li and ^{6}Li NMR spectra obtained for samples of TCO at 10mV.

The results of the ^{6}Li NMR investigation for SnO and TCO during the first electrochemical cycle are shown in **Figure 4.18 and 4.19**. The consistent appearance of a narrow peak at ~0 ppm arises from electrolyte, or surface-electrolyte interface (SEI), and will serve as an internal reference in our analysis, but is not included in the calculations of relative intensities. The data for the deconvolutions of the ^{6}Li NMR lineshapes are summarized in **Table 4.4**. On initial discharge to 750 mV, both the SnO and the TCO show a narrow signal, shifted to positive frequency with respect to the electrolyte. In SnO, this lineshape is deconvoluted with a single contribution at 3.9 ppm, and a line width of 0.15 kHz. In the case of TCO, an effective deconvolution requires two contributions: one at 1.0 ppm, of linewidth 0.125 kHz, and a second at 2.3 ppm, of linewidth 0.24 kHz. The first peak observed on discharge corresponds to the formation of the lithium-oxide matrix with the electrode. The shift is close to our experimental value for pristine crystalline Li_2O (3 ppm). The presence of two peaks in the TCO lineshape is a reflection of the various cation sites in the matrix, causing broadening of the lithium-oxide environments in this material. Upon further discharge of SnO to 250 mV, an effective fit of the lineshape now includes a broad peak centered at 9.7 ppm. The TCO electrode, discharged to 300 mV, also includes a new broad feature although its shift is only 4.5 ppm. At the bottom of discharge, these new broad features continue to move to higher frequency; in SnO at 15.5 ppm, with a linewidth of 0.83 kHz, and in TCO at 12.6 ppm, with a linewidth of 0.46 kHz. These lines represent 68% and 75% of the overall lineshapes respectively. These additional signals are attributed to the formation of a Li-Sn contact which grows in relative intensity as well as increasing in chemical shift as the cell reaches deepest discharge (maximum lithium concentration). The Sn-rich-TCO system gave similar spectra at full discharge.

Upon charge to 500 mV, the SnO and TCO behave quite differently. In the case of SnO, the dominant peak is now the original 3.7 ppm peak, which represents 40% of the overall intensity. As well, there are significant contributions from peaks at 7.1 ppm (33%) and 18.9 ppm (11%). While the latter reflects a small fraction of the total contribution, it is significant that this peak persists at high frequency. In the case of TCO, removal of 1/3 of the Li (500mV on charge), results in a shift of the peaks to lower δ, *i.e.* toward their original positions during the initial discharge. The most intense peak occurs at 3.7 ppm (41%), while the highest frequency peak is only at 5.1 ppm (22%). The contrasting behaviour between

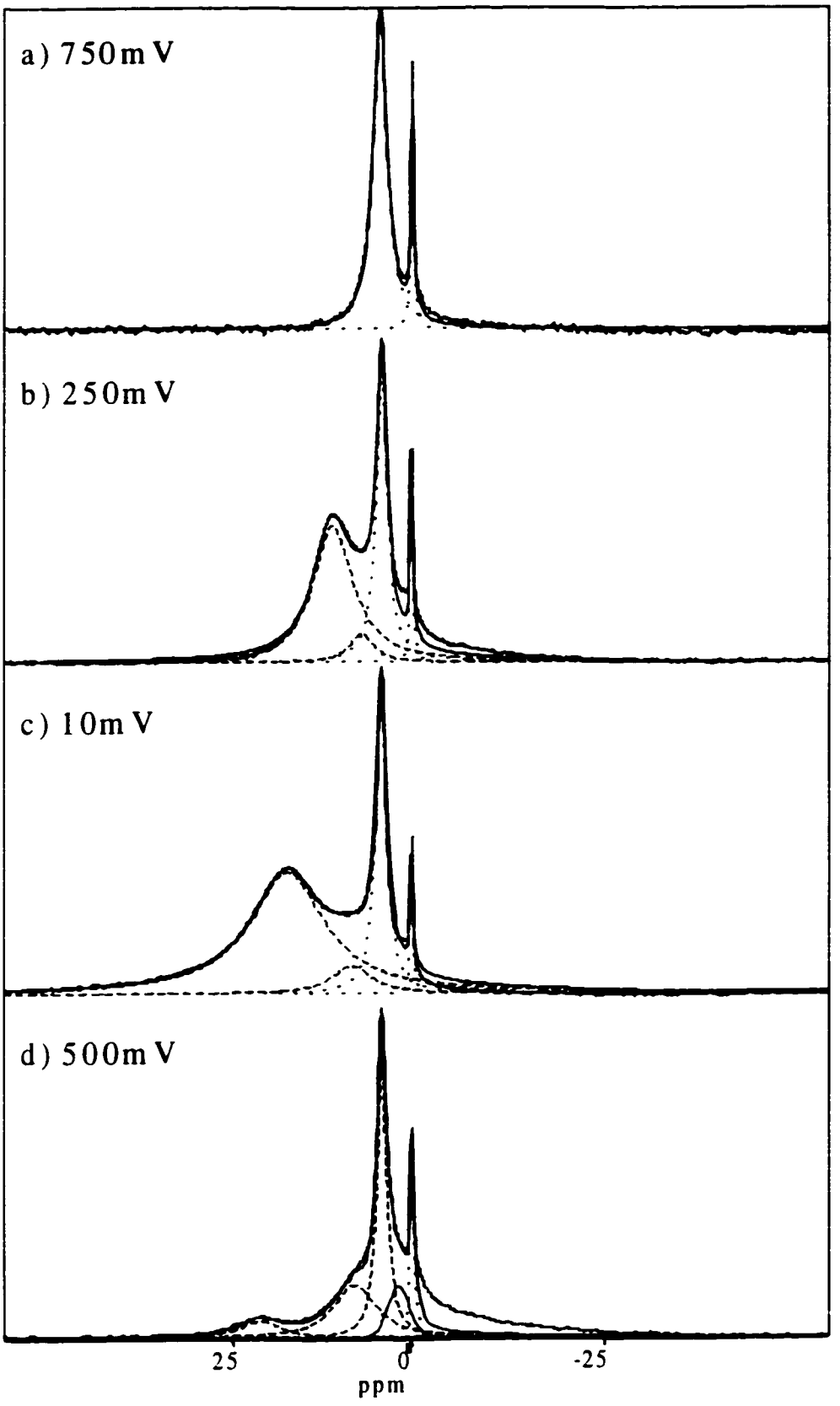

Figure 4.18 ^{6}Li NMR spectra of SnO electrodes at a) 750mV, b) 250mV, c) 10mV on discharge, and d) 500mV on charge. Deconvlutions of lineshapes are indicated.

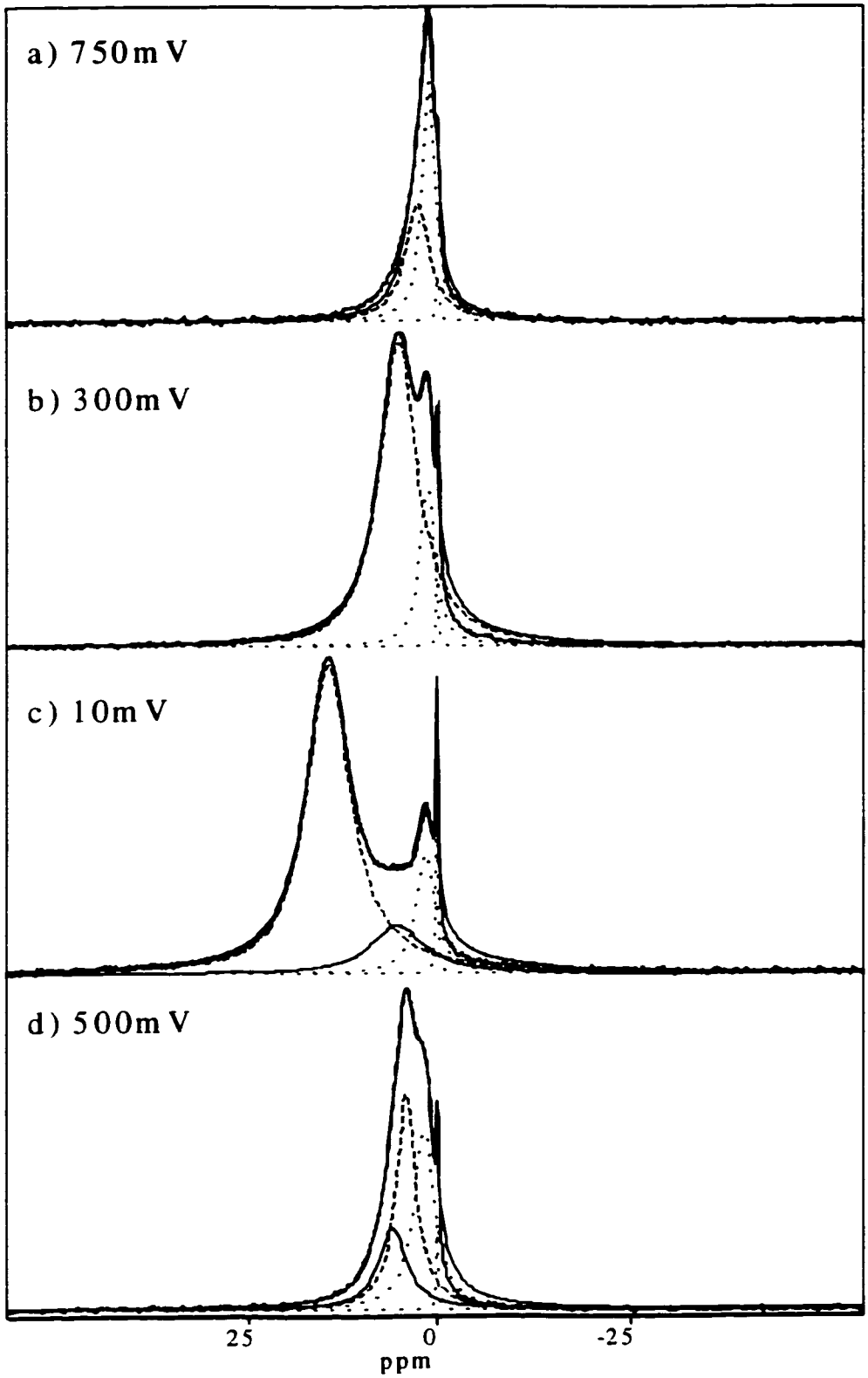

Figure 4.19 ^{6}Li NMR spectra of TCO electrodes at a) 750mV, b) 300mV, c) 10mV on discharge, and d) 500mV on charge. Deconvlutions of lineshapes are indicated.

TCO				SnO			
Electrode	Shift/ppm	Width/Hz	Intensity	Electrode	Shift/ppm	Width/Hz	Intensity
750mV	0.0	19		750mV	0.0	30	
	1.0	125	52%		3.9	150	100%
	2.3	240	48%				
					0.1	26	
300mV	0.1	11		250mV	3.7	117	
	1.2	147	17%		6.2	257	34%
	4.5	377	83%		9.7	434	7%
							59%
10mV	0.1	16		10mV	0.0	26	
	1.3	180	11%		3.8	113	24%
	4.6	541	14%		7.5	426	8%
	12.6	459	75%		15.5	832	68%
500mV	0.1	13		500mV	0.0	39	
charge	1.6	210	37%	charge	1.7	228	16%
	3.7	197	41%		3.7	101	40%
	5.1	278	22%		7.1	460	33%
					18.9	468	11%

Table 4.4 Parameters for deconvolutions of ^{6}Li NMR spectra of SnO and TCO electrodes

SnO and TCO is indicative of the relative ionicity of the interactions between lithium and tin in the two materials. Initial evidence shows that the Li-Sn contact established at deepest discharge is more reversible in the case of the TCO glass than for SnO.

Comparing the results obtained from ^{7}Li and ^{6}Li NMR studies, it is apparent that the interpretations of the data are consistent between the two isotopic studies and as well the deconvolutions of the ^{7}Li data are confirmed by the improved resolution of the ^{6}Li lineshapes.

4.5.3 *Serendipitous Aging Experiments*

Somewhat inadvertently, several of the original samples of SnO and SnO_2 electrodes were stored in rotors for a period of four months. (This occurred as a consequence of the disastrous quenching of our 11.7 T magnet in March of 1998, so serendipity might not be the correct term!) The original ^{7}Li NMR spectra of the fresh samples, as well as the spectra collected following the four month aging period are shown in **Figure 4.20.** The notable feature in these aged spectra is the new peak which appeared at 43 ppm. Although it is relatively weak in intensity, it is significant as it is substantially shifted to higher frequency with respect to the original resonances. This resonance occurs at the same frequency (43ppm) as one of the resonances in the lithium-poor LiSn phase described in section 4.5.1 This observation suggests that the Li-Sn phases, are not formed immediately during the electrochemical process, due to kinetic limitations, but ultimately are formed, if given time to aggregate and order themselves. It was surmised that this same effect occur upon prolonged cycling of the electrodes. This hypothesis was tested, and the results are presented in the next section.

4.5.4 *Cycling Experiments*

None of the chemical shift values observed in the electrode materials correspond to significant Knight shifts, as are expected if the lithium is undergoing true alloying process. The maximum shift observed for any of the electrodes on the first cycle was ~15 ppm; far less than the 114 ppm shift observed for a bulk $Li_{21}Sn_5$ alloy.[19] **Figure 4.21** shows ^{7}Li spectra for SnO, TCO and Sn-rich-TCO following 5 cycles, 10 cycles and 10 cycles respectively at full discharge. Significant differences are evident in the spectra. First, and

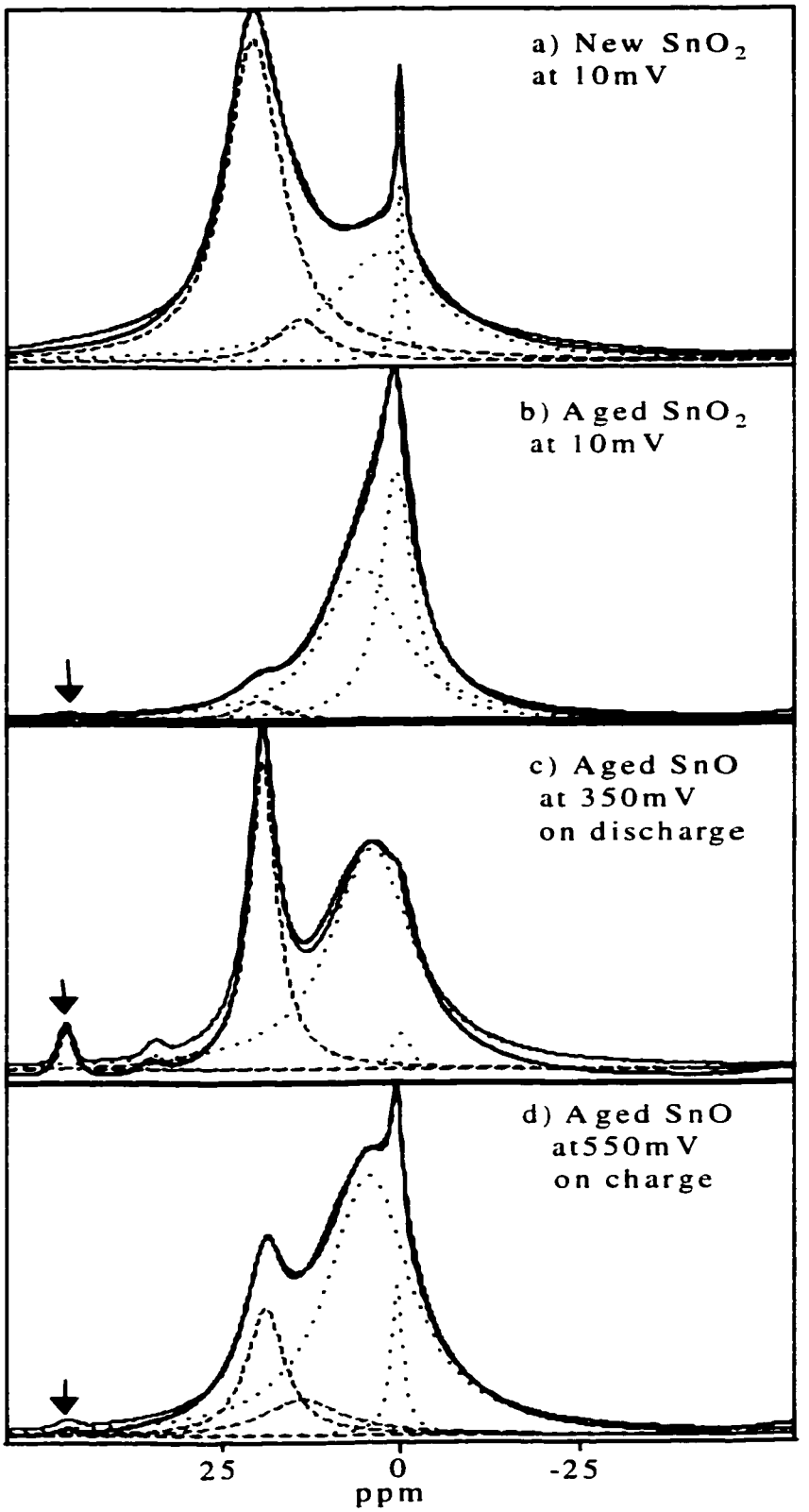

Figure 4.20 Serendipitous aging experiments, showing appearance of 43ppm peak in several samples. a) fresh sample of SnO_2 at 10mV compared to b)aged SnO_2 at 10mV, c) aged SnO at 350mV, and aged SnO at 550mV on charge.

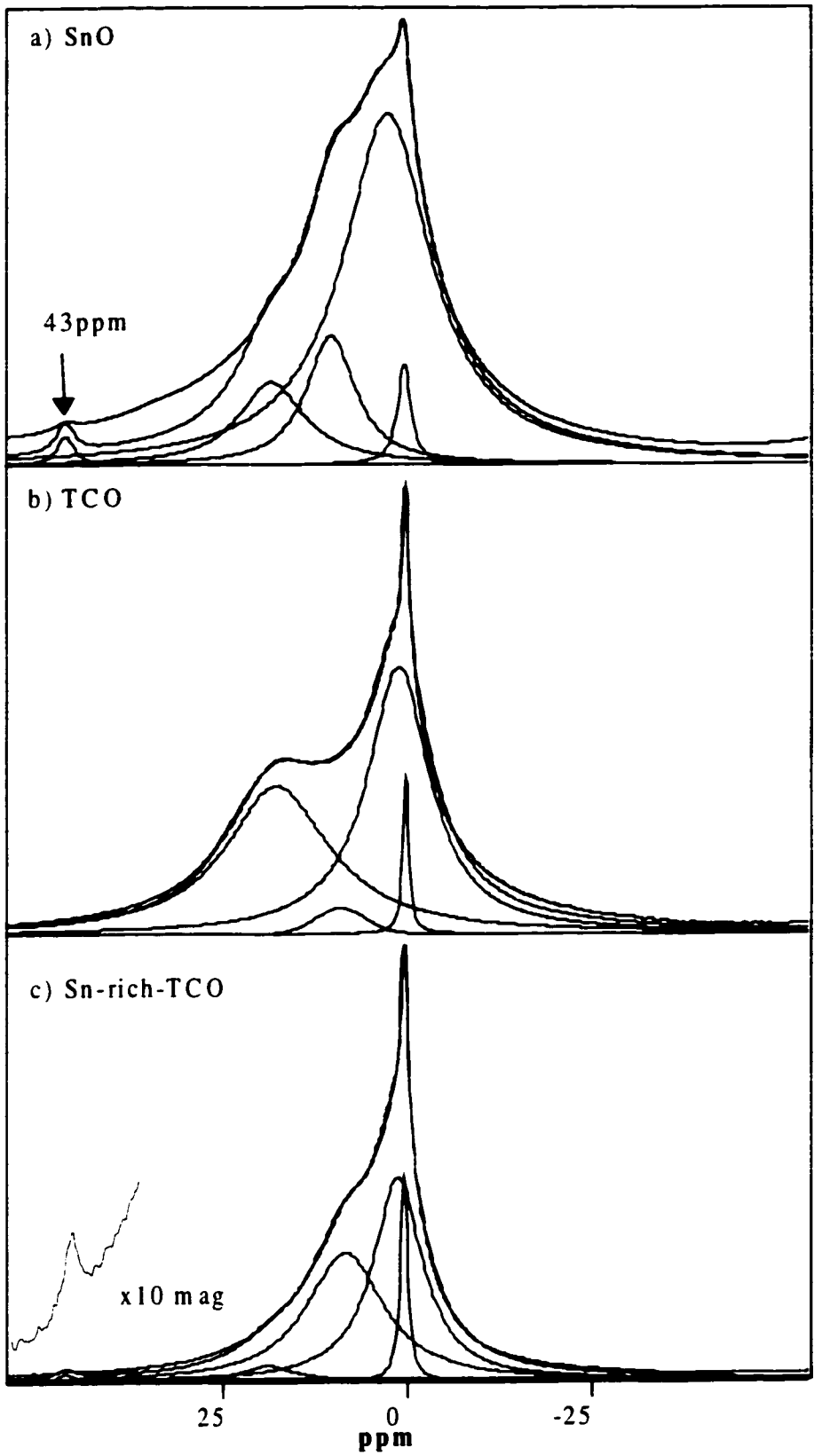

Figure 4.21 ^{7}Li NMR spectra for cycled electrodes a) SnO following 5 cycles, b) TCO following ten cycles and c) Sn-rich-TCO following ten cycles.

foremost, the TCO glass spectrum remains almost unchanged after 10 cycles. The spectrum can now be deconvoluted into 4 contributions, with the maximum shift at 16 ppm. This shift to higher frequency corresponds to an increasing Li-Sn contact, but it is a modest change from the original 12.6 ppm observed in the ^{6}Li spectrum on initial discharge. Contrasting results are seen in the case of SnO. While the shift never reaches a value of greater than 100 ppm, as expected for the most lithium rich alloy, the deconvolution of this lineshape reveals a complicated system with peaks ranging from 8-43 ppm. The parameters for the deconvolutions of these electrodes are given in **Table 4.5**. The spectrum of Sn-rich-TCO following 10 cycles shows an intermediate case, in which the small peak at 43 ppm is discernable, but weaker than that observed in SnO following only 5 cycles. The resonance at 43 ppm has been ascribed to Li-poor Li-Sn intermetallic compounds (*i.e.*, LiSn/Li_7Sn_3).[5] These peaks also appear upon long-term aging of the SnO samples: there is, however, no evidence of these new Li sites in TCO at deepest discharge even after 10 cycles. This indicates that deep cycling of SnO results in aggregation processes, and/or an oxygen-poorer Li-Sn environment that may limit the reversibility whereas this is not the case for TCO.

Cycled Electrodes	Peak Position/ppm	Peak Width/kHz	Integrated Intensity
SnO (5 cycles)	0.5	0.3	
	2.6	2.1	72%
	9.7	1.1	14%
	17	1.6	13%
	42.8	0.4	1%
TCO (10 cycles)	0.3	0.1	
	1.2	1.5	50%
	16.4	2.5	46%
	8.4	1.1	4%
Sn-rich-TCO (10 cycles)	0.5	0.2	
	1.3	1.2	49.2%
	7.9	1.8	46.0%
	17.5	1.3	4.2%
	42.8	0.4	0.6%

Table 4.5 Parameters for deconvolutions of ^{7}Li NMR spectra of cycled electrode materials, including peak position in ppm, linewidth in kHz, and integrated intensity (the SEI peak is omitted from the calculation of the integrated intensity).

4.5.5 *Discussion of TCO and related systems*

Absence of Knight Shifts - Implications for Particle Size and Surface Energy

Although no direct calculation of particle size is possible from lithium NMR data, the data clearly support our contention that various factors limit the size of the active centres within these materials. Two general observations from the ^{6,7}Li NMR data are significant. First, the absence of a large Knight shift is notable, as it indicates that lithium is not present in a metallic environment, such as an alloy. We and others[16] have documented the shift of $Li_{21}Sn_5$ to be on the order of 100 ppm. If the formation of bulk lithium-tin alloy particles occurs on deep discharge, this would be clearly visible in this region of the ^{6,7}Li NMR spectra. Also crucial is the study of the cycling behaviour of these electrodes, where the differences in the number and positions of discernable contributions to the Li NMR spectra demonstrate the reasons for the enhanced cyclability of the glass.

The majority of previous work in the area of Knight shift phenomena has focused on bulk metals, alloys or intermetallics, where the smallest particle sizes encountered were in the formation of micron-sized lithium metal particles within a LiF crystal;[20] there is also a set of unpublished data on alkali clusters.[21] In the materials studied here, the Sn particles formed on initial discharge to 750 mV (2Li) are only about 30 Å for TCO, and 200Å for SnO, based on X-ray linewidth broadening (see Chapter 6). The question arises whether the Knight shift mechanism is inhibited in particles of such small size. In the case of particles formed *in situ* within an oxide framework, there are two interdependent reasons for the observed shifts. First, if the surface/volume ratio of the particles is sufficiently large (*i.e.* the particles are very small) the proximity of electronegative oxygen in the matrix and large fraction of M-O bonds on the surface of the particle will polarize the electron density, leaving the lithium more electron-poor than it would be in an alloy particle embedded in a metal matrix. Second, the size of the Li-Sn nanophase may be small enough to prevent the free motion of conduction electrons that would be possible in a bulk metal, hence limiting the observable Knight shift. Inevitably these two factors are equally significant.

Initially, we observe the formation of a lithium oxide matrix in both materials. The ^{6}Li NMR spectrum of TCO at 750 mV is deconvoluted into 2 overlapping contributions. This arises from the various types of Li-O-X interactions possible in TCO glasses, as

opposed to the unique Li-O-Sn interaction present in SnO. Further discharge to an intermediate level of reduction reveals the presence of a Li-Sn interaction that is shifted to higher frequency as the lithium concentration increases. The oxide-rich matrix mediates the Li-Sn interaction, with the result that any otherwise observable Knight shift is inhibited. At the point of deepest discharge the Li-Sn interaction dominates the spectra in both cases and results in a shift to even higher frequency, with the SnO phase showing a higher shift than that of TCO. We suggest that this interaction represents a lithium-tin 'nanophase' with proximal oxide, in which the particle size is small enough to inhibit the free motion of conduction electrons. The issue of particle size is a difficult one, as we have no direct method of measuring the size of the domains. Since the observed shifts for Li-Sn in SnO exceed those of TCO at deepest discharge, it is likely that the nano-phases formed in the SnO electrodes are somewhat larger than those created in TCO. We believe that the ability to maintain smaller Li-Sn domains is a key feature in the cyclability of the TCO material.

Upon charging the cells to 500 mV the differences in the ^{6}Li NMR spectra give vital clues as to the origin of the enhanced cyclability of TCO. The immediate shift of the TCO peaks to low frequency after even a partial charge is indicative of the dissolution of the Li-Sn interaction, whereas the persistence of peaks at higher chemical shift in SnO demonstrates that these interactions are maintained to a greater extent. This suggests that in TCO, there is intimate contact between the oxide matrix and the Li-Sn nano-phases, which is only possible if the particles are in the cluster-size regime. These results also suggest that it is the ability of the TCO framework to readily undergo structural rearrangement that allows it to cycle more reversibly than SnO.

The structural adaptability proposed here is congruent with the observed ^{7}Li NMR behaviour on cycling, in which more substantial Li-Sn contacts at 43 ppm were observed in the SnO electrode after extended cycling. The latter is an important signature, as a similar peak was observed in a bulk synthetic LiSn/Li_7Sn_3 alloy mixture prepared at high temperature. This indicates the formation of Li-Sn domains is favoured in SnO, and may therefore lead to detrimental effects upon cycling. As well, the serendipitous aging of several SnO and SnO_2 electrodes also resulted in the appearance of this signature peak. The fact that it is not observed in the TCO spectra, even following 10 cycles of the cell is further evidence that the Li-Sn domains are limited in size in TCO, whereas these domains are able

to grow in SnO. This size-limiting mechanism appears to be the key to improved electrochemical properties.

Thermodynamic arguments predict that in bulk phases the reaction between lithium metal and tin oxide should result in the formation of lithium oxide and tin metal. Based on the Gibbs free energy of this reaction, it should be spontaneous in the forward direction, and hence irreversible unless equivalent energy is imparted to the system to drive the reaction in the reverse. This is indeed the case for bulk materials. We propose that the reactions occurring within the TCO glass are taking place in a size-limiting regime. Hence, the thermodynamics are strongly affected by the high surface energy of the particles, namely by the surface reactions that occur spontaneously between lithium, tin and oxygen. The reaction between lithium and tin, which is stoichiometrically controlled from a macroscopic perspective with a maximum lithium content corresponding to the most lithium-rich Li-Sn line phase, is also much more complex on a microscopic level. The model we propose is that the tin clusters formed on reduction of the cell are in close proximity with both lithium and oxygen as a result of these particles having a very high surface area: volume ratio. As the concentration of lithium in the electrode increases, the lithium-tin interaction will necessarily increase, but this makes no requirement for the interaction to be that of a true lithium-tin compound phase. In fact, the kinetics of the system inevitably limit the formation of microcrystalline phases at ambient temperature, even in tin oxide itself. As well, the surface energy of these particles allows the "back-reaction" of lithium with oxygen to be reversible at a lower potential than predicted from simple considerations that exclude surface energy contributions. The proximity and availability of oxygen in the host matrix is surmised to enhance the reversibility and cyclability of the cell. Availability of matrix bound oxygen will be determined by the surface energy of the electrochemically active particles, hence the smaller the aggregates, the more reactive they will be.

4.5.6 Spectator Ions: ^{27}Al Data

All of the 'spectator ions' are NMR active nuclei, allowing for the thorough investigation of their participation in the electrochemical process *via* the observation of the changes in their local environments upon charge/discharge of the electrodes. The use of solid-state NMR as a tool for elucidation of both short and intermediate range order in glasses is very well known. This topic is too large to be developed in this thesis, but

references to several relevant papers are given here.[22,23] The TCO glass itself is quite complex, including several Group III and V elements, which act as network formers (Al, B, and P). Elements from group I and II are known to act as network modifiers, hence the addition of lithium to the glass will not only result in reduction of the tin centers, but will also significantly affect the structure of the glass. In other glass networks, the presence of network modifiers causes the depolymerization of the network by creating non-bridging oxygen species. While this effect is usually observed in glasses that included Group I or II elements in the glass formation, it is reasonable to expect that a similar depolymerization process is at work during lithium insertion, thereby affecting all the glass constituents equivalently. Even from this small amount of information concerning glass behaviour, it is evident that the glass network will have a much more complex role during lithium insertion than that of a simple oxide. Whether the network is only passively affected by the inserted lithium ions and corresponding electrons, or whether it acts, to aid in the reversible reaction of lithium with the TCO glass, is yet to be determined.

Figure 4.22 shows the ^{27}Al NMR spectra collected for the glass at the various potentials. It is clear from these data that the Al coordination changes throughout the charge and discharge processes. The pristine glass itself shows two types of Al sites, namely octahedral (centered at 0 ppm) and five-coordinate (centered at 50 ppm). The signal/noise ratio in this spectrum is much better than the subsequent spectra collected on discharge/charge, since the amount of active material is greater in the case of the pristine material by more than an order of magnitude. Nevertheless, on discharge the changes in the coordination environment at aluminum centres are evident from the variations of the peak positions. The peaks are never clearly resolved, owing to the glassy nature of the active material, but at 750 mV a departure from octahedrally coordinated Al clearly occurs, in favour of tetrahedrally coordinated Al (centered at 80 ppm). This trend continues throughout the discharge sweep, and is subsequently is reversed on charge, indicating a flexible aluminum oxide environment. The sharpness of the regenerated peak at 0 ppm (500 mV on charge) indicates the presence of some moderately crystalline or well-ordered regions. Further charging to 1.5 V shows that this crystallization is limited, and the reappearance of the five coordinate Al indicates a regeneration of the original glass.

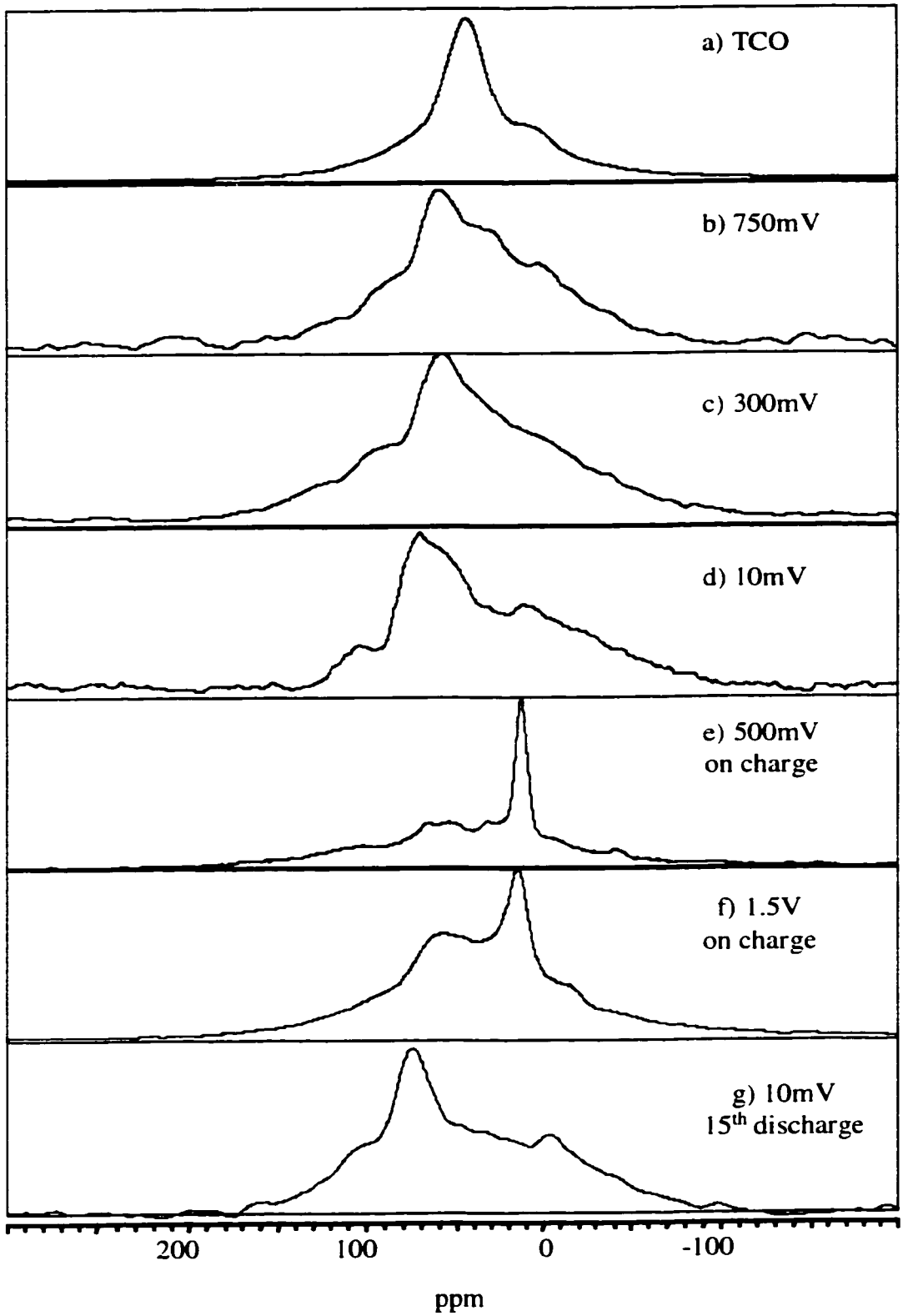

Figure 4.22 ^{27}Al NMR spectra for a) pristine TCO, and TCO electrodes at b) 750mV, c) 300mV, d) 10mV on discharge, e) 500mV, f) 1.5V on charge, and g) 10mV on 15th discharge.

Following 15 cycles of the battery, the Al environment in the glass at the bottom of discharge remains similar to that observed on the first cycle. Therefore up to 15 cycles, crystallization of Al species on charge seems reversible on subsequent discharge. It is unlikely that this process is highly reversible, but time constraints prevented further investigation. The ^{27}Al spectrum of pristine Sn-rich-TCO shows the same two features as TCO itself, corresponding to octahedral and five-coordinate Al, and upon discharge to 10 mV, again the spectrum is similar to that found for TCO.

4.5.7 Spectator Ions: ^{31}P Data

Figure 4.25 shows the ^{31}P NMR spectra collected for the glass at the same points in the TCO electrochemical cycle as those chosen for ^{27}Al. The pristine glass begins with a single broad ^{31}P NMR signal, centered at −16ppm. This shift correlates to observed signals for crystalline aluminum, boron, and tin phosphates.[24] The broadness arises due to the amorphous nature of this sample. On discharge to only 750 mV, the ^{31}P spectrum is extremely broad, and is barely observable at 12 ppm. This large shift away from the original position demonstrates the structural changes occurring in the glass at this potential. Upon further discharge the peak position is maintained, and the peak narrows and intensifies until full discharge is achieved. The chemical shift value matches that observed for crystalline lithium phosphates.[24] During the charge cycle a new resonance appears at −12 ppm. This sharp peak which increases in intensity upon further charging to 1.5 V, represents the formation of a crystalline phosphate regions during the oxidation process. At the bottom of discharge following the 15th cycle of the cell, the ^{31}P spectrum contains only a single peak at +16 ppm, with no evidence of the crystalline component. Both the ^{27}Al and ^{31}P NMR results indicate the formation of some crystalline domains within the electrodes upon charge. This crystallite formation appears to be reversible during the first 15 cycles, but would likely become irreversible upon extended cycling.

4.5.8 Spectator Ions: ^{11}B Data

Figure 4.26 shows the corresponding ^{11}B NMR spectra of the TCO glass. The pristine glass spectrum contains sharp features, including contributions from both relatively crystalline B, likely in a tetrahedral environment (sharp lineshape), as well as trigonally

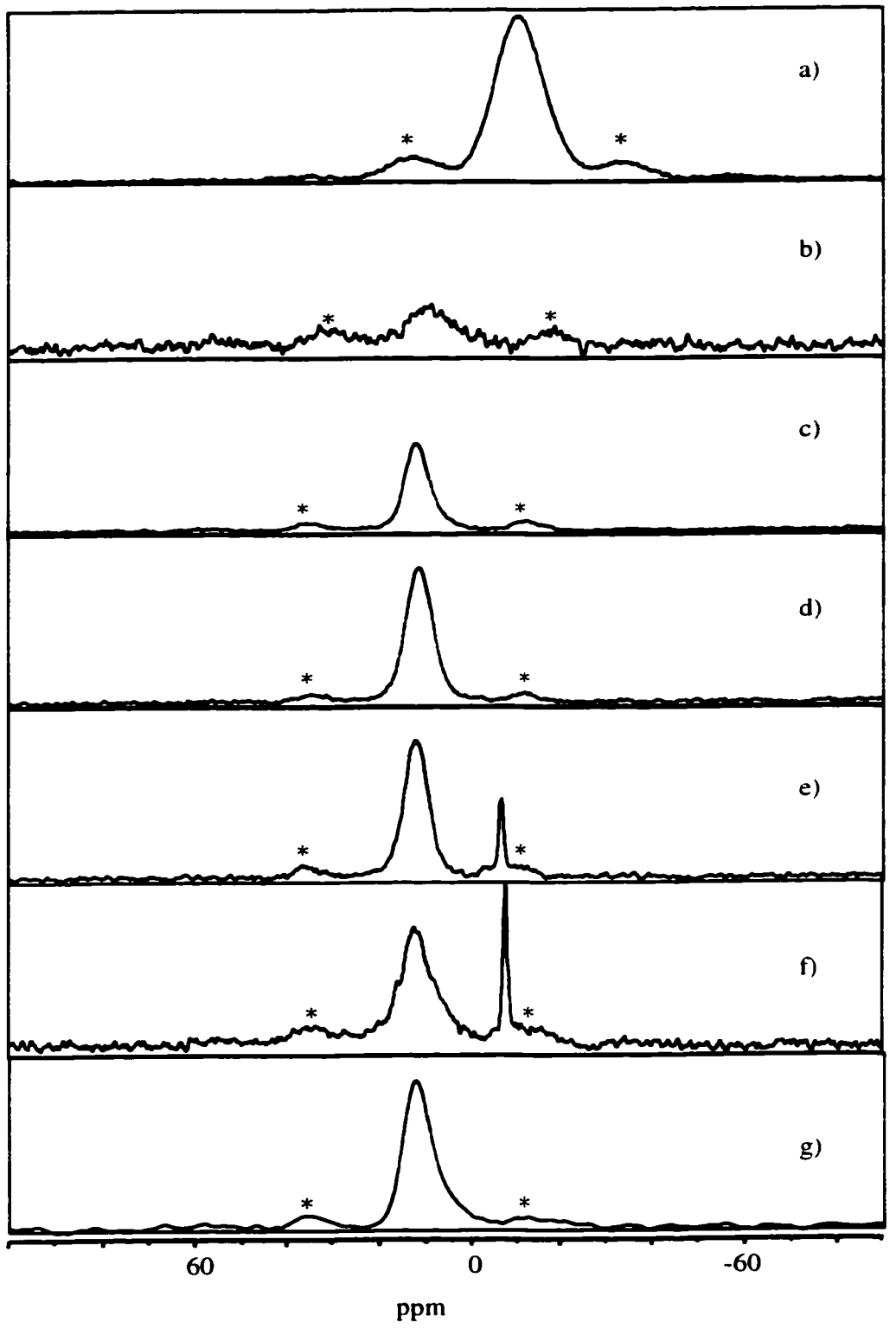

Figure 4.23 ^{31}P NMR spectra of a) pristine TCO and TCO electrodes at b) 750mV, c) 300mV, d) 10mV on discharge, e) 500mV , f) 1.5V on charge, and g) 10mV on 15th cycle. Spinning side bands marked by (*)

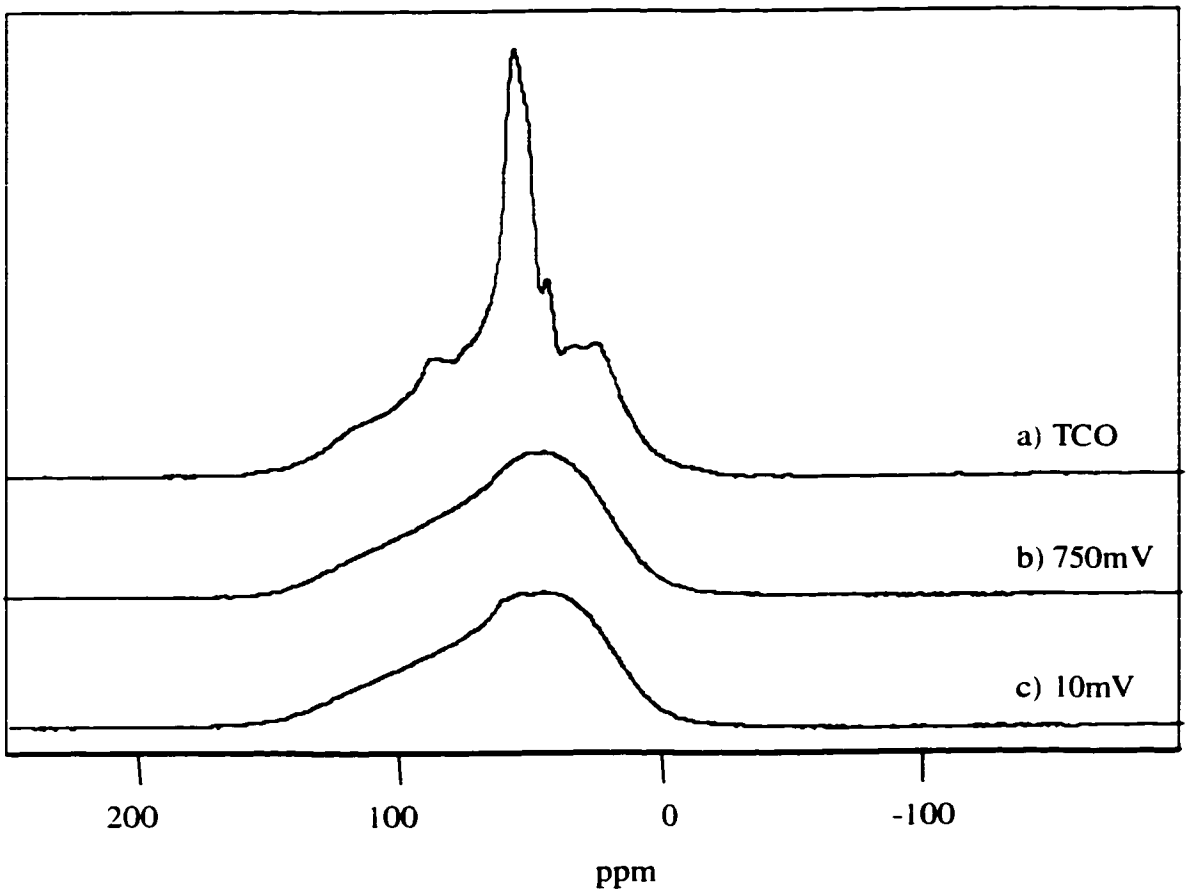

Figure 4.24 ^{11}B NMR spectra for a) pristine TCO, and TCO electrodes at b) 750mV, and c) 10mV on discharge.

coordinated B (broad lineshape).[23] These sharp features disappear upon discharge to 750 mV, leaving only a broad peak centered at 0 ppm. The ^{11}B spectra acquired upon further cycling do not change from that observed at 750 mV and are characterized by broad featureless lineshapes.

4.5.9 Discussion : Role of Spectator Ions

Evidence for the role of the components of the oxide matrix in these materials is provided by the solid-state NMR studies performed on the 'spectator ions'. Our results from ^{31}P and ^{11}B NMR strongly suggest that lithium inserts not only into Sn-O-Sn bonds, but also into Sn-O-X bonds, and X-O-X bonds, where X is Al, B, or P in the composite glasses. The ^{31}P NMR spectrum, which displays a well-resolved peak for the pristine glass, is transformed into a very broad signal at 750 mV (equivalent to insertion of 2 Li), indicative of dramatic structural changes in the phosphate environments. If, on discharge, signal intensity at the original position had been maintained along with the appearance of a peak at +12 ppm (Li_3PO_4), this would have been evidence for preferential reaction of lithium with the Sn-O-P bonds in the glass which leaves the X-O-P bonds intact. The results, however, indicate that even partial lithium insertion causes an all-encompassing rearrangement of the glass. Our interpretation is corroborated by the changes in the ^{11}B NMR spectra. In the pristine glass there are two distinct boron environments, whereas in the 750 mV-electrode material the sharp tetrahedral site has disappeared, leaving only a broad, featureless lineshape corresponding to trigonally coordinated boron. Again, the NMR spectra reveal the drastic structural rearrangements that occur in the glass during the insertion of the first 2-3 moles of Li. We note that other recent IR studies of Li insertion into SnO-P_2O_5-B_2O_3 glasses have provided a similar conclusion.[25] Our interpretations are strongly supported by the CPR measurements (detailed in Chapter 3); particularly in the first portion of the CPR curve for each material. A single process occurs in the case of SnO; nonetheless the TCO curves undergo two distinct processes during the insertion of the first 2-3 equivalents of Li. To explain this observation we can consider the types of bonds that are broken and reformed in each case. For SnO, Li can only insert into the Sn-O-Sn bond, whereas the TCO network comprises both Sn-O-X as well as X-O-X interactions, where X = Al, B or P. It is questionable as to whether the lithium should be expected to insert into an X-O type bond,

but both our CPR data and several of the NMR spectra of the 'spectator ions' point to this conclusion. The CPR results for TCO indicate that the insertion process up to the first 2-3 Li is much more kinetically inhibited than the equivalent process in SnO. If the lithium were selectively inserted into Sn-O bonds in both cases, the kinetics of the reaction would be expected to be equivalent. On this basis, it seems likely that the lithium is not selective, but reacts as well with the other bonds present. The fact that these oxides themselves are electrochemically inert suggests that the reason for the slow kinetics is the initial step as the glass is rearranged.

The ^{27}Al NMR results similarly demonstrate the flexibility of the oxide framework. Changes in the coordination environment from predominantly five-coordinate in the pristine glass, toward tetrahedral upon discharge, and then back toward octahedral upon charge are clearly evident. The adaptability of the multi-component framework may allow for the facile movement of oxygen within the structure, and thus expediate the reaction of the lithium with tin in the TCO glass and accommodate the reversibility of this process.

4.5.10 ^{119}Sn Data for Pristine Materials

The ^{119}Sn NMR data for SnO SnO_2 and TCO is shown in **Figure 4.25**. The broad signal of the TCO glass spans from +100 ppm to –1000 ppm. The sideband manifold of SnO_2 covers from –600 to –800 ppm while the spectrum of SnO spans a much larger chemical shift range from +150 ppm to –850 ppm. The TCO spectrum being intermediate between these two oxide signals is proposed to contain both Sn^{2+} and Sn^{4+} rather than uniquely Sn^{2+} as reported by Fuji. This interpretation is corroborated by our Auger-XPS data obtained for TCO. By this surface sensitive technique the oxidation state of tin was exclusively Sn^{4+}. Nevertheless the discharge capacity of TCO on the first cycle is 1000 mAh/g which agrees very well with the electrochemical performance described in the publication by Idota *et al.*[15]

As the tin atoms are the electrochemically relevant species in the TCO glasses, hence it would be valuable to obtain information on the changing environments at these nuclei during the electrochemical process. Unfortunately the ^{119}Sn NMR studies proved relatively difficult, even for the pristine TCO samples. Therefore other complementary techniques

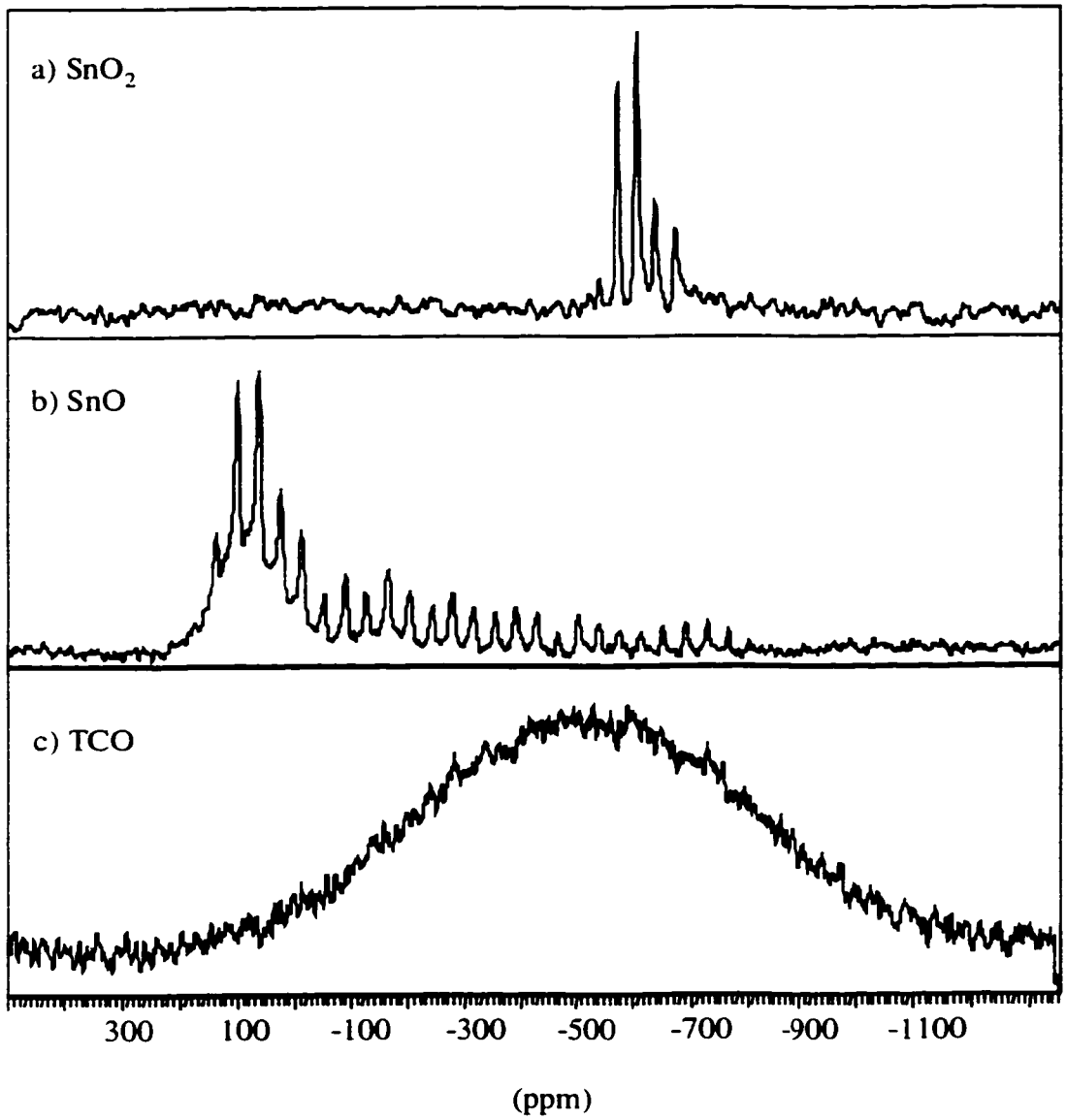

Figure 4.25 ^{119}Sn NMR spectra of a) SnO_2, b) SnO, and c) TCO glass.

were chosen which could probe the Sn centers more effectively. The data from X-ray scattering and absorption studies are presented in the following chapters.

4.5.11 ^{6,7}Li NMR Studies of Tin Metal Electrodes

The lack of "true" Knight shifts in the ^{6,7}Li NMR spectra of the TCO and SnO electrodes prompted an investigation of the behaviour of tin metal itself. The electrochemistry of Sn metal has been well documented, as described in Chapter 3. Particularly at elevated temperature, the voltage profile follows the expected plateaux and compositions corresponding to the formation of the series of Li-Sn linephases. Since our electrochemical system accommodates only ambient temperature analysis, tin metal electrodes were prepared in a similar fashion to the other test materials described, and the corresponding NMR spectra were collected. The ^{6}Li NMR data are presented in **Figure 4.26**. Samples were obtained at 5 different levels of discharge, corresponding to voltage cutoffs of 1.2 V, 700 mV, 500 mV, 300 mV, and 10 mV respectively. Several things are surprising about this data set. First of all, the relative intensities of the spectra differ widely, although the sample size in each case was comparable. The center spectrum, collected for a sample at 500 mV on discharge, was acquired over a period of 4 hours, and includes more than 14500 scans. In contrast, the other four spectra all include approximately 4000 scans. Yet, the 500 mV spectrum has the least relative intensity. Secondly, the observed trends in the frequency and number of resonances is surprisingly unlike the expected trends. The spectra at 1200 mV and 700 mV are basically identical, having a single narrow resonance at 0ppm. Examining the cyclic voltammogram for Sn metal (**Figure 3.9a**), it is clear that these resonances correspond to a very small amount of inserted lithium, likely arising from the formation of the SEI layer, and subsequent reaction of lithium with oxide on the surface of the particles. These voltage cutoffs correspond to the insertion of 0.3 and 0.5Li respectively. Beyond this at 500 mV the ^{6}Li NMR spectrum shows 6 resonances; three of which are shifted to high frequency, at 77, 42, and 30 ppm respectively. This voltage cutoff corresponds to the insertion of 1.5 lithium. The presence of several relatively sharp resonances indicates the presence of more than one Li:Sn environment; possibly within one crystallographic phase, but more likely representing the presence of more than one Li:Sn

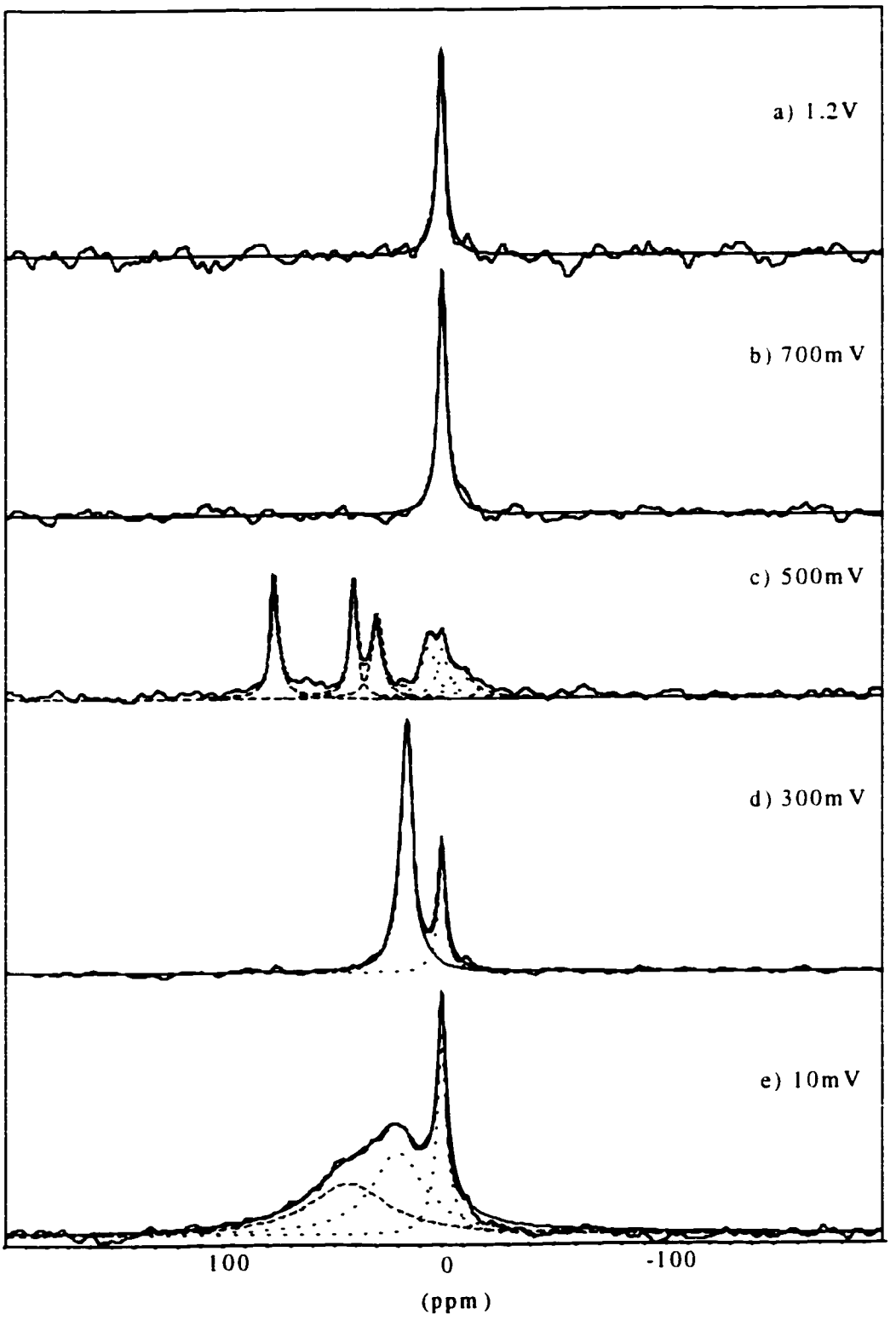

Figure 4.26 ^{6}Li NMR spectra of Sn-metal electrodes at a) 1.2V, b) 700mV, c) 500mV, d) 300mV, and e) 10mV on discharge.

phase at this point. Surprisingly, going to deeper discharge does not lead to a greater shift to higher frequency. On the contrary, the peaks observed for the 300 mV (2.7Li) sample occur at 16 ppm and 0 ppm. These peaks are also relatively narrow, with the 16ppm peak having a linewidth of 0.5 kHz. At the bottom of discharge, corresponding to the insertion of 4.4Li, the lineshape has broadened significantly, and now includes three contributing features. The peak at 0 ppm remains narrow, while two new features at 20 ppm and 43 ppm have linewidths of 2.2 and 3.3 kHz respectively.

Most importantly these spectra are significantly different from both the spectra obtained for the bulk $Li_{21}Sn_5$ phase and from the spectra obtained for the oxide electrodes, but show some similarities to the intermediate lithium content Li_7Sn_3 phase. Secondly, well ordered phases are created at low levels of lithium content, but increasing the lithium concentration appears to disrupt the formation of these phases, as observed through the broadening of the ^{6}Li NMR lineshapes. A similar result was found in the powder X-ray diffraction study by Courtney *et al.*, where clearly resolved reflections were obtained for lithium concentration up to the 1:1 Li-Sn linephase.[26] Beyond this point, the subsequent phases were assumed to form, but were not identifiable on the basis of their diffraction patterns. Rather, the reflections broadened and overlapped such that no peaks were resolved.

At deep discharge, to 10mV, the ^{6}Li NMR spectrum of the Sn-metal electrode exhibits broad features at shifts as high as 60ppm. This differs dramatically from the spectra obtained for both the TCO glasses and SnO itself at deep discharge. In all of these cases, the chemical shift range was limited to less than 10ppm. This discrepancy indicates that the distribution of charge in the oxide materials is such that the lithium remains in an ionic environment throughout the discharge process. In contrast, the lithium inserted into the tin metal electrodes is in a more metallic environment, consistent with the observed Knight shift in the ^{6}Li NMR spectrum. Thus, we conclude that the mechanism of interaction of lithium with tin in the oxide materials is different from the interactions which occur in a metallic host. This conclusion differs from other investigations which have concluded that the two mechanisms are indistinguishable by Mossbauer spectroscopy.[27]

These data clearly indicate that discretion must be used when interpreting results. The assumption that the electrochemical reaction that occurs in an electrode at ambient temperature is the same as that predicted by the Li-Sn phase diagram, or even that it matches

the expected voltage profile originally documented for Li-Sn at high temperature, is incorrect. The complexities observed in this series of ^{6}Li NMR spectra point to a reaction that is strongly affected by kinetics, and that becomes increasingly difficult as the amount of lithium inserted increases. Again, this echoes the results discussed by Dahn *et al.* in a paper in which the diffraction pattern of a disordered $Li_{4.4}Sn$ phases is substantially different than that of the crystalline phase.[28]

The results obtained for the Sn electrodes are also quite distinct from those obtained for the tin-oxide based systems. This re-enforces the conclusion that the oxide framework, and moreover, the complex TCO framework provide essential support to the reversible reaction of the electrochemically active tin particles.

4.5.12 Relaxation Studies

Definite evidence for a Knight shift mechanism in the NMR resonance can be obtained through measurement of the relaxation properties of the given resonance. According to the Korringa relationship, the product of the spin-lattice relaxation time (T_1) and the temperature (T) must be a constant for a system in which relaxation is occurring through a conduction- electron mechanism. To test the relaxation behaviour of various electrodes inversion-recovery experiments were carried out according to the pulse sequence described in section 4.4

It is important to start this section by acknowledging the difficulties presented by this data. It was shown in the previous section that the broad lineshape in the ^{7}Li NMR spectra of both the SnO and TCO electrode materials at deep discharge are in fact composed of at least two contributing features, one corresponding to the Li_2O matrix, and the second overlapping signal corresponding to the Li-Sn interaction. However these signals are indistinguishable within the temperature range of our inversion-recovery experiments. This is unfortunate, as it is inevitable that the relaxation behaviours would be quite different for an ionic matrix as compared to an alloy-like particle. But due to the limited chemical shift range of the lithium spectra, the relaxation times cannot be measured independently. Nevertheless, valuable data can be gleaned from a comparison of the relaxation times of the discernable SEI signal and the broad composite lineshape of the electrochemically relevant species.

Relaxation data for various electrodes of TCO, Sn-rich TCO, SnO, and SnO_2 are recorded in **Table 4.6**. The relaxation times at room temperature for both the electrochemically active composite lineshape (broad), as well as the inactive SEI resonance signal (narrow) are indicated, as well as the slope of the T_1*T vs T curve for the broad lineshape of each sample over the temperature range 300-360K. **Figure 4.27** shows the 1D spectra obtained from an inversion-recovery experiment for TCO at 10mV. This data is presented to demonstrate the overlap between the various components of the broad lineshape. In the accessible temperature range the experiments, the components did not exhibit different relaxation rates.

Several trends can be discerned. Comparing the T_1 values of lithium metal (137 ms) and lithium oxide (3600 s), it is clear that the relaxation mechanisms within the metal are much more efficient than in the crystalline oxide. This is attributed to the role of conduction electrons, which induce relaxation in the ^7Li nuclei of the metal. In the case of the oxide the dominant relaxation route is the quadrupolar mechanism, but due to the high local symmetry of the lithium oxide, the relaxation time is relatively long. These two reference compounds are used as end points in the study of the relaxation behaviour of the electrodes. The relaxation times of all materials are the shortest for electrodes in the fully discharged state (10 mV). Following this trend, the relaxation times of both the TCO and Sn-rich TCO samples decrease continuously from early in the discharge process (750 mV), reaching a minimum at 10 mV, and then increase again upon charge. This trend is observed in all systems studied. As well, the relaxation time of the SEI lineshape is consistently longer than that of the electrochemically active components, with only two exceptions. This trend indicates that relaxation effects caused by either unpaired, or conduction electrons in the system are predominant in the electrochemically active species. Surprisingly though, the T_1 of the SEI, which is composed of lithium carbonate and other ionic decomposition products, is strongly influenced by the relaxation mechanisms in the electrochemically active components. This demonstrates that the SEI is in close proximity with the other components of the electrodes, consistent with a high surface area composite.

Sample	T_1/ms (Broad Line)	T_1(ms) (Narrow Line)	Slope of T_1*T (Broad Line)
Lithium metal	137 (one line only)		-0.019
Lithium Oxide	3600 (one line only)		-6.370
SnO – 350mV	1200	2500	-2.766
10mV	440	582	-0.866
SnO_2 – 350mV	858	1560	-1.528
10mV	221	312	-0.206
TCO – 750mV	1280 (one line only)		-1.099
300mV	869	1090	-0.999
10mV	405	563	-0.772
500mV	727	739	+0.859
1.5V	863 (one line only)		-0.799
10mV	448	710	-0.325
Sn-rich TCO – 750mV	1030	606	-1.094
300mV	758	905	-1.506
10mV	210	298	-0.200
500mV	722	725	+1.245
1.5V	1360	895	+4.277

Table 4.6 T_1 relaxation times for various electrode samples at ambient temperature

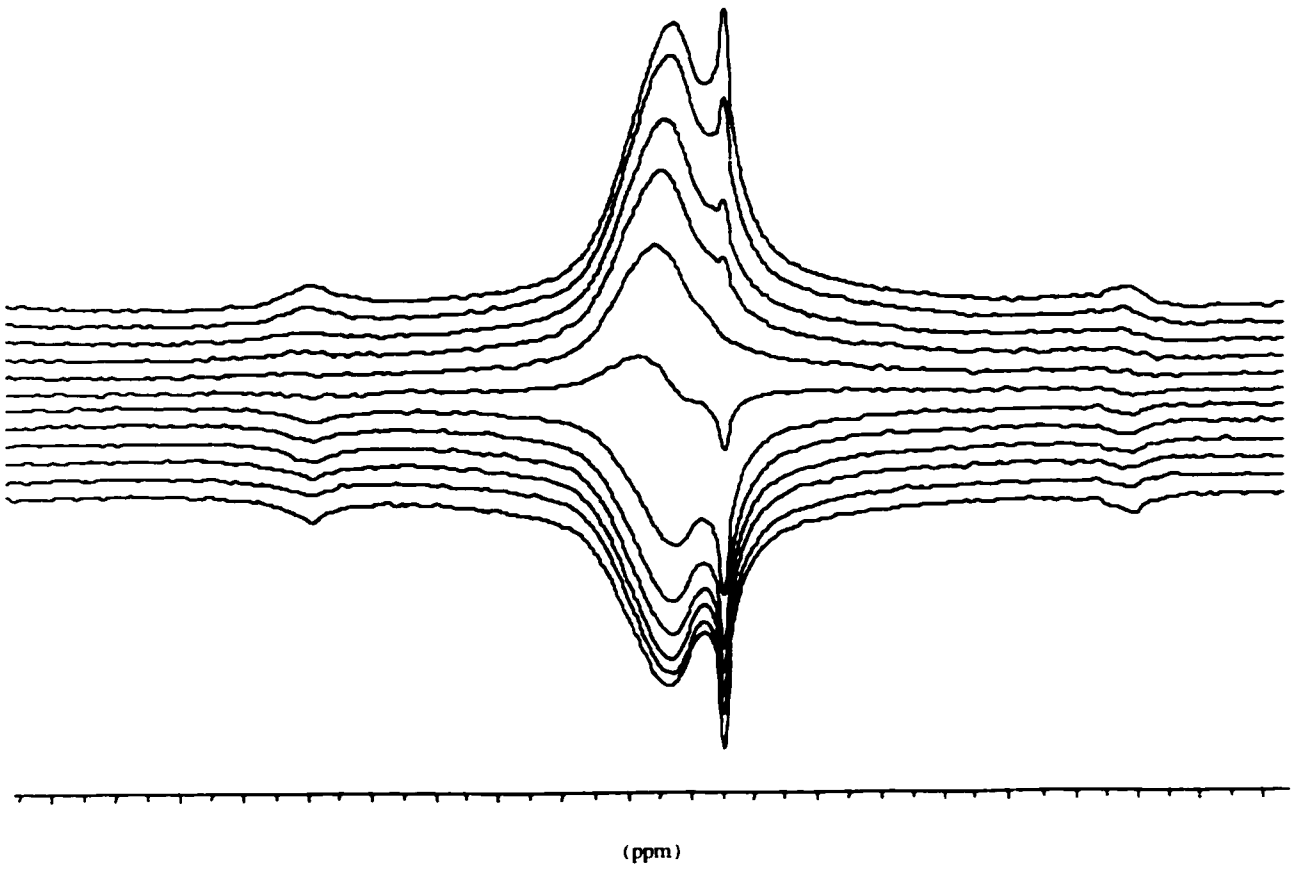

Figure 4.27 Spectra from an inversion-recovery experiment for a TCO electrode at 10mV, at ambient temperature. Spectra recorded for each increment of the delay time τ, where the completely inverted spectra represents the shortest τ.

The relaxation of the narrow peak is distinguished from the relaxation of the broad peak, but features within the broad peak are obscured.

Plotting $\ln(T_1)$ versus 1000/T gives the "T_1 curve" for each electrode. Selected data for TCO and Sn-rich TCO are presented in **Figure 4.28**. Since the T_1 behaviour for electrodes in early discharge, or late charge are comparatively uninformative, due to the poorer spectral resolution at these points, only the data for the 10mV electrodes are presented. Similar T_1 curves were recorded for both SnO and SnO_2. **Figure 4.29** plots T_1*T versus temperature for the broad lineshape of all 10mV electrodes, as well as that of lithium metal. True Korringa behaviour is demonstrated by a relaxation time which is independent of temperature, giving a T_1*T curve with a slope of 0, as in the case of lithium metal. In all cases, the narrow peaks exhibit non-Korringa relaxation, characteristic of temperature dependent relaxation of ionic lithium. The T_1*T curves of the broad lineshapes all have non-zero slopes, but as with the absolute T_1 values, the trend upon discharge is similar among the materials studies; the slope tends toward zero with increasing levels of discharge. Also significant is a comparison of the T_1*T slope for TCO at deepest discharge after the first cycle (-0.771) and after the second cycle (-0.325). This indicates that the electrochemically active material is closer to Korringa behaviour on subsequent cycles.

These data show that the composites formed within the electrode during discharge become more and more influenced by the presence of conduction electrons upon increasing insertion of lithium. While the observed 1D ^{6,7}Li NMR spectra clearly showed that the electrochemically active species are not agglomerating to a size of particle where a Knight shift of large magnitude can be observed, the T_1 data strongly demonstrate that the relaxation behaviour tends toward conduction electron mechanisms upon deep discharge.

4.6 Discussion of NMR data and Electrochemistry

Since the charge distribution in these electrodes does not involve the participation of metallic lithium, as is indicated by the NMR results, but yet the amount of lithium (and corresponding electrons) inserted into the electrode indicates a deep level of reduction, the question arises; *where are the electrons going?* One option is that the electronic charge is distributed in the fashion of a Zintl phase, such as those described in Chapter 2, where the tin carries a negative charge, and lithium a positive charge. Nevertheless, it was clear from the ^{7}Li NMR studies of the bulk lithium tin phases that the magnitude of the Knight shift

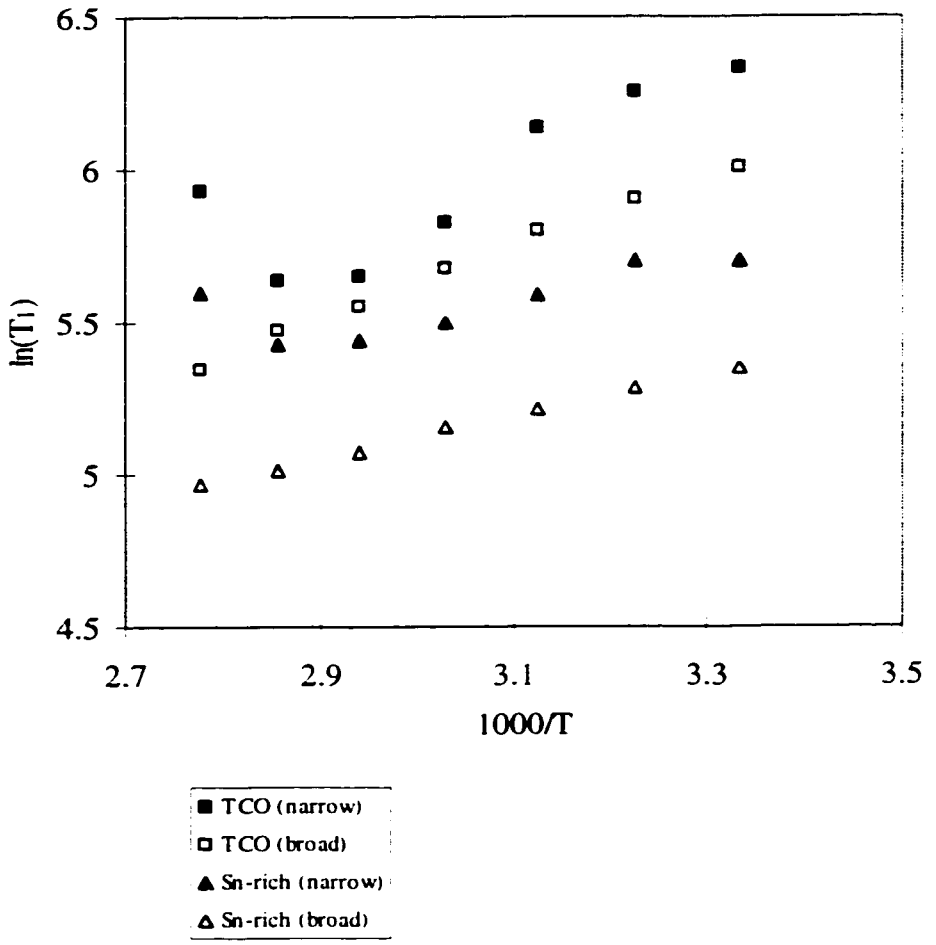

Figure 4.28 T_1 curves for TCO and Sn-rich TCO at 10mV, including both the narrow lineshape, corresponding to the SEI, and the broad lineshape, which includes the electrochemically active lithium.

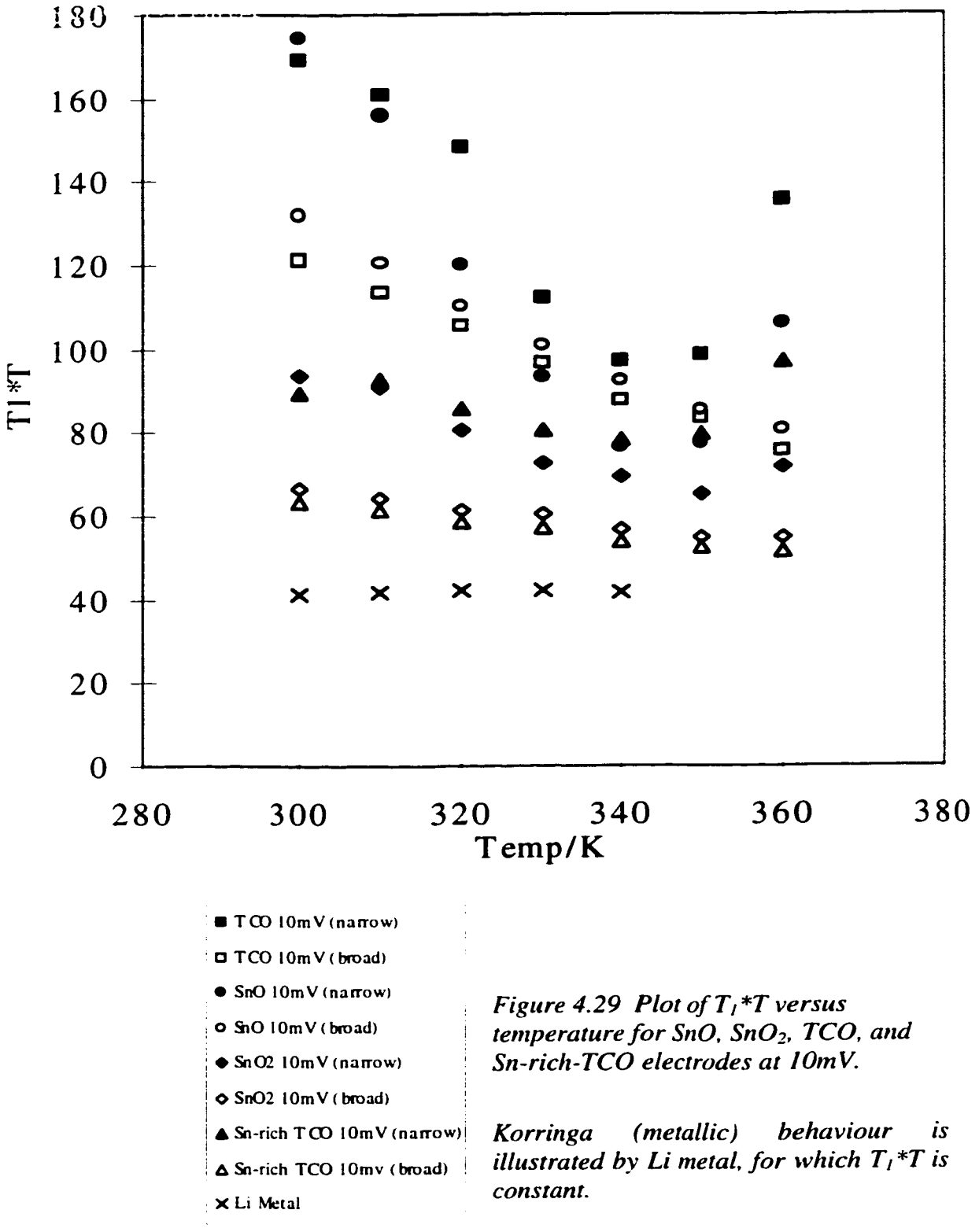

*Figure 4.29 Plot of T_1*T versus temperature for SnO, SnO_2, TCO, and Sn-rich-TCO electrodes at 10mV.*

*Korringa (metallic) behaviour is illustrated by Li metal, for which T_1*T is constant.*

was much larger than that observed for any of the electrode materials. It is tempting to appeal to the participation of oxygen as an electron acceptor, but this at first seems to be preposterous and without precedent. It is useful at this point to consider the theoretical work of Ceder *et al.* [29] While this work addressed cathode materials, specifically aluminum doped lithium cobalt oxides, we project that a similar principle may be at work in the anode materials discussed here.

The publication by Ceder *et al.* reported on their findings concerning the substitution of non-transition metals (eg. Al) for transition metals (eg Co) in the host structure of a cathode material. The resulting compounds were predicted to have higher cell voltages, while also offering reduced specific capacity due to the reduced relative mass of aluminum compared to cobalt. More interesting to us were their calculations of the electron density distribution within such a material. **Figure 4.30** shows an image, scanned from their original paper, which illustrates the positive part of the electron density difference between the two compounds, $Li(Al_{0.33}Co_{0.67})O_2$ and $(Al_{0.33}Co_{0.67})O_2$ (ie before and after deintercalation of one lithium from the structure). The slice shown is in the plane perpendicular to the layering of the structure. The gray gradient indicates the concentration of electron density, with darker regions corresponding to higher concentrations of electron density. Clearly, the oxygen atoms in this structure carry a large portion of the charge in the lithiated structure, as does the cobalt. The increased electron density following delithiation of structure is consistent with the change in oxidation state from Co^{4+} to Co^{3+}, but the increase in charge on the oxygen atoms would not be predicted by traditional thinking of electrochemists.

On the basis of their calculations and our observations, we believe it is a logical hypothesis that the oxygen associated with lithium in the electrodes is able to carry charge density. This hypothesis is consistent with the enhanced capacity of the TCO electrodes and the high capacity of the $AMoO_3$ material, discussed subsequently in Chapter 8. As well limited ^{6,7}Li-NMR chemical shift range observed for all electrode materials (indicative of ionicity or low charge density on lithium), and the known non-existence of Li-Mo alloys beg the question of how the electron density is being distributed in these systems. To account for all of these observations, the participation of oxygen in the electrochemical process is the most probable conclusion.

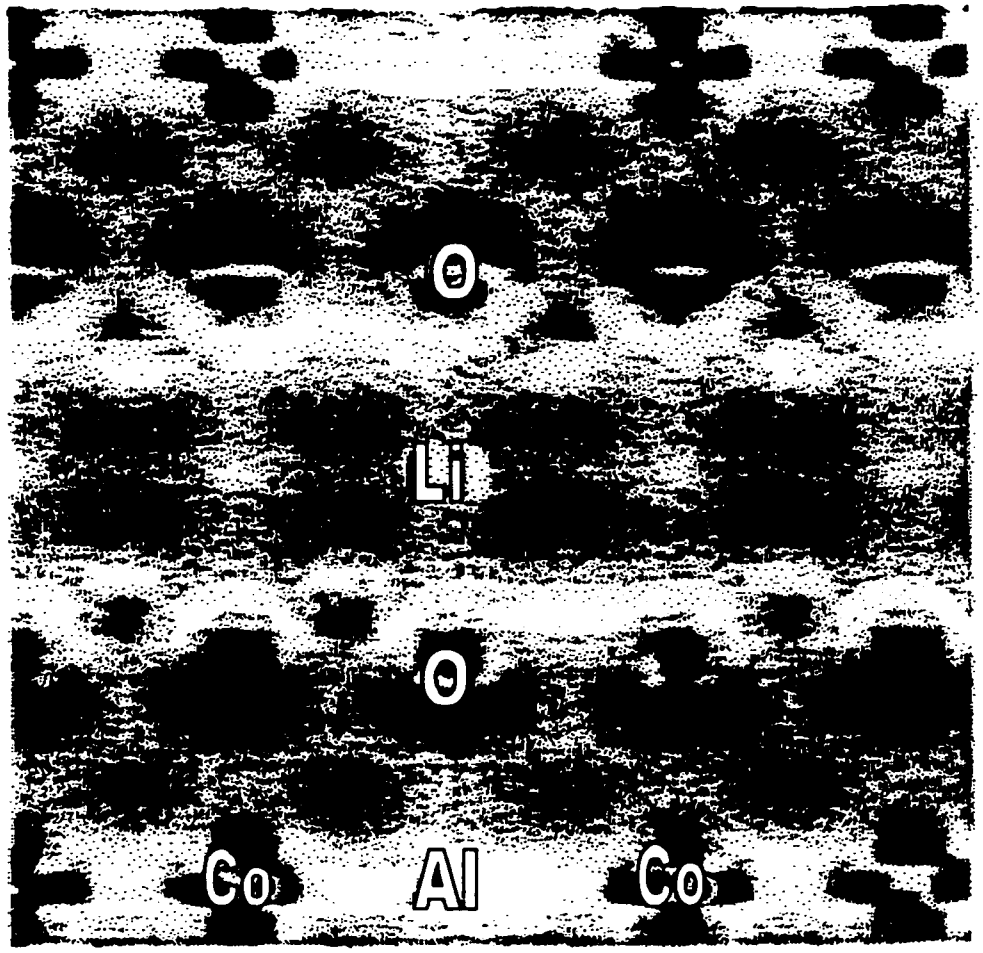

Figure 4.30 Electron density map showing excess electron density on oxygen atoms:

Positive part of the electron density difference between lithiated $Li(Al_{0.33}Co_{0.67})O_2$ and delithiated $(Al_{0.33}Co_{0.67})O_2$ in the plane perpendicular to the direction of the layering in the structure. Darker indicates larger electron density.[29]

This hypothesis will be further expounded in the results obtained by XAS and PDF data analysis presented in Chapters 6.

Returning to the analogy of the *fugue*, the various results obtained by the multi-nuclear NMR studies voice the subjects and counter subjects of the thesis. Addressing the subject of electrochemical properties, the ^{6,7}Li NMR data voice the contrasting behaviour of TCO compared to SnO through the differences in chemical shifts both for initial and cycled electrodes. The countersubject concerning the role of the spectator ions, is voiced in the aluminum, phosphorous, and boron NMR data, which illustrate the substantial changes occurring at these centers throughout the electrochemical processes. More subtly, the countersubject of the role of oxygen is heard only as an echo of the NMR data, implying a significant participation for these centers, but without empirical evidence. Finally the countersubject of particle size is eluded to by the modest magnitude of the lithium chemical shifts. All of these voices heard in the NMR data come together to demonstrate the differences between SnO and the tin composite oxide glasses.

4.7 References

[1] R.K. Harris Nuclear Magnetic Resonance Spectroscopy a Physiochemical View John Wiley and Sons, New York, 1985. Chapter 3 pg 75

[2] see *ibid* Harris, (1985) pg 249.

[3] see *ibid* Harris, (1985) pg 81.

[4] see *ibid* Harris, (1985) pg 85.

[5] C.P. Slichter, Principles of Magnetic Resonance. p.113-126 Springer-Verlag Berlin 1990.

[6] M. Carewska, S. Scaccia, F. Croce, S. Arumugam, Y. Wang, S. Greenbaum. *Solid State Ionics* **93** 227 (1997).

[7] A. Saadoune M. Menetrier and C. Delmas, *Journal of Materials Chemistry* **7** 2505 (1997).

[8] M.Menetrier, A.Saadoune, S.Levasseur and C.Delmas *Journal of Materials Chemistry* **9** 1135 (1999).

[9] B.Gee, C.R.Horne, E.J.Cairns, and J.A.Reimer *Journal of Physical Chemistry B* **102** (1998).

[10] K.R.Morgan, S.Collier, G.Burns, and K.Ooi *J.Chem.Soc.,Chem.Commun.*, 1719 (1994).

[11] Y.J. Lee, F.Wang, and C.P. Grey *Journal of the American Chemical Society* **120** 12601(1998).

[12] K. Sato M. Noguchi, A. Demachi, N.Oki, M. Endo *Science* **264** 556 (1994).

[13] Y.Dai, Y.Wang, V.Eshkenazi, E.Peled, and S.G.Greenbaum. *Journal of the Electrochemical Society*, **145** 1179 (1998).

[14] S. Hayes, L. van Wullen, H. Eckert, W.R. Even, R.W. Crocker, Z. Zhang, *Chemistry of Materials*, **9** 901 (1997).

[15] Y. Idota, T. Kubota, A. Matsufuji, Y. Maekawa, T. Miyasaka, *Science* 1997, **276,** 1395.

[16] Y. Wang, J. Sakamoto, C.K. Huang, S. Surampudi, and S.G.Greenbaum *Solid State Ionics* **110**167 (1998).

[17] WINNMR Version 96-0901 Bruker-Franzen Analytik GmnH

[18] H. Eckert, *Progress in NMR Spectroscopy*, **24**, 159 (1992).

[19] F. Leroux, G.R. Goward, W. P. Power and L.F. Nazar, *Electrochemical and Solid State Letters*, **1**, 255 (1998)

[20] G.C. Carter, L.H. Bennett and D.J. Kahan, in: Metallic Shifts in NMR: Progress in Materials Science, Vol 20, Pergamon Press, Oxford, 1977.

[21] J. M. Snowel, PhD Dissertation, Yale University 1993.

[22] E.Ratai, M.Janssen, H.Eckert, *Solid State Ionics* **105** 25 (1998).

[23] J.C.Chan, M.Bertmer, H.Eckert *Journal of the American Chemical Society* **121** 5238 (1999).

[24] T.M. Duncan, A Compilation of Chemical Shift Anisotropies, AT&T Bell Laboratories, USA, 1990.

[25] S. Machill, T. Shodai, Y. Sakurai, and J. Yamaki, *Journal of Solid State Electrochemistry*, **3** 97 (1999).

[26] I.A. Courtney and J.R. Dahn, *Journal of the Electrochemical Society*, **144** 2045 (1997).

[27] R.A. Dunlap, O. Mao, J.R. Dahn, *Physical Review B*, **59**, 3494 (1999).

[28] J.R. Dahn, I.A. Courtney, O. Mao, *Solid State Ionics*, **111**, 289 (1998).

[29] G.Ceder, M.Chiang, D.R.Sadoway, M.K.Aydinol, Y.I.Jang, B.Huang *Nature* **392** 694 (1998).

Chapter 5 Density of States Calculations for Li-Sn Phases

5.1 Introduction

As discussed in Chapter 4, the magnitude of the Knight shift observed in the ^{6,7}Li NMR spectrum is determined by the electron density at the s-state orbitals, $\langle|\psi_s(0)|^2\rangle_{FS}$ and by the electron spin paramagnetic susceptibility, χ_s^e. Empirical evidence was given in Chapter 4, which demonstrated that the magnitude of the Knight shift increased with increasing concentration of lithium in the Li-Sn phases. Unfortunately, due to synthetic difficulties in obtaining high purity samples for each of the Li-Sn phases, only two data points, besides the pristine metal, were obtained.

Another approach that we investigated was the calculation of the Knight shift of the individual Li-Sn linephases, based on a knowledge of the crystal structures. The full calculation of the Knight shift was not possible, due to difficulties in obtaining values for χ_s^e for the various phases. Nevertheless, using extended Huckel density of states calculations, the electron density in the 2s orbitals up to the Fermi level were calculated. The trends in the electron density are consistent with an increasing Knight shift as the concentration of lithium in the lithium-tin line phase is increased.

5.2 More Detailed History of Knight Shifts

Recalling the formula for the Knight shift from Chapter 4,

$$K = \frac{\Delta H}{H_o} = \frac{8\pi}{3}\left\langle|\Psi_k(0)|^2\right\rangle_{FS}\chi_s^e \qquad (5.1)$$

It is clear that the formula may be verified if the quantities $\Delta H/H_o$, χ_s^e, and $\langle|\psi_k(0)|^2\rangle_{FS}$ can be obtained independently. In this study our intent was to obtain the latter two variables and thereby calculate the Knight shift for each of the line phases in the Li-Sn phase diagram. Reviewing two studies in which these variables were obtained for lithium metal itself is instructive at this juncture.

The fundamental problem in measuring the paramagnetic spin susceptibility of the electron is how to distinguish this from all other contributions to the total paramagnetic spin susceptibility of the substance of interest. The approach adopted by Schmacher and Slichter was to compare the spin resonance of the conduction electrons with the spin resonance of the metal nuclei in the *same sample*.[1] By varying the magnetic field strength to obtain the resonance frequency of the electron (~5 gauss) and subsequently the resonance frequency of the nuclei (~10 000 gauss), and comparing the ratio of the areas for the two signals, the value of the electron spin susceptibility was obtained.

$$\chi_s^e = \chi_s^n \frac{\gamma_e}{\gamma_n} \frac{\int \chi_e'' d H_o}{\int \chi_n'' d H_o} = \chi_s^n \frac{\gamma_e}{\gamma_n} \frac{A_e}{A_n} \tag{5.2}$$

where γ_e and γ_n are the magnetogyric ratios of the electron and the nucleus, respectively. A_e and A_n are the areas of the respective resonances as obtained from an oscilloscope and photographic method, and χ_s^n is the nuclear susceptibility. The latter is calculable according to the Langevin-Debye formula

$$\chi_s^n = \frac{N \gamma^2 \hbar^2 I(I+1)}{3kT} \tag{5.3}$$

where N is the number of nuclei per unit volume, and γ, I, $\hbar$, k and T have their usual meanings (see Chapter 4). Since conduction electron spin resonance arises only from the spin magnetization, therefore the strength of the resonance is determined by the magnitude of the spin magnetization, allowing for the measurement of χ_s^e.

Unfortunately this type of measurement was not possible for the Li-Sn phases of interest, since the methodologies described are not available to us. As well, we were hoping to calculate the Knight shift directly, and avoid synthesizing numerous samples.

A second study of interest is the physical measurement of electron density at the nucleus of metallic lithium, performed by Ch. Ryter.[2] In this experiment single crystals of lithium fluoride were irradiated with thermal neutrons to create a few percent of lithium atoms. Annealing the crystals at 700°C caused the atoms to aggregate into micron sized particles. The electron spin resonance (ESR) lines from the metallic grains were shifted using the Overhauser effect. By partially saturating the ESR, the nuclear polarization is

greatly increased, and the frequency of the ESR is shifted. The shift is related to the nuclear magnetization (H_n) by

$$H_n = \left(\frac{8\pi}{3}\right)|\psi_F(0)|^2 \gamma_n \hbar \langle I_z \rangle \tag{5.4}$$

where

$$I_z = I(I+1)\frac{\hbar\gamma_n H_o}{3kT}|\Psi_F(0)|^2 \frac{\gamma_e}{\gamma_n}\frac{p}{\alpha+p} \tag{5.5}$$

and p is the saturating microwave power, with α being a constant dependent on the apparatus. Plotting $1/H_nT$ versus $1/p$ gives a straight line, the intercept of which can be related to the electronic density at the nucleus by:

$$(H_nT)_{max} = \frac{8\pi}{3}\langle \Psi_F^2 \rangle \gamma_e \gamma_n \hbar H_o I(I+1)\beta \tag{5.6}$$

Here β is a correction factor which accounts for the ratio of ^{7}Li to ^{6}Li in the sample. Thus from the measured $(H_nT)_{max}$ and the known hyperfine structure constant of atomic ^{7}Li the value of ε was extracted.

$$\varepsilon = \frac{\langle \Psi_F^2 \rangle}{|\Psi_A(0)|^2} = 0.442 \pm 0.015 \tag{5.7}$$

ε is the ratio between the wave function density at the nucleus in the metal and the wave function density at the nucleus of the free atom, both being normalized to the atomic volume. This value compares well with other reported values of ε.[3]

This value for the electron density at the nucleus could be combined with the experimental value of χ described above, to obtain an experimental value of the Knight shift. Although these experiments are very elegant, they are also very demanding and much beyond what would be practical for verifying Knight shifts on a routine basis. Instead of experimental methods, the electron density at the nucleus could also be obtained from calculation of the density of states (DOS) for a given material. This approach was taken in our case.

5.3 DOS calculations

A density of states curve for a solid is simply a plot of the distribution of electrons in energy (E). The density of states is defined as follows:

DOS(E)dE = number of levels between E and E + dE

The integral of the DOS up to the Fermi level gives the total number of occupied molecular orbitals.[4] This approach has been used to describe electronic structures of organic and inorganic solids for many years. Examples include the original work of Hoffmann, as well as more recent studies of transition metal oxides and even lithium containing Zintl phases.[5,6] A study of lithium germanide discusses the structural arrangement of the Ge atoms, but the lithium component is neglected, making comparison with our work unfruitful. Our objective was to assign the electron density specifically to the lithium and tin centers in the Li-Sn line phases. This can be accomplished computationally through the use of "projections of the DOS", which allows for the decomposition of the DOS among the atoms. The integral of these projections up to the Fermi level thus gives the total electron density at a specific atom or orbital. In our case, integration of the electron density in the projected Li *2s* orbital allowed for correlation of the increasing ratio of Li:Sn with a corresponding increase in Li *2s* electron density.

5.3.1 Setting up the Input Files

Calculations of the electronic density of states for the series of Li-Sn phases were carried out *via* extended Huckel theory, using the YAeHMOP (Yet Another extended Huckel Molecular Orbital Package) software, developed by Dr. Greg Landrum in the group of Roald Hoffmann.[7] Input files were set up to request calculation of the total DOS, as well as the projected DOS for the lithium 2s orbitals, and the Fermi level, ε_f. A sample input file is given the Appendix. The input file requires the fractional coordinates of every atom in the unit cell, which must be given in Cartesian space. This is a severe limitation of the software, since the positions of all symmetry equivalent atoms must be generated and then translated into Cartesian space. This process, though not difficult, is time-consuming and tedious, particularly for large cells, such as $Li_{21.25}Sn_5$ which contains 420 atoms per cell. In order to define one unit cell, three extra atoms are given in the input file, which mark the distance to

the neighboring cells. If there is an atom at the origin, (0,0,0) the simplest choice is (1,0,0), (0,1,0) and (0,0,1). The cell parameters, a,b,c and α,β,γ are given as well as the electron count for a unit cell.

The calculation of the electronic structure of an extended system requires that the calculation be carried out over a sampling of the first Brillouin zone of the lattice. Thus an appropriate number of k-points which sample this space must be given in the input file. These are provided to the software in the form of fractional coordinates in the reciprocal lattice. For the most accurate calculations, the space group of the lattice is used to optimize the k values and their relative weight. In this case, where we hoped only to capture in a "broad-brush" manner the trends among these structures, a simple 30 k-point set has been used for each calculation, regardless of the space group symmetry.

The energy range for the DOS calculation was in each case –12 to –3 eV. The step size was 0.05 eV, with a Gaussian broadening factor of 10. The calculation of the projected DOS requires that the orbitals contributing to the desired DOS be specified. The parameters used for lithium and tin are taken from the compilation by S. Alvarez, and are listed in **Table 5.1**.[8]

Atomic Orbital	H_{ii}(eV)	ζ_{ii}
Li (2s)	-5.4	0.65
Li(2p)	-3.5	0.65
Sn(5s)	-16.16	2.12
Sn(5p)	-8.32	1.82

Table 5.1 Ionization potentials (H_{ii}) and Slater coefficients (ζ_{ii}) for Lithium and Tin orbitals

Supplied with a set of atoms, a unit cell lattice, and a set of k points, the program executes four steps.[9]

1. Generation of N_{orb} crystal orbitals and their energies at each of N_k k points.
2. Orbitals sorted in order of increasing energy
3. Occupation of orbitals determined by filling the lowest levels with electrons.
4. Calculation of required projected DOSs, or other optional data.

Further details of the methods of extended Huckel calculations are available in the thesis of Dr. Greg Landrum.[9]

5.3.2 *Results and Discussion*

The results of a calculation of the total DOS for lithium metal is given in **Figure 5.1a**, with the Fermi level indicated by the dashed line. As expected for a metal, the Fermi level occurs in a region of high electron density. For comparison, the total DOS for the phase BaTl is shown in **Figure 5.1b**. This compound is a known Zintl phase, with a predicted charge distribution of $Ba^{+}Tl^{-}$. The anticipated distribution of charge is evident in the projected DOS curve for the Ba orbitals. As well, the location of the Fermi level is in this case consistent with an insulator or semi-conductor. This data was taken from the thesis of Greg Landrum, author of YAeHMOP.[10] In this thesis, the results of an extended Huckel calculation (which is a semi-empirical method) are compared to those obtained for a Linear Muffin Tin Orbital (LMTO) calculation, and found to be comparable. This gives some assurance that the parameter sets used by YAeHMOP are reliable, although not as accurate as the basis sets used in *ab initio* methods.

The example of BaTl is used primarily since this phase is similar to the lithium-tin phases in terms of the distribution of electron density. BaTl is clearly a Zintl phase, and thus the electron density on Ba is expected to be small. Similarly, we anticipate that lithium will carry a small portion of the electron density in the lithium-tin phases. Moreover, we predict that the concentration of electron density on lithium will increase as the ratio of lithium:tin increases across the phase diagram. This prediction was originally based on the simple premise that the lithium environment on the atomic scale becomes more and more like that of a lithium atom in lithium metal as the ratio of lithium to tin increases. As well, the observed increase in the ^{7}Li NMR Knight shift in the series of Li_7Sn_3 – $Li_{21}Sn_5$ – Li metal points to an increase in the electron density on lithium through this series. After reflection

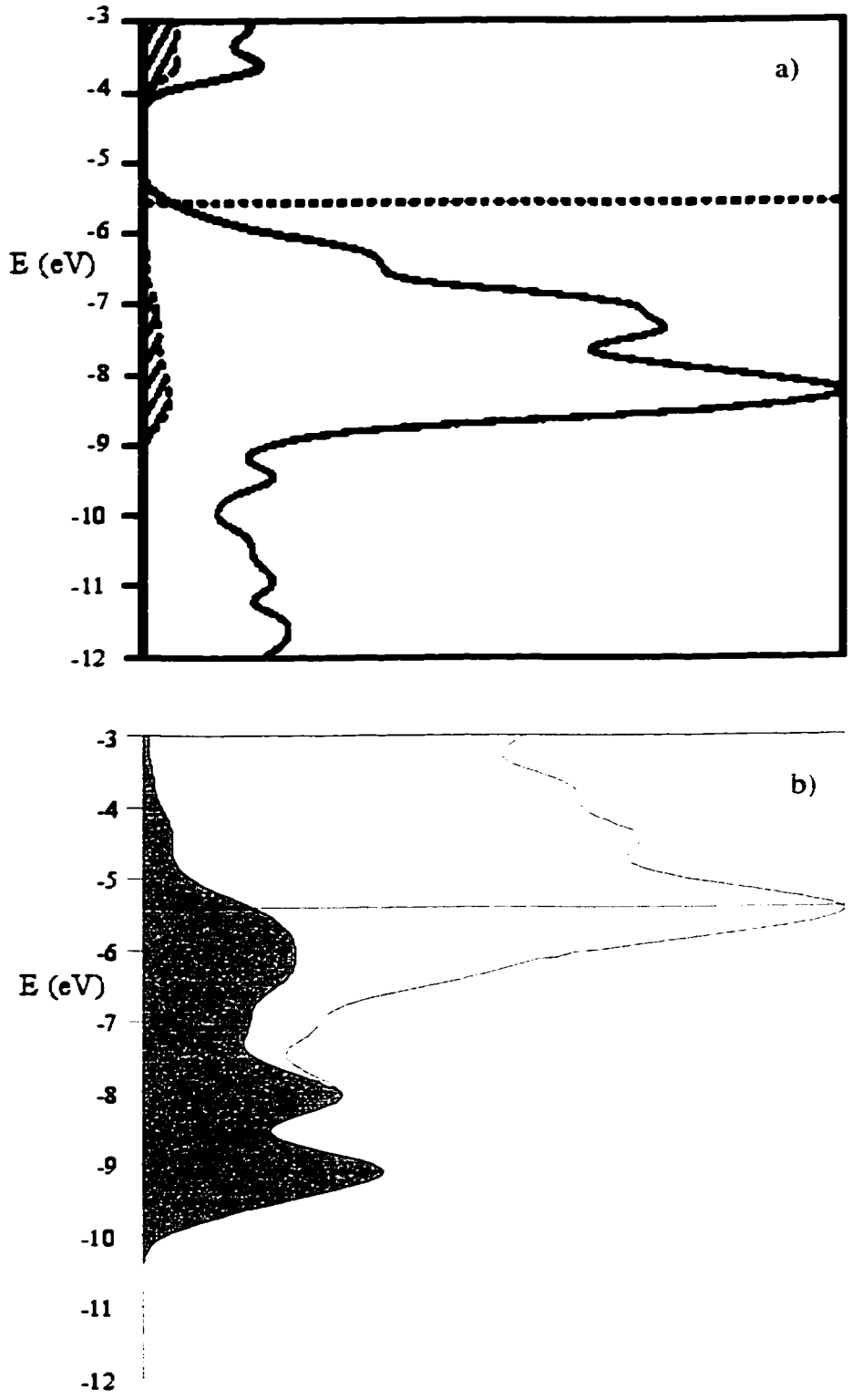

Figure 5.1 Density of States cuves for a) $Ba^{+}Tl^{-}$ Zintl salt, with Ba^{+} 6s orbitals projected, and b) Li metal with Li 2s orbitals projected. Projections filled in gray. Fermi Level marked with horizontal line.

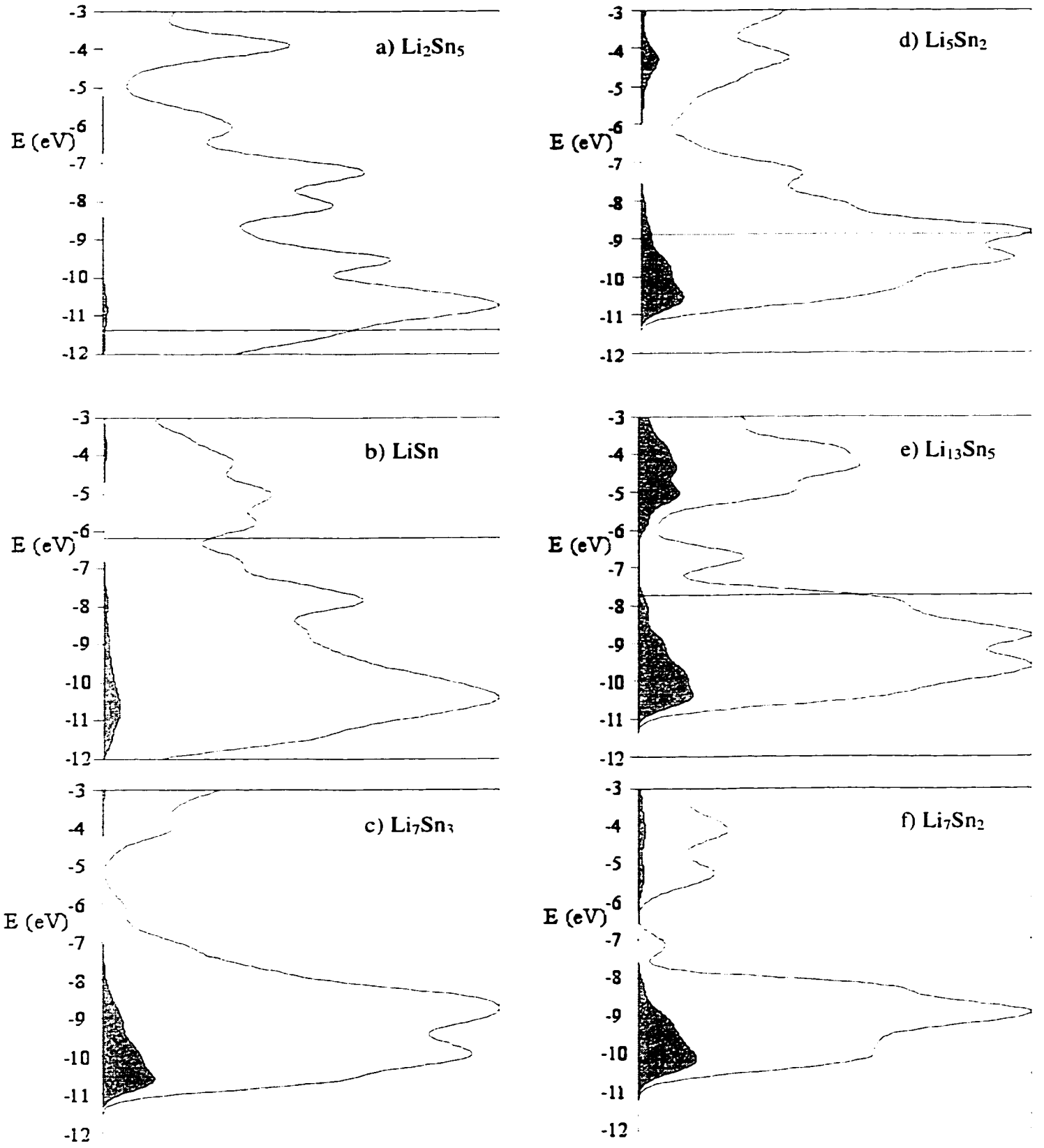

Figure 5.2 DOS with projected Li 2s orbitals (filled in gray) for Li-Sn phases

on this issue, it seemed necessary to develop this idea further, providing some more substantive evidence for this hypothesis.

The results of the DOS calculations for Li_2Sn_5, LiSn, Li_7Sn_3, Li_5Sn_2, $Li_{13}Sn_5$, Li_7Sn_2, are presented in **Figure 5.2**. Attempts to calculate the DOS for $Li_{21.25}Sn_4$ failed because the computer (Saanich, an IRIX SGI) had insufficient memory to process this extremely large cell. The observable trend from the projected DOS for the Li (*2s*) orbitals is the increasing proportion of electron density with increasing ratio of Li:Sn. This is demonstrated even more effectively in the plot of the relative integrated intensity of the Li (*2s*) orbital (up to the Fermi level) versus the ratio of Li:Sn (**Figure 5.3**). Within experimental (or calculational) error the data fall on a straight line. The data is also given in **Table 5.2** for each Li-Sn phase, with the integrated intensity given as a percentage of the Total DOS up to the Fermi Level.

Figure 5.3 Plot of the integrated Li 2s electron density up to the Fermi level as a function of the ratio of Li:Sn for the series of Li-Sn phases.

Phase	Integrated Intensity of Li (2s) Projected DOS up to E_f
Li_2Sn_5	1.1%
LiSn	3.2%
Li_7Sn_3	8.2%
Li_5Sn_2	9.7%
$Li_{13}Sn_5$	9.4%
Li_7Sn_2	11.6%
$Li_{21.25}Sn_5$	Not calculated

Table 5.2 Integrated Intensity of electron density in Li 2s orbitals up to the Fermi Level

The data thus follow the expected trend, with increasing electron density at the lithium nucleus being correlated with the increase. In the absence of any information concerning the possible changes in the χ_s^c, it seems valid that the magnitude of the lithium Knight shift should increase with the increasing concentration of lithium in the lithium-tin phases. Two related challenges remain un-addressed in this study. First, the accuracy with which the Fermi level is determined by EHT is limited, as is the distribution of electrons among the nuclei. Secondly, it is known that the Knight shift arises from *unpaired* conduction electrons; those *at* the Fermi level, as opposed to all electrons up to the Fermi level. The combined influence of paired conduction electrons would cancel each other. Thus our approach does not unequivocally prove the expected trend in Knight shifts of the lithium tin line phases. A more accurate approach would involve the use of self-consistent field calculations, for which both the electron distribution, and the Fermi level can be ascertained with greater confidence. Our study was limited to these model crystal structures, although it is obvious from the other data presented that the phases that occur in tin-based electrodes are quite distinct from those predicted by the Li-Sn phase diagram. Ideally this study would be extended to investigations of the effect of particle size and/or the addition of oxygen to the phases calculated.

In the *fugue* the voice of the density of states calculations complements the voices of the NMR data. Providing insight on the issue of the magnitude of the Knight shift anticipated for the series of Li-Sn phases these calculations thus complement the interpretations of the NMR data presented in Chapter 4. As the voices of the *fugue* are woven together, harmonies are created by the data which support and blend with each other.

5.4 References

[1] R.T.Schumacher and C.P.Slichter *Physical Review* **101** 58 (1956)

[2] Ch.Ryter *Physical Review Letters* **5** 10 (1960).

[3] C.P. Slichter, Principles of Magnetic Resonance. p.113-126 Springer-Verlag Berlin 1990.123.

[4] R. Hoffmann, Solids and Surfaces: A Chemist's View of Bonding in Extended Structures. VCH Publishers Inc. (1988).

[5] E. Canadell and M.-H Whangbo, *Chemical Review*, **91** 965 (1991).

[6] P. Sherwood and R. Hoffmann *Journal of the American Chemical Society* **112** 2881 (1990).

[7] YAeHMOP Web site: http://overlap.tn.cornell.edu:8080/~landrum/yaehmop.html

[8] S.Alvarez Table of Parameters for Extended Huckel Calculations Barcelona, (1985).

[9] G. Landrum Ph.D.Thesis, Cornell University (1997) Chapter 8.

[10] G. Landrum Ph.D.Thesis, Cornell University (1997) Chapter 1.

Chapter 6 ***X-ray Studies:*** *X-ray Absorption Spectroscopy and X-ray Scattering including Pair Distribution Function Analysis*

A recurring theme in this thesis is the necessity to utilize physical analysis methods that are not limited by a lack of crystallinity in the system of interest. This chapter combines the results obtained through X-ray Absorption Spectroscopy (XAS) and those obtained through X-ray scattering, including Pair Distribution Function Analysis (PDF). Both of these techniques are able to provide information even on disordered materials. While the solid-state NMR studies provided a detailed picture of the interactions of lithium with the glass, as well as revealing information about the participation of the aluminum, boron, and phosphorous ions, the elusive element is the tin itself. Since tin is the predominant electroactive element in the TCO glasses, it was imperative to find a satisfactory way of probing the tin interactions directly. The individual strengths and weaknesses of XAS and PDF as analysis methods are described here. The data obtained from the combined methods provide a fascinating, if complex, view of the interactions occurring at the tin centers. By combining the results of the solid-state NMR data with the scattering data obtained at BNL and the EXAFS data obtained at le LURE we have obtained a complete picture of the nature of lithium sites accessed following electrochemical lithium insertion, as well as the response of the tin centers in the oxides and oxide-based glasses. This unique combination of techniques allows us to probe the changes in co-ordination environment around Sn and the various environments experienced by Li as well as the interaction within these domains of the anode composite.

The voices of XAS and PDF are at times dissonant, at times complementary, and overall add exquisite melody to the counterpoint of the thesis. In the analogy of the *fugue*, the voices expressed by these two techniques are best heard in harmony. Together these two voices are able to probe the tin centers in the electrode materials, thus adding a unique subject to the *fugue*.

The chapter is broken down into descriptions of the theory behind each technique, including in the case of XAS a review of relevant studies of electrode materials. This is followed by a description of the sample preparations and experimental methods, as well as

the results obtained from each study. The chapter concludes with an in depth discussion of the models which may be used to interpret the data, with emphasis on the similarities and differences between our observations and interpretations and those made by other groups. This discussion leads into the conclusions presented in Chapter 8, which incorporate all of the pertinent data, giving an overview of the electrochemical processes studied in this thesis.

The first section of this chapter describes the X-ray absorption spectroscopy (XAS) studies that were carried out on the SnO and TCO electrode systems. This work was possible through a collaboration with Dr. Fabrice Leroux and Prof. Guy Ouvrard. Experiments were performed at le Laboratoire d'Utilisation du Rayonnement Electromagnetique (le LURE) France. The advantage of this technique is the ability to select a particular element by tuning the energy of the X-ray probe to the absorption edge of the element of interest. In this way we are able to access the tin centers directly, and probe the local environment of these atoms with ease. The issue of being able to study disordered materials is minimized in this method, although coherent back-scattering of the emitted electrons is necessary to ensure satisfactory data processing. The majority of the data were not adversely affected by the disorder inherent in the TCO glass. Only at deep discharge was there a problem with acquiring satisfactory data. The studies of SnO itself were successful even at low potential.

The second section of this chapter presents the theory and methodology of PDF, a method complementary to the XAS studies, which was available to us through collaboration with Prof. Takeshi Egami and Dr. Wojtek Dmowski, of the Materials Science Department at the University of Pennsylvannia. This method, similar to XAS, relies on high energy X-ray diffraction data acquisition, performed at a synchrotron; in this case at beamline X7A at the National Synchrotron Light Source at Brookhaven Nation Laboratory. The beauty of this technique is that the pair distribution function is derived from a direct Fourier transform of the diffraction data, and thus does not rely on comparison with model structures. In contrast, XAS depends on the calculation of the absorption coefficient for a model structure with a particular number of and distance to its nearest neighbors. The solution is therefore not unique, as more than one model system may adequately approximate the experimental EXAFS.

As we believe that this is the first time that the PDF technique has been applied to electrode materials, no review of relevant background experiments is given.

6.1 The Theory of XAS

When X-rays interact with matter, one of several effects that can arise is the absorption of the X-ray photon by the inner shells of the atoms, resulting in the ejection of an electron from the occupied shells to the unoccupied shells. This effect is well studied, primarily for the absorption of the X-ray photon at the most tightly bound 1s (K edge) or 2s and 2p (L edge) levels. The resulting data give information concerning the short range order within the material, as the ejected electron is influenced by the interactions with the immediate coordination shells. This is advantageous, since equivalent information is accessible for crystalline, disordered, and non-crystalline systems.

The absorption coefficient of a given element increases sharply at the absorption edge for the given shell, referred to as the "edge", *i.e.* K edge for the 1s shell. In the condensed phase, the absorption coefficient varies as a function of energy. Three areas are distinguished in the spectrum, as shown in **Figure 6.1**.[1] The pre-edge area, at energies lower than the edge itself, is referred to as the X-ray absorption near edge structure, XANES, while the area beyond the edge is the extended X-ray absorption fine structure, EXAFS. As the region before and after the absorption edge is scanned in energy, the ejected photo electron probes the electronic levels below and above the Fermi levels of the material. This resultant photoelectron is modified by single scattering from atoms in its coordination sphere.

During an absorption event, the incoming X-ray photon, with energy hν, is absorbed by the K shell, and a photoelectron, with kinetic energy E is emitted. As energy must be conserved, this kinetic energy is equal to

$$E = h\nu - E_K \qquad (6.1)$$

where E_K is the binding energy for the 1s electron. On the high energy side of the absorption edge, the absorption coefficient, μ_x, fluctuates, giving rise to the fine structure which is EXAFS. The absorption coefficient is defined as

$$\mu_x = \ln(I_o/I) \qquad (6.2)$$

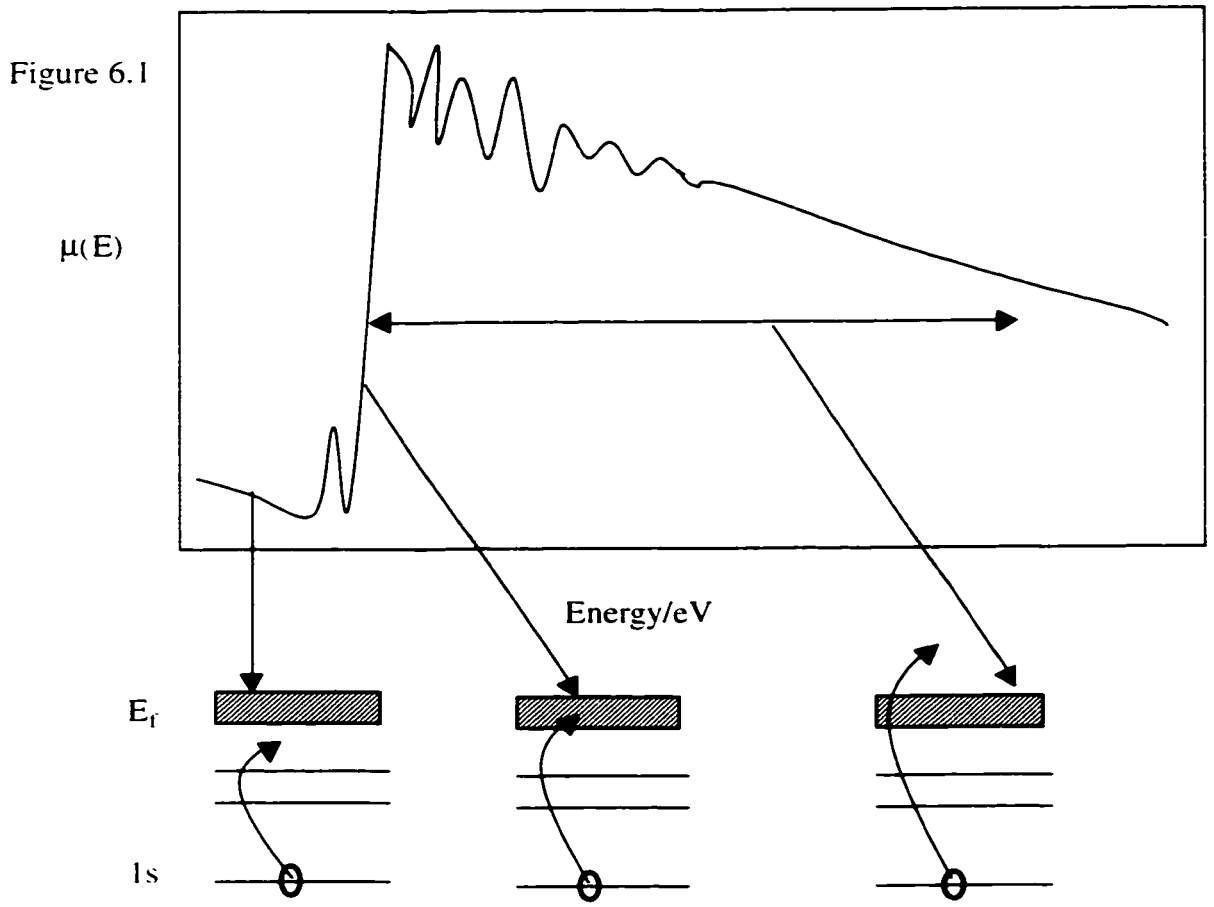

Figure 6.1 The XAS process: correlation between the emitted electron and the X-ray absorption spectrum. Low energy corresponds to pre-edge (XANES), while high energy corresponds to extended absorption (EXAFS). Between these is the absorption edge of the atom of interest.[3]

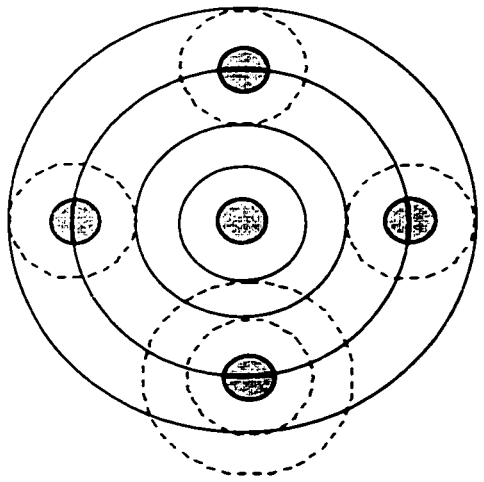

Figure 6.2 Schematic of the radial portion of the emitted photoelectron wave. The solid lines represent the outgoing wave, and the dashed lines represent portions of the scattered wave from the surrounding atoms.[2]

where μ is the linear absorption coefficient, x is the thickness of the absorbing sample, I_o is the incident X-ray intensity and I is the transmitted intensity.

The interference between the wavefunction of the photoelectron and the nearest neighbors is depicted in **Figure 6.2**. The initial state of the system is constant, but the final state of the photoelectron is scattered by surrounding atoms. The outgoing wavefunction is depicted by the solid lines, while scattering effects from neighboring atoms are shown with dotted lines. Both constructive and destructive interference contribute to the observed fine structure. EXAFS can be thought of as an electron diffraction method, in which the electrons originate within the material. In the case of single short-range, single electron, single scattering of the photoelectron, EXAFS absorption can be described as[3]

$$\chi(E)=\frac{\mu(E)-\mu_o(E)}{\mu_o(E)} \tag{6.3}$$

where $\mu_o(E)$ is the background absorptions and $\mu(E)$ is the observed absorption coefficient. It has been shown that the EXAFS can be related to the structural parameters according to[4]

$$\chi(k)=\frac{m}{4\pi\hbar^2 k}\sum_j \frac{N_j}{R_j^2} t_j(2k) e^{-2R_j/\lambda} \sin\left[2kR_j+2\delta_j(k)\right] e^{-2k^2\sigma_j^2} \tag{6.4}$$

where k is the electron wave vector, N_j is the number of atoms in the *j*th coordination sphere, R_j is the average radial distance to the *j*th atoms, $t_j(2k)$ is the back-scattering matrix element encountered by the electrons, λ is the mean free path of the electron, the second exponential containing σ_j^2 is a Debye-Waller-type term where σ_j accounts for thermal vibrations and static disorder of the atoms about R_j, and $\delta_j(k)$ is the phase shift experienced by the photoelectron. The form of this equation represents the sine-like scattering contributed by each shell of atoms at a distance, R_j. The period of the sine function for each shell is $2kR_j$. The intensity of the EXAFS signal is proportional to the number of atoms N_j surrounding the absorbing atom, and inversely proportional to the square of the distance R_j^2.

Analysis of experimental EXAFS data for numbers of nearest neighbors and distances between the absorbing atom and its neighbors involves the conversion of intensity versus energy data to a radial distribution function. Several steps are involved, the first of which is the calculation of the absorption coefficient from the experimental values I_o, I and E according to Eq. 6.2. Subsequently the Fourier transform of the data in momentum space

(k) into distance space (R) is taken, resulting in a *pseudo*-radial distribution function. Fourier analysis of the EXAFS transforms the $\chi(k)$ function, in momentum space to the $\rho(R)$ function, in distance space, thus giving the spatial dependence of the matrix surrounding the excited atoms. The required Fourier transform is given here[3].

$$\rho(R)=\frac{1}{(2\pi)^{1/2}}\int_{k_{min}}^{k_{max}} k^n \chi(k)\exp(2ikr)dk \qquad (6.5)$$

where $\rho(R)$ is the radial distribution function, and n is usually 1 or 3. It was found empirically that setting n = 3 results in a transform that is less sensitive to the value of k_{min}. The peaks in the radial distribution function, $\rho(R)$ are shifted from the true distance, R´, by an amount α = R´-R, where α is approximately 0.2-0.5Å, depending upon the elements in the sample. The value of α is determined from comparisons of known structures to calculate distances. Similarly, the value of the phase shift, δ_j, may be determined empirically from known structures and then applied to an unknown compound.[5] The phase shift arises from inelastic backscattering processes which alter the momentum of the emitted electron. Since electrons interact strongly with matter (compared to X-rays), the momentum of an electron may be changed substantially by its interactions with the material. This effect gives rise to the observed phase shifts.

To construct a model structure for an unknown material, the desired structural information, N_j and R_j, are determined through an iterative curve fitting and inverse Fourier transform procedure. The optimal solution gives the best fit between the experimental and calculated EXAFS spectrum. This dependence of the *pseudo*-radial distribution function on a comparative model-compound-based solution is the major weakness of EXAFS, since more than one solution may give an appropriate fit of the Fourier transformed EXAFS spectrum. This caveat is avoided in PDF analysis. Nevertheless, EXAFS offers several advantages, including 1) revealing short range order for the environment of a desired atom in a non-crystalline system, 2) excellent atomic sensitivity based on the energy of an element's K or L edge, allowing effective elucidation of structures in multi-component systems, 3) ease and efficiency of data acquisition (typical samples require 30 minutes of acquisition time).

6.2 Overview of XAS studies on Electrode Systems

XAS techniques have long been used by researchers interested in exploring the environments of specific atomic species in multi-component non-crystalline systems. For example, in the area of heterogenous catalysis, few other techniques can give the desired information about the catalytic centers, which are in most cases a very small percentage of the material and are typically supported on an amorphous material.[6] Beginning about a decade ago, material scientists working in the area of battery materials have taken advantage of XAS to examine the local environment around electrochemically active species. Both XAS effects, XANES and EXAFS, have been used to advantage by a number of groups interested in the reaction of lithium with various electrode materials.

The previously reported studies involve transition metal oxide electrode materials, with well understood crystal structures. In this context, changes in the EXAFS or XANES can be interpreted directly in terms of changes in site symmetry and coordination environment within these known structures. For example, a study by Ammundsen *et al.* on the effect of chromium substitution into spinel lithium manganates at both the Cr and Mn K edges, showed that the d^4 Mn^{3+} ions are subject to Jahn-Teller distortion, as expected.[7] Substitution of d^3 Cr^{3+} gave rise to regular octahedral geometry around the Cr centers with six equal Cr-O distances. By analysis of the XANES and EXAFS, it was evident that the local disorder present in the lattice around the Mn^{3+} sites was eliminated when chromium was substituted for manganese. This was evident both in the changes in the TM-O distances and also in the magnitude of the Debye-Waller factors, which decreased corresponding to the more ordered lattice created by chromium substitution. A similar investigation of Jahn-Teller distortions was published by Peres *et al.*, for the system $Li_{0.65-z}Ni_{1+z}O_2$.[8] The goal of that study was to resolve the debate surrounding the phase transformation observed in this material upon de-intercalation of lithium ions.

The question of the structural changes occurring during the electrochemical insertion of lithium into vanadium oxide aerogels[9] and xerogels[10] has also been addressed using XAS at the vanadium K edge. The latter of these studies described an *in situ* data collection, a method which is gaining popularity among the XAS community. This method allows for the examination of the EXAFS at multiple stages during the electrochemical process without

requiring a separate sample for each data point. The data set acquired for the V_2O_5 xerogel demonstrated the reversibility of the electrochemical reaction. The intensity of the pre-edge peak was correlated with the oxidation state of the vanadium. As well, plots of the pre-edge and edge energies *versus* moles of intercalated lithium produced a linear relationship on discharge which was reversed upon charge. The EXAFS data was not analyzed quantitatively, but similar trends could be observed from a qualitative analysis of the spectra.

Nickel vanadate, a material being considered as an anode for lithium ion batteries, has also been studied using *in situ* XAS at both the Ni and V K edges.[11] Investigations of the first discharge process showed a significant structural change, corresponding to the insertion of the first lithium. This first lithium is inserted irreversibly. The material starts out as a spinel, with vanadium on the tetrahedral sites and lithium and nickel on the octahedral sites. Analysis of the XANES showed a sharp pre-edge intensity in the pristine material that corresponds to the tetrahedrally coordinated vanadium. Upon insertion of the first lithium, this peak diminished significantly, indicative of a loss of symmetry. The EXAFS showed that the coordination at the vanadium matched a distorted octahedral environment. Beyond the insertion of the first lithium, no significant structural changes were observed at either the vanadium or nickel centers. Thus, one conclusion drawn from this study was that the structural changes observed at the beginning of the insertion process are necessary to allow for the reversible insertion of other lithium.

Finally, preliminary results from one highly relevant study were introduced at the JECS meeting in Edinburgh, 1998, including EXAFS data for the TCO glass system.[12] *In situ* data were shown for the electrochemical insertion of lithium into TCO at numerous points in the discharge curve. The data showed a Sn-O distance of 2.12Å in the pristine glass. Initial discharge indicated the formation of amorphous, highly dispersed metallic Sn-particles. Deeper discharge was correlated with the formation of Li-Sn alloy phases, although it was stated that these phases differed substantially from their crystalline counterparts. Significantly, no evidence was found for the re-emergence of an Sn-O contact upon charge. On this point, their EXAFS data differs from ours (shown below). While the sheer volume of EXAFS data was impressive, the analysis must be tempered with the observation that their discharge capacity for their TCO material only reached 5.4Li,

substantially below the anticipated 8.4Li. No diffraction pattern for their TCO material was presented, but we suspect that the crystallization of aluminum phosphate in their product is giving rise to the limited capacity.

6.3 *Theory behind Pair-Distribution-Function Analysis*

Generally, the procedure for determining the structure of a material, even if that material is disordered, is through crystallography. The draw back of this approach is that crystallographic analysis is inherently dependent on the premise that the lattice structure has long range periodicity. Hence, crystallographic methods can only describe disorder in terms of the partial occupancy of atomic positions or in terms of the large Debye-Waller (thermal) parameters. Diffuse scattering in a traditional crystallographic analysis is treated as background and subtracted following curve fitting of the Bragg reflections. This diffuse scattering may contain valuable data concerning the nature of the disorder in the material. It is immediately apparent that crystallography provides extremely limited information about disordered systems. It is preferable in such a case to describe the local atomic structure relative to the positions of the atoms.

The pair distribution function is obtained from diffraction data, and is frequently used to describe non-crystalline systems. In a material with an average density of

$$\rho_o = N/V \tag{6.6}$$

where N/V is the number of atoms per unit volume, the probability of finding another atom at a distance r from the origin atom corresponds to $\rho_o g(r)$, where g(r) is the pair distribution function.[13] The PDF can be defined by

$$\rho(r) = \rho_o g(r) = \frac{1}{N}\left\langle \sum_j \sum_k \delta\{r - (r_j - r_k)\} \right\rangle - \delta(r) \tag{6.7}$$

where $\rho(r)$ is the radial density function, and ρ_o is the average number density. For comparison, the radial distribution function is related to the pair distribution function, and describes the number of atoms in a spherical shell of depth R+dR, according to $4\pi r^2\rho_o g(r)$. The coordination number, n, is given by the average number of atoms in the region between r_1 and r_2 according to the integral of the radial distribution function over this space.

$$n = \int_{r_1}^{r_2} 4\pi r^2 \rho_o g(r) dr \qquad (6.8)$$

The atomic pair density function is obtained directly from the powder diffraction data *via* a Fourier transform. The PDF of an amorphous material is characterized by broad features on account of the wide range of bond distances and environments present in these materials. To calculate the PDF, the Fourier transform of the experimentally determined structure factor is taken over the region sampled in Q ($Q = 4\pi\sin\theta/\lambda$).

$$\rho_o g(r) = \rho_o + \frac{1}{2\pi^2 r}\int_0^\infty [S(Q)-1]\sin(Qr) Q dQ \qquad (6.9)$$

where ρ_o is the number density of atoms. The critical factor is the accurate determination of the structure factor, S(Q), from the measure diffraction intensity, I(Q). The scattering intensity includes not only coherent scattering from the sample, but also incoherent scattering, multiple scattering, and background scattering from the sample holder. In order to get an accurate S(Q), all of these parameters must be appropriately measured and subtracted. The structure factor S(Q) used here is distinct from that described in Chapter 2, F(hkl), since S(Q) is defined per unit volume in reciprocal space, while the crystallographic structure factor is defined as the integral of the particular Bragg peak, *hkl*.[14]

The PDF method is not widely used due to the necessity to collect data at very high Q. The range of Q is limited by the wavelength of the scattering probe, thus typical X-ray targets, such as Mo (0.7107Å), provides data only to $17Å^{-1}$. This results in termination errors in the Fourier transformation, which give rise to spurious oscillations of the PDF at low r. The use of high energy, high intensity X-rays, such as those available at the National Synchrotron Light Source (NSLS) can be utilized to achieve the short wavelength high values of Q necessary for accurate PDF analysis.

6.4 PDF Analysis Method[15]

The experimental diffraction intensity, I_E, includes both the absorption (A_C) and intensity (I_C) from the sample container, as well as the intensity and absorption from the sample, (I_S and A_S respectively) such that

$$I_E = A_C I_C + I_S A_S \qquad (6.10)$$

To isolate the intensity from the sample, the other contributions are measured and subtracted. The intensity from the sample includes both coherent and incoherent scattering, described as

$$I_S = X\,[F_{coherent} * A_S(R_1, \mu_C, \mu_S) + F_{Compton} * A_S(R_1, \mu_C, \mu_S)] \qquad (6.11)$$

where X is a normalization constant, based on the flux of X-rays, analyzed by the monitor during the data acquisition, and $A_S(R_1, \mu_C, \mu_S)$ is the absorption coefficient for the sample, including the linear absorption coefficients of the container, μ_C, and the sample, μ_S, and the linear distance through the sample, R_1. From this equation, the coherent scattering, $F_{coherent}$ is desired, since it contains the structure factor, S(Q).

$$F_{coherent} = \langle f^2 \rangle - \langle f \rangle^2 + \langle f \rangle^2 * S(Q) \qquad (6.12)$$

where f_i is the atomic scattering factor for each element as a function of Q, available in the International Tables of Crystallography,[16] and $\langle f \rangle$ is the compositional average of the atomic scattering factors for the material of interest. **Figure 6.3a** shows schematically the typical dependence of f_i on Q for lithium metal compared to tin metal.[16] This describes the way each element coherently scatters X-rays as a function of Q. **Figure 6.3b** shows the dependence of the incoherent, or Compton scattering as a function of Q. At high Q the function becomes asymptotic with the Z value of the element, where Z equals the number of electrons. From these figures, the inherent problem with the experiment is apparent. The coherent scattering, which is governed by f, decreases with increasing Q, whereas the Compton scattering increases with increasing Q. Also, f depends on the square of Z, whereas the Compton scattering depends on Z directly, thus for light elements, the Compton scattering overtakes the coherent scattering for relatively low values of Q. In the case of the TCO glass, the concentration of light elements is quite large, with only tin providing strong scattering.

The structure factor by definition goes to unity at high Q, thus as Q goes to infinity, the value of $F_{coherent}$ becomes equal to $\langle f^2 \rangle$. At very high Q, the observed scattering is caused by individual atoms, since at high Q, d is very small, and thus the atoms do not "see" each other. For example, at Q = 20Å^{-1}, d = 0.3Å, which is much smaller than any reasonable interatomic distance. Thus no interference occurs. The scattering intensity from the sample is now expressed as

$$I_S = X[A_S^{elastic}(\langle f^2 \rangle - \langle f \rangle^2 + \langle f \rangle^2 * S(Q)) + Compton * A_S^{Compton}] \qquad (6.13)$$

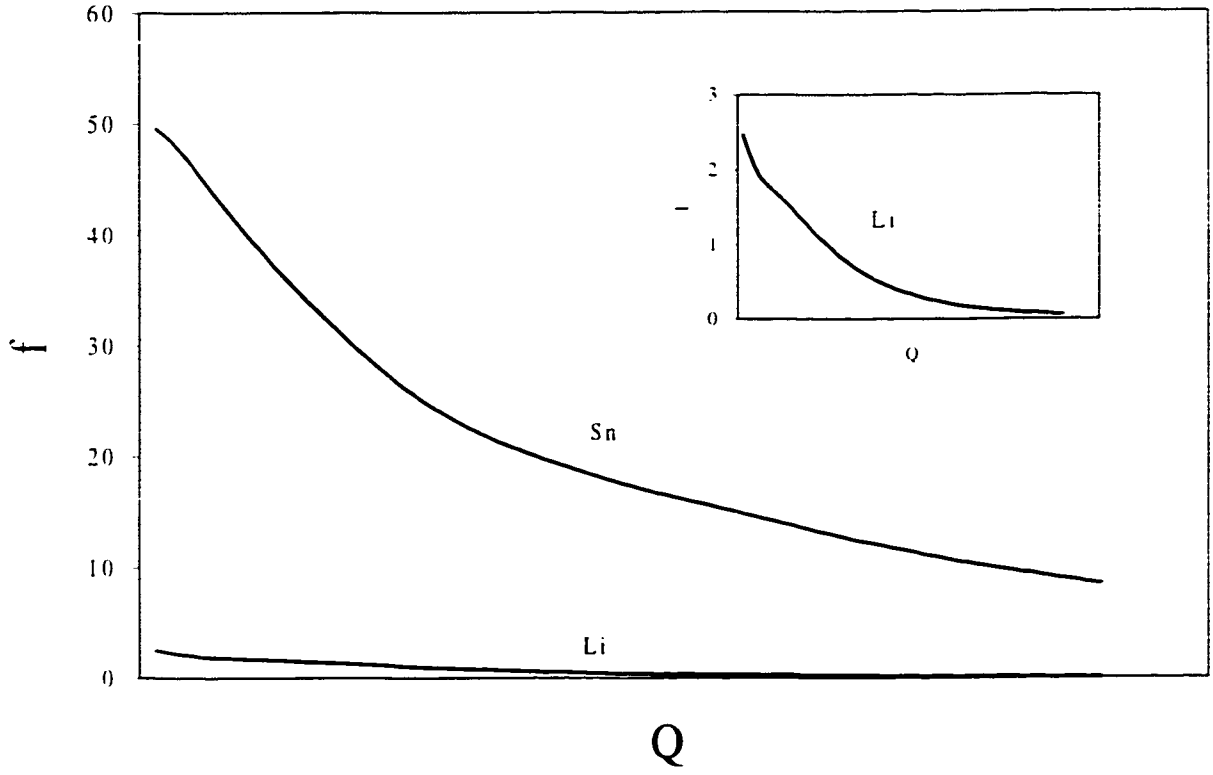

Figure 6.3 Structure factors as a function of angle for tin compared to lithium (inset structure factor of lithium on an expanded scale)

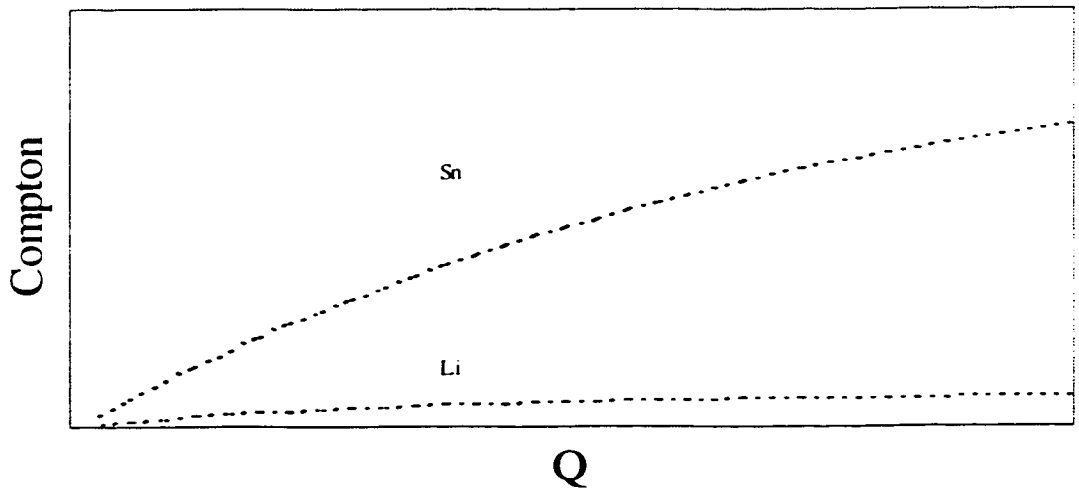

Figure 6.4 Inelastic or Compton scattering as a function of angle for tin and lithium.

The normalization constant, X, is calculated from the assumption that S(Q) tends to unity at high values of Q, and is thus obtained from averaging over Q = 17 - 19Å. From this it is now possible to obtain the structure factor according to

$$S(Q)=\left\{\left[I_S(Q)/X - Compton * A_S^{Compton}\right] * 1/A_S^{coherent} - \langle f^2\rangle + \langle f\rangle^2\right\} \Big/ \langle f\rangle^2 \quad (6.14)$$

The PDF, in real space, is then obtained from the Fourier transform of the structure factor, in reciprocal space, according to equation 6.9.

6.5 *Sample Preparation and Data Acquisition*

XAS studies were undertaken at LURE (Orsay, France) using X-ray synchrotron radiation emitted by the DCI storage ring (1.85 GeV positrons, average intensity of 250 mA). Data were collected in transmission mode at the Sn K edge (29.200 eV), using a double crystal Ge (400) monochromator. Experiments were performed by Dr. Fabrice Leroux of the Université Blaise-Pascal, France.

All samples were prepared electrochemically as described in Chapter 3. Typical sample size was 25 mg, hence a slower discharge rate of 10 mV/hour was used. In order to avoid any contamination with nitrogen, oxygen, or moisture, the samples were sent to le LURE in sealed pyrex ampoules. The powder sample was placed in an appropriate sample holder, sealed with Mylar™ windows on both sides to allow X-rays to pass freely through. The thickness of the sample was measured, as this parameter is critical to the subsequent data analysis.

For PDF analysis the electrode samples were transferred to glass capillaries purchased from the Charles Super Company, of 1mm outer diameter, and wall thickness 10 micron. Although extremely fragile, these thin-walled capillaries allowed for minimal absorption of X-ray intensity through the sample holder. Since the number density of the sample was critical to the data analysis, the mass of each capillary was taken before and

after sample loading. This, combined with the volume of the sample gave the density for each sample.

X-ray scattering studies for PDF analysis were performed at the NSLS (Brookhaven, NY, USA), using X-ray synchrotron radiation. For determination of the structure factor, S(Q), three independent diffractograms were required. The first of the sample itself which includes scattering from the container, the second of the empty sample container, and the third of the background absorption. The latter was measured using the straight-through beam, with an appropriate beam stop to minimize the intensity of radiation at the detector. A solid state Ge detector, cooled with liquid nitrogen, was used. The wavelength of radiation used was $\lambda = 0.555$Å, which was obtained using the Ge 111 monochromator. The beam was 8mm across, and 1.5mm high, centered on the sample using a telescope. The capillary was mounted in a 4-axis goniometer, and enclosed within a Kapton™ chamber filled with helium to minimized scattering by the atmosphere. The data was acquired over the range of Q from $Q = 0.4$Å^{-} to $Q = 20$Å^{-1}. Typically the acquisition was divided into four portions, 0.4-6.0, 6-10, 10-15, and 15-20 Å^{-1}, each with step sizes of 0.01Å^{-1} and with scan rates for each of 8, 12, 15, and 20 seconds per step for the four portions respectively.

6.6 EXAFS Results

The events occurring at the atomic scale in the bulk of the electrode materials, are revealed by the XAS data collected at the Sn K-edge. The *pseudo*-radial distribution functions (RDFs) obtained for SnO and TCO electrodes are shown in **Figure 6.5** and **Figure 6.6** respectively. The refinement of SnO itself was based on the structure including both SnO and Sn-Sn distances; for pristine TCO only Sn-O distances were used since the Sn-Sn contacts (**Figure 6.6b**) are sufficiently distant or disordered that they are not visible. The details of the EXAFS data are listed in **Table 6.1**.

Upon insertion of 2Li into either structure at 750 mV (**Figure 6.5b and 6.6c**), dramatic changes are apparent. A strong feature appears in both curves (SnO and TCO) corresponding to a Sn-Sn peak at 3.0 Å, similar to the distance in β-tin. This is consistent with previous reports for SnO, where XRD, Raman and TEM demonstrate collapse of the

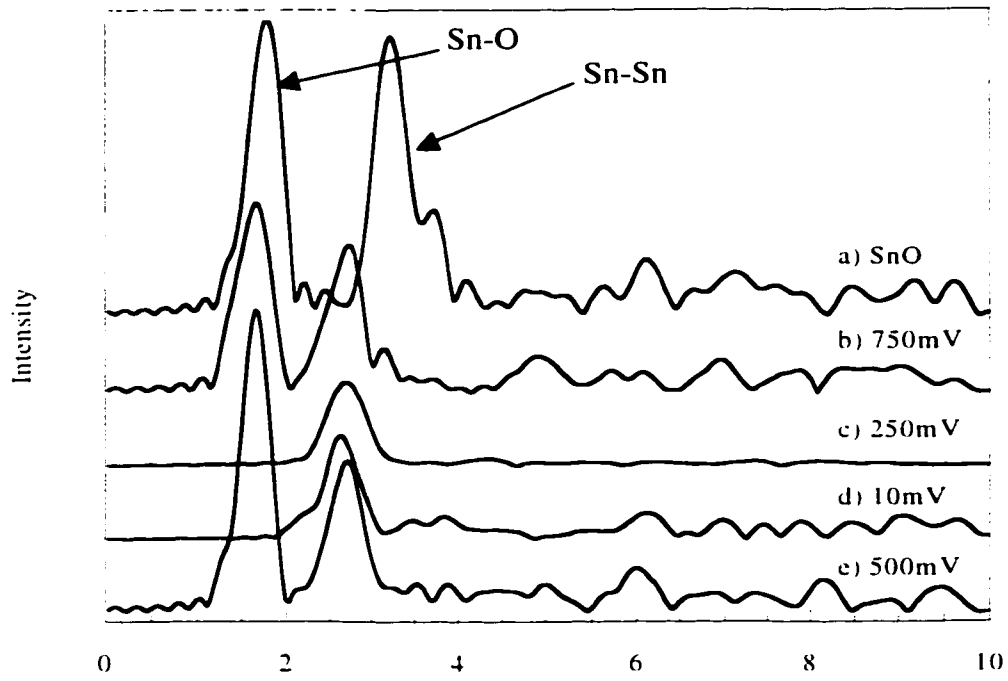

Figure 6.6 Pseudo-radial distribution functions for a) SnO, and SnO electrodes at b) 750mV, c) 250mV, and d) 10mV on discharge, and e) 500mV on charge. (Not corrected for phase shift)

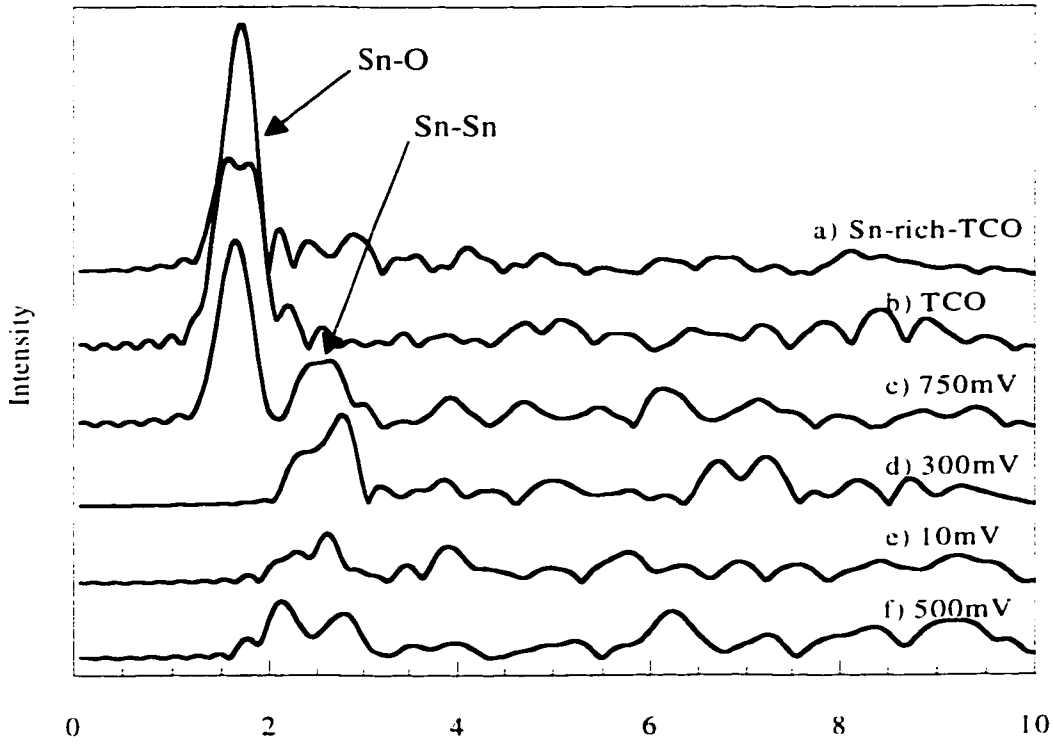

Figure 6.5 Pseudo-radial distribution functions for a) pristine Sn-rich-TCO and b) TCO, as well as, TCO electrodes at c) 750mV, d) 250mV, and e) 10mV on discharge, and f) 500mV on charge. (Not corrected for phase shift)

Material	Atom	R(Å)	N	σ (Å)*	ρ(%)
SnO[b]	O	2.23	4.93	0.08	
	Sn	3.56	3.33	0.075	2.4
	Sn	3.74	3.03	0.075	
	Sn	3.87	2.06	0.075	
750mV	O	2.13	2.06	0.068	5.7
	Sn	2.99	0.67	0.088	
	Sn	3.05	0.94	0.088	
10mV[c]	Sn	2.95	1.10	0.087	8.2
500mV on	O	2.09	2.71	0.067	6.1
charge	Sn	3.03	1.65	0.091	
Fuji glass	O	2.17	2.60	0.070	
	O	2.30	0.71	0.070	2.6
750mV	O	2.12	1.88	0.069	3.0
	Sn	3.01	0.52	0.095	
10mV[c]	O	2.57	0.35	0.070	11.0
	Sn	2.90	0.2	0.085	
	Sn	2.99	0.35	0.085	
500mV[c] on	O	2.56	0.49	0.046	7.6
charge	Sn	3.02	0.50	0.094	

Table 6.1 EXAFS study of SnO and TCO and the corresponding electrode materials at the Sn K edge, where R is the interatomic distance, N is the number of nearest neighbors, σ is the Debye-Waller thermal parameter, and ρ is the goodness of fit.

* *Scale factor $S_0^2(Sn)=0.551$, and free mean path, $\Gamma(Sn/O)=0.461$ and $\Gamma(Sn/Sn)=0.652$, were obtained from refinement of the reference sample, SnO_2: crystallographic data for SnO_2 (rutile) –oxygen: 2.051 [4] and 2.057Å [2], averaged at 2.054Å, tin: 3.185 [2] and 3.709Å [8].*

[a] *σ was linked for the same type of backscattering atoms, i.e. O or Sn.*

[b] *SnO, PbO type structure, crystallographic data: -oxygen: 2.219[4] Å, - tin: 3.532[4], 3.702[4] and 3.799[4] Å.*

[c] *Δk = 3.5 to 14 $Å^{-1}$.*

lattice at this stage coincident with nucleation of metallic Sn.[17,18,19] We conclude that a similar process occurs for TCO, although a more disordered Sn environment results. Importantly, the EXAFS shows that an altered Sn-O environment is maintained in *both cases* after the insertion of 2 Li. The number of oxygen neighbors for Sn decreases, and the Sn-O distance is reduced (to 2.1 Å from 2.2 Å in crystalline SnO, and to a lesser degree in TCO). As we are close to equilibrium conditions in these slow potentiostatic discharge conditions, this contradicts a single biphasic process where 2 Li simply sequester oxygen from the lattice to form Li_2O and Sn: either for SnO or TCO. At deeper discharge, differences between SnO and TCO are more evident. At 10 mV in SnO (**Figure 6.5d**), a shorter Sn-Sn contact at 2.95 Å alone dominates the RDF. If any Sn-O interactions exist, they are sufficiently highly disordered and/or in the second shell and are not visible in the EXAFS. In contrast, at 10 mV in TCO, the RDF shows few obvious features although a weak Sn-Sn interaction is still visible, suggesting a very high degree of disorder. It is possible to simulate the EXAFS with a two-shell model with a long Sn-O distance (2.5 Å) and additional Sn-Sn distances (2.9 and 3.0 Å) although the fit is not as good as in the other cases. This implies that Sn-O bonds are not completely lost in the glass on discharge, and there is a very high degree of disorder implicit in the material. There is a slight shortening in the Sn-Sn distance in both highly reduced tin alloys and reduced tin clusters, as might be expected from electronic considerations.

On charge to 500 mV, corresponding to extraction of two ($Li + e^-$) from SnO (**Figure 6.6f**), the Sn-Sn distance increases slightly. Most compelling is the reappearance of an Sn-O peak. This implies that the oxygen near the tin particle must be at a relatively close distance, and/or the Sn particle is of extremely small dimensions in order for a reassembly of such a partially developed Sn-oxide structure to occur. In turn, if Li-Sn phases are formed, they cannot be ordered phases of large dimensions akin to those in the high-temperature phases. The EXAFS data for TCO on charge are even more complex than at 10 mV, due to a very high degree of disorder that affects the coherent back-scattering process. Analysis will hence rely on direct Fourier transform of X-ray scattering data to obtain the PDF.

6.7 X-ray Scattering and PDF analysis

6.7.1 The First Data Set - Oxidation Issues

The diffraction patterns for the series of TCO and SnO electrode samples studied in October of 1998 are shown in **Figure 6.7**. The diffraction data for pristine TCO matches well with that reported by Idota *et al.*[20] All other samples except the sample of TCO at 500mV on charge were shipped to France for XAS studies prior to being taken to Brookhaven for PDF analysis. One of the XAS samples was compromised, therefore a fresh sample of TCO at 500mV was prepared. The diffraction data for this sample stands out sharply from the other electrode diffraction patterns (shown in **Figure 6.12**), as it was the only pattern which is not dominated by the reflections indexed as Sn metal. The observation of tin metal particles was not initially surprising, but upon further discussions of the data, it was suspected that these samples had been exposed to the atmosphere during return shipment from France. Hence, this data was disregarded.

6.7.2 SnO_2 - a Model Compound

Figure 6.8 shows the structure factor function obtained from the scattering data for SnO_2. This diffraction pattern was acquired as a reference compound, for which the PDF could be calculated both from the experimental diffraction pattern, and from direct calculation. The comparison of the calculated and experimental PDF data are plotted in **Figure 6.9**. The fit of the two data sets is very good, with discrepancies in the experimental PDF resulting from termination errors in the Fourier transform (since the data set cannot be acquired to infinite Q). The position of the first peak at 2.07Å matches the known Sn-O distance in SnO_2 of 2.06Å very well. Similarly the strong Sn-Sn peak correlates with the known metal-metal distance in this structure. These known distances are listed in **Table 6.2**. The position of the PDF peaks are included with the other experimental data in **Table 6.3**. These data are distinct from the *pseudo*-RDF data obtained from EXAFS in that the distances in the PDF are the physical distances present in the material.

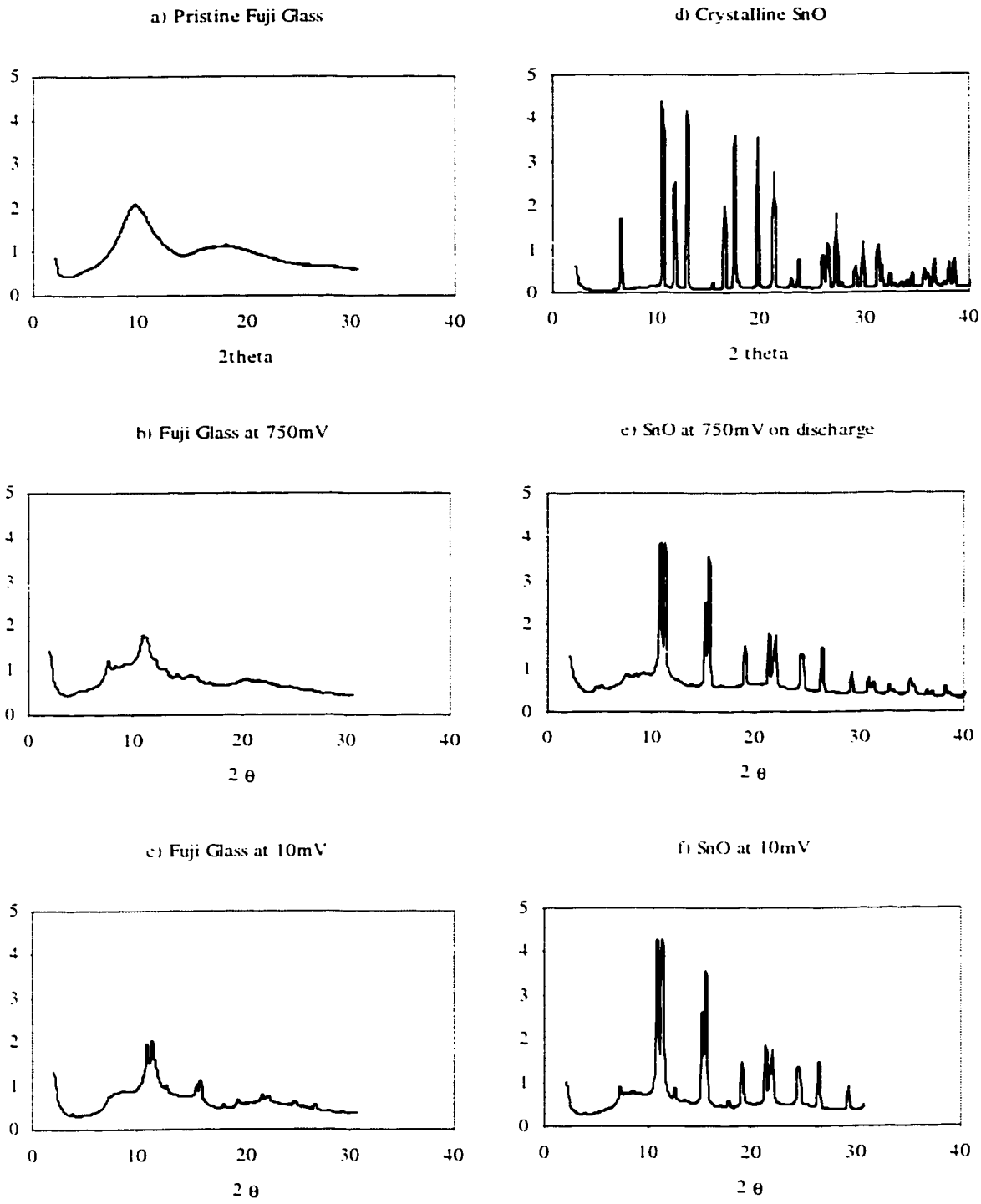

Figure 6.7 Diffraction patterns for samples run at the NSLS. Electrode samples b), c), e) and f) were oxidized, as is evidenced by the strong reflections, particularly for the SnO samples. These reflections correspond to β-tin.

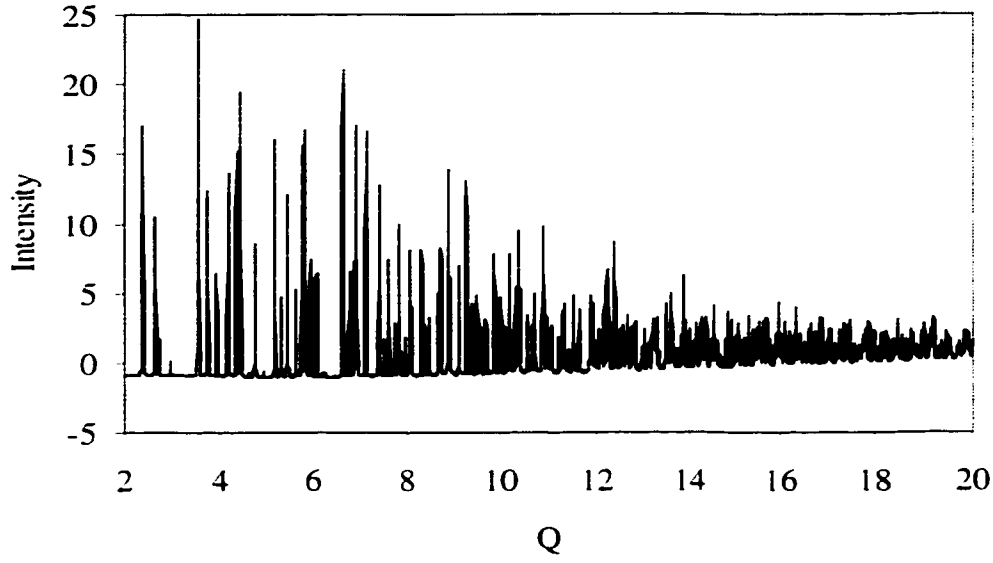

Figure 6.8 Structure factor S(Q) for SnO_2 as a function of scattering angle, Q.

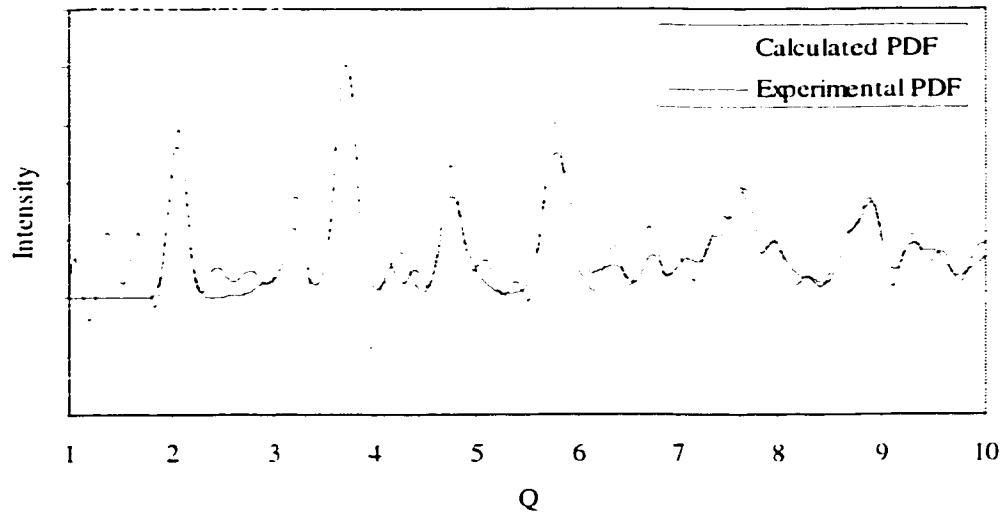

Figure 6.9 Calculated and experimental PDF for SnO_2

	Sn-O Å	Sn-Sn Å
SnO_2	2.04, 2.06, 3.60, 4.23,	3.19, 3.71, 4.74, 5.71

Table 6.2 Interatomic distances in SnO_2[21]

6.7.3 SnO Electrodes

Figure 6.10 shows the structure factor function obtained from the scattering data for SnO itself, as well as three electrodes at 750mV and 10mV on discharge, and at 500mV on charge. The changes in the electrode material are most striking between the pristine material and the electrode at 750mV. The structure has been rearranged from SnO to Sn-metal, yielding a diffraction pattern in which all of the reflections match the phase β-Sn.[22] This phase change is not unexpected, but the high level of order in the tin particles, indicated by the narrowness of the reflections, is surprising. Using the Debye Scherrer equation (equation 2.6) to evaluate the size of the tin particles, an estimated particle size of 375Å was obtained. At deep discharge, the diffraction pattern reflects a much less ordered structure, which is very similar to that calculated by Dahn *et al.* for disordered tin tetrahedra on a bcc lattice.[23] This phase was attributed to the richest lithium-tin phase, $Li_{21}Sn_5$. The implications of this pattern are addressed further in the discussion.

The particle size, or coherence length, calculated on the peak at $2.8Å^{-1}$, is 175Å. This decrease in particle size compared to that found for the electrode at 750mV can be attributed to two related phenomena. First, it is known that volume changes occurring within the particles upon lithium insertion result in crumbling or pulverization of the particles. This is anticipated in large particles, but is less likely in these small domains. Another, related explanation is that the value 175Å represents a coherence length, meaning that the particle itself is still intact, but lithium insertion is not occurring in an ordered fashion, leaving only some ordered domain, within an overall disordered particle. The diffraction pattern for the SnO electrode at 500mV on charge has not changed substantially from that at 10mV, with the exception of a new reflection at $Q = 1.7Å^{-1}$. More intriguing insights are obtained from the PDF data.

The Fourier transform of S(Q) yields the PDF. The PDF data for these diffraction patterns are shown in **Figure 6.11** (excluding SnO itself). The prominent peaks in the PDFs include a short Sn-Sn distance of approximately 3Å, which correlates with the EXAFS data.

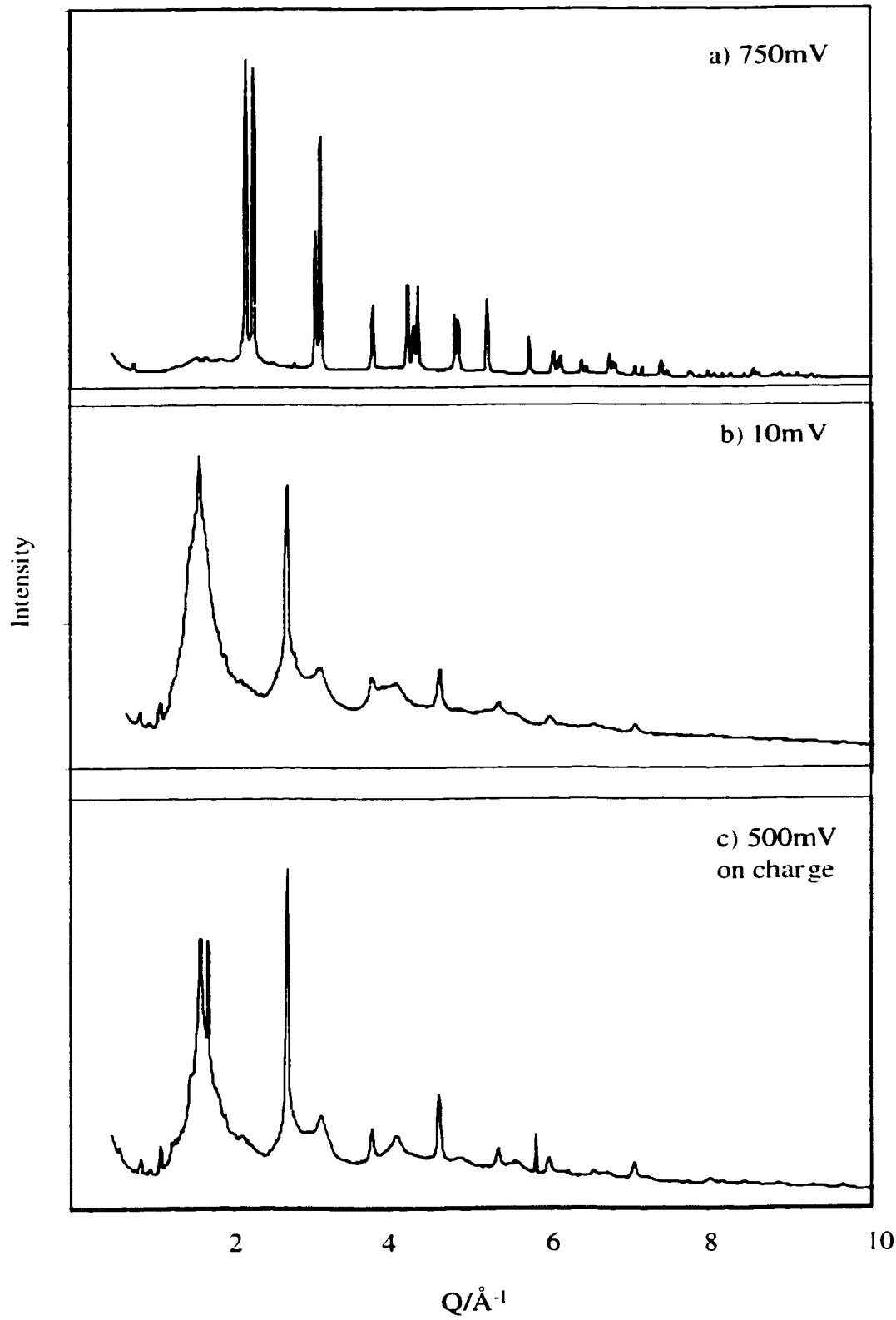

Figure 6.10 X-ray diffraction data for SnO electrodes at a) 750mV and b) 10mV on discharge, and c) 500mV on charge.

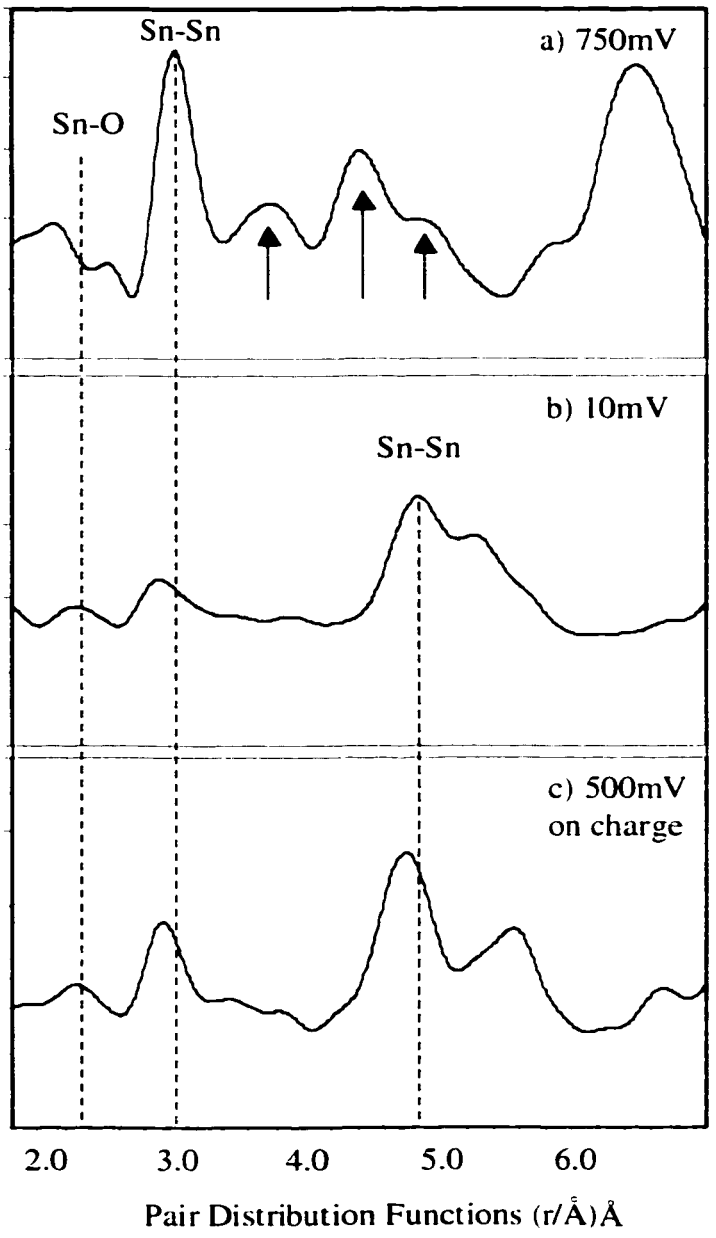

Figure 6.11 Pair Distribution Functions for SnO electrodes at a) 750mV and b) 10mV on discharge, and c) 500mV on charge.

Material	Sn-O Å	Sn-Sn Å	Sn-Sn Å
SnO_2	2.07	3.75, 3.24	4.83, 5.83
TCO Pristine	2.16	3.65	4.4
750mV (discharge)	2.43	2.96	4.76
300mV	2.2-2.45	2.98	4.92
10mV	2.38	2.95	4.96
500mV (charge)	2.30	2.98	4.84
1.5V	2.32	3.06	--
10mV (2^{nd} discharge)	2.32	2.98	4.91, 5.26
SnO 750mV	2.18, 2.57	3.07, 3.8	4.47, 5.0,
10mV	2.34	2.98	4.9, 5.32
500mV (charge)	2.36	3.0	4.8, 5.6

Table 6.3 Sn-O and Sn-Sn distances from PDF analysis of SnO_2, TCO and SnO electrodes

Phase	Sn-Sn distances Å
Sn metal	3.02, 3.18, 3.77, 4.41
Li_2Sn_5	3.13, 3.11, 3.31, 4.91, 5.22, 6.20, 6.08,
LiSn	3.00, 3.16, 3.18, 4.48, 5.17, 6.07,
Li_7Sn_3	2.94, 4.59, 4.67, 4.68, 5.53
Li_5Sn_2	2.883, 4.62, 4.74, 7.15
$Li_{13}Sn_5$	2.865, 4.62, 4.69, 6.64, 7.14
Li_7Sn_2	2.999, 4.75, 4.89, 5.15, 5.17, 7.02
$Li_{21}Sn_5$	4.65, 4.99, 5.07, 5.14, 5.29, 5.46

Table 6.4 Sn-Sn distances in crystalline Li-Sn phases

and with the formation of metallic β-Sn. As well a weak Sn-O peak persists throughout. The persistence of the Sn-O contact at deep discharge differs from the EXAFS data for the same electrode material, in which no Sn-O contact was found, likely due to the high degree of disorder in the material at this potential. The significance of this Sn-O contact will be discussed further in reference to the TCO electrodes. A third feature, which appears only at deep discharge, is the long Sn-Sn contact spanning 5Å. This long Sn-Sn contact is similar to distances found in the Li-Sn phases. The Sn-Sn distance for the Li-Sn phases are listed in **Table 6.4**. Significant among these Sn-Sn distances in the absence of a 3Å distance in the richest lithium phase, $Li_{21}Sn_5$. Each of the other lithium-tin phases include a short Sn-Sn distance of approximately 3Å, as well as a range of longer distances between 4 and 5.5Å. Thus, if the end product of the lithium insertion process were $Li_{21}Sn_5$, there should be no 3Å Sn-Sn distance in the PDF of the electrode at deepest discharge. Since the batteries were run under slow potentiostatic conditions, as described in Chapter 3, we are confident that we are close to equilibrium at all points in the discharge process. The positions of the PDF peaks are listed in **Table 6.3**. Discussions of three models to which this data can be related are given in section 7.6.

6.7.4 TCO Electrodes

The structure factor functions obtained from the scattering data for TCO and the TCO electrodes are shown in **Figure 6.12**. In contrast to the diffraction data obtained for SnO at 750mV, in the case of TCO at 750mV, reflections related to metallic tin cannot be distinguished. This is likely due to the highly amorphous nature of the tin aggregates in the glass. At deep discharge the diffraction patterns are more similar to those obtained for SnO at the equivalent potential. Calculations of the particle size at 10mV for each material gives 175Å vs 30Å for SnO and TCO respectively, proving that the glass matrix acts to prevent aggregation of large tin centers. The structure factor of TCO at 10mV on the second discharge is very similar to that obtained at 10mV on the first discharge, which is indicative of the reversibility of lithium insertion in this material. The minor sharp peaks observed at low Q in all electrode samples are attributed to $LiPF_6$, and other SEI or electrolyte components.

The corresponding PDF data are shown in **Figure 6.13**. **Table 6.3** lists the SnO, short Sn-Sn, and long Sn-Sn contacts present in the PDF data of each electrode system. Again, the PDF patterns of the electrode materials include a short Sn-Sn distance at 3Å. This distance is contracted compared to the Sn-Sn contact in TCO itself, which is 4.4Å. The shortened Sn-Sn contact agrees with the EXAFS data obtained. This 3Å distance persists throughout the PDF patterns, for electrodes at deep discharge, as well as on charge. In contrast, the broader feature centered at 5Å is not present in the PDF of TCO at 750mV, but appears in the PDF of TCO at 300mV on discharge, and is present in the PDF patterns of the TCO electrodes at deep discharge to 10mV and at 500mV on charge. Upon further charge to 1.5V, this feature disappears from the PDF. Concurrent with the appearance of the long tin-tin contact, the shorter tin-tin distance becomes broadened and weaker in intensiy, indicative of increasing disorder with increasing lithium insertion. This observation in the PDF mirrors the changes in coherence length observed in the diffraction patterns of the SnO electrodes. Analogously, in SnO the long tin-tin contact is present at 10mV and at 500mV on charge, but is absent in the PDF of the electrode that was only discharged to 750mV. Thus, the broad 5Å peaks are attributed to the formation of alloy-like domains that are disordered in nature. Moreover, the persistence of the Sn-O peak at all levels of discharge and charge evidences the participation of oxygen in the electrochemical processes.

The relative intensities of the Sn-Sn and Sn-O PDF peaks are somewhat misleading compared to the peaks observed in the EXAFS patterns. This ambiguity arises because the intensity of the PDF peaks is related to the atomic scattering factors for the individual elements. Thus an Sn-Sn interaction will diffract much more strongly than an Sn-O or Sn-Li interaction of comparable distance. For this reason, the relative intensities are not quantitatively useful.

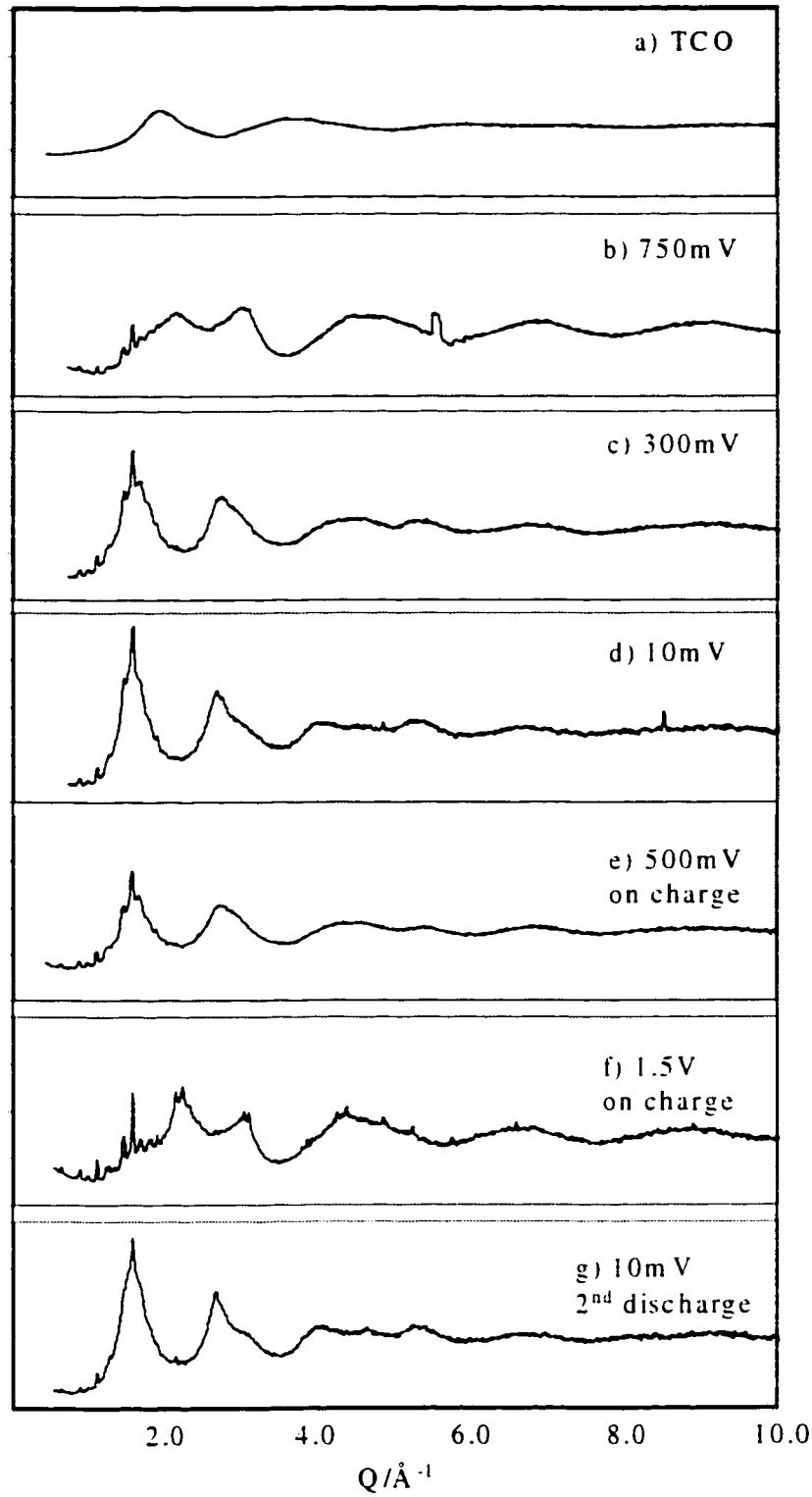

Figure 6.12 X-ray diffraction data for a) TCO, and TCO electrodes at b) 750mV (discontinuity due to beam dump), c) 300mV, and d) 10mV on discharge, d) 500mV and e) 1.5V on charge, and f) 10mV on second discharge.

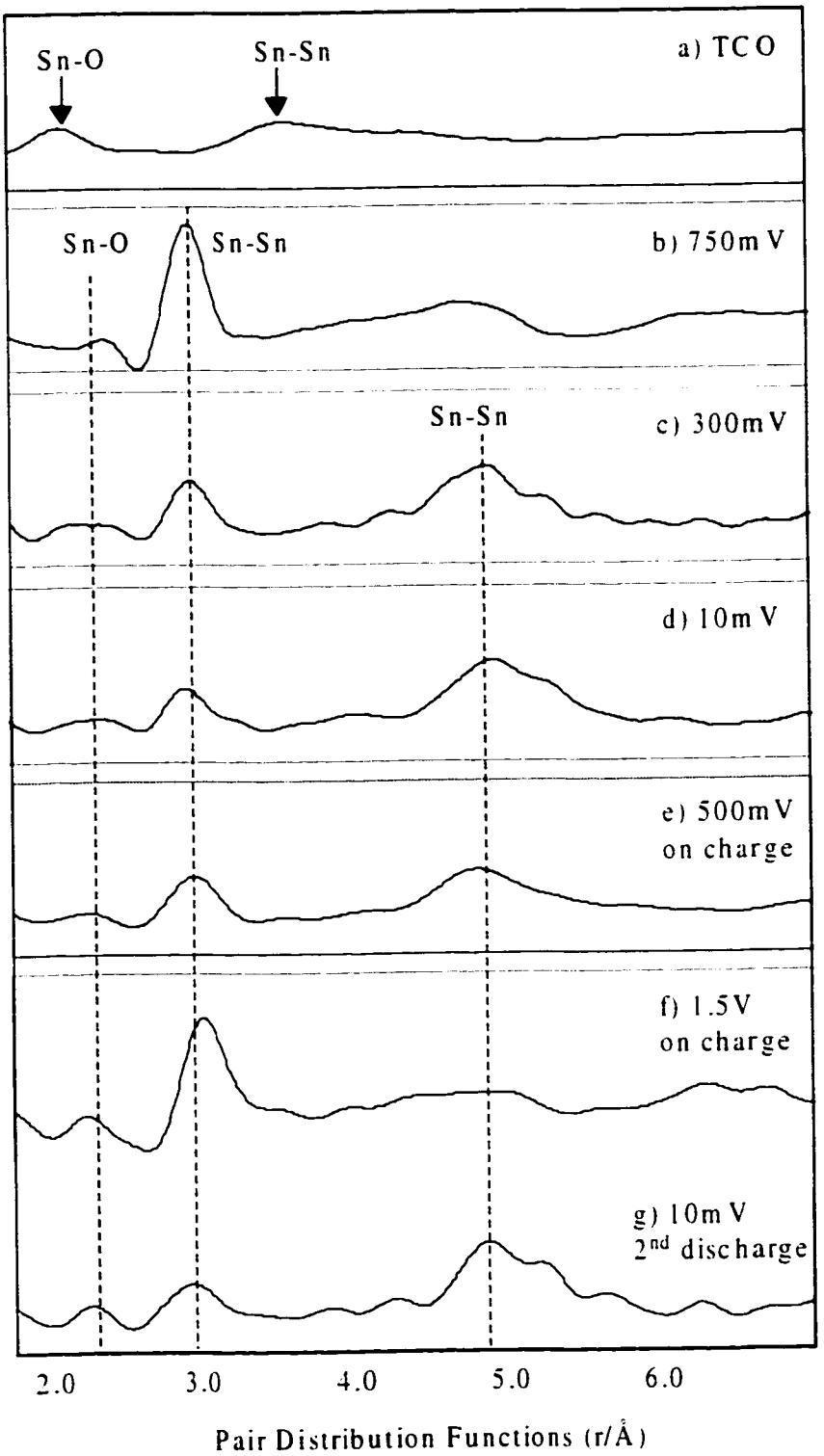

Figure 6.13 Pair distribution functions for a) TCO, and TCO electrodes at b) 750mV, c) 300mV, and d) 10mV on discharge, e)500mV, and f) 1.5V on charge, and g) 10mV on second discharge.

6.8 Interpretations and Comparison of the EXAFS and PDF data

Many fascinating parallels can be drawn between the EXAFS and PDF data and the studies described in the preceding chapters. These data provide the final voice in the counterpoint of the *fugue*. In their own voices the data respond to the subjects of particle size, the formation of alloy domains, and the role of oxygen in the electrochemical processes. Some amount of dissonance arises between the data obtained from EXAFS and PDF, but this is resolved harmoniously by examining the strengths and weaknesses of the methods themselves. For example, the EXAFS data analysis is limited by incoherent backscattering, caused by disorder. Thus Sn-O contacts, which are observed in the PDF, may be obscured in the EXAFS data by the amorphous nature of the system. Similarly, the dependence of the PDF intensities on the atomic scattering factors diminishes the usefulness of comparing intensities in the PDF patterns. Acknowledging these limitations, the combined results nevertheless provide a clearer view of the processes occurring in these systems than any results published to date.

We have contemplated three models for the interactions between tin and the other components of the electrodes. In the context of the data presented in this chapter, arguments for and against each model can be found. The first model is based on the formation of tin clusters such as Sn_5^{2-} or Sn_9^{4-} during discharge. These clusters would be surrounded by oxygen, and enveloped by lithium. The Sn-Sn distances in the tin clusters (Sn_9^{4-}, Sn_5^{2-}) fall into the range of 2.8-3.1 Å and 4.8 Å,[25,26] as illustrated in **Figure 6.14**. This model fits the distances observed in the PDF data, and allows for the persistence of the short Sn-O contact throughout the discharge process. On the other hand, the crystallization of metallic tin particles, as clearly evidenced in the PDF data for SnO at 750mV, and affirmed by the Sn-Sn distances found in the EXAFS studies of both materials at 750mV negates the probability that these metallic tin particles would revert to small, individual clusters with increasing level of discharge.

The second model, purported by the group of Jeff Dahn, involves the formation of lithium-tin domains which resemble the thermodynamically predicted phases, with the exception of being disordered in nature.[24] Deep discharge is correlated with the formation

a)

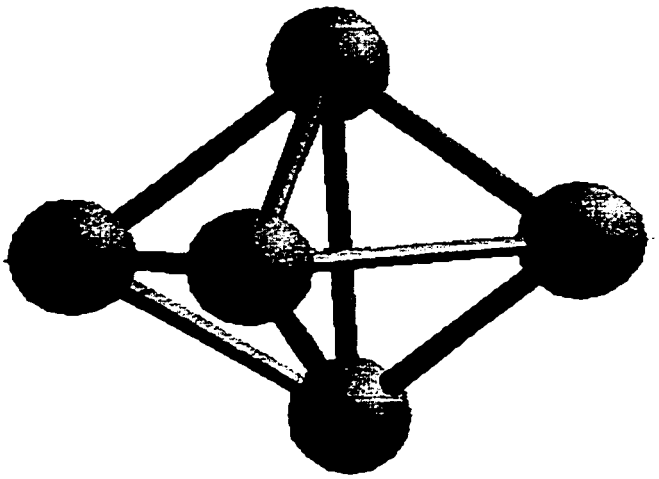

b)

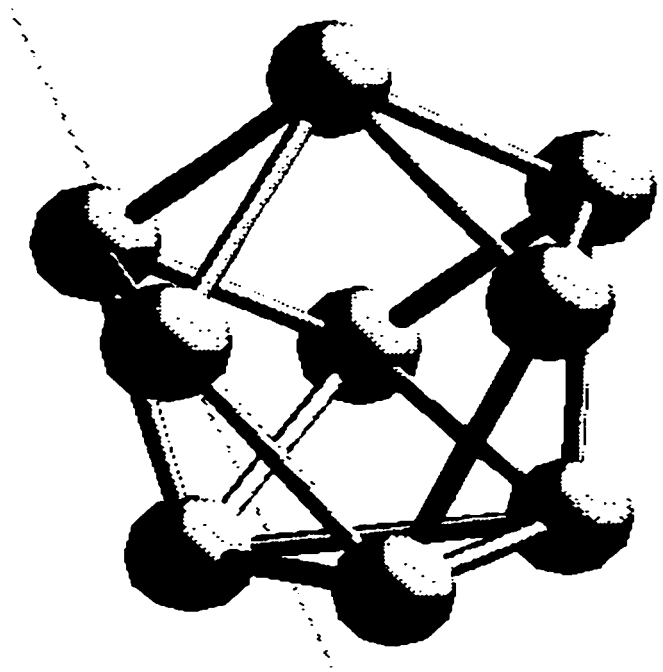

Figure 6.14 a) $(Sn_5)^{2-}$ and b) $(Sn_9)^{4-}$ clusters which have short tin contacts of approximately 3.02Å and 2.97Å respectively , and longer contacts of 4.48 Å and 4.77Å respectively [25,26]

of a disordered $Li_{21}Sn_5$ phase. In this model, the reaction occurring in SnO or TCO is equivalent to that which occurs in tin metal, or other electrode materials which exclude oxygen.[27] A more detailed examination of the calculation of the diffraction pattern for a disordered arrangement of Sn-tetrahedra, is beneficial at this point.[23] The calculated diffraction pattern, and the corresponding hypothetical structures are shown in **Figure 6.15**. This work was carried out to address the consistent appearance of a broad oscillation in the diffraction patterns of tin-based electrodes at Li:Sn ratios of 2.5-4.4. While the calculation is based on a disordered version of the structure of the lithium rich phase, $Li_{21}Sn_5$, it is significant that this diffraction pattern was observed even at moderate levels of discharge, at which this phase was not anticipated to form. We note that this structural moiety, the tetrahderal arrangement of tin atoms around a central lithium atom, is common among several of the Li-Sn phases, including Li_7Sn_3, Li_5Sn_2, $Li_{13}Sn_5$, Li_7Sn_2, and $Li_{21}Sn_5$.[28] Thus it is debatable whether the diffraction pattern observed by Dahn *et al.* and ourselves is unique to the phase $Li_{21}Sn_5$, be it disordered or ordered.

In this second model the oxygen, in the form of lithium oxide, remains at the surface of the lithium-tin domains. In both our EXAFS and PDF studies, the initial formation of metallic tin particles is confirmed. As well, subsequent discharge gives rise to a strong broad feature in the PDF, at 5Å, which is common to all the Li-Sn alloys (see **Table 6.4**). While having much in common, our data refute this model in one key area. This difference between our data and the model of Courtney *et al.* is the presence of a short Sn-O contact throughout the discharge process.[24] The EXAFS data for SnO clearly showed the return of an Sn-O contact upon charge, which may be obscured at deep discharge by excessive disorder. Moreover, the Sn-O contact is present in all of the PDF data, varying slightly in position, but maintaining its intensity. The intensity appears low, but considering the relative atomic scattering factors of Sn and O, it is clear that this is in fact a prominent feature of these data. For such a contact to be observed in the PDF, it must correspond not to a surface Sn-O interaction on the outside of a sizeable Li-Sn domain, but rather to an intimate Sn-O interaction that persists since it is part of electrochemical process.

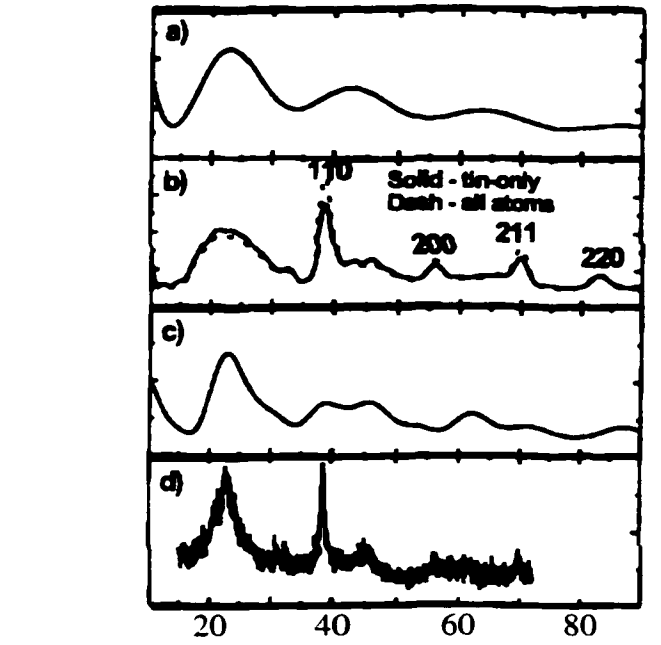

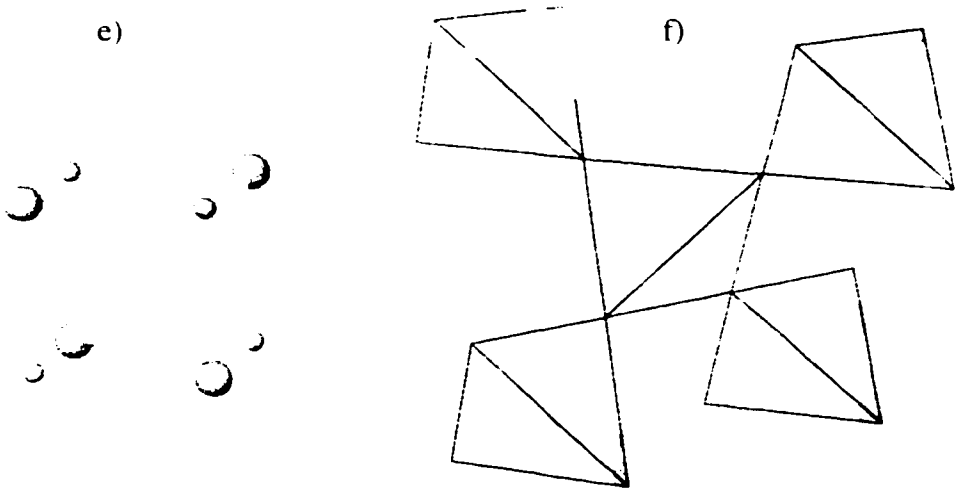

Figure 6.15 Powder diffraction patterns calculated for a) a single tin tetrahedron (depicted in e), b) disordered tin tetrahedra c) grouping of 16 tin atoms, depicted if (f), and d) experimental data obtained by Dahn et al.[23]

One hypothesis is given by Huggins in a recent review of this subject.[29] He develops the idea that the formation of thermodynamically predicted Li-Sn phases is not favoured under dynamic electrochemical conditions. Rather, he proposes that the mobile species (lithium) may reach equilibrium, while the host lattice does not. This would allow for the tin atoms to remain in non-equilibrium positions, while permitting the incorporation of the stoichiometric amount of lithium.

The third model, which in this thesis carries the most credence, is that the lithium-tin interactions in these electrodes are mediated by the presence of oxygen. In the PDF patterns the averaged 5Å distance observed on deep discharge in these electrodes is indicative of the aggregation of lithium-tin alloy like domains. We propose that the domains of Li-Sn alloy-like phases, which give rise to the observed distances in the PDF and EXAFS data, are in fact domains in which oxygen is a substantial component. Support for this model is drawn from the work of Corbett *et al.*, who have expended tremendous research effort in proving the existence of a wide range of interstitial "impurities" present in a variety of intermetallic phases.[30] Examples include Zr_5Sn_3O and La_5Sn_3O.[31,32] In these materials, oxygen may be replaced by carbon, gallium, or germanium, among others. These interstitials have negligible effects on the crystal structure of the parent intermetallics, causing only subtle changes in the unit cell volume. Thus, the argument of Corbett is that such interstitials historically have gone unnoticed, even in bulk phases. We appeal to the work of Corbett *et al.* to support the hypothesis that the electrode materials studied here incorporate large amounts of oxygen as an "interstitial impurity".[30]

Calculations of theoretical PDF curves for the crystalline Li-Sn phases are shown in **Figure 6.16.** This data was surprising due to the presence of a feature at ~3 Å in the PDF of $Li_{21}Sn_5$. This feature arises not from a short Sn-Sn contact, but rather from the preponderance of 3 Å Li-Sn contacts present in this structure. This is surprising due to the low atomic scattering factor of lithium. These results shed a degree of ambiguity onto the interpretations of the experimental PDF data, and rule out the possibility of uniquely identifying the phases formed at each level of discharge. In light of the PDF data, both the lithium-tin alloy formation and the Li-Sn-O ternary phase formation are equally probable.

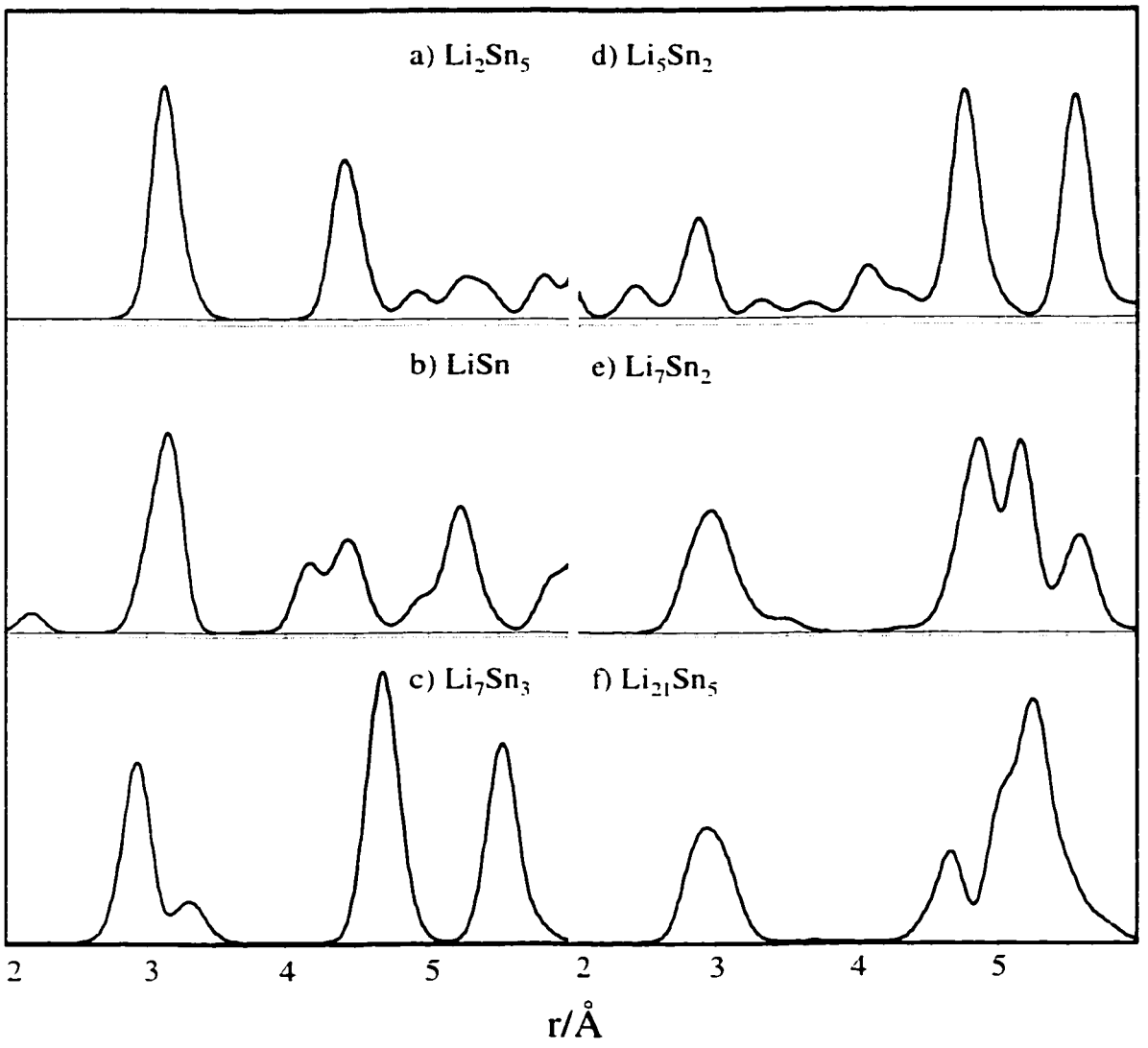

Figure 6.16 Calculated Pair Distribution Functions for Li-Sn Line Phases

At this point we must rely on the ^{6,7}Li NMR evidence to distinguish between the two models. As was shown in the ^{6,7}Li NMR data (Chapter 4), the insertion of lithium into the electrode does not correlate with the formation of phases or domains which exhibit the anticipated Knight shifts. The corollary of this can be drawn from the PDF data. Both the small chemical shift observed in the ^{6,7}Li NMR spectra, indicative of an ionic local environment at lithium, and the presence of an Sn-O contact in the PDF data are manifestations of the role oxygen plays during the electrochemical lithium insertion.

Since the experimental capacity matches the theoretical capacity of SnO (6.4Li), the material has incorporated this lithium without forming $Li_{21}Sn_5$. Thus we return to the question of *where are the electrons?* The fact that oxygen is present at all levels of discharge gives further support to the hypothesis that oxygen may be able to carry extra charge in these materials. As purported in Chapter 4, the calculations of Ceder *et al.* demonstrate that oxygen is capable of carrying charge in positive electrodes (at high potential).[33] We infer that the same participation of oxygen as a charge carrier is probable at low potential. With the combined evidence of the achievable lithium insertion capacity, and the PDF data discussed above, we conclude that the proximity of oxygen throughout the lithium insertion process allows for the electrode materials to accept a significant amount of lithium without undergoing the anticipated phase changes which would be necessary in bulk phases. This enables the electrode to reversibly insert lithium without being hampered by the kinetics limitations of phase formation.

6.9 References

[1] E.A. Stern, *Physical Review B* **10** 3027 (1974).

[2] E.A. Stern in *Chemical Analysis*, vol. **92**. X-ray Absorption, edited by D.C. Koningsberger and R. Prins

[3] B.K. Teo and D.C. Joy EXAFS Spectroscopy Techniques and Applications Plenum Press, New York (1981).

[4] F.W. Lytle, D.E. Sayers, and E.A. Stern *Physical Review B* **11** 4825 (1975).

[5] Y. Waseda, *Progress in Material Science* **26** 1 (1981).

[6] S. Mukerjee and J. McBreen, *Journal of the Electrochemical Society* **146** 600 (1999).

[7] B. Ammundsen, D.J.Jones, J.Roziere, F.Villain *Journal of Physical Chemistry B* **102** 7939 (1998).

[8] J.P. Peres, A. Demourgues, C. Delmas, *Solid State Ionics* **111** 135 (1998).

[9] S. Passerini, D.B. Le, W.H. Smyrl, B. Berrettoni, R. Tossici, R. Marassi, M. Giorgetti *Solid State Ionics* **104** 195 (1997).

[10] M. Gioretti, S. Passerini, W.H. Smyrl, S.Mukerjee, X.Q.Wang, J.McBreen *Journal of the Electrochemical Society* **146** 2387 (1999).

[11] C. Rossignol, G. Ouvrard, E. Baudrin, J.M. Tarascon, Proceedings of the Electrochemical Society Meeting, Edinburgh 1998.

[12] S. Mukerjee *et al.* Proceedings of the Electrochemical Society Meeting, Edinburgh 1998.

[13] Y. Waseda The Structure of Non-Crystalline Materials: Liquids and Amorphous Solids McGraw-Hill NewYork, 1980.

[14] B.H. Toby and T. Egami, *Acta Crystallographica* **A48** 336 (1992).

[15] Analysis method based on private communication with Wojtek Dmowski

[16] International Tables of Crystallography Volume C: Mathematical, Physical and Chemical Tables, ed. A.J.C. Willson, Kluwer Academic Publishers, (1992).

[17] Y. Wang, J. Sakamoto, C.K. Huang, S. Surampudi, S.G. Greenbaum. *Solid State Ionics* **110**, 167 (1998).

[18] T. Brousse, R. Retoux, U. Herterich, D.M. Schleich. *J.Electrochem.Soc.* **145**, 1 (1998).

[19] W. Liu, X. Huang, Z. Wang, H. Li, and L. Chen *J.Electrochem.Soc.* **145**, 59 (1998).

[20] Y. Idota, T. Kubota, A. Matsufuji, Y. Maekawa and T. Miyasaka, *Science*, **276**, 1395 (1997).

[21] M.J.P. Musgrave, *Proceedings of the Royal Society (London)*, **272**, 503 (1963).

[22] JC-PDS International Center for Diffraction Data, 1996 USA.

[23] J.R. Dahn, I.A. Courtney, and Ou. Mao, *Solid State Ionics*, **111**, 289 (1998).

[24] I.A. Courtney and J.R. Dahn, *Journal of the Electrochemical Society*, **144** 2045 (1997).

[25] J.D. Corbett and P. A. Edwards, *Journal of the American Chemical Society*, **99**, 3313 (1977).

[26] P. A. Edwards and J.D. Corbett, *Inorganic Chemistry*, **16**, 903 (1977).

[27] O. Mao, R.L. Turner, I.A. Courtney, B.D. Fredericksen, M.I. Buckett, L.J Krausse, and J.R. Dahn, *Electrochemical and Solid State Letters*, **2**, 3 (1999).

[28] U. Frank and W. Muller, *Z. Naturforschung* **30b** 316 (1975).

[29] R.A. Huggins *Journal of Power Sources* **81-82** 13 (1999).

[30] J.D. Corbett, E. Garcia, A.M. Guloy, W-.M. Hurng, Y-.U. Kwon, E.A. Leon-Escamilla *Chemistry of Materials* **10** 2824 (1998).

[31] Y-.U. Kwon, J.D. Corbett *Chemistry of Materials* **4** 1348 (1992).

[32] Y-.U. Kwon, M.A. Rzeznik, A.M. Guloy, J.D. Corbett *Chemistry of Materials* **2** 546 (1990).

[33] G.Ceder, M.Chiang, D.R.Sadoway, M.K.Aydinol, Y.I.Jang, B.Huang *Nature* **392** 694 (1998).

Chapter 7 Parallel Studies of $NaMoO_3$ Electrodes

In the *fugue* a transition from the tonic (I) key to the dominant (V) key for a period of several bars may be used to add musical character. In the analogy to the *fugue*, this chapter is comparable to a modulation to a separate key, where the original TCO glass represented the tonic key and $NaMoO_3$, a related anode material, represents the dominant key. This chapter describes the studies of the electrochemical performance and properties of a transition metal oxide anode material, drawing on the similarities and differences between this material and the tin oxide materials described previously to highlight the intriguing characteristics of TCO.

7.1 Electrochemical Performance

The electrochemical performance of amorphous $NaMoO_3$ was evaluated as an anode material. This material was patented by Leroux and Nazar and exhibits excellent reversible capacity and cyclability.[1] The voltage profile for discharge, charge, and second discharge and the corresponding cyclic voltammogram are shown in **Figure 7.1**. Characterizations of the electrochemical properties of this system are presented elsewhere.[2] For comparative studies with the tin oxide systems, several electrode samples were prepared and characterized using solid-state NMR. The interaction between lithium and the transition metal center is purported to be quite different than the interaction between tin and lithium. This hypothesis is born out in the NMR and EXAFS results obtained.

7.2 1D NMR Analysis of $NaMoO_3$

Figure 7.2 shows the spectra acquired under MAS conditions for a sample at a *very* shallow depth of discharge (2.5V). The single narrow peak at ~0.2 ppm is ascribed to Li^+ in a highly ionic environment: namely electrolyte adsorbed near the Mo-oxide surface or electrolyte decomposition products on the surface of the oxide (SEI formation). Deeper discharge to 300 mV (corresponding to 6.4 moles of Li) results in the lineshape shown in **Figure 7.2b**. The data for the deconvolutions are listed in **Table 7.1**.

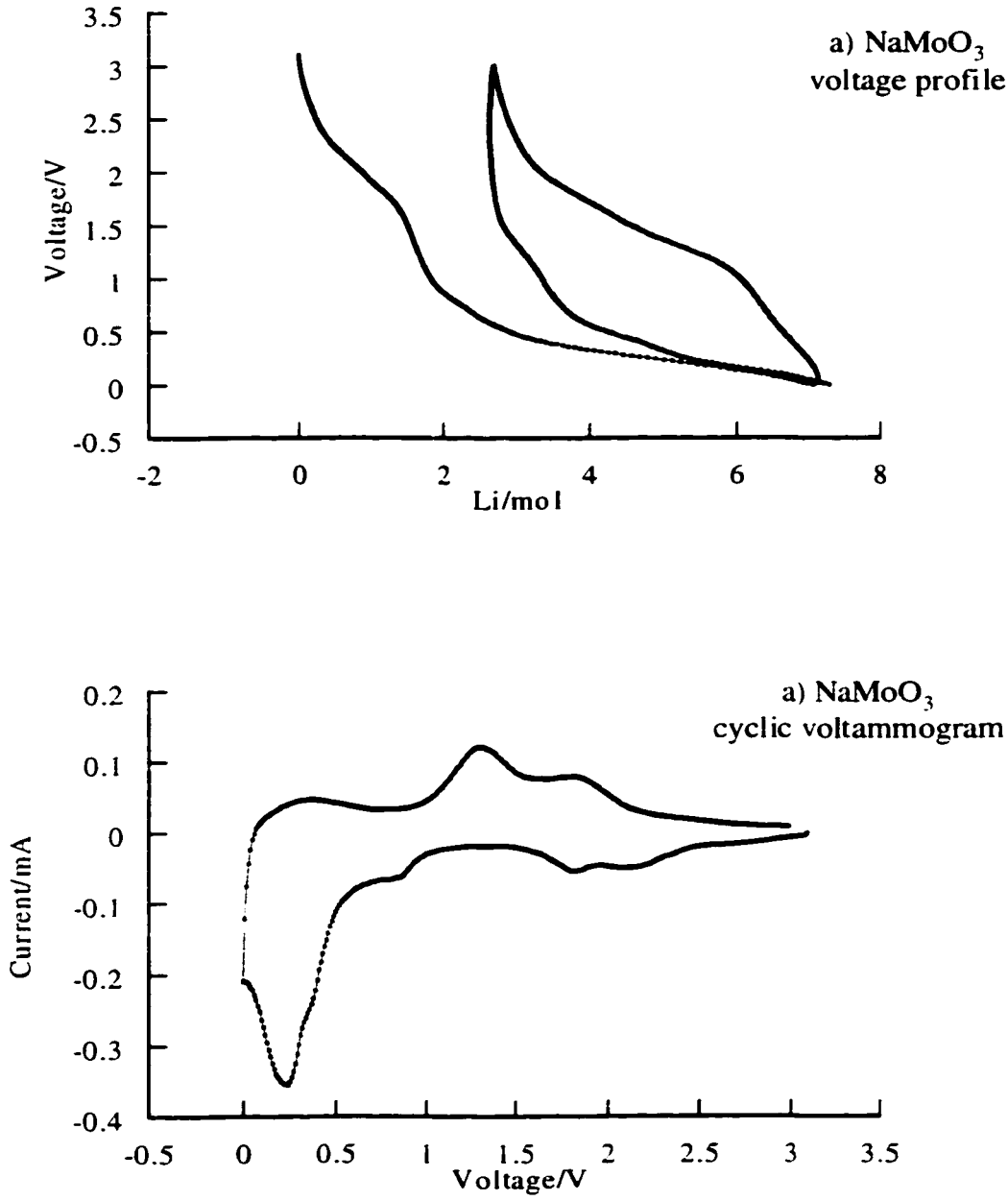

Figure 7.1 Electrochemical characterization of $NaMoO_3$a) voltage profile and b) cyclic volammogram

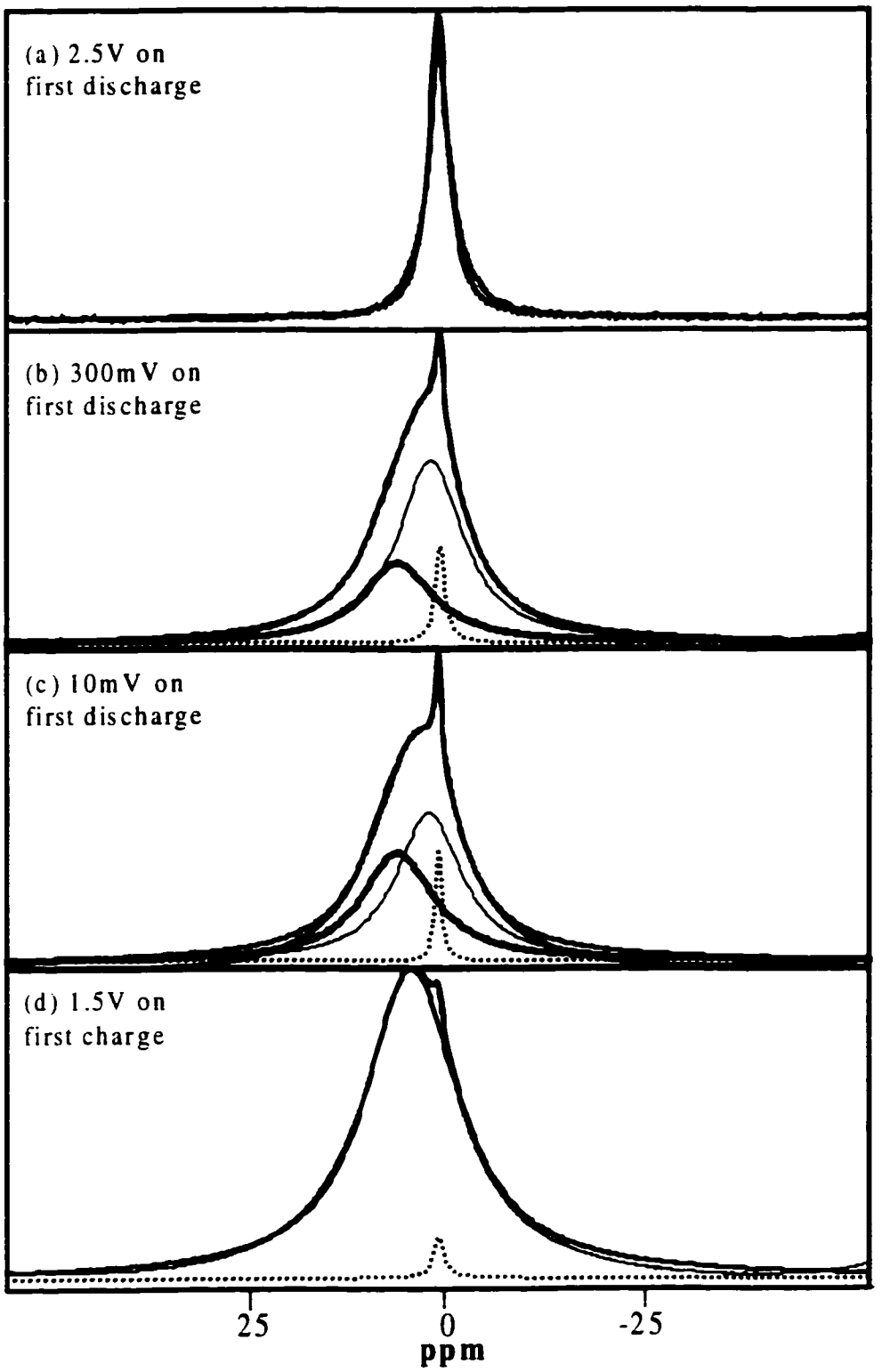

Figure 7.2 ^{7}Li NMR data for $NaMoO_3$ electrodes at a) 2.5V, b) 300mV, and c) 10mV on discharge, and d) 1.5V on charge

In addition to the electrolyte contribution (0.2ppm, 5% integrated intensity, I), two Li sites of roughly equal line width are evident. We ascribe peak (1) at 1.4 ppm (I=63%) to a "lithium oxide-like" species, and peak (2) at 5.2 ppm (I=32%) to a highly reduced, disordered Li-Mo-suboxide. This assignment is made partly on the basis that the latter peak increases in relative intensity on full discharge (x= 7.8Li) to 10mV (**Figure 7.2c**), such that the ratio of (1)/(2) is now approximately 1:1; and partly on the basis of our observation of similar lineshapes and chemical shifts in tin oxides on discharge and charge cycles.[3] We note that no sites are apparent at higher frequency that would correspond to metallic Li (256ppm), lithium in a "metallic" environment that would give rise to a substantial Knight shift. Knight shifts have been well documented for a number of intermetallic compounds and alloys, although the magnitude of the shift is significantly less for alloys than the parent metals.[4] Lithium in the highly reduced anode is also not in direct contact with paramagnetic Mo centres, as this would result in a contact-shift to extremely high frequency which is not observed. **Figure 7.2d** shows the spectrum obtained on subsequent charging of the electrode to 1.5V (x= 4.0). Along with the minor electrolyte contribution, only a single broad site can be distinguished at 3.4ppm. During de-insertion, redistribution of lithium into a variety of different environments appears to cause "smearing" of the lithium sites, and hence overlap of the spectral lineshapes. This can be correlated with the hysteresis observed between discharge and charge processes: *i.e.*, the two processes are notably inequivalent.

$NaMoO_3$ Electrode	Peak Position/ppm	Linewidth/kHz	Integrated Intensity
2.5V	0.25	0.4	100%
300mV	0.3	0.4	
	1.4	1.9	66%
	5.2	1.5	34%
10mV	0.2	0.2	
	2.0	1.6	48%
	5.2	2.0	52%
1.5V on charge	0.3	0.2	
	3.4	2	100%

Table 7.1 Deconvolution parameters for ^7Li NMR of $NaMoO_3$ electrodes

7.3 Relaxation Studies of $NaMoO_3$

Since the possible relaxation mechanisms in $NaMoO_3$ are different than those in the tin oxide based materials, this material is treated separately. The transition metal is known to be paramagnetic, and hence the relaxation behaviour of lithium in this system will be dominated by interaction with this electron. In the tin-oxide based materials, the accessible oxidation state of Sn are limited to Sn^0, Sn^{2+}, and Sn^{4+}, all of which are diamagnetic species. Hence relaxation mechanisms due to unpaired electrons are not possible in these systems.

Unlike studies of paramagnetic electrodes by other groups, no evidence for significant Fermi contact shifts was found for the $NaMoO_3$ electrodes studied. On the other hand, the extremely short relaxation time (20ms at ambient temperature) indicates that this nucleus is subject to relaxation mechanisms which are more efficient than those operable in the tin-oxide based systems, and in fact, even more efficient than the conduction electron mechanism effecting the relaxation time of lithium metal. The T_1*T versus temperature data are plotted in **Figure 7.3**, and are also compared to the data for lithium metal. In contrast to the Li-Sn system, there are no known bulk phases of Mo-Li alloys, making the identity of the material formed at the end of electrochemical reduction highly intriguing. The thermodynamic stability of this species created at this potential is undoubtedly very low. Again, the relaxation mechanisms of the electrochemically active species dramatically effect the T_1 values of the SEI.

This Korringa predicted behavior was exhibited by Li metal, whose ^{7}Li MAS NMR spectrum displayed a single peak with a typical Knight shift of 256 ppm and constant T_1*T relaxation behaviour (see upper linear curve). The *non*-linear curves for the reduced Mo-bronze, however, are not indicative of simple metallic behavior. Significantly, the broad lineshape, comprising both the "Li_2O" and Li-Mo species, experiences spin-lattice relaxation more rapid than "ionic" lithium, and even faster than that of Li metal. The rapid relaxation implies strong interaction of the ^{7}Li nucleus in close proximity (but not direct contact) with paramagnetic Mo centers, since the linewidth demonstrates that local quadrupolar coupling is too small to account for such short relaxation times. The narrow lineshape attributed to electrolyte/SEI shows

dependence on T which is relatively linear as expected, although the absolute value of T_1 is comparable to Li metal, and much lower than expected for lithium in a strictly ionic enviroment. There is, however, some degree of complex behavior suggestive of contribution from paramagnetic effects. The degree of curvature of the lineshape in both cases can be rationalized by considering spin-diffusion, which allows the relaxation of one set of ^{7}Li nuclei to influence the relaxation of a neighbouring ^{7}Li nuclei. The lithium sites corresponding to the"Li_2O"/Li-Mo species and the electrolyte/SEI layer hence are in intimate contact with each other, such that spin-diffusion mechanisms between them can occur. Spin diffusion is very efficient between Li nuclei owing to the high γ, natural abundance of the ^{7}Li nucleus, as well as their presumed proximity. Spin diffusion allows the relaxation of one ^{7}Li nucleus to affect the relaxation of a neighbouring nucleus. This interaction can approach a length scale of 200Å for ^{1}H nuclei in organic polymers. It is clear that the two types of lithium are in intimate contact with each other, such that spin-diffusion mechanisms come into play.

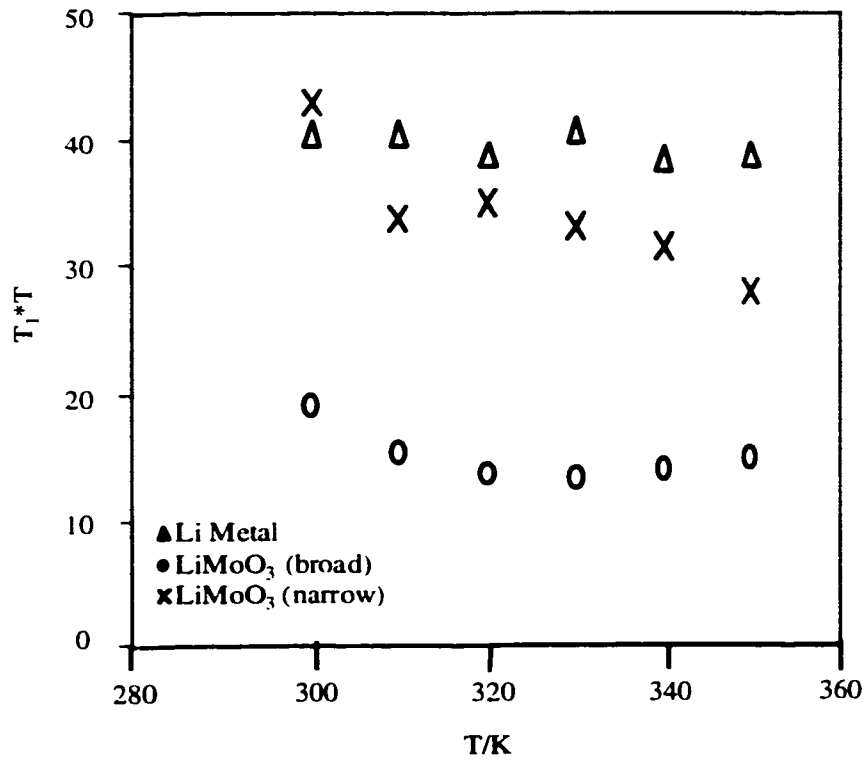

*Figure 7.3 T_1*T versus temperature for an $NaMoO_3$ electrode at 10mV compared to Li metal*

In summary, NMR shows that there is strong evidence for two general types of lithium environment (aside from the electrolyte contribution). These cannot be distinguished by their T_1 behavior, but can be distinguished by lineshape deconvolution. One is more closely associated with oxygen and ionic in nature (1.4 ppm); the other is less ionic (5.2 ppm), and more closely associated with the Mo centres.

7.4 EXAFS data for $NaMoO_3$ Electrodes

The data presented in this section was collected and analyzed by Dr. Fabrice Leroux.[2] It is given here for completeness. We examined the *pseudo*-radial distribution functions (RDF) derived from the EXAFS spectra, shown in **Figure 7.4**. Similar to the studies of the tin oxide electrodes, the question is whether the Mo is indeed reduced to its metallic state, and if not, how Mo and oxygen are distributed in the matrix. Progressive deep discharge of the Mo-bronze results in a drastic change in the local enviroment compared to the structural arrangement of the starting material, $NaMoO_3$, and shows that the material becomes more disordered as a function of reduction potential, consistent with its amorphous nature. Diminution of the first Mo-O shell interaction also occurs, as shown by the intensity decay of the first peak, which implies a loss of oxygen at low potential. The results of the fit for the first two shell contributions (Mo-O and Mo-Mo) are given in **Table 7.2**. The lineshape for the starting material, $NaMoO_3$ was fit using four different <Mo-O> distances, providing a model similar to the structure of α-MoO_3.[5] Note that with increasing degree of reduction, the "long" distances decrease, and the number of oxygen nearest neighbors decreases from roughly six to one. The <Mo-O> first shell distances converge to a long and short distance. Hence for the reduced materials, two <Mo-O> bond lengths yielded an excellent fit. The <Mo-Mo> distance also changes with Li insertion, decreasing from 3.46 Å in α-MoO_3, to 2.51Å in the material discharged to 5 mV. The latter span is exactly the same as the <Mo-Mo> between edge-sharing octahedra within chains of MoO_2 in the rutile structure, and

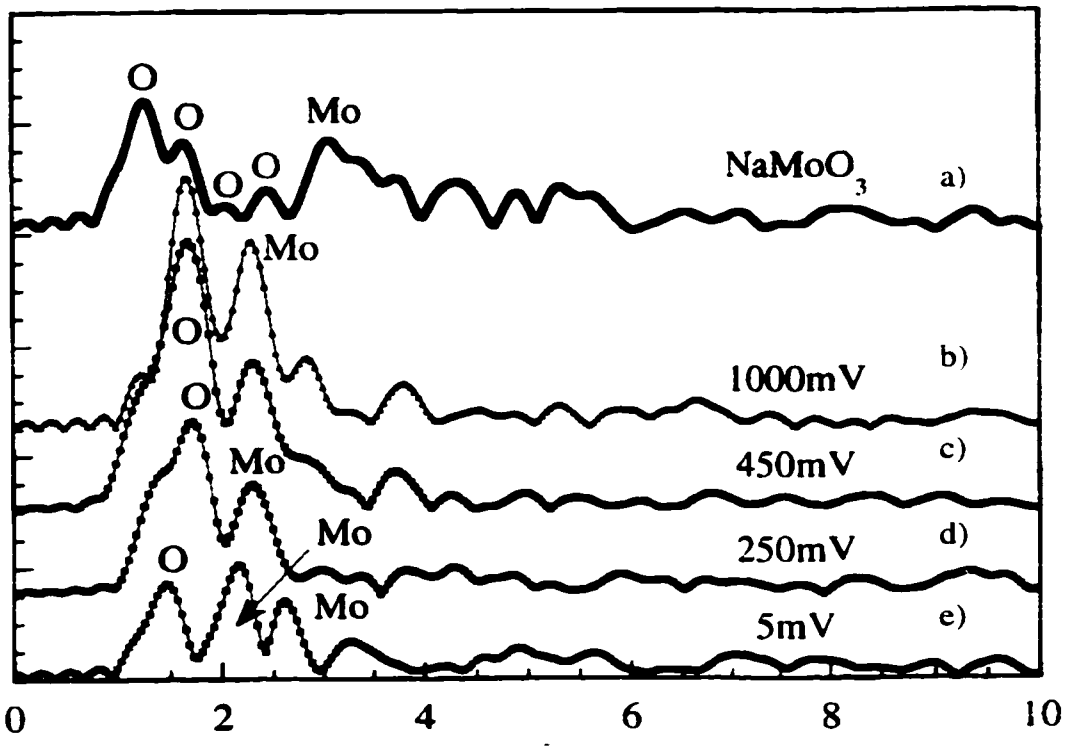

Figure 7.4 Pseudo-radial distribution functions for a) pristine $NaMoO_3$ as well as electrode materials extracted following lithium insertion at b) 1000mV, c) 450mV,d) 250mV, and e) 5mV.

Material	Atom	R(Å)	N	σ(Å)[a]	ρ(%)
	O	1.74(0)	1.93	0.066	
$NaMoO_3$[b]	O	1.95(5)	1.71	0.066	2.3
	O	2.23(1)	0.42	0.066	7.7
	O	2.43(6)	1.62	0.066	
	O	2.09(4)	3.64	0.069	
1000mV	O	2.23(1)	1.67	0.069	0.9
	Mo	2.58(9)	1.08	0.078	
	O	2.06(6)	3.98	0.072	
450mV	O	2.15(3)	2.62	0.072	1.4
	Mo	2.59(5)	0.84	0.077	
	O	2.02(3)	1.91	0.073	
250mV	O	2.12(8)	2.98	0.073	0.6
	Mo	2.56(7)	0.92	0.096	
	O	1.99(6)	0.27	0.058	
5mV[c]	O	2.10(3)	0.70	0.058	6.2
	Mo	2.51(5)	1.30	0.111	

Table 7.2 EXAFS results for MoO_2 (used as reference), $NaMoO_3$, $NaMoO_3$-electrode materials after different depths of discharge, using Δk=3 to 16 $Å^{-1}$. R=coordination distance, N=coordination number, σ=Debye-Waller factor and ρ=quality of the refinement.*

**Scale factor, $S_0^2(Mo)$=0.629, and free mean path, Γ(Mo/O)=0.822 and Γ(Mo/Mo)=0.206, were obtained from refinement of the reference sample, MoO_2: crystallographic data for MoO_2 (rutile) - oxygen: 1.972 [1], 1.977 [1], 1.984 [1] and 1.995 [1] Å, averaged at 1.982, 2.065 [1] and 2.073 [1] Å, averaged at 2.069 Å, molybdenum: 2.511 [1] and 3.112 [1] Å).*

[a] σ was linked for the oxygen shell refinements.

[b] Two different fits were carried out (closest distances and the whole shell).

[c] Δk=3.5 to 12 $Å^{-1}$

slightly shorter than that within Mo metal itself . Our estimate of the Mo-valency from simple bond-sum calculations[6] based on these results (assuming O^{2-}) yield an average oxidation state of $Mo^{+0.6}$ for the material discharged to 5mV. The consistent picture of the process that occurs with increasing Li insertion/reduction is hence one of increasing contraction, and disarrangement of the molybdenum oxide structure until a disordered molybdenum *sub*-oxide of low Mo-valency is formed at the lowest potential. The removal of oxygen nearest neighbors from the Mo first shell is presumably accompanied by formation of an amorphous lithium oxide, similar to what has been proposed for the first stage in the Sn-oxide systems.[7] This also gives rise to the high cell polarization observed during the reverse process (charge), as some migration of the oxide ions within the lattice must occur during this step.

7.5 Discussion of NMR and EXAFS data for $NaMoO_3$

The combined electrochemical, NMR and XAS data provide direct evidence for a mechanism in which Li insertion in $Na_{0.25}MoO_3$ at low potential can be summarized by the following:

$$Na_{0.25}MoO_3 + 7.8\ (Li^+ + e^-) \rightarrow y(Na,Li)_2O + Li_zMoO_{3-y}$$

where (y*2+z)= 7.8. The cohesive picture that emerges from these studies is one of formation of a disordered, highly oxygen deficient lithium/molybdenum based-nanocomposite at low potential, in intimate association with lithium oxide. Such composite mixtures have been hypothesized to account for Li "uptake" in other metal oxides.[8] The process hence gives rise to an irreversible capacity corresponding to the formation of lithium oxide, and a reversible capacity (up to 940 mAh/g in the voltage window 3.5- 0.005V).

Quantitatively, the situation is slightly more complex than this, however. The values of y and z that result from simple consideration of the irreversible component in the electrochemistry are 1.3 and 5.2, respectively, indicating a formulation of $Li_{5.2}MoO_{1.7}$ for the sub-oxide. The NMR data suggests that at full discharge, the ratio of Li in "lithium-oxide" is approximately equal to that in the Li-Mo-oxide of stoichiometry $Li_{3.8}MoO_{1.0}$. Based on this, there must be more significant participation of the Li in the so-called lithium oxide in the reversible electrochemical process. Therefore, the material

displays a relatively high average charge potential consistent with the necessity of oxygen transport from the Li_2O to the lithium/TM sub-oxide on charge during oxidation. This gives rise to partial reformation of the higher molybdenum oxide and the observed hysteresis.

7.6 Comparison of Tin and Molybdenum Oxide Electrodes

The intriguing comparison between the two systems, tin oxide and molybdenum oxide stems from the nature of their interaction with lithium in the bulk. While lithium-tin alloys are well documented phases, no such corresponding lithium-molybdenum alloys are known. Yet $NaMoO_3$ has been shown to insert very large molar ratios of lithium, corresponding to very deep reduction of the molybdenum centers. If this interaction does not involve the formation of an alloy, as is unlikely due to their non-existence in the bulk phases, it is also plausible that the interaction of lithium with tin is not one of the anticipated alloy formation. At least, not in the case of the TCO glasses, and possibly even tin oxide itself.

One cannot readily distinguish between a disordered Li-Sn nanophase in which Li is homogeneously distributed within the entire particle or an electron-rich Sn cluster that is surrounded by Li (and oxygen). Deep discharge of Li into molybdenum oxides to form highly reduced, lithium rich Li-Mo-O nanocomposites gives rise to ^7Li chemical shifts comparable to those found for fully discharged TCO, 5.2 ppm and 10ppm respectively. As Li-Mo alloy formation is not known to occur, partial sharing of the Li environment and the electronic charge distribution which probably involves oxygen must occur in these materials. By analogy, a similar electronic distribution and proximity of oxygen may also be responsible for the observed chemical shifts in the tin oxide systems. As well, the presence of interstitial oxygen has been established for many intermetallic phases previously thought to be pure metals.[9]

Thus our departure from the original key has added a voice to the counterpoint of the *fugue*. Drawing on the data obtained from this separate material, $NaMoO_3$ support for the countersubject concerning the participation of oxygen in the tin-composite-oxide electrodes is attained.

7.7 References

[1] F.Leroux and L.F.Nazar, US Patent # 9-199,635

[2] F. Leroux, G.R. Goward, W.P. Power, and L.F. Nazar *Electrochemical and Solid State Letters*, **1**, 255 (1998).

[3] G.R. Goward, F. Leroux, W.P. Power G. Ouvrard, W. Dmowski, T. Egami, and L.F. Nazar, *Electrochemical and Solid State Letters* **2** 367 (1999).

[4] G. C. Carter, L.H. Bennett and D.J. Kahan, Progress in Materials Science, Ed. B. Chalmers, J.W. Christian, and T.B. Massalski, Chap 3, Pergammon Press (1977).

[5] L. Kihlborg, *Ark. Kemi*, **221**, 357 (1963).

[6] R.E. McCarley, *Polyhedron*, **5**, 51 (1986).

[7] I.A. Courtney, and J.R. Dahn, *J. Electrochem. Soc.*, **144**, 2943 (1997).

[8] S. Denis, E. Baudrin, M. Touboul, and J-M. Tarascon, *J. Electrochem. Soc.*, **144**, 4099 (1997).

[9] J. Corbett, E. Garcia, A. M. Guloy, W-M. Hurng, Y-U Kwon and E. A. Leon-Escamilla, *Chemistry of Materials*, **10**, 2824 (1998).

Chapter 8 Summary and Outlook

The 1997 report of Li insertion into TCO demonstrated that the electrochemical performance of the glass was enhanced compared to that of crystalline SnO, and also suggested that the reaction mechanism was one of insertion as opposed to an alloying process. In view of the extensive studies that have appeared recently suggesting that the fundamental process in tin oxides must involve the reaction of lithium with tin centers to a maximum stoichiometry of $Li_{21}Sn_5$, it is evident that the mechanism of reaction is at issue. It is also unclear precisely what allows TCO glass to exhibit such improved electrochemical response compared to SnO. Our studies presented here shed light on the mechanisms at work in these very different materials. The critical insights gained include an understanding of the interplay between the lithium and tin and oxygen centers; the role of thermodynamics in this process; and evidence for the participation of framework cations in the reversible reactions within the electrode.

The first conclusion of this thesis concerns the role of the glass network ions, including aluminum, phosphorus and boron, which was ascertained through multi-nuclear NMR studies. The conclusion drawn from these studies is that the network ions are participants in the electrochemical insertion of lithium into TCO, acting as a flexible host and allowing oxygen, tin and lithium to reversibly react during discharge and charge. The glass network also inhibits the aggregation of lithium-tin domains, as was evidenced directly through the X-ray scattering data for SnO compared to TCO at deep discharge. The average particle size in these two materials differs by almost an order of magnitude. The effect of particle size was also observed indirectly through the $^{6,7}Li$ NMR of the two materials. Upon charge, the TCO lithium returned immediately to lower, chemical shift, indicative of the close proximity of oxygen, and the highly ionic nature of the lithium, whereas this process was impeded in SnO. This effect was illustrated more dramatically in the ^{7}Li NMR spectra of the cycled electrodes, in which the tendency toward aggregation of Li-Sn domains in SnO was observed through the appearance of a high frequency resonance following 5 cycles of the battery. In contrast, no such aggregation occurred in TCO, even following 10 battery cycles. Therefore, limiting the particle size

of the tin domains in the electrode is key to ensuring its cyclability. This is achieved in TCO through the participation of the flexible glass matrix.

The second fundamental finding of this thesis is the significant role played by oxygen in the TCO, and SnO electrode materials. While the original study by Fuji indicated that the electrochemical reaction with lithium involved and insertion process, in which the oxide remained in tact, the contending theory of Dahn *et al.* is based on the *in-situ* formation of lithium-tin alloys in both oxide, and other mixed conductor electrode materials. We have proposed that the interactions of tin and oxygen are important to the electrochemistry, based on the observed persistence of Sn-O contacts throughout the discharge and charge processes. We conclude that the model which most fits all of the PDF, EXAFS, and multi-nuclear solid-state NMR data is one in which the insertion of lithium into TCO results in the formation of highly sub-divided amorphous metallic tin, followed by the creation of ternary phase domains, incorporating lithium, tin, and oxygen. The tendency to include oxygen is favoured by the purported ability of oxygen to carry charge, thus allowing for the insertion of the full amount of lithium, without necessitating the complete structural rearrangement of the tin coordination to form $Li_{21}Sn_5$. The rearrangement of the tin sub-lattice is kinetically hindered, particularly at ambient temperature. The $^{6,7}Li$ NMR data, prove that lithium remains highly ionic throughout the electrochemical process, thus favouring a highly oxidic environment, as opposed to the intermetallic environment of the Li-Sn bulk phases.

Returning to the theme of the *fugue*, the thesis has called on a variety of voices to address the subject of the electrochemical behaviour of TCO as compared to SnO. The countersubjects, including the role of "spectator" glass network ions, the effect of particle size, and the participation of oxygen have been addressed indirectly or directly by each voice. The coutrapuntal texture of the data has come together to produce the intricate web, each pointing to the unifying subject of the thesis.

Future work in this area may involve a more extensive investigation of the variety of elements that could comprise a composite glass. Thus far, the focus has been on tin-based glasses, in response to the announcement by Fuji. Nevertheless, numerous other

composition could be considered, leading to new endeavours in both synthesis, and electrochemical characterization. In particular, further investigation of the bismuth-containing glasses would undoubtedly be fruitful.

In both the PDF and EXAFS studies, investigations of cycled electrode materials were prohibitive due to the amount of sample required for these experiments, and thus the requisite time for the electrochemical experiment. Future possibilities would include long term studies of cycled samples, or alternatively, *in-situ* characterization. As well, these techniques are both excellent tools for the study of other electrode materials. In particular, since PDF has not been applied to electrochemical systems previously, further development of the method for this application is warranted.

Continuing the multi-nuclear NMR studies of electrode materials will be a focus of much future work. In particular, a wealthy lab group should attempt the ^{17}O NMR investigation of the electrode materials. As oxygen has been implicated heavily in the electrochemical processes, such a study would prove very revealing. The by-now-standard $^{6,7}Li$ NMR studies of electrode materials can be extended to a variety of systems in which the mechanism of lithium insertion is unclear. Examples in our own lab group include transition metal nitrides and lithiated iron or vanadium phosphates, both of which are being studied for their electrochemical properties. Extending the NMR work beyond simple 1D studies would also be intriguing. For example, multiple quantum magic angle spinning studies of the aluminum in the TCO glass would give further information as to its coordination environment, and the structural changes occurring during discharge.

Finally, on the wish-list of the lab group is an *in-situ* electrochemical cell/NMR probe. Building such a probe was beyond the engineering capabilities of this student, nevertheless, such probes are under development in other labs, and would increase the rate of data acquisition by orders of magnitude!